DPT. DE FÍSICA E INGENIERÍA DE SUPERFICIES
INSTITUTO DE CIENCIA DE MATERIALES DE MADRID
CONSEJO SUPERIOR DE INVESTIGACIONES CIENTÍFICAS

CSIC

PhD. Thesis:

STUDY OF BORON-CARBON-NITROGEN COMPOUNDS FOR HARD COATING APPLICATIONS.

Raúl Gago Fernández

Supervision:
José María Albella Martín
Ignacio Jiménez Guerrero

Madrid, September of 2000

DEPARTAMENTO DE FÍSICA APLICADA,
FACULTAD DE CIENCIAS
UNIVERSIDAD AUTÓNOMA DE MADRID

To my family.

ACKNOWLEDMENTS:

I am indebted to Dr. J.M. Albella for accepting me in his group and for the supervision of my work during these five years.

I am also indebted to Dr. I. Jiménez for the supervision of this thesis and the intense work performed during these years. I would like to acknowledge the experience transmitted during the synchrotron work and, specially, his friendship. Now, I know how to use the chopsticks!

I would like to thank Dr. A. Climent-Font his tutorial during my PhD studies at the Universidad Autónoma de Madrid and for his help with the IBA measurements.

Thanks to Javier Ortíz for his help with the deposition system and for the technical support during this work.

Special mention to all the people that have worked with me day by day in the lab: Alex, Cristina, Fernando, Felix, Gema, Jimena, Marian, Marimar, Olga, Pachi, etc.

I am also indebted to Dr. J. Robertson and Dr. L.J. Terminello for accepting me in their groups during my short stays in their labs.

I also would like to mention the following people that have contributed to the achievement of this thesis:

D. Cáceres and I. Vergara for the nanoindentation measurements at Universidad Carlos III de Madrid and for the discussion of the mechanical properties.

F. Agulló-Rueda for the Raman measurements.

E. Román and O. Böhme for the AES measurements and the discussion of the results.

T. Sajavaara, E. Rauhala and J. Raisänen for their help with the IBA measurements at the University of Helsinki.

P. Parent and C. Laffon for their help with the synchrotron work at the LURE.

Iñaki García for the measurements of the coefficient of friction.

B. Doyle and J.C. Banks for their help at Sandia Labs.

Finally, I would like to acknowledge the financial support from the Spanish MEC. The synchrotron work was financed by the NATO project No.CRG-971539 at SSRL and the Training Mobility of Researchers (TMR) program of the European Union at LURE.

ACKNOWLEDMENTS i

INDEX iii

CHAPTER 1: INTRODUCTION 1

1.1. MECHANICAL PROPERTIES OF MATERIALS 4
1.1.1. Elasticity: Basic concepts 4
1.1.2. Hardness 6
a) Definition 6
b) Indentation: The hardness test 6
c) Microindentation 8
d) Nanoindentation 8
e) The load-displacement curve as a material "fingerprint" 9
1.1.3. Friction and wear 10
a) Tribology 10
b) Measurement of the coefficient of friction and wear 11
1.2. HARD COATINGS TECHNOLOGY 11
1.2.1. Hard materials for coating applications 12
1.2.2. Advanced layer concepts 15
1.2.3. Deposition methods in hard coating technology 16
1.2. THE SEARCH OF NEW SUPERHARD MATERIALS: THE BCN SYSTEM 18
1.3.1. Novel hypothetical β-C_3N_4 phase 20
1.3.2. Ternary BCN compounds 21
1.3.3. Amorphous carbon (a-C) and amorphous carbon nitride (a-CN_x) 21
1.4. MOTIVATION OF THIS WORK 22
REFERENCES 23

CHAPTER 2: EXPERIMENTAL SYSTEM 25

2.1. DEPOSITION SYSTEM 27
2.1.1. Electron beam evaporation 30
a) Basic concepts 30
b) Instrumentation 30
c) Evaporation of graphite and boron carbide (B_4C) 31
2.1.2. Ion beam assistance 33
a) Basic concepts 33
b) Relevant ion assistance parameters 37
c) Instrumentation 39
d) Ion beam characterisation 41
2.2. CHARACTERISATION TECHNIQUES 46
2.2.1. Profilometry 46
2.2.2. Vibrational spectroscopies: 46
a) Infrared (IR) spectroscopy 46
b) Raman spectroscopy 48
2.2.3. Ion beam analysis 48
a) Rutherford Backscattering Spectrometry (RBS) 48
b) Elastic Recoil Detection Analysis (ERDA) 50
c) Time-of-Flight Elastic Recoil Detection analysis (TOF-ERDA) 51
2.2.4. Core level spectroscopies 53
a) Auger Electron Spectroscopy (AES) 53
b) X-Ray Photoemission Spectroscopy (XPS) 54
c) X-Ray Absorption Near Edge Spectroscopy (XANES) 54
2.2.5. Mechanical properties: Nanoindentation 56
REFERENCES 58

CHAPTER 3: AMORPHOUS CARBON FILMS (a-C) 61

3.1 INTRODUCTION 63
3.2. FILM COMPOSITION 66
3.3. DEPOSITION RATE AND FILM DENSITY 67
3.4. BONDING STRUCTURE 69
3.4.1. Auger electron spectroscopy (AES). 69
3.4.2. X-Ray Absorption Near Edge Spectroscopy (XANES). 71
3.5. MICROSTRUCTURE 74
3.6. THERMAL STABILITY 77
3.7. MECHANICAL PROPERTIES 78
3.8. GROWTH MECHANISM 79
3.8.1. The IBAD growth method 79
3.8.2. Microstructure and bonding structure 80
3.9. CONCLUSIONS 82
REFERENCES 83

CHAPTER 4: AMORPHOUS CARBON NITRIDE FILMS (a-CNx) 87

4.1. INTRODUCTION 89
4.2. FILM COMPOSITION AND DEPOSITION RATE 90
4.2.1. Ion assistance with 100% N_2. 92
4.2.2. Ion assistance with N_2/Ar gas mixtures. 93
4.3. BONDING STRUCTURE 94
4.3.1. X-Ray Photoemission Spectroscopy (XPS) 94
4.3.2. X-Ray Absorption Near Edge Spectroscopy (XANES) 95
4.3.3. Identification of different bonding environments in graphitic a-CN_x 96
a) Ion assistance with 100% N_2. 96
b) Ion assistance with N_2/Ar gas mixtures. 99
4.3.4. Dependence of XANES features on X=[N]/[C]. 100
4.3.5. Superstructure of graphitic planes 101
a) Ion assistance with 100% N_2. 102
b) Ion assistance with N_2/Ar gas mixtures. 107
4.4. MICROSTRUCTURE 108
4.5. THERMAL STUDIES OF a-CN_x FILMS 110
4.5.1. Influence of the substrate temperature during deposition 110
4.5.2. Influence of post-deposition annealing 111
4.6. MECHANICAL PROPERTIES 113
4.6.1. Ion assistance with 100% N_2. 113
4.6.2. Ion assistance with N_2/Ar gas mixtures 114
4.7. CONCLUSIONS 115
REFERENCES 116

CHAPTER 5: TERNARY BORON-CARBON-NITROGEN FILMS 119

5.1. INTRODUCTION 121
5.2. FILM COMPOSITION AND DEPOSITION RATE 122
5.2.1. Ion assistance with 100% N_2. 122
5.2.2. Ion assistance with N_2/Ar gas mixtures. 125
5.2.3. Ion assistance with N_2/CH_4 gas mixtures. 127
5.2.4. Ion assistance with N_2/Ar/CH_4 gas mixtures. 127
5.3. IDENTIFICATION OF TERNARY PHASES 129
5.3.1. Ion assistance with 100% N_2: Identification of hexagonal ternary phases 130
a) Infrared spectroscopy (IRS) 131
b) Visible Raman spectroscopy 132

c) X-Ray Absorption Near Edge Spectroscopy (XANES) 133
5.3.2. Ion assistance with N_2+Ar: Identification of cubic ternary phases 135
5.3.3. Ion assistance with N_2+CH_4: Effect of the carbon content on h-BCN 138
5.3.4. Ion assistance with N_2+Ar+CH_4: Effect of the carbon content on c-BCN 139
5.4. PREFERENTIAL ORIENTATION OF TERNARY PHASES. 140
5.5. CONTROL OF HEXAGONAL/CUBIC PHASES. 142
5.6. THERMAL STABILITY OF TERNARY PHASES 143
5.6.1. Influence of deposition temperature 143
5.6.2. Influence of the annealing temperature 145
a) Hexagonal ternary phases 145
b) Cubic ternary phases 146
5.7. MECHANICAL PROPERTIES 147
5.8. CONCLUSIONS 148
REFERENCES 149

CHAPTER 6: APPLICATIONS AND FUTURE DIRECTIONS OF THIS WORK 153

6.1. HARD COATING APPLICATIONS 155
6.2. FIELD EMISSION DISPLAYS (FED) 157
6.2.1. Introduction 157
6.2.2. Experimental set-up: Measurement of electron emission. 158
6.2.3. Electron emission of BCN films 159
a) Amorphous carbon films. 159
b) Amorphous carbon nitride films. 160
c) Hexagonal/B_xC-like ternary BCN compounds. 161
d) Hexagonal/Cubic BCN ternary compounds. 162
6.3. MULTILAYERS 163
6.3.1. Introduction. 163
6.3.2. Multilayers with BCN materials 164
6.4. CONCLUSIONS 165
REFERENCES 166

CHAPTER 7: CONCLUSIONS 167

7.1. ION ASSISTANCE DURING GRAPHITE EVAPORATION 169
7.2. ION ASSISTANCE DURING BORON CARBIDE (B_4C) EVAPORATION 169
7.3. APPLICATIONS AND FUTURE DIRECTIONS OF THIS WORK 170

APPENDIX: RESUMEN Y CONCLUSIONES 171

A. RESUMEN 173
B. CONCLUSIONES 176
B.1. Asistencia con iones durante la evaporación de grafito 176
B.2. Asistencia con iones durante la evaporación de carburo de boro (B_4C) 177
B.3. Aplicaciones y perspectivas de futuro 177

Chapter 1:

Introduction

1. INTRODUCTION

Nowadays, many industrial processes require of protective coatings in machining tools. During operation, these tools suffer severe friction against counteracting parts and reach high temperatures. The development of materials for hard coatings applications has permitted the improvement of the tool performances by increasing the durability of the tools and avoiding the use of hazardous coolants [1]. In this way, there is an increment of the productivity, a reduction of the production cost and a major protection of the environment [2]. The importance of hard coatings is illustrated by the fact that today more than 40% of all cutting tools are coated and the market is growing fast [2].

The practical use of a material as protective coating is governed by the actual performance of the substrate/ /layer structure [3]. Figure 1.1 provides some important requirements of the substrate/layer composite. In this way, one can distinguish three different zones in the substrate/layer composite, each having different property requirements. Region I considers the substrate/film interface. In this case, adherence, interaction/reaction of the substrate with the layer and strains by thermal expansion misfit are critical points. In the second region or layer material, the composition and microstructure determine properties such as hardness, strength, internal stress or thermal stability. Finally, in the third layer, which corresponds to the layer surface, the interaction of the layer material with the work piece (friction) or with the environment (chemical inertness) has to be considered.

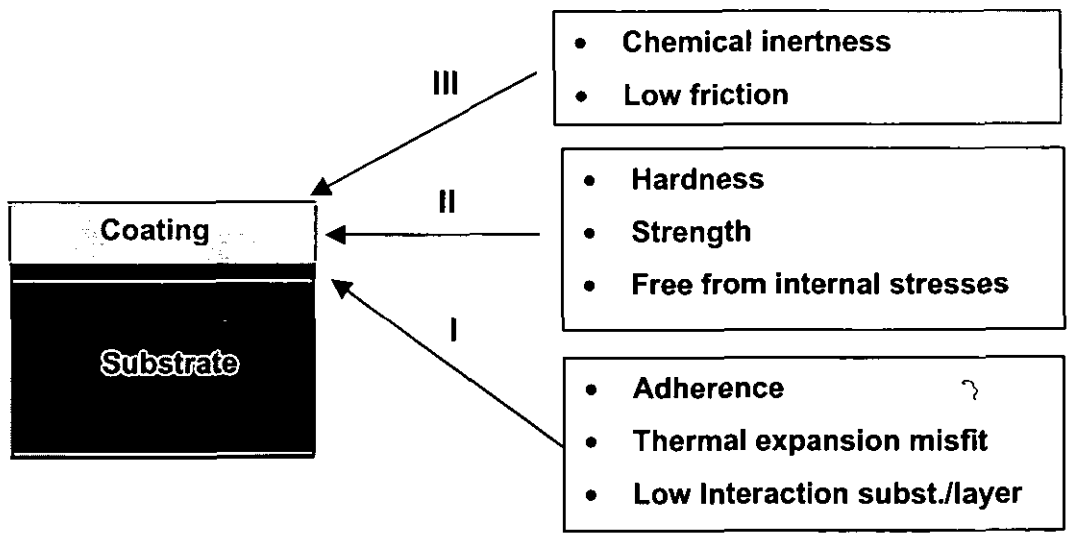

Figure 1.1. Important requirements for the substrate-layer composite.

In this work we mostly focus on the improvement of the intrinsic properties of the coating such as hardness. In this introduction, we first introduce basic concepts about the mechanical properties of materials and how they can be measured. Then we review the existing materials in hard coating

technology. Finally, we present the content of this thesis as the study of novel materials in the Boron-Carbon-Nitrogen (BCN) system for hard coatings applications.

1.1. MECHANICAL PROPERTIES OF MATERIALS

The mechanical properties define how a material withstands an applied force. The characteristics of the material such as composition, bonding environments, crystallinity, defects, etc determine these properties. The knowledge of the mechanical behaviour is fundamental in order to discern the potential applications of the material. Adherence, wear resistance, hardness, friction coefficient, etc., are relevance parameters to be considered. In the following, we describe important aspects regarding the mechanical properties of materials and how they can be measured. We devote especial attention to materials in thin film form.

1.1.1. Elasticity: Basic concepts.

In order to study the basic mechanical properties we consider the simplest mechanical test, i.e. the tensile test [4]. This test measures the resistance of a material to a static or slowly applied unidirectional force, as illustrated in the left part of Figure 1.2. The mechanical behaviour of a material is characterised by the load-deformation curve, as shown in the figure [4]. The stress, σ, is defined as the applied load (F) over the cross-sectional area of the specimen before the test begins (A_0) and the strain, ε, corresponds to the length increase ($L-L_0$) over the initial length of the material (L_0). From the tensile test information concerning the strength, stiffness and ductibility of a material can be obtained [4].

As the load is initially applied, the material is deformed elastically, i.e. the original shape would be recovered after removing the load. In this regime, the stress and strain follow a linear relation as the material behaves like a spring (Hook's law). The **yield strength** is the stress at which plastic or permanent deformation becomes noticeable. Therefore, the yield strength divides the elastic and plastic behaviour of the material. In the plastic regime, the material is easily deformed and, hence, the stress increase necessary to produce a certain strain is lower than in the elastic case. The stress obtained at the highest applied force is defined as the **tensile strength**. At some point, one region deforms more than the others do and a large local decrease in the cross-sectional area occurs (neck). Because the cross-sectional area becomes smaller at this point, a lower force is required to continue deformation and the stress (F/A_0) decreases. The tensile strength is the stress at which necking begins in ductile materials. For increasing stress, the cross-sectional area becomes smaller and smaller until **fracture** of the material takes place. The **ductibility** of a material is the amount of plastic deformation that a material can withstand without breaking.

In the elastic regime, the behaviour of the material is characterised by several parameters. The **elastic modulus** or **Young modulus**, $E=\sigma/\varepsilon$, corresponds to the slope of the stress-strain curve in the

elastic region. The elastic modulus is closed related to the binding energies. A high E value indicates that high forces are required to separate atoms and cause the material to stretch elastically. Therefore, the elastic modulus is a measure of the **stiffness** of a material. A stiff material maintains its size and shape after recovery of an elastic load.

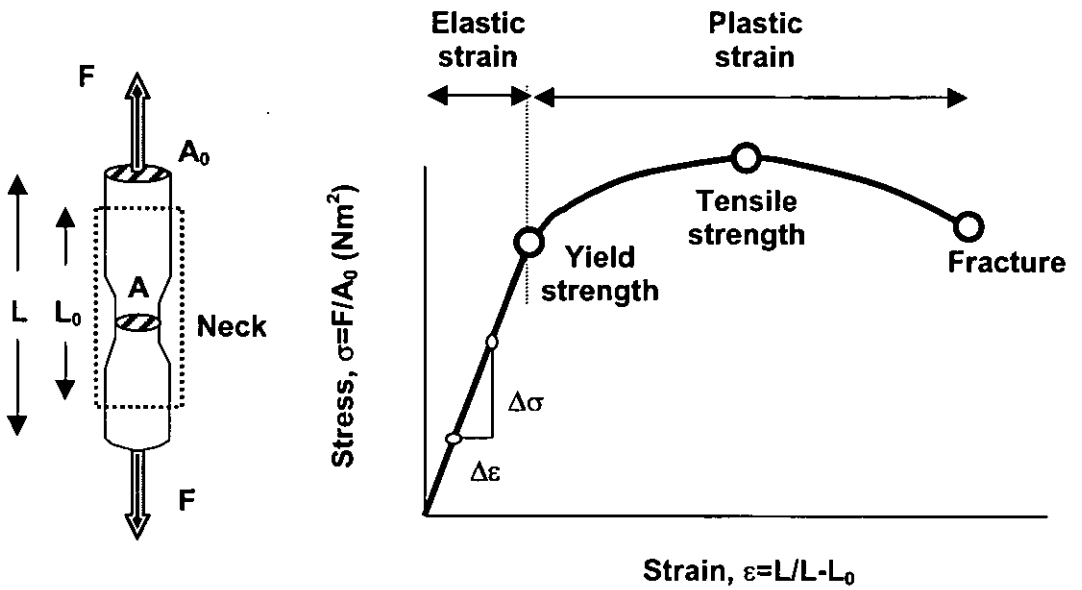

Figure 1.2. Tensile test and typical stress-strain curve of a material.

Another parameter of interest that determines the elastic properties of a material is the **Poisson's ratio**, $\nu = -\varepsilon_{lateral}/\varepsilon_{longitudinal}$, which relates the longitudinal elastic deformation produced by a simple tensile or compressive stress to the lateral deformation that occurs simultaneously. The Poisson's ratio is typically about 0.3.

When the force is not unidirectional other parameters apart from those described determine the elastic response of a material. The **bulk modulus**, $K=\Delta\sigma/(-\Delta V)$, corresponds to the pressure necessary to produce a relative volumetric deformation of the material and, therefore, is proportional to the material compressibility. The **shear modulus**, $G=\Delta\tau/\Delta\gamma$, gives the angle of deformation, γ, produced by the application of a shear stress, τ, in the solid without a change in the volume.

The bulk modulus and the shear modulus can be expressed as a function of the elastic modulus, E, and Poisson's ratio, ν, by $K=E/3(1-\nu)$ and $G=E/2(1+\nu)$. Therefore, the basic mechanical properties are correlated and we only have to know two of them in order to characterise the elastic response of a material.

1.1.2. Hardness

a) Definition

Hardness is a mechanical property difficult to define and also to measure. In a general sense, hardness is defined as the resistance offered by a given material to an external mechanical action looking to produce a permanent deformation [5]. In order to approach hardness from a theoretical point of view, we must simplify the problem adopting several assumptions. First, we can assume a perfect bulk crystal and the application of an isostatic pressure as external action. In this way, hardness could be proportional to the deformation of the material and, hence, to the bulk modulus. Of course, another external mechanical actions such as shear stress can be considered being, in this case, the hardness proportional to the shear modulus. An external action can also be composed of shear and tensile stress, making difficult a correlation between hardness and intrinsic parameters of the material such as bulk or shear modulus. In addition, in a real material deformation occurs more easily than in a perfect crystal due to the presence of dislocations [6]. If we assume that hardness is proportional to the bulk modulus, theoretical high hardness requires of high bond energy, high coordination number and small bond length [7]. The practical hardness can be less than that predicted by the bulk modulus because hardness is also determined by the microstructure, which can hinder the multiplication and movement of dislocations [7].

In order to apply a material in a real coating it is clear that we have to consider the practical and not the theoretical value of hardness. However, this is not a trivial question to answer since, as previously discussed, hardness depends on the specific mechanical action test. In this way, the nature of the load defines at least three hardness categories: (i) **Scratch hardness**: the test consists in scratching the surface applying a known load. An example of this test is the Martens or Mohs scale (employed by mineralogists). (ii) **Static indentation hardness**: In this case, a normal load is applied at low velocity upon the sample recording the resulting indentation depth. (iii) **Dynamic hardness**: The indenter falls in the gravity from a given height, measuring the indentation as a function of the impact energy [8].

Among the methods described above, the static indentation tests have been much favoured owing to their many advantages when applied to coating systems [9,10]. The most relevant feature of this method is the ability to distinguish the deformation of individual components in the sample. It therefore offers potential means of calculating the individual properties of the coating and substrate.

b) Indentation: The hardness test.

The principle of the indentation test is based on the measurement of the impression produced in the material by applying, with a specific indenter in contact with the surface of the material, a constant load for a fixed time. The hardness is determined by the ratio between the applied load and the plastic area deformation. Therefore, hardness is expressed in pressure units. A schematic diagram of an indentation test is displayed in Figure 1.3.

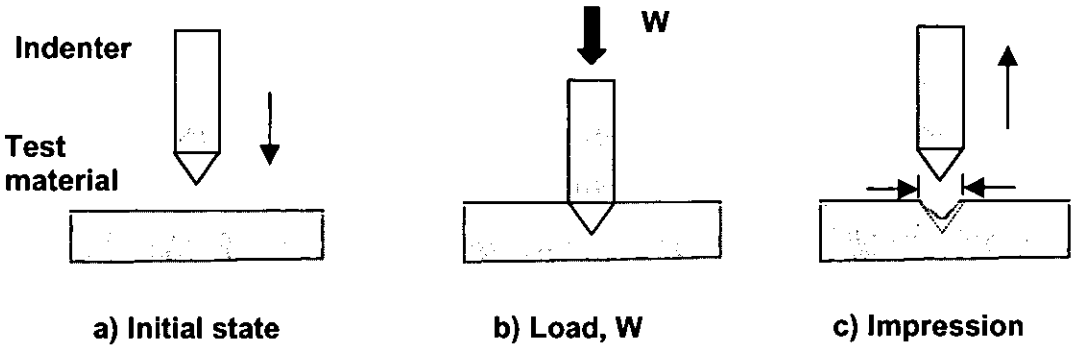

Figure 1.3. The indentation test. The hardness value is obtained from the ratio between the applied load, W, and the surface area of the impression.

The different indentation methods are classified regarding the tip geometry. The shape of the projected area of the impression depends on the specific tip geometry and their parameters (diameter, diagonals, etc.) are generally measured optically in order to calculate the hardness value. Traditionally, sharp pyramidal indenters have been used for indentation experiments, primarily because they will create the large shear stresses necessary to cause plastic flow [11]. However, non-faceted indenter shapes, for example hemispheres, create stress fields which are more amenable to analytical solution, avoid the problems associated with characterising the exact geometry of the tip-end shape, may allow a greater range of strains during indentation and allow easier measurements of the elastic constants [12,13]. Thus, a range of indenter geometries may be needed to provide complete mechanical characterisation of a system. Some of these methods are illustrated in Figure 1.4.

In the Brinell test, a hardened steel or tungsten carbide ball is pressed into the surface for a standard time (~10-15 secs) under a standard load. After removing the load, the diameter of the circular impression is then measured. The Brinell harness value is calculated from the diameter of the ball, D, and the indentation diameter, d. In order to obtain accurate Brinell values the relationship d/D should be between 0.25 and 0.5. In this way, the ball diameter and the load applied is specific for the material under test. In the Brinell test the impression is large (~2-4 mm) and, therefore, is not proper for thin films. Finally, very hard materials may deform the indenter.

The Vickers indenter is a square based pyramid with an included angle of 136°. The tip is made of diamond and, therefore, this test is suitable for hard as well as soft materials. The Vickers method can be applied to all kind of materials with the only criterion that the impression should be large enough to be measured accurately. In addition, the Vickers value range is proportional to the hardness. These facts have motivated the use of Vickers as a standard test in the hardness measurement.

There are other pyramidal indenters such as Knoop and Berkovich. The Knoop indenter is rhombic pyramid whereas Berkovich is triangular. The shape of the Knoop indenter is more suitable for thin films than the Vickers one since permits to penetrate less under the same load. The Berkovich indenter produces full plasticity at very small loads and, therefore, it is ideal for ultra-low load testing (nanoindentation) [14]. The Berkovich hardness can be directly compared with that obtained with the Vickers method and, in addition, it is easier to manufacture than the Vickers geometry.

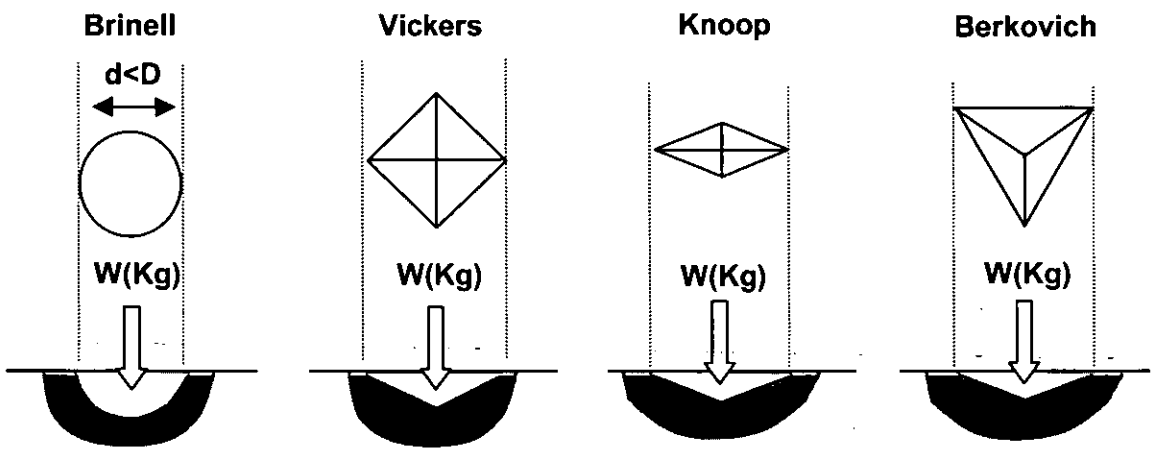

Figure 1.4. Different indentation tests regarding the tip geometry. The scheme shows the corresponding surface projected impression for each indenter.

c) Microindentation

When the material is in thin film form, i.e. thickness of several microns, the indentation depth has to be in the range of a micron to exclude the effect of substrate deformation. In this case, to obtain a reliable measure the maximum indentation depth has to be less than 5% of the film thickness [15]. Therefore, film thickness ≥ 5 μm is required to obtain good measurements.

Vickers indenters are normally used in microhardness tests. However, this method provides a small size of the impression. In order to reduce this problem, the material has to be polished flat and we have to be secured that the surface is perpendicular to the indenter [4].

d) Nanoindentation

In standard deposition methods (see section 1.2.1b) it is generally difficult to attain film thickness over 1 μm. Therefore, in order to measure the mechanical properties of very thin films excluding the effect of the substrate, we have to perform nanoindentations, i.e. penetrations depths below 1 μm. The development of load and depth sensing methods with resolution around 1 μN and 1 nm, respectively,

have permitted to measure indentations in the submicron range [16]. Typical load ranges are approximately 0.1-100 mN and displacements as small as 0.2 nm can be measured [17]. This development has allowed testing very thin films and surface layers. As in microindentation, the penetration depth has to be only a small fraction of the coating thickness [18].

However, for very low indentations new factor must be considered since the smaller the indentation depth the higher indentation size effect (ISE), which accounts for an increase of the hardness for very small displacements [19]. In addition, in nanoindentation we have to be careful with the effect of surface contamination, roughness of the surface and creeping effects. Taken into account this facts, indentation depths around 10% of the film thickness are generally accepted in order to obtain optimal results.

e) The load-displacement curve as a material's 'fingerprint'

In micro and nanoindentation the measurement of the residual impression can be a difficult task due to the small indentation size. This problem can be solved since the mechanical properties such as hardness and elastic modulus can be also derived from the data of the load-unload cycle [19]. In the loading and unloading process, the penetration of a diamond tip is recorded as a function of the applied load. An example of typical load-displacement curves for different behaviours is shown in Figure 1.5. Curve (a) displays a highly plastic response, which is characteristic of most metals. In this case, there is large permanent deformation as the displacement at maximum load is close to the displacement after the load is removed. A highly elastic response is shown in curve (b), which is typical of many ceramics and implies a high elastic recovery of the material.

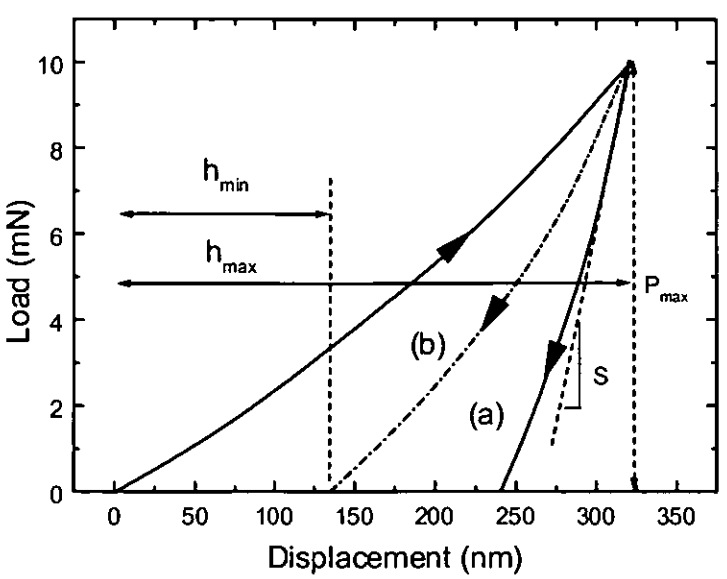

Figure 1.5. Load-displacement curves during the load-unloading process for a highly plastic response (a) and highly elastic response (b).

The elastic or reduced modulus, E_r, is obtained from the slope of the unloading curve (stiffness, S) at the maximum load [20]. The projected contact area for the calculation of the hardness and elastic modulus can be extracted directly from the load-displacement data based on the notion that, at peak load, the material conforms to the shape of the indenter to some depth, which is established by the data [21]. The analysis is based on analytical solutions accounting the curvature of the unloading data and the indenter shape function to establish the contact area at peak load.

The elastic recovery is an additional parameter than can be computed from the load-displacement curve. Its value is the ratio between the displacement after loading (h_{min} in Fig. 1.4) and the displacement at maximum load (h_{max} in Fig. 1.4). The analytical expressions for the computation of the elastic modulus works well when the unloading curve approximates to either a linear behaviour or some power-law relation [22]. However, when there is considerable elastic recovery, which unfortunately applies to many stiff and hard coating systems, non of the existing analytical models work particularly well.

1.1.3. Friction and wear.

a) Tribology

The field of science and technology that deals with contacting surfaces in relative motion is called **tribology** [23]. Interacting surfaces in relative motion occur extensively in technology such as bearing, joints, gears, sliders, etc. The variety of conditions where the surfaces are expected to fulfil demanding requirements is thus extremely wide. In manufacturing processes such as metal cutting or extrusion, the tool surface is exposed to severe conditions by a counterface, which is generally in a fast-moving and high temperature state. In addition, the moving counterfaces can be hard and sharp edged, producing a high wear rate in the machining tool. The wear and friction are the phenomena involved in tribological studies.

Friction refers to the tangential resistance to motion, which is experienced when one body moves relative to the other [24]. The coefficient of friction, $\mu=F/N$, is the frictional force F divided by the normal load, N, on the contact. Note that on a macroscopic scale, the friction coefficient is independent of the contact area for each combination of counteracting materials. However, in a microscopic scale friction does depend on the contact region between the two sliding surfaces. Friction at an atomic scale is an active area of research in Surface Science.

Wear has been defined as the removal of material from solid surfaces as a result of one contacting surface moving over other [23]. Thus both friction and wear are simultaneously the result of the same tribological contact process that takes place between two moving surfaces. However, the interrelationship between wear and friction is not well understood. Experimentally, it has been found a linear relation [25] although this is not a general case.

b) Measurement of the coefficient of friction and wear.

Given the variety of possible mechanisms operating during a tribological contact, it is not surprising that there are very many different configurations available to test the friction and wear. Generally, sliding tests are performed [23]. In these tests, the relative motion between the specimen and a probe in contact with the specimen is measured as a function of normal load, W, applied with the probe. The wear rate is obtained from the size reduction of the probe or the weight loss of the material. Figure 1.6 illustrates the basic principles for some of the most relevant sliding tests. The pin on disk test (figure 1.6a) is by far the most widely used method [26]. In this test, a pin or ball rubes against a disc. The control of humidity and temperature is critical to perform repeatable tests. In the pin on flat test (1.6b) the pin or ball rubes against a plate. The coefficient of friction is measured by reciprocating at a sliding fixed frequency. Both methods are suitable for coating evaluation. Other methods may be designed to simulate the actual contact conditions during a certain operation and, therefore, the results become easier to transfer to a specific application.

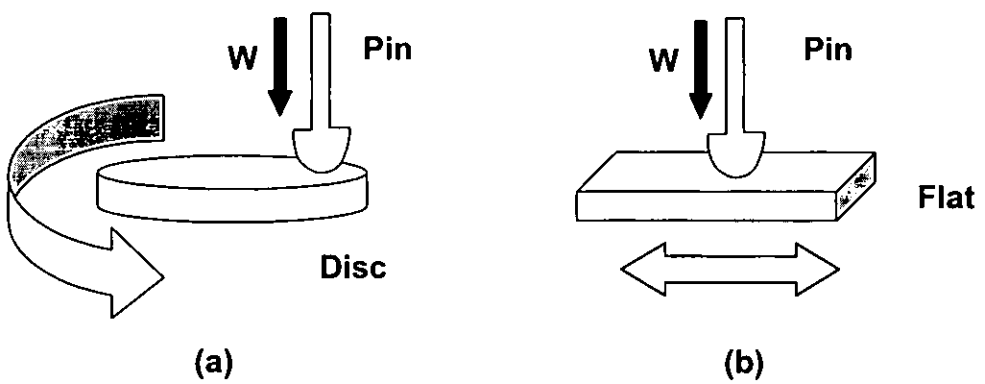

Figure 1.6. Basic principles of some sliding tests for the measurement of the coefficient of friction: (a) Pin on disc and (b) pin on flat.

1.2. HARD COATING TECHNOLOGY

The reduction of the wear rate has been subject of intense research. This technological challenge has been achieved by design changes, selecting improved bulk materials, or by utilising lubrication techniques [23]. A recent approach is the use of surface treatments and coatings to improve the tribological properties of materials. This has led to the growth of a new discipline called Surface Engineering [27], which has been encouraged by two main factors. The first has been the development of new coatings and treatment methods, which provide tribological characteristics previously unachievable. The second reason has been the recognition that the surface is the most important part in many

engineering components. We focus the discussion on the modification of the tribological properties by means of a coating.

The tribological behaviour of a coated surface is mostly influenced by the relationship between the hardness of the coating and that of the substrate. In this way, it is common to consider hard and soft coatings separately [28], as illustrated in Figure 1.7. The frictional force, F, is ideally the product of the shear strength, τ, and the contact area, A. The advantage of using a soft coating on a hard substrate to reduce the wear is explained by a decrease of the friction since the interfacial shear strength is lower. A hard coating on a softer substrate can reduce wear by reducing the contact area and, therefore, the frictional force. The use of a hard coating over a soft substrate can also reduce the wear by preventing ploughing. In this thesis we are interested on the study of hard materials for coating applications. In the following, the most relevant aspects of hard coating technology are summarised.

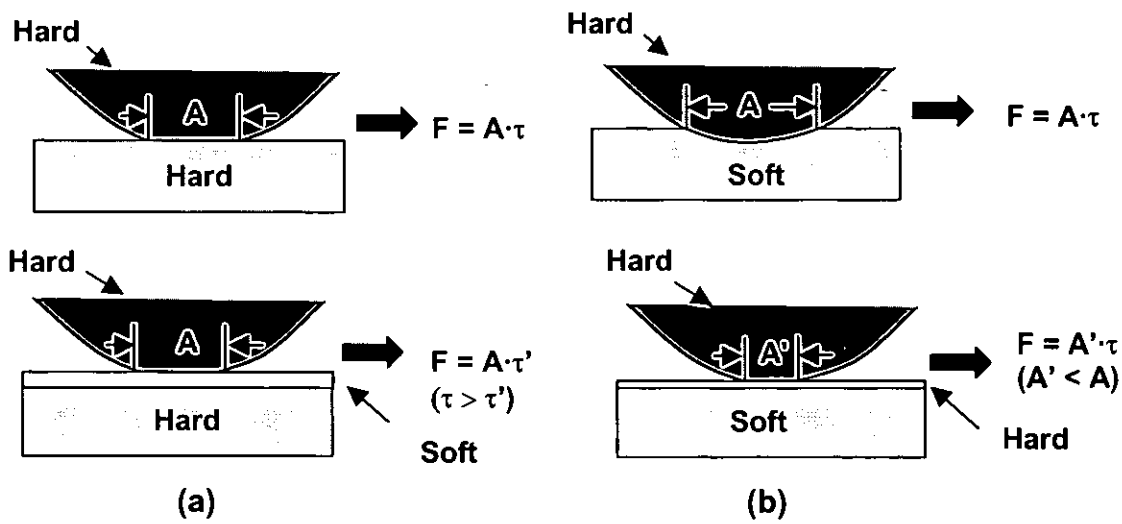

Figure 1.7. Friction reduction by depositing a soft coating on a hard substrate (a) or a hard coating on a soft substrate (b).

1.2.1. Hard materials for coatings applications

The range of Vickers hardness for a selection of different hard materials is shown in Figure 1.8. In a general sense, superhard materials can be defined as having a hardness value above 40 GPa [29]. From Fig. 1.8 it is evident that diamond has an outstanding position as far as hardness is concerned.

The hard materials that are illustrated in Fig. 1.8 are characterised by a great variety of compositions resulting from differences in the chemical bonding and structure [30]. Three groups can be distinguished according to their chemical bonding character as shown in Figure 1.9. Despite this classification, all materials of interest for protective layers are characterised by mixed bonding [31].

Metallic hard materials denote substances with a considerable fraction of metal-metal bonds. In this group, borides, carbides and nitrides of transition metals are included. **Covalent** hard materials are characterised by highly directional covalent bonds such as borides, carbides and nitrides of Al, Si, and B, as well as diamond. Finally, **ionic or heteropolar** substances, which must also have covalent bond fractions (oxides of Al, Zr, Ti, and Be).

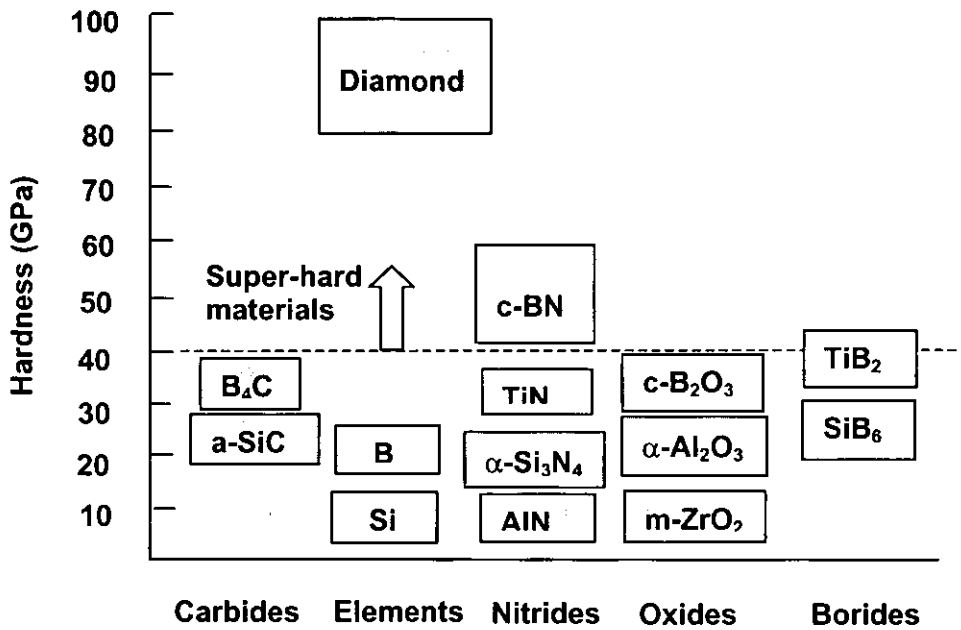

Figure 1.8. Range of hardness of some hard materials. The nomenclature c-X means cubic phases whereas m-X is referred to monoclinic.

The structures that confer good mechanical properties to each of the three groups can also be seen in Fig. 1.9. The carbides, nitrides and borides of the transition metals crystallise in so-called interstitial structures, i.e. densely packed lattices of large metal atoms with the non-metal atoms positioned in the octahedral holes and joined to the metal lattice by covalent and heteropolar bonding fractions. In heteropolar ionic materials we observe the opposite behaviour since the small cations are distributed regularly over the relatively simple sublattices of large oxygen anions. Covalent materials crystallise in the arrangement typical of highly directional, saturated bonds, with a resultant lesser tendency to interact with other materials at interfaces. Finally, it is important to note that many hard materials are based on one of the previous structures but lack of long-range order being, hence, amorphous. However, the short-range order of the bonding structure is similar to their crystalline equivalent and keeps to some extent the properties of the crystalline phases.

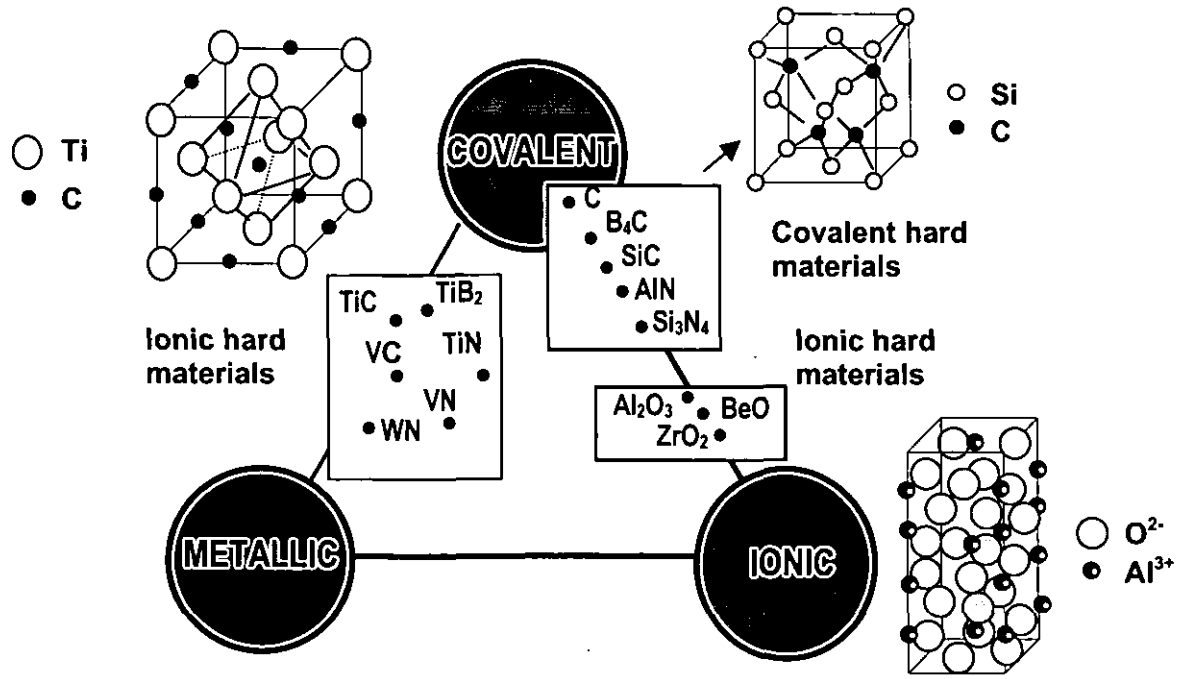

Figure 1.9. Groups of hard materials for coatings and typical structures as a function of the different types of bonding.

Diamond and **diamond-like** coatings have attracted rapidly much interest since the middle of 1980's and they are probably today the most intensively studied surface coatings [32]. Diamond is the hardest material known (H~90-100 GPa). Its crystalline structure is a cubic lattice with zincblende configuration with a four-fold sp^3 covalent bond structure [33]. Diamond is the stable carbon phase under high pressure and high temperature (HPHT) conditions but becomes metastable at room temperature and pressure. Diamond-like carbon (DLC) coatings are dense, metastable forms of amorphous carbon (a-C) or hydrogenated amorphous carbon (a-C:H) containing a significant amount of sp^3 carbon atoms [34]. The formation of sp^3 hybrids confers to diamond and diamond like coatings unique properties such as high hardness, scratch and wear resistance, IR and visible transparency and chemical inertness [34]. The commercial interest in diamond and diamond-like coatings is considerably, not only because of their great potential in tribological properties but also because of their potential as high temperature semiconductor and optical thin film material [35].

Titanium nitride (TiN) is very suitable as a hard coating due to its high hardness (~30 GPa), good adhesion to steel substrates and chemical stability [23]. It is mainly used on high speed steel tools for metal cutting but has also found other tribological applications, such as bearings, seals and as an erosion protection layer. One important attraction is its golden colour, which has also encouraged its use in decorative applications.

Even though titanium nitride coatings have a dominant market position there has been a variety of other **nitride coatings** with good mechanical performances. Aluminium nitride (AlN), boron nitride (BN), chromium nitride (CrN), silicon nitride (Si_3N_3), etc., have been extensively studied. The main uses of these nitride coatings have been in applications such as cutting tools, turbine blades, forming tools and pump components [36]. Among these nitrides, **boron nitride** has attracted much interest due to its isoelectronic character with elemental carbon, i.e. it can be found in a hexagonal arrangement (h-BN) similar to graphite and in a cubic zincblende structure (c-BN) similar to diamond [58]. Cubic boron nitride (c-BN) is the second hardest material and, in analogy with diamond, presents also chemical inertness, high resistivity, high thermal conductivity and transparency [37]. In addition, c-BN is also thermodynamically stable at HPHT conditions but become metastable phases under ambient conditions.

Boron carbide (B_4C) and **silicon carbide** (SiC) are also interesting materials. In particular, B_4C is the third hardest material (30-40 GPa) [38]. The complex structure of this material is based on icosahedrons units and three-atom linear chain [39]. Although the stoichiometry compound is nominally B_4C, the boron to carbon ratio can vary over a broad range by partial substitution of B by C atoms, both in the chains and in the icosahedra.

Metal carbides are generally hard, have a high melting point and good tribological properties. The coefficient of friction for bulk carbides sliding on themselves is low (~0.2) [40]. This is about one third of the coefficient of friction value of steel sliding against steel. Metal carbides such as titanium carbide (TiC), tungsten carbide (WC) and chromium carbide (CrC) are interesting coating materials.

Boride coatings are generally very hard and can be used mainly in tribological applications where good abrasive wear resistance is needed. The coefficient of friction in contacts with boride coatings is generally fairly high. Interesting boride coatings are titanium diboride (TiB_2), silicon boride (SiB_6) and iron boride (FeB). Iron boride may be useful as brake materials because of their peculiar property of giving very low wear and high friction at the same time.

Finally, **oxide coatings** of a few micrometers thick can resist high forces and temperatures and, therefore, may improve the tool lifetime by a factor of ~10 [41]. Aluminium oxide (Al_2O_3) is commonly used in sliding contacts. Other oxides such as beryllium (BeO) and zirconium oxide (ZrO_2) posses exceptional properties.

1.2.2. Advanced layer concepts.

Problems with the application of a coating arise mainly because many desired properties can not be found simultaneously. For example, a hard and inert phase is difficult to adhere strongly to any substrate. Because of complex requirements such as hardness and toughness, weak adhesion at the surface and, at the same time, good adherence at the substrate-layer boundary, multilayer or multiphase coatings seem to be the best compromise. These advanced layer concepts rely in the use of all possibilities to

deposit from the vapour phase novel materials modelled in terms of composition, structure and properties, and the possibility of producing modulated structures.

The basic principle of gradient layers is a layer design in which the substrate is first covered with a highly adhesive layer, whose composition changes gradually towards a stable outer layer with low interaction tendency. The adhesive layer should be a hard material with a relatively large fraction of metallic bonds. Examples of gradient coatings on metallic substrates are the transition WC-TiC-TiN or WC-TiN-Al_2O_3. The outer layer corresponds to the last material. In the former case, the gradient layers have shown better performances during wear tests than the materials deposited in a monophase layer [42]. In addition, the adhesion and coefficient of friction has been also reduced in amorphous carbon films with gradient layers of Cr-CrC-C [43].

The formation of solid solutions in an equilibrium state or a metastable supersaturated state generally results in strengthening [30]. This mechanism also leads to an increase in hardness, especially at high temperatures. The practical use of these structures requires of a good miscibility of the phases involved. In this context, many hard materials are miscible although present miscibility gaps at low temperatures [44]. Some mixed nitride layers materials such as (Ti,Hf)N [45], (Ti,Zr)N [46], (Ti,Nb)N [47] have been described in the literature. Also mixed carbide layers such as (Ti,V)C [48] and (Ti,W)C [42] and carbonitride layers Ti(C,N) [42] have been studied. In these materials, hardness peaks are obtained as a function of the composition and, at the same time, an increase in the time for crack propagation. Up to now, only the mixed carbonitride Ti(C,N) has found wide-spread application.

An increase in the toughness of a protective coating can exert a particularly influence on wear resistance [44]. In ceramic bulk materials, a fine-grained multiphase structure with a large number of interfaces often results on an increase in toughness. A similar type of behaviour has been detected in layers in which interfaces were introduced by multilayers parallel to the substrate surface [49]. In this type of structures, an appropriate design of the multilayer can result in a hardness enhancement [50]. Systematic studies have been performed for layer systems such as TiC-TiB_2, TiN-TiB_2 and TiC-TiN [49]. The multilayers are normally composed of 200-500 individual layers with a layer thickness of a few tens of nm. In this way, optimum characteristics with regards to crack propagation resistance and wear behaviour were obtained. There are indications showing that the cracks are deflected at the interface zones and, in this way, do not destroy the layer.

1.2.3. Deposition methods in hard coating technology

The rapid development of hard coating technology is largely due to the availability of new coating methods, which can provide properties that previously were unachievable [23]. Such properties include morphology, composition, structure and adhesion. Regarding industrial applications, it is important to consider growth processes with low cost, able to coat different surface shapes and easily

large-scaled. Also, practical coatings require film thickness over a micron and high growth rates are necessary to reduce the processing time.

The general classification system for the deposition processes considers four categories [27]: (i) gaseous state processes, (ii) solution state processes, (iii) molten or semi-molten state processes and (iv) solid state processes. The relevant techniques that belong to each category are illustrated in Figure 1.10. The two important characteristic parameters for the coating process are the coating thickness that can be achieved and the deposition temperature.

In this section we will concentrate in gaseous state process, which have mostly caused the development of coating technology. As discussed above, the hardest materials, diamond and c-BN, are thermodynamically stable at high pressure and high temperature but become metastable phases under ambient conditions. Therefore, conventional synthesis of these materials proceeds via shock-compression of graphitic or amorphous starting compounds [51,37]. The use of gaseous state processes under metastable conditions has permitted the deposition of these materials at low temperature (<500°C) and in thin film form.

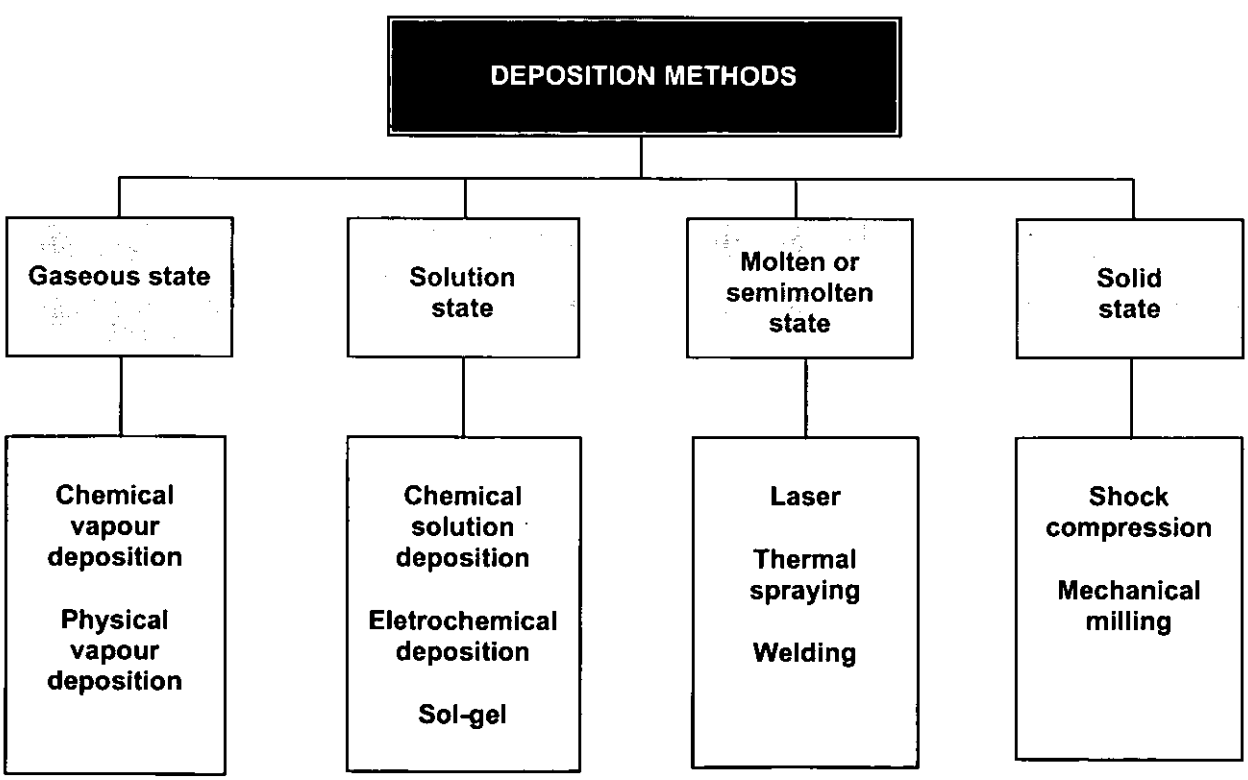

Figure 1.10. General classification of coatings deposition methods.

The gaseous state processes cover techniques in which the coating passes through a gaseous or vapour phase prior to depositing on the surface. The main generic subgroups are Chemical Vapour Deposition (CVD) and Physical Vapour Deposition (PVD) [52]. The CVD techniques use gaseous reactants as the source of coating species whereas in PVD methods at least one of the coating species is evaporated or otherwise atomised from solid within the coating chamber.

In the basic of CVD process, gases containing volatile compounds of the element or elements to be deposited are introduced into the reaction chamber and condense on to the substrate to form a coating. The different CVD methods are classified regarding the activation mechanism of the homogeneous reactions responsible of the formation of the coating. If the activation is thermal, we can differentiate between atmospheric pressure (APCVD) and low pressure (LPCVD) methods. The CVD methods based on the assistance of a plasma discharge (PACVD) to activate the deposition are classified regarding the nature of the discharge (DC, RF, ECR, etc.). The CVD techniques have the advantage of producing a conformal coating, allowing the deposition on complex shapes.

The different PVD techniques are classified regarding the physical process to obtain the vapour of the material to be condensed in the form of a film. The main PVD methods are thermal evaporation, electron beam evaporation, laser ablation, sputtering, arc discharge, etc. An advantage introduced by the PVD methods is the possibility to deposit alloy compounds, multilayer compositions and structures and the ability to vary coating characteristics continuously throughout the film, giving the concept of a functionality graded coating. These advanced coating concepts were introduced in the previous section.

1.3. SEARCH OF NEW SUPERHARD MATERIALS: THE BCN SYSTEM

The central challenge to modern Materials Science is the rational design and synthesis of new materials possessing exceptional properties [53,54,55,56]. An exciting example of this process of designing materials is the ongoing search for new superhard materials [57]. The synthesis of superhard materials is of great fundamental and technological interest [58]. The search of superhard materials is both driven by scientific curiosity to explore the possibilities of synthesising a material whose hardness could approach or even exceed that of diamond and the technical importance of hard and superhard materials for wear protection coatings.

Despite of their outstanding hardness, diamond and c-BN suffer the drawback that their use is limited for certain applications and the growth of these materials require of severe conditions (high pressure and high temperature). In particular, diamond is not stable in an oxygen atmosphere at temperatures above 600°C [59] and reacts with iron leading to the formation of iron carbide [60]. These facts limit the use of diamond as protective coating in cutting tools and high temperature devices. Cubic boron nitride is thermally very stable and can be used up to 1400°C in air [61]. However, its structure

presents high compressive stress (10-30 GPa), which limits the adhesion to the substrate and the maximum thickness of the material [62,63].

Between the candidates to exhibit superhardness only materials with pure covalent bonds are valid options. In this context, the promotion of the sp^3 hybridisations typical of diamond and c-BN seems to be of major importance. Since the three hardest materials known (diamond, c-BN and B_4C) belongs to the BCN composition triangle we concentrate in the study of boron-carbon-nitrogen materials. The most relevance materials in this ternary system are illustrated in Figure 1.11.

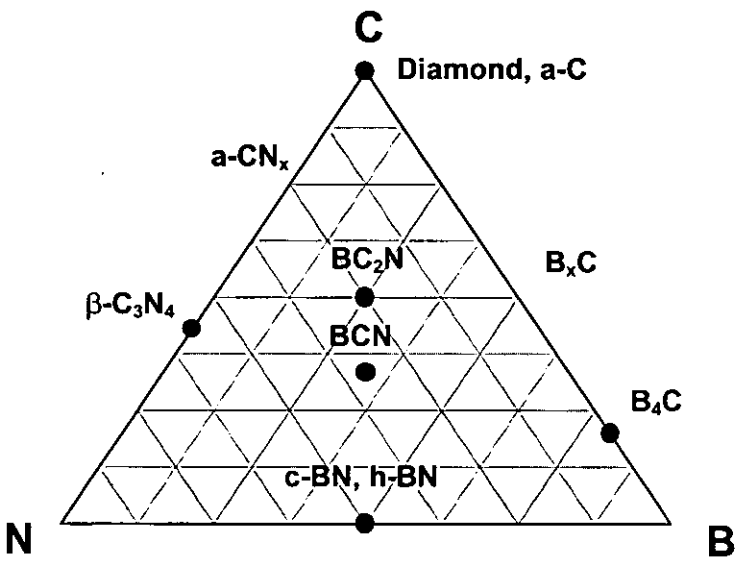

Figure 1.11. Most relevant materials in the B-C-N system.

The different structures that can be found in the BCN system are summarised in Figure 1.12. The hexagonal structure, typical of graphite and h-BN, is displayed in panel (b). In this structure, each atom presents a trigonal coordination with three nearest neighbours in the basal plane. The planes are piled rather loosely on one another since they are only attached by Van der Waals forces. In graphite, the distant between first neighbours in the basal planes is 1.42 Å and the distance between planes is 3.4 Å. The density of graphite is 2.26 g/cm^3 whereas it is 1.8 g/cm^3 for h-BN. The zincblende cubic structure, typical of diamond and c-BN, is shown in panel (b). The zincblende structure is a face centred cubic (f.c.c.) structure with two atoms in the unit cell. The atoms present a tetrahedral coordination with a short bond length (1.54 Å for diamond). This highly packed structure confers high density to the material, e.g. 3.51 g/cm^3 in diamond. The rhombohedral structure of boron based material is shown in panel (c). This structure is found in boron carbide and the unit cell of the rhombohedral lattice is composed of a icosahedral unit and a three atoms linear chain. Boron carbides exist within this structure over a wide range of compositions, from a carbon-saturated limit of 20 at. % (B_4C) to a boron-saturated limit of 91 at.

% ($B_{10}C$). The carbon and boron atoms are distributed within a unit cell of 15 atoms among four distinct crystallographic sites: (i) six equivalent equatorial sites in the icosahedron, (ii) six remaining polar icosahedral sites, (iii) two sites at the end of the chain and (iv) the unique site at the centre of the chain. The interchange of carbon and boron within these locations, together with the possibility of B_{12}, $B_{11}C$ and $B_{10}C_2$ icosahedra, and CBB, CBC and CCC chains, leads to the wide single phase region of boron carbides [64]. The distance between the atoms in each position is shown in the figure. The density of boron carbide is ~2.45 g/cm^3.

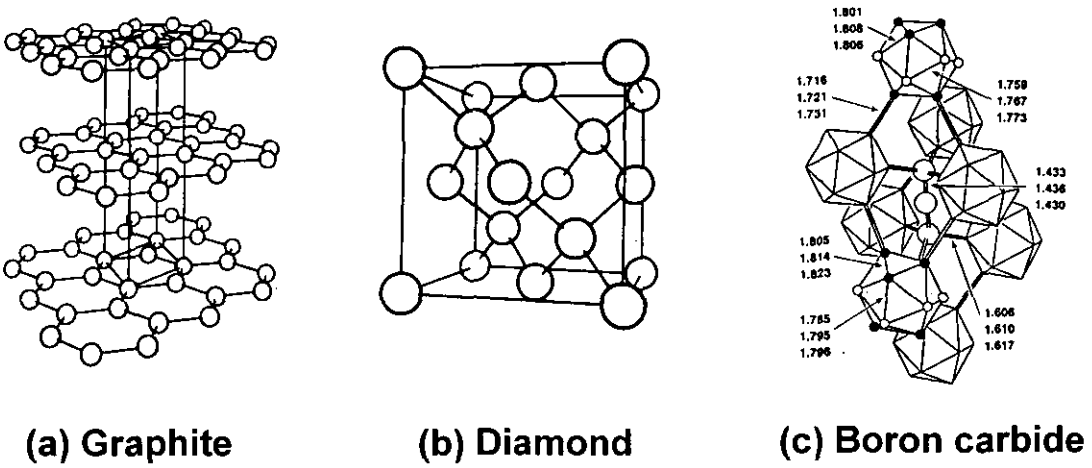

Figure 1.12. Different atom arrangements that can be found in the BCN system:
(a) Hexagonal (graphite), (b) tetrahedral (diamond) and (c) icosahedral (boron carbide).

1.3.1. Novel hypothetical β-C_3N_4 phase.

In 1985 Marvin Cohen developed an empirical relation between the bulk modulus of tetrahedrally coordinated materials to the length and ionicity of their chemical bonds [65]. This model was successfully applied for the prediction of the bulk modulus of diamond and the β-Si_3N_4 phase. From the relationship derived, Cohen predicted that a tetrahedral carbon nitride phase would exhibit a bulk modulus of 496 GPa, higher than that of diamond (443 GPa), due to the short length and high covalency of the C-N bond. Therefore, hardness even higher than diamond should be expected if this material could be synthesised.

The study of CN materials was followed by the theoretical work of Cohen and Liu on an isostructural carbon nitride phase with β-Si_3N_4 [66]. The structure of β-C_3N_4 is based on that of β-Si_3N_4. In this structure, the unit cell is hexagonal. Carbon is tetrahedrally surrounded by nitrogen atoms, whereas nitrogen has a nearly planar trigonal coordination. As a consequence, carbon presents a sp^3 hybridisation

whereas nitrogen is in a sp^2-hybridised state. For this structure, ab initio calculations revealed a bulk modulus of 427 GPa [66], therefore approaching that of diamond.

Based on the above results, the hypothetical carbon nitride phase has motivated extensive theoretical and experimental efforts to study and synthesise this material. Despite many experimental works, there has been little success in achieving crystalline and tetrahedral structures of carbon nitride. Most of the attempts performed with conventional CVD and PVD techniques have resulted in amorphous CN_x with a limitation in the nitrogen content in the structure [67]. The attempts to synthesise carbon nitride by shock compression of organic nitrogen-containing precursors have also resulted in no evidence of tetrahedral bonding [68].

The lacks in the experimental synthesis of the β-C_3N_4 phase have posed the question if this material can be really synthesised. Recently, the energetic stability of the β-C_3N_4 phase has been questioned upon both chemical and thermodynamical grounds [69]. In addition, apart from the possible synthesis of this material, there is some uncertainty regarding the expected superhardness based on the questionable assumption that the bulk modulus is the only predictor of hardness [50]. Nevertheless, the theoretical works indicate that carbon nitride has a potential to be a solid with compressibility at least comparable to that of diamond.

1.3.2. Ternary BCN compounds.

Boron carbonitrides (BCN) are another promising candidate for the achievement of superhard materials. These compounds can be considered as solid solutions of carbon and BN. The possible achievement of ternary phases is based on the similarity between graphite and hexagonal boron nitride (h-BN) and between diamond and c-BN. Despite the close structural relationship between the known BN and C phases, only a few reports have been published in the field of ternary solid solutions, especially with cubic symmetry [70,71].

The BCN phases are expected to be thermally very stable (above 1000°C) as corresponding to boron nitride phases [72]. In addition, for cubic BCN phases, intermediate properties between diamond and c-BN would be expected [57]. Finally, the interest of these materials is reinforced since they have been scarcely studied and their bonding structure is poorly known.

1.3.3. Amorphous carbon (a-C) and amorphous carbon nitride (a-CN_x).

Finding materials harder than diamond seems to be a difficult task. Therefore, rather than finding harder materials, it might be more productive to consider the possibility of materials that, although with poorer performances as compared to c-BN and diamond, are more useful for certain applications. In this context, structures like amorphous carbon (a-C) and carbon nitride (a-CN_x) may offer interesting

performances. The interesting features of these materials are that they can be grown at room temperature, require easy growth conditions and present high hardness (~20-30 GPa) [73]. These materials are already being applied as protective coatings in hard disk industry [74].

1.4. MOTIVATION OF THIS WORK

This work has been developed in the Department of Surface Science and Physics Engineering of the Materials Science Institute of Madrid under the supervision of Dr. J.M. Albella and Dr. I. Jiménez. During the last decades, our group has been studying the synthesis of several materials in thin film form. Among the projects faced, an extensive work has been devoted to hard coating materials. The first works in this field dealt with the synthesis of diamond [75] and BN [76] by CVD methods.

As mentioned above, the drawbacks that are found for diamond and c-BN have motivated the study of materials with properties comparable to those of diamond and c-BN or that require less severe deposition conditions. Attending to the former premise, we have studied the deposition of diamond-like amorphous carbon films by PACVD. The main results of this study are collected in the graduate thesis *"Preparación y caracterización de láminas delgadas de DLC crecidas mediante PACVD a 35 kHz"* presented by me in 1998. The main advantage of these films is that they can be grown at room temperature. However, the PACVD technique presents the drawbacks that it is difficult to be large-scaled due to the confinement of the plasma and that the use of hydrocarbon gas precursors induces a high hydrogen intake (40-60 at. %). The high hydrogen content breaks the interconnectivity of the network and produces polymeric films, which results in a reduction of the hardness.

This work represents a further step on the search of alternative materials to diamond and c-BN. We have studied materials grown by PVD belonging to the Boron-Carbon-Nitrogen system. The use of PVD techniques permits the growth of hydrogen-free samples and the synthesis of a large number of materials only by changing the target material. The films have been grown by ion beam assisted evaporation, which belongs to the generic group of Ion Beam Assisted Deposition (IBAD) methods. The advantage of the evaporation method is its flexibility to deposit any kind of material, since there is no restriction on the starting source material as long as the evaporation temperature can be achieved. In addition, high deposition rates can be reached and large areas can be deposited in the evaporation process. However, the thermal energy (~KT) conferred to the evaporated atoms is not enough to promote the growth of energetic configurations such as sp^3 hybridisations. Therefore, the evaporation process is assisted with a concurrent bombardment that can be performed either with inert (Ar), reactive (N_2) ions or a mixture of both. The use of reactive ions is interesting in processes where the stoichiometry is important. The momentum transfer in the ion-atom collisions is the mechanism that confers hyperthermal energies to the incoming atoms. This mechanism plays and important role in the deposition although other additional effects have to be considered, as will be discussed in Chapter 2.

The main subject of this thesis is to study the bonding structure of different materials in the BCN system and its relation with the mechanical performances. These films are expected to present optimal applications as protective coatings on high-temperature and high-speed cutting tools so hardness, friction and thermal stability are important factors to be considered. In order to characterise the films, the composition, bonding structure and mechanical properties are measured as a function of the deposition parameters. Among the techniques employed, it is remarkable the compositional analysis performed with TOF-ERDA and the study of the bonding structure with XANES. The mechanical properties are determined by nanoindentation experiments. The film analysis is also completed with more conventional techniques like IR, Raman, XPS and AES.

The text is divided in seven chapters. In Chapter 1 we have introduced the main aspects and actual tendencies in hard coatings. In Chapter 2, the experimental system is described regarding the deposition system and characterisation techniques. The results of the thesis are presented through chapters 3 to 6. Chapters 3, 4 and 5 refer to the synthesis of a-C, a-CN_x and $B_xC_yN_z$ materials, respectively. The synthesis of a-CN_x and $B_xC_yN_z$ implies a further step in the IBAD process since reactive ions are used in the deposition process. A global discussion gathering all the results is presented in Chapter 6 concerning possible applications of the coatings obtained and future directions of this work. Finally, the main conclusions are summarised in Chapter 7.

REFERENCES

1. S. Veprek, J. Vac. Sci. Technol. A 17 (5) (1999) 2401.
2. T. Cselle, A. Barimani, Surf. Coat. Technol. 76-77 (1995) 712.
3. H. Holleck, J. Vac. Sci. Technol. A 4 (6) (1986) 2661.
4. D.R. Askeland, *"The Science and Engineering of Materials"*, Chapman&Hall (1996)
5. A. Szymanski and J.M. Szymanski, *"Hardness Estimation of Minerals, Rocks and Ceramic Materials"*, Elsevier, Amsterdam (1989).
6. C. Kittel, *"Introduction in Solid State Physics"*, Wiley, New York (1971).
7. R.W. Hertzberg, *"Deformation and Fracture Mechanics of Engineering Materials"*, Wiley, New York (1989).
8. J.S. Koehler, *"The hardness of metals"*, Clarendon, Oxford (1951).
9. K.C. Tang, R.D. Arnell, Thin Solid Films 355-356 (1999) 263.
10. B.D. Fabes, W.C. Oliver, R.A. McKee, F.J. Walker, J. Mater. Res. 7 (11) (1992) 3056.
11. T.F. Page, S.V. Hainsworth, Surf. Coat. Technol. 61 (1993) 201.
12. T.J.Bell, J.S. Field, M.V. Swain, Thin Solid Films 220 (1992) 289.
13. J.S. Field, M.V. Swain, J. Mater. Res. 8 (2) (1993) 297.
14. J. Hay, *"Mechanical testing by indentation"*, Applied Nano Metrics, Inc.

15. P.J. Burnett, D.S. Rickerby, Surf. Eng. 3 (1987) 69.
16. D. Stone, W.R. LaFontaine, P. Alexopoulus, T. Wu, C. Li, J. Mat. Res. 3 (1988) 141.
17. J.B. Pethica, R. Hutchings, W.C. Oliver, Philos. Mag. A 48 (1983) 593.
18. G.M. Pharr, W.C. Oliver, Mater. Res. Soc. Bull. 17 (1992) 28.
19. M.F. Doerner, W.D. Nix, J. Mat. Res. 1 (1986) 601.
20. G.M. Pharr, W.C. Oliver, F.R. Brotzen, J. Mater. Res. 7 (1992) 613.
21. J.B. Pethica, R. Hutchings, W.C. Oliver, Philos. Mag. A 48 (1983) 593.
22. S.V. Hainsworth, H.W. Chandler, T.F. Page, J. Mater. Res. 11 (1996) 8.
23. K.Holmberg, A. Matthews, *"Coatings Tribology: Properties, Techniques and Applications in Surface Engineering"*, Elsevier, Amsterdand (1994)
24. M. Alonso, E.J. Finn, *"Física vol. I: Mecánica"*, Addison-Wesley, México (1986)
25. P.C. Michael, N. Saka, E. Rabinowicz, Wear, 127(1) 15.
26. A. Matthews, K. Holmberg, *"Advanced Techniques for Surface Engeneering"*, Kluwer (1992)
27. D.S. Rickerby, A. Matthews, *"Advanced Surface Coatings: A handbook of surface engineering"*, Blacke, Glasgow (1991).
28. R.D. Arnell, Surf. Coat. Technol. 43/44 (1990) 674.
29. C.M. Sung, M. Sung, Mat. Chem. Phys. 43 (1996) 1.
30. H. Holleck, Surf. Coat. Technol. 43/44 (1990) 245.
31. H. Holleck, Metall 43 (1989) 614.
32. S. Neuville, A. Mattews, MRS Bulletin 9 (1997) 22.
33. B.H. Mahan, *"Química"*, Fondo Educativo Iberoamericano (1975).
34. J. Robertson, Pure & Appl. Chem. 66 (9) (1994) 1789.
35. J.C. Angus, C.C. Hayman, Science 241 (1988) 877.
36. H. Randhawa, P.C. Jonhson, R. Cunningham, J. Vac. Sci. Technol. A6 (3) (1988) 2136.
37. R.H. Wentorf, J. Chem. Phys. 26 (1957) 956.
38. F. Thévenot, J. Eur. Ceram. Soc. 6 (1990) 205.
39. G.H. Kwei, B. Morosin, J. Phys. Chem. 100 (1996) 8031.
40. B.L. Mordike, Wear 3 (1960) 374.
41. B. Lux, C. Colomber, H. Altena, K. Stjernberg, Thin Solid Films 138 (1986) 49.
42. R. Fella, H. Holleck, H. Schulz, Surf. and Coat. Technol. 36 (1988) 257.
43. V. Rigato, G. Maggioni, D. Boscarino, G. Mariotto, E. Bontempi, A.H.S. Jones, D. Camino, D. Teer, C. Santini, Surf. Coat. Technol. 119 (9) (1999) 580.
44. H.W. Holleck, Vacuum 41 (7-9) (1990) 2220.
45. G.R. Frenske, N. Kaufherr, W. Sproul, Thin Solid Films 153 (1987) 159.

46. S. Boelens, S. Veltrop, Surf. Coat. Technol. 33 (1987) 63.
47. U. König, Surf. Coat. Technol. 33 (1987) 91.
48. R. Nimmagadda, R.F. Bunshah, Thin Solid Films 45 (1977) 447.
49. H. Holleck, H. Schulz, Surf. Coat. Technol. 36 (1987) 11.
50. J.S. Koehler, Phys. Rev. B 2 (1970) 547.
51. P.S. DeCarli, J.C. Jamieson, Science 133 (1961) 1821.
52. J.L. Vossen, W. Kern, *"Thin Film Processes"*, Academic Press (1978).
53. M.L. Cohen, Science 234 (1986) 549.
54. M.L. Cohen, Nature 338 (1989) 291.
55. C.R.A. Catlow, G.D. Price, Nature 347 (1990) 243.
56. M.L. Cohen, Science 261 (1993) 308.
57. D.M. Teter, MRS. Bulletin 23 (1) (1998) 22.
58. R. Riedel, Adv. Mat. 6 (7/8) (1994) 549.
59. R. Rameshan, T. Roppel, C. Ellis, B.F. Hayeck, J. Electrochem. Soc. 137 (10) (1990) 3203.
60. M.S. Wong, R. Meilunas, T.P. Ong, R.P.H. Chang, Appl. Phys. Lett. 54 (1989) 2006.
61. R. Riedel, Adv. Mat. 4 (11) (1992) 759.
62. J. Ullmann, A.J. Kellock, J.E.E. Baglin, Thin Solid Films 341 (1999) 238.
63. M. Okamoto, Y. Utsumi, Y. Osaka, Jpn. J. Appl. Phys. 29 (1990) L1004.
64. D. Emin, Phys. Rev. B 38 (1988) 6041.
65. M.L. Cohen, Phys. Rev. B 32 (1985) 7988.
66. A.Y. Liu, A.Y., M.L. Cohen, Science 245 (1989) 841.
67. C. Ronning, H. Feldermann, R. Merk, H. Hofsäss, P. Reinke, J.U. Thiele, Phys. Rev. B 58 (4) (1998) 2207.
68. M.R. Wixom, J. Am. Ceram. Soc. 73 (1990) 1973.
69. J.V. Baddin, D.C. Nesting, Chem. Mater. 8 (1996) 535.
70. A.R. Badzian, Mater. Res. Bull. 16 (1981) 1385.
71. R. Riedel, J. Bill, G. Passing, Adv. Mat. 3 (1991) 551.
72. L. Vel, G. Demazeau, J. Etourneau, Mater. Sci. Eng. B 10 (1991) 149.
73. H. Ehrhardt, Surf. Coat. Technol. 74-75 (1995) 29.
74. A. Khurshudow, K. Kato, S. Daisuke, J. Vac. Sci. Technol. A 14 (5) (1996) 2935.
75. M.M. García, PhD. Thesis *"Estudio de la Nucleación y el Crecimiento de Láminas de Diamante"*, (1998).
76. E. Abdelhadi, PhD. Thesis, *"Síntesis de nitruro de boro y compuestos ternarios del tipo BNX (con X=Si,C) por técnicas de CVD"*, (1996).

Chapter 2:

Experimental system

2. EXPERIMENTAL SYSTEM

2.1. DEPOSITION SYSTEM

The thin films presented in this work have been grown using an ion beam assisted deposition (IBAD) system developed in our laboratory. A schematic diagram of the IBAD system is displayed in Figure 2.1. The deposition chamber is equipped with an electron beam evaporator and an ion gun. The film deposition consists in the thermal evaporation of the appropriate target material (graphite, boron carbide, etc) by electron-beam heating. The properties of the evaporated film can be modified with concurrent assistance with ion bombardment over the growing surface during deposition. In the following sections, we will describe in more detail the evaporation and assistance processes.

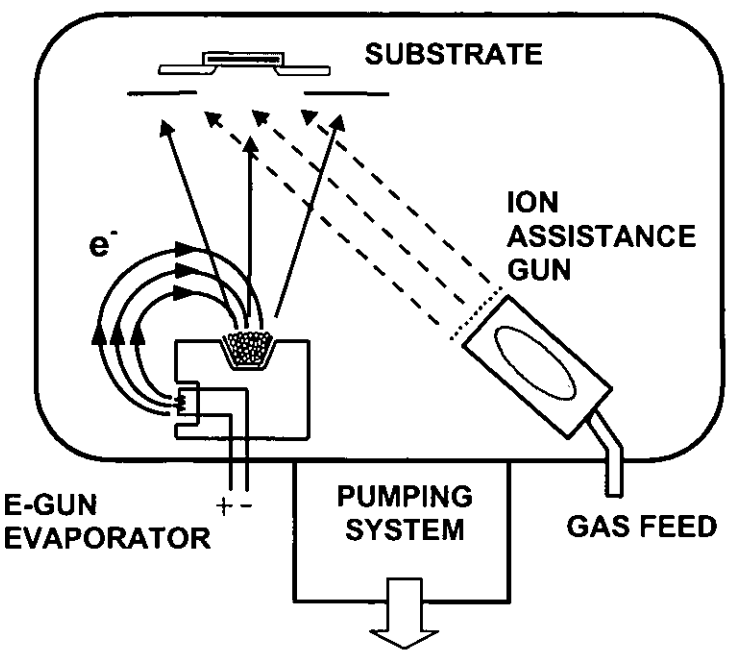

Figure 2.1. Diagram of the deposition system.

The operation of the IBAD system requires of working pressures between 10^{-3}-10^{-4} mbar as will be described below. The deposition chamber is evacuated with a Balzers DIF 200 diffusion pump, with a nominal pumping speed of 2000 l/s at 10^{-4} mbar for air. The rough vacuum, from atmospheric pressure to 0.1 mbar, is performed with a Balzers DUO 30A rotary pump with nominal pumping speed of 30 m^3/h at 10^3 mbar for air. With this pumping system, the residual pressure achieved prior to deposition is 2 10^{-7} mbar. During normal operation, the working pressure can be set in the optimal range selecting the gas inlet with UNIT gas flow controllers. For Ar and N_2, flows in the range of a few standard square cubic centimetres per minute (sccm) are necessary to achieve the working pressure within 10^{-3}-10^{-4} mbar.

2.1.1. Electron Beam evaporation.

a) Basic concepts

The evaporation process consists in the transformation of a solid source into vapour and the posterior condensation of the vapour on the substrate. The transition from the condensed state to gas phase is achieved by heating the target until the vapour pressure of the material is below the pressure in the chamber. The different evaporation methods are classified depending on the way of heating the target (resistive wires, electron beams, laser beams, etc.).

Electrons thermoionically emitted from a hot filament and accelerated towards the source material can generate enough energy density to evaporate any material [1]. This fact is the basis of electron beam evaporation sources, in which an electron beam is focalised on the target to be evaporated [2]. The electrons are accelerated with a high voltage, typically in the range between 5 to 10 kV, in order to heat the target through energy transfer during the bombardment. In this way, very high temperatures are reached (>3000°C) in controlled narrow areas, keeping the rest of the system at lower temperature. This permits high evaporation rates and minimises the interaction between the target and the container, which precludes contamination of the evaporated beam.

The evaporation process is performed in high vacuum, with a working pressure bellow 10^{-5} mbar (10^{-4} torr). This condition is needed to avoid oxidation of the source and of the coating. At the same time, in this pressure range the mean free path of the evaporated atoms is higher than the chamber dimensions (~50 cm), avoiding the dispersion of the beam as a result of collisions in the gas phase and, hence, resulting in a directional beam. At the working pressure, certain materials can sublimate and, therefore, achieve the transition to the gas phase without reaching the intermediate liquid phase.

b) Instrumentation

Our system is equipped with a commercial AVM-5 electron bent beam evaporator manufactured by AP&T. The electron beam is generated by means of an incandescent filament and extracted with a high voltage. A magnetic field is employed to bend the electron beam towards the target. This method offers the advantage that the electron source and the evaporated beam are separated. The deflection unit is equipped with electromagnets in order to sweep the target surface in the X and Y directions.

The power supply for the electron gun is an AP&T CARRERA5 unit. With this unit, acceleration voltages between 4-10 kV and electron beam currents up to 500 mA can be supplied. All the experiments described in this work were performed with an acceleration voltage of 7 kV. The electron currents were set at values below 200 mA, depending on the desired evaporation rate. Finally, the evaporation system is completed with a quartz crystal microbalance located near the substrate position and a shutter for the evaporation source.

In our experiments, the starting material was stored in a 4 cm^3 liner. The function of the liner is twofold. On the one hand, the liner reduces the volume of the container and lower power is necessary to reach the desired rate. On the other hand, the liner precludes the contamination of the source material with the remains of other materials and of the sample with impurities from the container.

c) Evaporation of graphite and boron carbide (B_4C)

BCN compounds were grown starting from graphite and boron carbide (B_4C) targets. Table 2.1 shows useful data of these materials regarding the evaporation process. Both materials have a different thermal behaviour at typical working pressures since graphite sublimes while B_4C evaporates. In the case of graphite, the sublimation process makes difficult a fine control of the evaporation rate since the size and form of the target also affects the process. We have found the best results with small lumps of approximately 2 mm size. The evaporation rate for both materials has been ranged between 1-5 Å/s with electron currents varying from 50 to 200 mA.

Table 2.1. Properties of target materials: graphite and B_4C.

	Properties	Graphite	B_4C
Physical	Density	2.25 g/cm^3	2.45 g/cm^3
	Melting point (T_f)	3700 °C	2450 °C
	Boiling point	5000 °C	
	Vapour pressure 10^{-8} Torr	1657 °C	2500 °C
	10^{-6} Torr	1867 °C	2580 °C
	10^{-4} Torr	2137 °C	2650 °C
Thermal	Thermal expansion coefficient	1-4 10^{-6} K^{-1}	5.6 10^{-6} K^{-1}
	Specific Heat	712 $JK^{-1}kg$	950 $JK^{-1}kg$
	Thermal conductivity	80-240 $Wm^{-1}K^{-1}$	90 $Wm^{-1}K^{-1}$
Electrical	Electrical resistivity	1.375 10^{-3} Ωcm	Semiconductor with gap ~0.8 eV

We have found some problems during the evaporation process of graphite and B_4C. First, the evaporation of these materials is accompanied by particle spitting from the liner. This fact is attributed to the thermal expansion of the gas occluded in these materials. The problem can be avoided by heating the target very slowly (~1-2 mA/min) until reaching the working temperature. Second, the microbalance was successfully used for evaporation of metals like aluminium but, in the case of B_4C and graphite, it could not be used since a "fail message" always appears after opening the shutter. The sensor head of the

microbalance is designed for a temperature operation range of -40° - 100°C. In the case of B_4C and graphite, we observe high radiation heat from the incandescent liner (~2000°C), which overheat the quart crystal despite the water-cooling system. In fact, the walls of the vacuum chamber near the evaporation source reach a temperature of ~100°C during evaporation. .

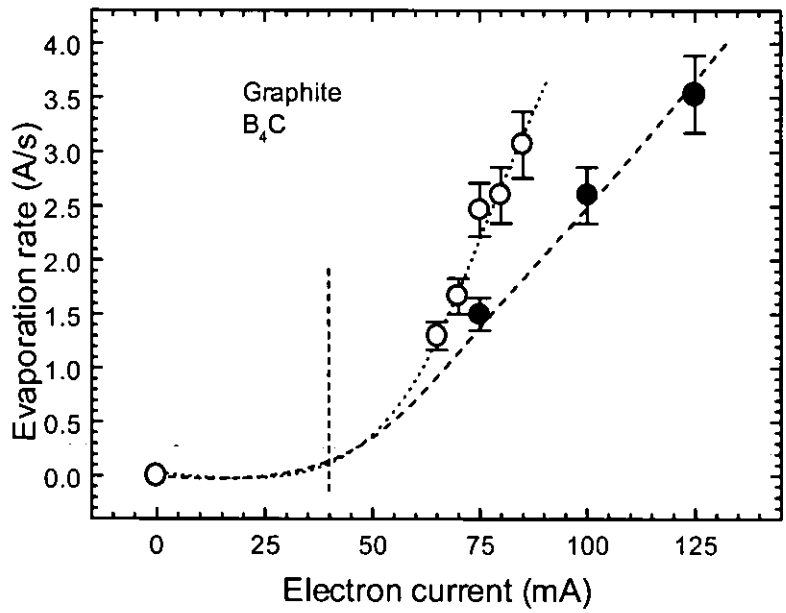

Figure 2.2 Evaporation rate as a function of the electron current for graphite (solid dots) and boron carbide (open dots) targets.

The evaporation rate depends, for each material, on the power density of the electron beam. The power density is determined by the acceleration voltage, electron current and beam area. Since the voltage and the area bombarded with the electron-beam are kept constant during the experiments, only the electron current controls the evaporation rate. Figure 2.2 shows the evaporation rate for graphite and boron carbide as a function of the electron current. B_4C is evaporated easier than graphite despite the vapour pressure of graphite being lower than that of B_4C. This is explained by the different thermal conductivity that leads, in the case of graphite, to a higher loss of the heating power towards the cooling system. A certain current is needed to start the evaporation in order to reach the evaporation temperature. Above this current threshold and for the range studied in this work, the evaporation rate depends linearly with the electron current.

Since the use of the quartz balance is not possible, we have to check the time dependence of the evaporation rate. The average evaporation rate can be calculated from the film thickness grown in a certain deposition time. Figure 2.3 displays the thickness of films grown by evaporation of B_4C as a function of the evaporation time. Clearly, the thickness does not increase linearly with time and, hence, the evaporation rate is not constant. This fact is not important for short evaporation times (< 20 min) but

must be compensated for longer times by increasing the electron current so that the evaporation rate remains constant. This is an important limitation if we want to grow films thicker than 0.5 μm.

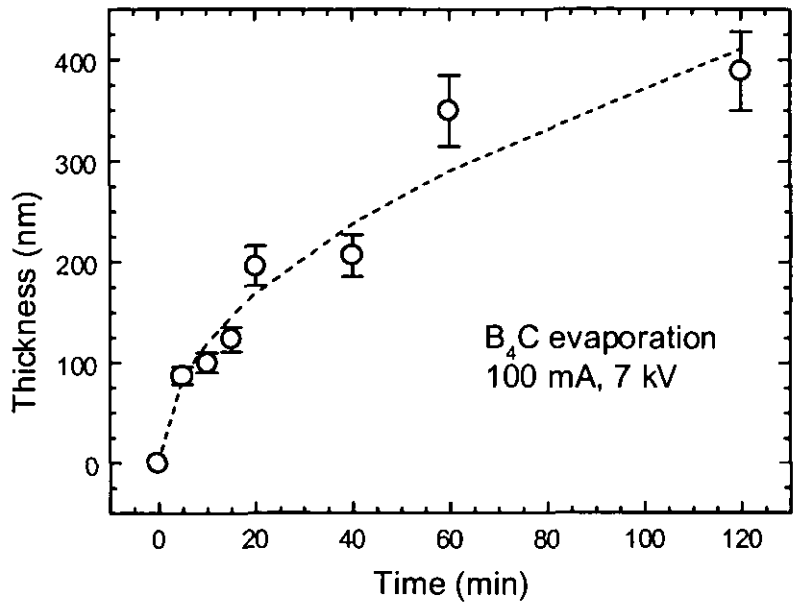

Figure 2.3. Thickness as a function of the evaporation time for boron carbide.

The electron beam spot size is 8 mm × 4 mm in the focused mode. In our case, we sweep a broader area of ~2 cm × 2 cm in order to heat the target homogeneously. In this way, we avoid the production of high temperature gradients and particle spitting. Despite the sweep, the evaporation is mostly achieved in a ~5 mm central region of the target as revealed by the presence of a crater after evaporation. The decrease in the evaporation rate with time can be explained as the result of the formation of this crater since the bombarded area is increasing during deposition.

2.1.2. Ion beam assistance.

a) Basic concepts

Hyperthermal species, i.e. with energy ~1-1000 eV, are used extensively in thin film processing for fabrication of a variety of materials including metals, semiconductors and insulators. The high energy is attained by the use of ions arising from plasmas and ion sources.

The use of a concurrent ion beam to assist the growth process of a material is known as Ion Beam Assisted Deposition (IBAD) [3]. The purpose of using ions is to impart kinetic energy or/and chemical activity to the precursor particles incoming the substrate. The ions are normally generated in a plasma discharge and extracted out of the plasma region by means of either acceleration voltages, substrate

polarisation or acceleration grids. In the latter case, the device is also known as ion gun since it provides a directional beam with a fine control of the energy and flux. The advantage of using ion guns respect to other ion-assisted methods relies in the generation of the ion beam far away from the substrate. This simplifies the process, since no additional mechanisms regarding interactions of the plasma with the substrate have to be considered. The assistance is normally performed with noble gases but also reactive gases can be used such as nitrogen, oxygen, etc. This process has been extensively used in many applications over the last decades in order to modify the film properties [4,5,6].

a.1) Effects induced by the ion bombardment

The physical effects of energetic particles on surfaces and films depend on the mass, flux and energy of the bombarding particles [7,8]. Figure 2.4 depicts the effects of ion bombardment with energetic species on the surface and sub-surface regions.

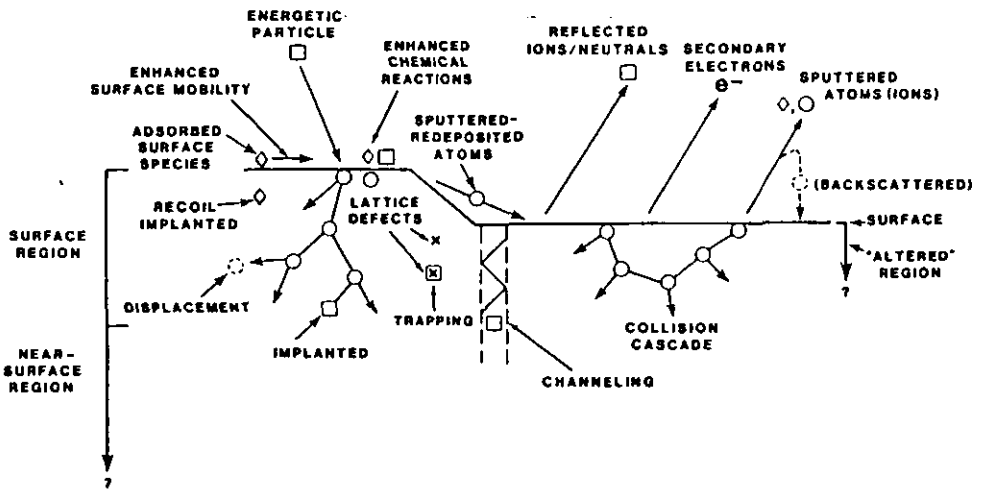

Figure 2.4. Schematic picture of the effects produced by energetic particle bombardment on surfaces and growing films (from ref. 7)

On the one hand, the surface effects include (i) desorption of surface species, (ii) ejection of secondary electrons, (iii) reflection of the energetic species as high-energy neutrals, (iv) sputter ejection (physical sputtering) of surface atoms, (v) re-deposition of sputtered species, (vi) enhanced surface mobility of atoms in the surface and (vii) enhanced chemical reaction of absorbed atoms to produced condensed species ("reactive deposition") or volatile species ("ion etching"). On the other hand, in the sub-surface regions we have to include the effects of (i) physical implantation of the impinging particles, (ii) atom displacement and lattice defects as a result of collision cascades, (iii) implantation of surface

species, (iv) trapping of mobile species in the lattice defects and (iv) the conversion of the kinetic energy of the incoming particles into heat.

Desorption of impurity species on the surface can be produced as a result of particle bombardment of the film. This species are normally weakly bonded to the substrate and, therefore, the particle energies required range between 1 and 100 eV. If the ion bombardment is performed prior to deposition, this procedure can be employed to clean the substrate surface from native oxides, water, hydrocarbon contaminants, etc. If the ion bombardment is performed during the deposition process it can also reduce the incorporation of contaminants in the growing surface [9].

Secondary emission of electrons plays an important role in plasma processes. These electrons are necessary to sustain the discharge. In addition, they may also play an important role in the chemical processes that occur on the surface.

Physical sputtering of a surface may lead to some texturing and roughening of the surface [10] for particle energies in the range of 10^2-10^5 eV. Preferential orientation of the exposed crystallographic planes may appear if some orientations are etched at a faster rate than others are. This preferential sputtering can also result in changes in the bonding structure and chemical composition of surfaces.

Concurrent bombardment with energetic particles can also activate chemical reactions at the surface. In this case, the mechanisms involved are poorly understood since heating, physical collisions, molecular fragmentation, formation of intermediate species and the presence of energetic electrons may take place.

In order to produce a displacement of the lattice atoms certain energy has to be overcome. The displacement energy of lattice atoms is in the range of several tens of eV. This energy depends on the type of bonding and structure of the material. The displacement of atoms can generate lattice defects and metastable bonding configurations. Particle energies in the range of 10-10^5 eV are needed in order to produce appreciable effects in the lattice.

Direct incorporation of the incoming energetic particles or implantation is produced for particle bombardment with energies of several keV up to energies of MeV. In this energy range, the particles penetrate several tens of nanometers in the film. Normally, this process is performed as a post-deposition treatment of previously grown films in order to modify their properties.

a.2) <u>Modification of film properties by simultaneous ion bombardment</u>

As introduced previously, there are a large number of processes involved during the bombardment of a material with energetic particles. These processes can produce beneficial modifications of the film properties when used concurrently to the deposition. The different modifications depend on the energy and flux of the bombarding particles [7,11].

The material growth with concurrent ion bombardment is governed by the ion-atom collisions, either with incoming precursor atoms or atoms already attached to the surface. The type and degree of changes in the film properties depend on the nature (ion energy, incident angle, mass of ions and precursor atoms, etc.) and number of collisions that takes place. The number of collisions can be quantified by the ratio between the incoming atoms and ions, i.e. the number of ions bombarding the film per unit area per unit time, I, divided by the number of atoms depositing per unit area per unit time, A:

$$\frac{I}{A} = \frac{ions\ s^{-1}cm^{2}}{atoms\ s^{-1}cm^{2}} \tag{2.1}$$

The I/A ratio acts as a normalisation factor of the bombardment parameters to the rate of material deposition and plays an important role in IBAD processes. This parameter has particular interest for reactive ion assisted deposition where stoichiometry is critical.

The ion energy and the I/A ratio should not be looked at separately. The effect of a specific I/A ratio will vary depending on the energy of those ions. Likewise, the effect of bombardment at specific ion energy will also depend on the number of ions that are bombarding. There are certain cases where one of these factors will be dominant but, generally, they must be looked at concurrently. Figure 2.5 illustrates the effects on the film properties that occur as a function of the ion energy and ion to atom arrival ratio on the IBAD growth process. The example corresponds to evaporation of metals and ion assistance with Ar^{+} [11]. The range for ion implantation processes is also indicated in the figure.

For low ion energies and I/A ratios (region I) the ion bombardment has no effect on the film properties. As we increase both ion-assisting values (region II), the ion bombardment induces several mechanisms related to desorption of surface species such as removal of contaminant layers, generation of roughness, increase of the nucleation sites (defects and implanted species), decrease of interfacial voids, etc. These mechanisms may enhance the film adhesion when they occur either prior to or during the initial stages of film formation [7].

In our films, we have found problems with film adhesion since some films peeled off from the substrate after several hours of being deposited. We attribute this fact to the high residual stress, which induce buckling from the surface (compressive stress) or cracking. The stress becomes more important in thick films where spontaneous failure can occur. In our case, ion irradiation prior to deposition with an Ar^{+} beam has resulted in a better film adherence as a consequence of a better substrate-film interface.

In the range of hyperthermal energies, the irradiation process may lead to a densification of the film (region III). The densification is a consequence of the reduction in the number of voids and the increase of interstitials that are generated during the growth process. The ion bombardment can also induce the formation of dense and metastable configurations, like sp^{3} hybrids, that contribute to the density increase.

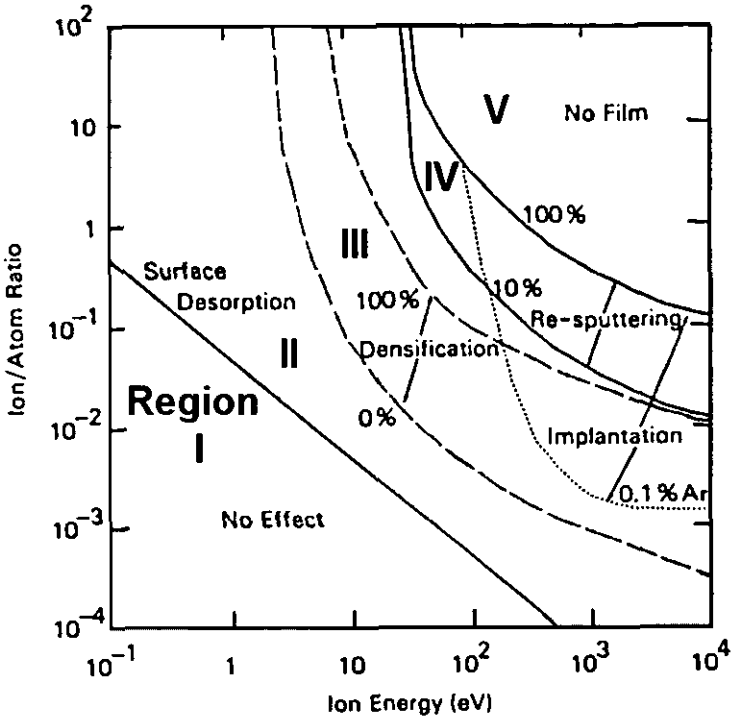

Figure 2.5. Different modifications of the film properties by concurrent ion bombardment during the film growth as a function of ion energy and ion to atom arrival ratio (from ref 11).

The physical sputtering and re-deposition can also play an important role in the range of hyperthermal energies (region IV). The effects and yield of the sputtering process depend on the ion energy and flux. The sputtering implies a re-emission or etching of the deposited atoms and, therefore, it results in a reduction of the deposition rate. For high sputtering yields the re-emission may equal deposition, leading to no film growth (region V). The physical sputtering can also result in a parallel increase of the density of the remaining material. In addition, possible preferential sputtering of weak phases can increase the fraction of strong and dense phases, contributing to the increase of the film density. Finally, sputtering may also be accompanied by an induced irradiation damage (creation of lattice defects, amorphisation, etc.).

b) Relevant ion assistance parameters

In order to understand the IBAD process, it is normally necessary to compare samples grown under different ion bombardment conditions (ion energy, I/A ratio, incident angle, etc). Since the ion bombardment parameters may not be independently controlled, this analysis requires the consideration of several parameters, beyond the individual values of ion energy, flux and species. The new parameters must also act as normalisation factor for films grown under the same ion assisting parameters but with different evaporation rate.

The energy per condensing atom represents the energy going into the films due to the ion bombardment per depositing atom. This parameter is the energy of the ions times the I/A ratio:

$$\frac{E}{A} = E_{ion} \times \frac{I}{A} \tag{2.2}$$

It is clear that this value can not be considered alone and that it should be always compared with the I/A ratio. However, when the physical processes that occur for the ion energy and I/A ratio ranges do not change significantly, E/A is a good metric for ion bombardment quantification. As an example, it is clear that we can not compare this parameter for two films grown, for example, with 1 eV and I/A=10 and 100 eV and I/A=0.1, respectively, since the physical effects involved are completely different. Although the E/A value in both cases is 10, in the former case the ions do not have enough energy to produce atom displacements. However, if the films are grown in a range of parameters where only densification occurs, the densification may be proportional to the E/A value.

Another value for quantifying the ion bombardment effects is the momentum transferred into the film, P, by the bombarding ions per depositing atom, A:

$$\frac{p}{A} = \frac{I}{A}\sqrt{2m\gamma E} \tag{2.3}$$

where E and m are the ion energy and mass, respectively. The γ parameter is a ballistic factor given by:

$$\gamma = \frac{4mM}{(m+M)^2} \tag{2.4}$$

being M the mass of the bombarded atoms and θ the assisting angle between the ion beam and the substrate normal. Equation 2.3 gives the value for maximum momentum transfer, with the assumptions that the collisions are binary and elastic. Obviously, the determination of momentum transfer becomes more complicated when the collisions involve more than two bodies, such as for an ion colliding with surface atoms of the growing film. The practical value of the momentum transfer is expected to be less that the resulting from the above equations. This is due to the statistical nature of the ion-atom collisions, which implies a random scattering angle.

For the sake of simplicity, we have chosen the ion energy per evaporated atom as the assisting parameter in our study. The analysis of the momentum transfer is more complex when operating with different types of ions (fragmentation of species, gas mixtures) and/or evaporation of compounds like B_4C. In our case the ion bombardment is performed with ion energies and I/A ratios between 100-1000 eV and 0.01-1, respectively. In this range of ion assistance, the physical processes are confined to that

occurring in regions III and IV of Fig. 2.5. Therefore, the E/A can be used to study the ion-induced effects for different samples.

c) Instrumentation

Our experimental system is equipped with a Kauffman ion gun of 3 cm beam diameter to assist the evaporation. This type of gridded broad-beam ion source permits the assistance with ion energies from 0.1 to 1.2 kV and maximum ion currents of 40 mA. This type of ion gun allows, in principle, a fine and independent control of the ion energy and current. In addition, the discharge needs of little maintain and the ionisation efficiency is high. A schematic drawing of the different parts of the ion gun and controller are illustrated in Figure 2.6.

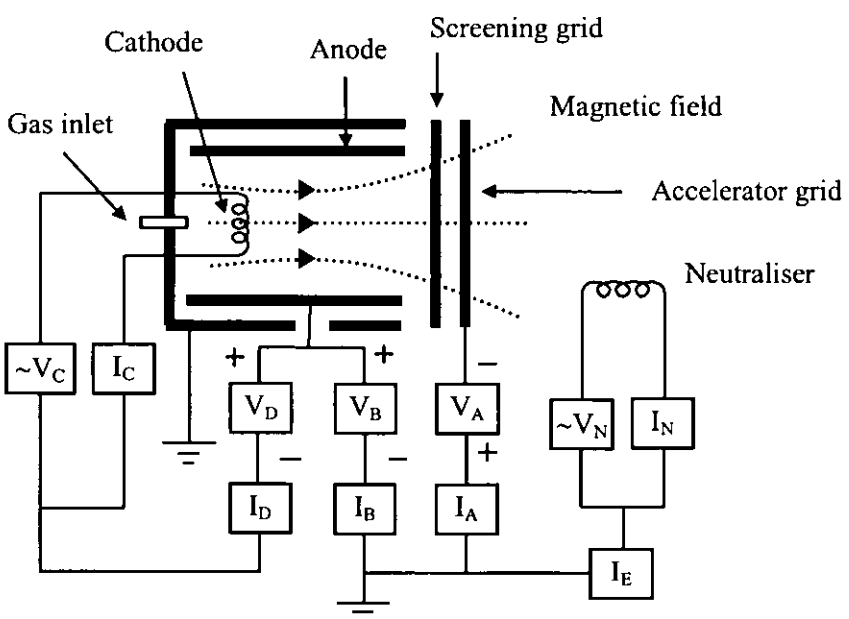

Figure 2.6. Schematic diagram of the Kauffman ion gun and control units.

The control unit of the Kauffman ion gun is composed of five power supplies as illustrated in Fig. 2.6. The working gas is introduced in the discharge chamber from the rear part of the gun. After turning on the filament, the discharge is initialised applying a voltage of 40 V (V_D) between the anode and cathode. In the discharge, the energetic electrons emitted by the cathode strike and ionise the atoms or molecules of the working gas. The use of permanent magnets in the discharge chamber confines the energetic electrons emitted from the cathode and, thereby improves the ionisation efficiency.

The discharge plasma is at a potential close to that of the anode. Therefore, the ions are directed towards the screening grid, which is at floating voltage and hence, close to the cathode voltage. The ions that approach the ion optics (screen and accelerator grids) are extracted from the discharge chamber and

accelerated into the ion beam. The acceleration of the ions is controlled by the voltage difference between the cathode and the anode, which depends mainly on the beam supply voltage, V_B, applied to the anode.

Apart from the extracted ions, there is a large amount of electron backstreaming in the beam that can distort the measurement of the ion current, I_B. These electrons must be repelled by means of a negative voltage, V_A, applied to the accelerator grid. The screening and acceleration grids are aligned to avoid direct ion impingement that could damage the optics and reduce the efficiency for extraction. Also, the acceleration voltage has to be as low as possible in order to reduce the sputter yield from the accelerator grid and prevent contamination problems.

The total voltage at which the ions are finally accelerated is the sum of the beam and accelerator voltage, V_B+V_A. In order to protect the accelerator grid, the accelerator voltage can not exceed 500 V. In addition, the beam voltage and the total voltage must be limited to 1000 V and 1200 V, respectively, in order to avoid excessive damage in the optics and overheating. In our case, we have chosen an accelerator voltage of 20 % respect to the beam voltage in order to minimise the sputtering yield for all the experiments.

The system is completed with the neutralisation source with the objective of adding electrons to the extracted beam. In this way, the repulsion between the ions, which broadens the beam, and charge effects in the case of insulator substrates are prevented. It is important to note that there is no real neutralisation (formation of neutrals) of the beam. In our case, we have not used the neutralisation source in order to broad the beam. This permits to irradiate larger areas and obtain a higher homogeneity in the substrate region. This is not a problem since we do not have charge effect in our substrate.

The extracted ion current is equal to the beam current. The maximum current that can be generated depends on the total voltage, $V_t= V_B+V_A$, and the distance between the grids, l_g. A theoretical value is given from Child's law [12]

$$I_B = \left(4\varepsilon_0 / 9\right) A_B \sqrt{e/m} \frac{V_t^{3/2}}{l_g^2} \qquad (2.5)$$

where A_B is the beam area. This equation is only approximate since the real discharge area is lower than the total area and the effective distance for acceleration is higher than l_g. The real current value is normally 20-50% of the Child's value. The maximum current shows a critical dependence with V_B as derived from equation 2.5. Figure 2.7 shows the experimental maximum current that can be obtained during normal operation as a function of beam voltage. The dependence found is $\sim V^{0.6}$, different from the theoretical value of 1.5, since the final current is also restricted by the normal operation parameters. In this case, the limitation arises from the threshold values of discharge and acceleration currents of 2.5 and 8 A, respectively, to avoid overheating of the source.

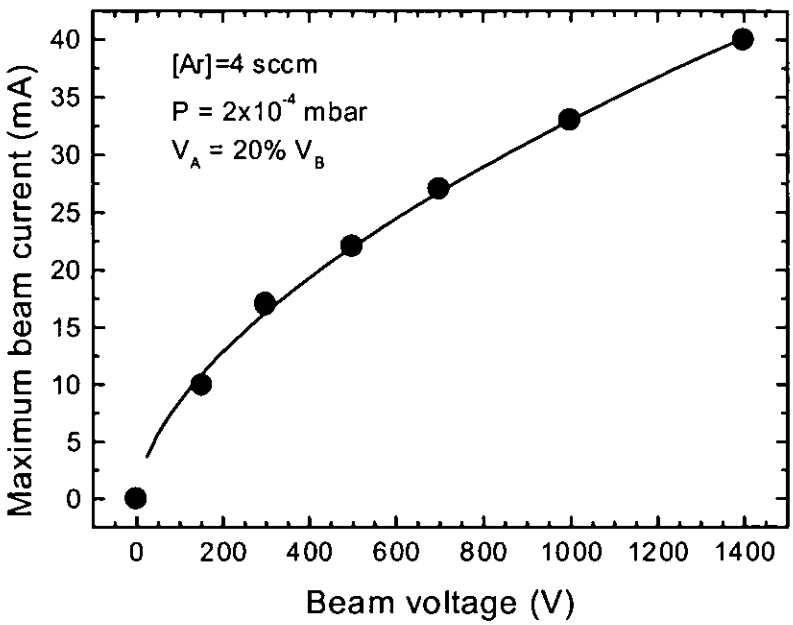

Figure 2.7. Maximum current as a function of beam voltage.

d) Ion beam characterisation

The major problem in using energetic particle bombardment from an ion beam is obtaining a uniform and controlled bombardment over a surface. Since the ion assistance is the basis of the whole synthesis work presented in this thesis, it is important to check the operation of the ion gun. We found that this calibration was necessary in order to understand the operation of the gun since the ion voltage and current density can not be independently controlled in the whole operation range.

At a first step, we study the sputtering yield for Ar^+ on silicon substrates. The behaviour of this value with the ion energy is well characterised and, therefore, it is a good reference point. Figure 2.10 shows the etched depth (solid dots) as a result of ion bombardment with different ion energies. The ion beam current (I_B) and exposure time were the same for all the experiments so the etched depth is proportional to the sputtering yield. The results obtained are compared with the experimental sputtering yield (open dots) reported in the literature [13]. The distinct behaviour between the etched depth and the sputtering yield indicates that the ion beam current is not constant as expected and, therefore, the ion beam voltage and current are not independent parameters.

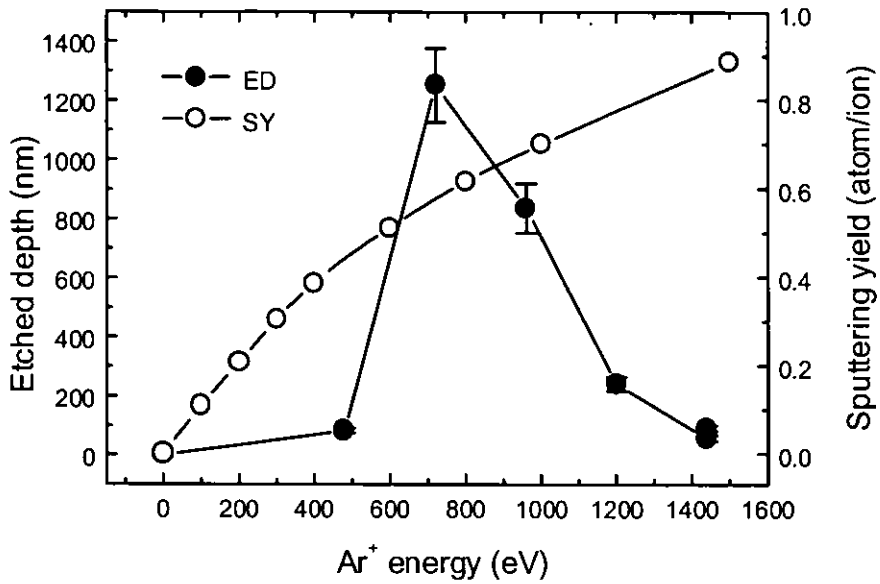

Figure 2.10. Etched depth (ED) as a function of the ion bombarding energy. The values can be compared with the reported sputtering yield (SY) in ref 13.

The above result reinforces the need of characterising the ion beam. For the analysis of the ion beam we built a probe assembled to the movable substrate holder. A diagram of the probe is displayed in Figure 2.11. The probe consists in a small metallic pin with a diameter of ~3 mm, isolated from the rest of the system. As a result of the exposure to the ion beam, a current in the range of μA is generated in the probe. This current leads to a voltage difference of several tens of volts between the terminals of a resistance of 1 MΩ, that is easily measured with a external voltmeter.

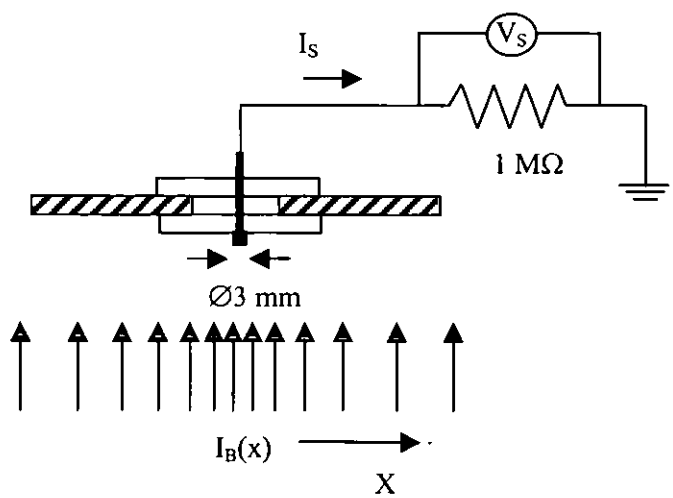

Figure 2.11. Probe for the characterisation of the ion beam.

The dependence of the intensity recorded with the ammeter for an Ar^+ beam as a function of the nominal ion assisting parameters are summarised in Figure 2.12. The figure also displays the full width at half maximum (FWHM) of the ion beam profile. The values obtained can be used to estimate the practical I/A ratio achieved in the deposition process. In the following, we try to explain the behaviours observed in the Fig. 2.12.

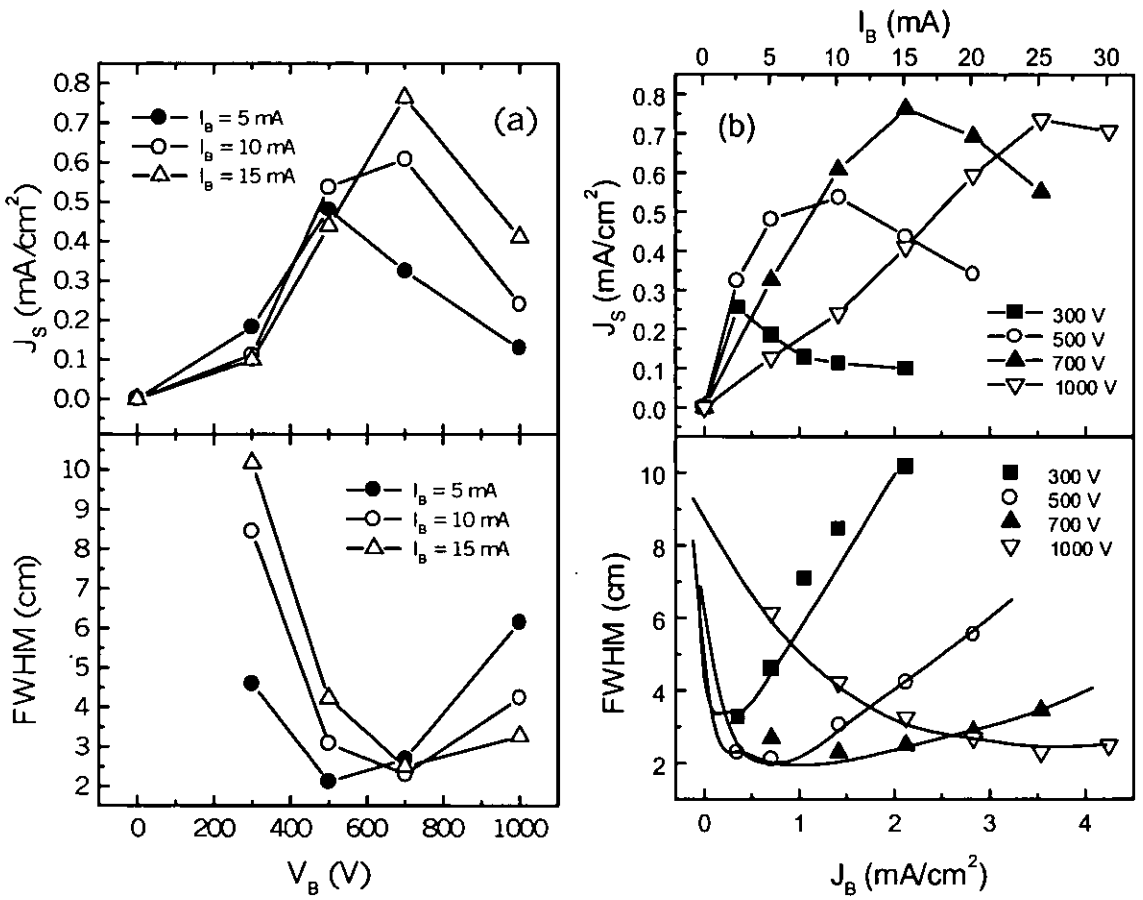

Figure 2.12. Sample current (J_s) and width of the ion beam distribution at half maximum (FWHM) as a function of V_B (panel a) and I_B (panel b).

The top panel of Fig. 2.12a displays the variation of the sample current as a function of the beam voltage for fixed nominal beam currents. Despite keeping the nominal current fixed, the sample current changes with the applied voltage with an initial increase and, then, a fast decay. Since the velocity of the ions is increased with the applied voltage, the trajectory deviation due to the space charge repulsion between the ions in the beam should be reduced, increasing the charge density that reaches the sample. The increase in the sample current is also followed by a reduction of the ion beam width, as shown in the bottom panel of Fig. 2.12a. These results indicate that the initial increase is due to a focalisation effect.

The decay in the current for higher ion energies is not well understood but could be related with the beam optics (acceleration grids). In this context, the extraction of the ions is not effective since the ion energy is very high in this range and precludes a fine confinement of the beam. This is corroborated by a broader ion beam profile, as derived from the bottom panel.

The top panel of Figure 2.12b displays the sample current as a function of the nominal beam current for fixed beam voltage. In this case, the ideal situation would be a linear relation between the nominal ion beam current density, J_B, and the sample current density, J_S. The deviation from this behaviour could be explained with the same arguments as above. As we select a higher current in the control unit the system increases the gas ionisation in the discharge chamber (higher discharge current), which results in the extraction of a higher current density. However, as we further increase the current density, the space charge repulsion or screening between the extracted ions produces a widening of the beam (bottom panel) and, therefore, a reduction of the sample current. Finally, the ionisation limit of the gas feed results in a saturation of the sample current. These arguments are illustrated in Figure 2.13.

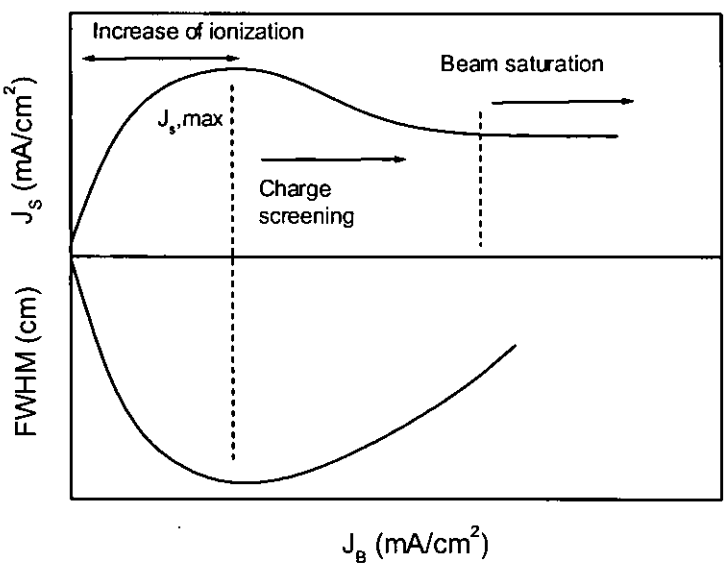

Figure 2.13. Effect of increasing the beam current on the current reaching the sample. Different processes are suggested depending on the beam current value.

From the top panel of Fig. 2.12b we can also appreciate that the beam current for maximum sample current, $J_{s,max}$, shifts to higher values as the acceleration voltage is increased. This current is much less that the maximum current that can be extracted for voltages below 500 V (see Fig. 2.9). For voltages around 500 V, $J_{s,max}$ and the maximum current are similar. Finally, for voltages over 500 eV, $J_{s,max}$ is below but close to the maximum current, which should be attributed to the defocalisation effect. These

results indicate that the optimum operation of the Kauffman ion source is obtained for voltages around 500 eV.

From the above analysis we can also extract information on the real ion beam area. This value determines the maximum area that can be bombarded with a uniform flux in order to obtain homogeneous coatings. The area of the substrates employed for the film deposition, typically 15x15 mm, has to be considered in order to analyse the experimental results. The corresponding profiles at different acceleration voltages for a nominal ion flux of 0.7 mA/cm^2 are shown in Figure 2.14. The profiles have been normalised for comparison purposes. Considering a tolerance of 10% with respect to the maximum value, the central region of the beam profile is always around 2-4 cm wide. These results indicate that we can expect a uniform beam for our 15x15 mm substrates. However, the proper ion assisting parameters have to be chosen when depositing larger areas.

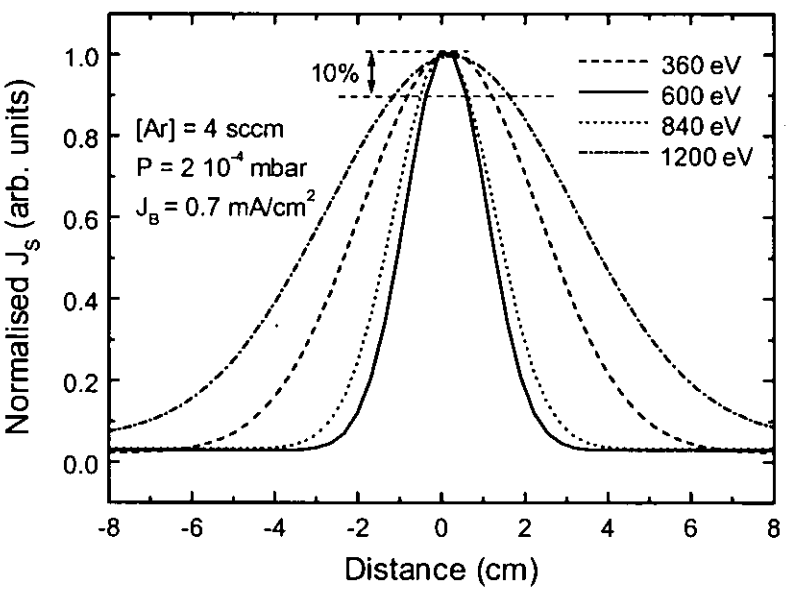

Figure 2.14. In beam profile for Ar^+ at different incident energies.

In the case of assistance with N_2 the same tendencies have been observed. However, several considerations have to be taken into account. First of all, the ion current extracted for nitrogen is below the value obtained with Ar^+ under identical operation conditions. Accounting to our results, this is attributed to a higher ionisation cross section for Ar. As it is well known, the pressure reading in ionisation vacuum gauges depends on the nature of the gas. The correction factor for Ar is 0.71 whereas it is 1 for N_2, indicating that at the same pressure and discharge conditions, Ar is easier to ionise [14]. Second, the beam in the case of N_2 is composed typically of 90% N_2^+ and 10% N^+ [15]. This is important for the calculation of assisting parameters such as momentum transfer.

2.2. CHARACTERISATION TECHNIQUES.

2.2.1. Profilometry

The film thickness was measured with a Dektak 3030 profiling system. The thickness value permits the calculation of the average deposition rate, i.e. final thickness over deposition time. This is an important parameter in industrial processes since high growth rates are of prime interest to reduce the cost of the process.

The profilometer performs a surface scan with a mobile diamond tip of 12.5 microns of diameter. The vertical displacements of the tip along its way over the surface are recorded with an electronic system. This scan provides a topographical profile of the sample surface by the relative height changes. Typical scan lengths and applied loads between 0.5-1.0 mm and 20-30 mN were used in the measurements, respectively. The resolution of the system is theoretically 0.1 nm. However, in practice, it is ~1 nm due to noise from ambient vibrations.

During deposition, the substrate was located over a substrate holder that works as a mask (see Fig. 2.1). The film thickness is measured in the step created between the deposited and non-deposited areas. The thickness was measured in four different points of each sample. The dispersion of the resulting values was around 10%, which is higher than the measurement error and, hence, is considered as the thickness error.

2.2.2. Vibrational spectroscopies:

a) Infrared (IR) spectroscopy.

We have used IR spectroscopy in the transmission mode to obtain compositional and structural characterisation of the grown materials. This method is based on the absorption of electromagnetic (em) radiation in the IR range when light travels through the material.

The IR radiation ranges between 0.02 and 2 eV ($0.7 < \lambda < 500$ μm), i.e. in the range of atom vibrational energies. Therefore, radiation is absorbed by excitation of lattice vibrations. These vibrations can be decomposed into several harmonic vibrations, which are known as normal modes. Each normal mode has assigned a certain frequency of vibration. The absorption of radiation is produced at these frequencies giving origin to absorption bands characteristic of the bonding environment.

The different vibrations are classified according to the movement relative to the bonding direction. As an example, the vibrations for the CO_2 molecule are shown in Figure 2.15. In the case of solids, the oscillations are more complex due to the new parameters introduced by the crystalline structure. Regarding the selection rules for angular momentum, only the vibrational modes that imply a change in the dipole moment are observed in IR [16]. In this context, mode (a) of Fig. 2.15 is not IR active since there is no net change of the dipole moment during the vibration. On the contrary, modes (b)

and (c) are IR active since the above criterion is satisfied. Table 2.2 summarises the main IR active bonding environments that can be detected in the BCN system.

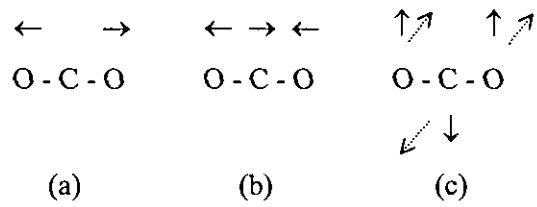

Figure. 2.15. Normal modes of vibration for the CO_2 molecule: symmetrical stretching (a), anti-symmetrical stretching (b) and bending (c).

The IR spectra were recorded with a commercial HITACHI 270-50 spectrometer of double beam. This type of system is based on the comparison between two beams originally equal, when the sample is located in the path of one of them. Both beams are produced in the same source and separated by a mirror system. After a monochromator system with several optics, a thermocouple of double window measure sequentially the intensity of the primary beam and the sample beam, generating an electric signal proportional to the difference of intensities. The wavenumbers of this spectrometer range between 250 and 4000 cm^{-1}. The overall spectral resolution is ±5 cm^{-1} between 4000-2000 cm^{-1} and ±2 between 2000-250 cm^{-1}.

Table 2.2. IR vibration frequencies for different BCN phases

Phase	Frequency (cm^{-1})	Reference
Si	600	
h-BN	750	[17,18]
c-BN	1050	[19]
B_4C	1100	[20]
BC_2	1200	[21]
C-N	1300	[22]
C=C	1360	
h-BN	1400	[17,18]
C=C	1550	
C=N	1600	[22]
C≡N	2170	[22]
C-H	2900	
N-H	3300	

b) Raman spectroscopy

Raman spectroscopy gives complementary information to IR since the selection rules for the active modes in both techniques are different. In the case of Raman, a change in the polarizability is required [16]. The Raman effect consists in a frequency change of the light due to the scattering with the phonons of the solid. Generally, an intense monochromatic source of light from a laser is employed as the incident or exciting radiation. Raman scattering is observed at certain frequencies (Raman lines) below and above the incident frequency. The lines of frequency lower than the incident light are known as Stokes lines, while high-frequency lines are termed anti-Stokes lines. The Raman shifts are the difference between the incident frequency and the Raman lines and correspond to the frequency of the normal vibrational modes excited in the solid. The Raman spectrum displays the intensity of the scattered light as a function of the frequency shift and, therefore, the spectra do not depend on the incident frequency.

The total intensity of all the scattered light is only of the order of 10^{-3}-10^{-5} times the intensity of the incident light and a large part of this light has the same frequency as the incident light (Rayleigh scattering). The Raman scattered light accounts for $< 10^{-7}$ of the incident intensity, so this effect is very weak. For this reason, it is essential to use very low stray-light monochromators, efficient optical systems and very sensitive detectors. Regarding vibration transitions, the anti-Stokes lies are usually considerably weaker than the Stokes lines. Therefore, since the same frequency shifts occur in both sets of lines, there is no point in recording spectra on the anti-Stokes side.

The experimental Raman spectra were collected with a Renishaw Ramascope 2000 microspectrometer at an excitation wavelength of 514.5 nm. The power density on the sample was about 5 GW/m^2. The spectral resolution achieved with this system is 1 cm^{-1} and the spectral slit width is 4 cm^{-1}.

2.2.3. Ion beam analysis.

a) Rutherford Backscattering spectrometry (RBS)

Rutherford Backscattering spectrometry (RBS) consists in the irradiation of a sample with energetic ions, typically α particles in the MeV range, and the detection of the back-scattered ions as a result of the interaction with the atoms in the sample. A schematic diagram of the RBS experiment is illustrated in Figure 2.16. This technique permits a quantitative analysis of the film composition without the use of comparative standards [23] and allows obtaining the composition depth profile of the sample with thickness values from 10 nm to a few microns.

The analytical power of RBS relies in the well-known process of nuclear and atomic scattering. The study of the scattering process by the atomic nuclei started in the beginning of the century with Rutherford experiments [24]. The energy of the detected ion depends on the initial energy (E_1), the projectile mass (M_1), the mass of the target atoms (M_2) and the depth where the collision takes place. For

an atom at the surface, the ratio between the energy of the scattered ions and the initial energy is given by the cinematic factor, K:

$$K = \frac{E_1}{E_0} = \frac{\left[\sqrt{1-\left(R\,\mathrm{sen}\,\theta\right)^2} + R\,\cos\theta\right]^2}{(1+R)^2} \approx 1 - \frac{2R}{(1+R)^2}(1-\cos\theta) \qquad (2.6)$$

where θ is the scattering angle and R is the ratio between M_1 and M_2. The approximation of this equation considers R<<1 and a scattering angle near 180°. For a good analysis, the scattering angle has to be as high as possible. When the collision takes place at a certain depth, there is an additional loss of energy ion in the way in and out of the sample.

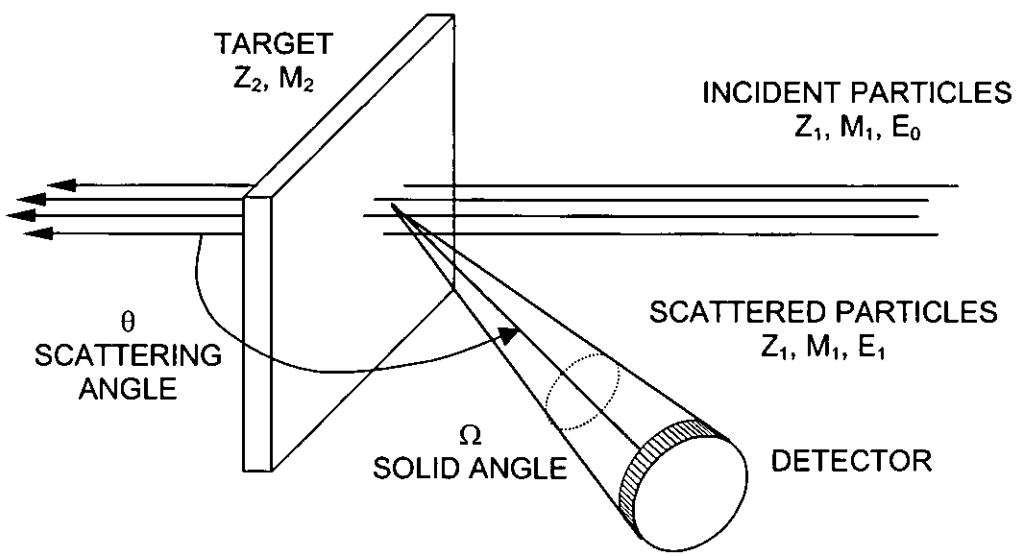

Figure 2.16. Schematic diagram of a RBS experiment.

The total number of ions that are backscattered with energy E at a certain angle θ will be given by the product of the ion dose, solid angle of the detector (Ω), areal density of atoms in the sample and the average cross section, σ. The scattering cross section can be calculated from the force that acts during the collision between the projectile and the target atom. For most cases, the force can be described as an unscreened Coulomb repulsion of the two positively charged nuclei. In this case, an analytical expression for the cross-section is given by:

$$\sigma = \left(\frac{Z_1 Z_2}{4E}\right)^2 \frac{4}{\mathrm{sen}^4\,\theta} \frac{\left[\sqrt{1-\left(R\,\mathrm{sen}\,\theta\right)^2} + \cos\theta\right]^2}{\sqrt{1-\left(R\,\mathrm{sen}\,\theta\right)^2}} \qquad (2.7)$$

The above expression was originally derived by Rutherford and, for this reason, it is known as Rutherford cross-section. The σ value increases with Z_2, which means that this technique is more sensitive for heavy atoms.

The experimental RBS spectrum represents the number of counts per energy channel. Each atomic mass generates a spectral band with a width proportional to the thickness of the layer where the mass is distributed. The intensity of the corresponding bands depends on the ion dose and atomic concentration. Since the channels only discern the ion energy, different atomic masses can contribute to the same energy channel, giving overlapping signals. We have to note that only a fraction of $\sim 10^{-6}$ of the incident ions is backscattered. Therefore, we need high ion doses and sufficient time to get good statistics.

The RBS experiments were carried out with the tandem accelerator facility at Sandia National Laboratories. The experiments were performed with 3.73 MeV ^{4}He and a scattering angle of 164°. Silicon solid state surface-barrier detectors are used, which gives an energy resolution for α particles of ~20 keV per channel. The energy was chosen in the range where the scattering cross-section for carbon is non-Rutherford in order to enhance the carbon signal by about seven times the Rutherford value [25,26]. Otherwise, the carbon signal in thin films (<0.5 μm) grown on Si substrates could be masked by the background noise. The quantification of the spectra was done with the computer code SIMNRA [27]. This code allows the simulation of the experimental spectra using Rutherford scattering cross section values, as well as non-Rutherford values, using tabulated data existing in the literature.

b) Elastic Recoil Detection Analysis (ERDA)

Elastic Recoil Detection Analysis (ERDA) [28] is a technique complementary to RBS. In analogy with RBS, ERDA experiments are based on energetic ions that irradiate the sample with ~1 MeV/amu. The difference between RBS and ERDA is that, in this case, the recoils or sputtered atoms from the sample are detected. For this reason, this technique is only sensitive to elements lighter than the projectile. A schematic diagram of the experimental set-up is shown in Figure 2.17.

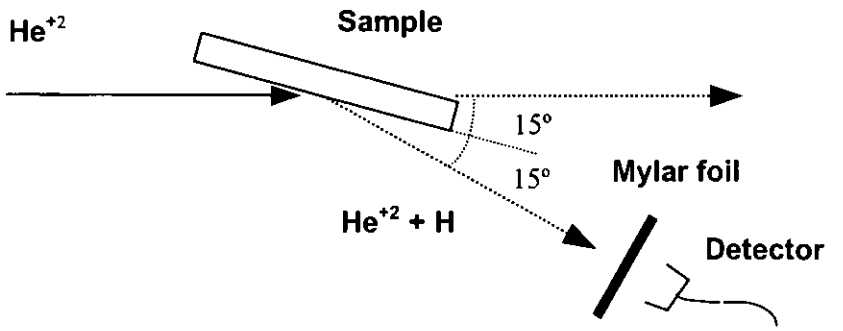

Figure 2.17. Schematic diagram of a ERDA experiment with α particles.
With this configuration, only hydrogen can be detected.

In order to avoid the incident ions reaching the detector, it is necessary the use of a range foil, typically mylar, to stop heavy particles. The thickness of the foil has to be chosen taking into account the incident energy and type of ions. ERDA is very simple and offers the possibility of detecting several elements at the same time.

As in RBS, the ERDA spectrum depends on the cinematic factor (K), the Rutherford cross-section, stopping powers of the elements in the foil and statistic fluctuations. The spectrum can also be transformed to a depth profile. The equations for the analysis of ERDA are the same as in RBS, considering that the atoms from the sample are detected. In this case, lighter elements are detected with a higher energy.

The ERDA experiments were also performed at Sandia Labs. The measurements were carried out with 26 MeV ^{28}Si ions and a range foil of Mylar 12 μm thick. The incident angle in the scattering geometry was 75° and the exiting angle 75°, leading to a scattering angle of 30°. As in RBS, the analysis was performed with the code SIMRA.

c) Time-Of-Flight Elastic Recoil Detection Analysis (TOF-ERDA)

Time-Of-Flight Elastic Recoil Detection Analysis (TOF-ERDA) is a powerful and recent technique for quantitative compositional analysis of materials [29]. The experimental set-up for ERDA in the Time-of-Flight configuration is shown in Figure 2.18. The basic concepts are the same as those described for ERDA although, in this case, the kinetic energy and velocity of the recoils are measured simultaneously.

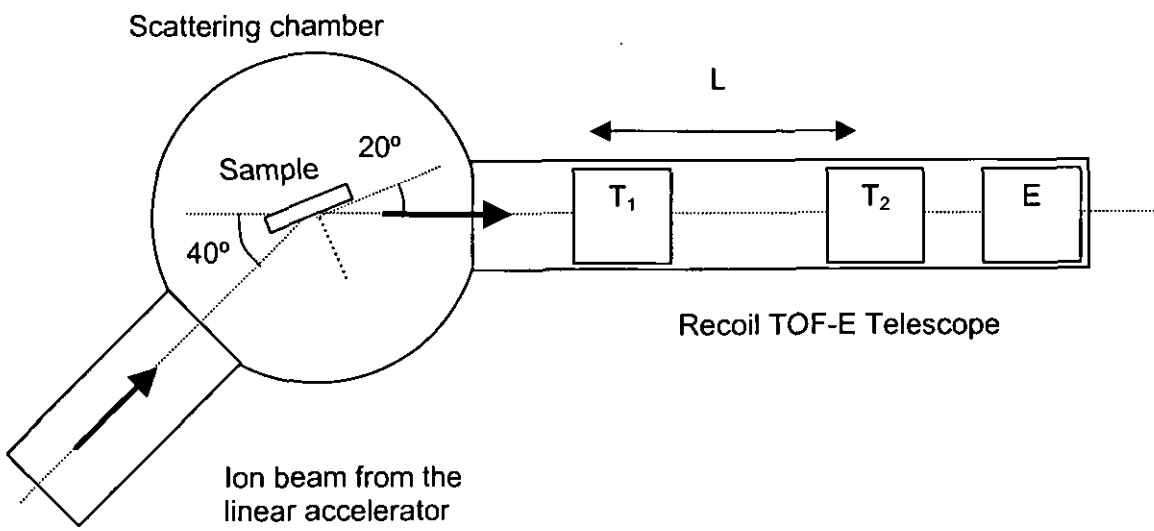

Figure 2.18. Experimental configuration for a TOF-ERDA experiment.

The kinetic energy is measured with a conventional surface barrier detector. The velocity is determined from the time interval between two consecutive detectors separated a distance L, as shown in the Fig. 2.18. The start and stop signals are generated in the form of a burst of secondary electrons as the recoils pass through a thin carbon foil of a few tens of nanometers. This analysis permits the determination of the mass of the recoil detected and, therefore, it is possible to separate the contribution of each mass. The resolution is increased by the elimination of the range foil since the energy straggling when the ions pass through the foil is avoided. Therefore, we can obtain practically clean spectra from unwanted background or interference from other signals. This feature is very helpful in the evaluation of the composition depth profile with a resolution of ~10 nm.

An example of the time of flight versus energy diagram for a ternary BCN sample is shown in Figure 2.19. The grey-scale represents the total number of simultaneous counts for the time and energy channels. The spectrum presents well-separated and intense lines corresponding to each atomic mass and some random background noise. In this case, the lighter the element the higher velocity and the lower energy are detected. Since the velocity of the recoils represents the time-of-flight value, the shape of the lines follows the classical square-root relation between the velocity and the energy. In the figure we have indicated the substrate and film regions. The stronger signal corresponds to the silicon substrate. In the near surface region, hence, high energy and high velocity, we detect the different masses corresponding to boron, carbon, hydrogen, oxygen and argon. The boron isotopes are detected in the percentage found in nature.

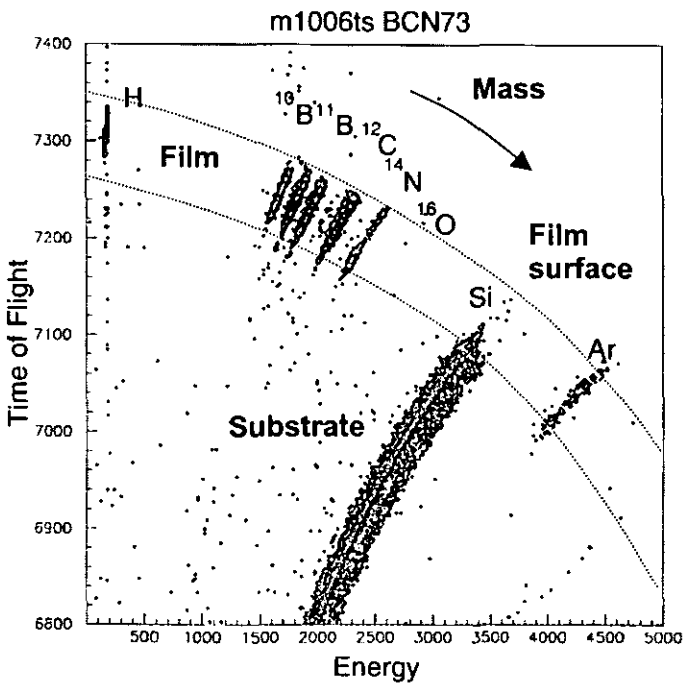

Figure 2.19. TOF-ERDA experimental diagram for a BCN sample.

In our case, the TOF-ERDA experiments were performed in the 5 MV tandem accelerator facility at University of Helsinki. The incident beam was 48 MeV I^{+9} and the recoils were detected for a scattering angle of 40 degrees.

2.2.4. Core-level spectroscopies:

a) Auger Spectroscopy (AES)

Auger spectroscopy (AES) studies the spectral emission of secondary electrons through Auger transitions [30]. The Auger transitions involve electronic levels of the atoms and provide a spectrum characteristic of each atom and also of a certain chemical environment. The experimental spectra are normally presented in the differential mode, i.e. dN/dE.

A representative scheme of a KLL Auger transition is shown in Figure 2.20. When an external source irradiates a sample (electrons, photons, etc.) the atoms are ionised and electrons from a core level are emitted. In the case of light elements, the electrons are emitted from the K shell. One electron from a level with lower binding energy (L_1 in the figure) decays, filling the hole created in the first ionisation process. The energy difference (E_{L1}- E_K) is transferred to a third electron in a level L_2, according with the example in the figure. In a general case, the transitions can take place between other atomic shells apart from those displayed in the example (K, L, M, N, ...). The transitions are labelled as KLL, LMM, MNN, etc., in correspondence with the atomic levels involved.

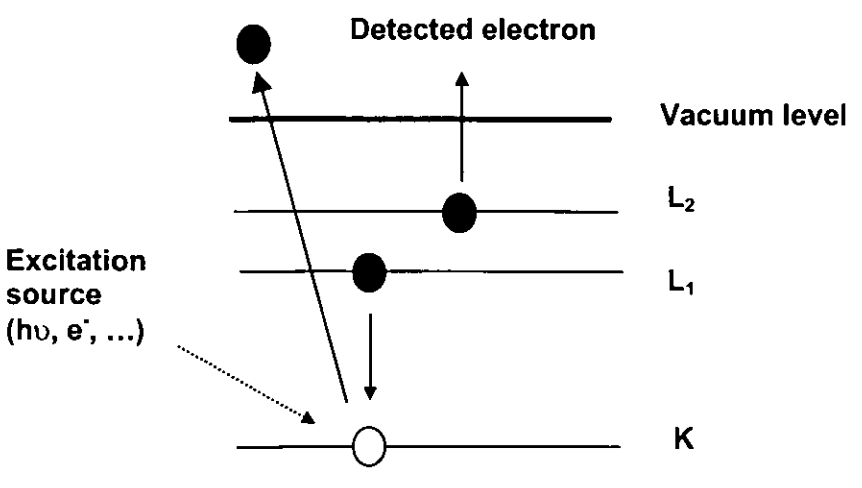

Figure 2.20. Diagram of an Auger transition.

The kinetic energy of an Auger electron depends only on the atomic levels involved (K, L_1 and L_2) and not in the excitation source:

$$E_{K,L1,L2}(Z) = E_K(Z) - E_{L1}(Z) - E_{L2}(Z+\Delta) - \phi_A \quad (2.8)$$

In this equation, ϕ_A is the work function of the detector and Δ takes into account that the energy of level L_2 does not correspond to the ground state.

b) X-Ray Photoemission Spectroscopy (XPS)

The photoemission process consists in the emission of electrons as a result of the absorption of photons irradiating the sample. For x-ray photons, the emission occurs from core levels and from the valence band and the technique is known as X-Ray Photoemission Spectroscopy (XPS). The XPS spectra represent the number of emitted electrons that are detected with a certain kinetic energy. Since the energy of the photon is constant, $\hbar\omega$, the kinetic energy, E_K, of an electron emitted from a core level with binding energy, E_B, is given by the relation:

$$\hbar\omega = E_B + \phi + E_K \tag{2.9}$$

where ϕ is the work function of the detector.

The experimental XPS spectrum is composed of several peaks, corresponding to core levels, and the density of states in the valence band. The valence band appears for binding energies below ~30 eV. The core level peaks are representative of the atoms present in the sample, which can be identified. A compositional analysis can be performed considering the relative height of the peaks corrected for the sensitivity factors of each element [31]. The position of the peaks depends on the chemical environment and, therefore, the technique can give information of the bonding structure.

The XPS measurements were performed with an excitation source of Mg Kα radiation. The data were acquired with a double pass cylindrical mirror analyser from Physical Electronics. The overall instrumental resolution is ~0.8 eV.

c) X-Ray Absorption Near Edge Spectroscopy (XANES)

Information on the bonding structure and chemical composition can be obtained with X-ray Absorption Spectroscopy (XAS). XAS experiments require of synchrotron radiation where a fine control of the photon energy and a high flux in the x-ray range can be achieved.

The XAS experiment is illustrated in Figure 2.21. The sample to be analysed is placed in the x-ray beam path from the synchrotron source, absorbing radiation. As a result of the absorption, there is secondary emission of photons and electrons from the sample. In this case, the absorption coefficient at each incident photon energy is proportional to the total electron or photon emission (total yield). The absorption is produced above a photon energy threshold necessary for the electrons to acquire enough energy to produce a transition to unoccupied states in the conduction band. This threshold leads to a

spectrum with an abrupt absorption edge. In the experiment, a gold-covered grid is placed upstream the x-ray path in order to normalise the x-ray intensity.

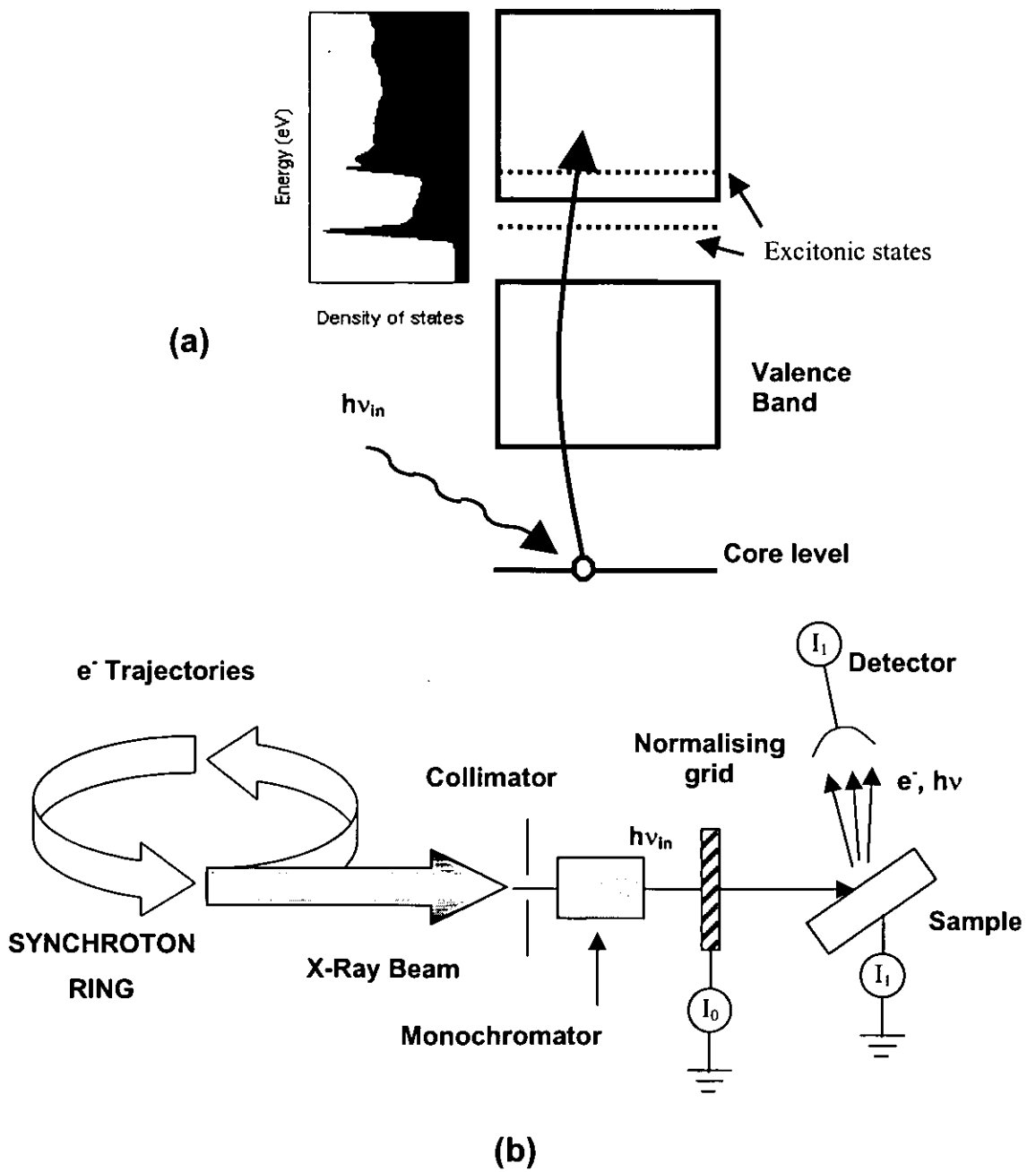

Figure 2.21. (a) Energy diagram and (b) instrumentation for a XAS experiment. The resulting spectra will reflect the density of states in the conduction band.

The XAS spectrum can be divided in two regions: the near edge region (XANES or NEXAFS) [32] and the extended fine structure (EXAFS) [33] region. The XANES region extends ~50 eV from the absorption edge whereas EXAFS takes into account the region from ~50 eV up to ~1000 eV from the

edge. XANES takes into account the position and shape of the absorption edge. The position of the edge depends on the chemical bonding and the shape reflects information of the conduction band. On the other hand, EXAFS studies the oscillations of the absorption coefficient for energies above the edge. The oscillations give information about the geometrical structure and, particularly, depend on the bond length, bond angle and coordination number.

We have focused our study in the near edge structure by XANES. This technique works well in amorphous and nanocrystalline systems and is especially interesting for the study of compounds with low atomic number atoms [34]. One of the most interesting features of XANES is the capability of giving distinct spectral shapes for sp^2 and sp^3 hybridisations, with similar absorption cross-section [35].

The XANES experiments were performed at the beamline 8.2 of the Stanford Synchrotron Radiation Laboratory (SSRL) and at the SACEMOR endstation (beam line SA72) of the Laboratoire pour L'Utilisation du Rayonnement Electromagnetique (LURE). Both lines operate in the 100-600 eV range, where the absorption edges for B, C, N and O can be studied. The data were collected in the total electron yield mode by recording with an ammeter the current drained to ground and with a channeltron the electron emission. The signal was normalised to the signal coming from a gold-covered grid located upstream in the x-ray path. The angle between the sample normal and the incident light was near the 55° magic angle to avoid preferential orientation effects, except when performing angle dependent studies.

2.2.5. Mechanical properties: Nanoindentation

The mechanical properties were determined from the load-displacement curve obtained by nanoindentation (see Chapter 1). A schematic diagram of the nanoindentation system is displayed in Figure 2.22. In this system, the applied load is derived from the attraction between a permanent magnet and a coil. The current through the coil, which is controlled by an external power supply, drives the resulting force. Simultaneously, the indentation depth is measured by the variation of the capacitance of a parallel plate capacitor. The load and depth scales have to be carefully calibrated previously to the experiment.

The nanoindentation experiments were made with a Nano Indenter® II (Nano Instruments, Inc) at Universidad Carlos III de Madrid. The system is equipped with a Berkovich indenter. As introduced in Chapter 1, the shape of this indenter produces full plasticity at very small loads [36] and, therefore, it is ideal for nanoindentation experiments. The load-displacement data was analysed using the method of Oliver and Pharr [37]. The determination of the mechanical properties was attained with two types of measurements:

1. **Hardness (H) and Young's modulus (E)**: The indenter was loaded and unloaded at increasing depths at a constant rate of 10% of the maximum depth per second. Each unloading was terminated at

10 % of the peak load to assure that the contact was maintained between the specimen and indenter. Hold periods of 10 seconds at the maximum load and 100 s at the minimum load of the final unloading were inserted to correct creep and thermal drift effects, respectively. Each indentation experiment was performed ten times in each sample and the mean value of hardness was taken as the result of the measure. The dispersion has been always below 8%, which has been considered as the error of the hardness determination for a certain depth.

2. **Elastic recovery**: In this case, a single indentation to maximum load followed by complete unload was performed. The indentation proceeded at a constant rate of 10% of the peak load per second. A hold period of 50 s was inserted at the maximum load to allow any time dependent plastic effect to diminish. After this hold period, the indenter was unloaded to 10% of maximum load and another hold period of 100 s was inserted to correct the thermal drift. Finally, the unloading was completed and the elastic recovery was computed from the final displacement over the maximum displacement.

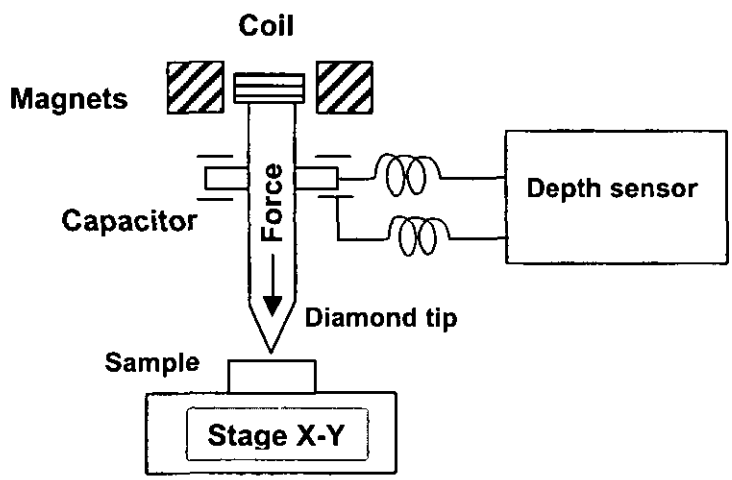

Figure 2.22. Schematic diagram of the nanoindentation system.

An example of load-displacement curves (left panels) and the corresponding analysis results (right panels) are shown in Figure. 2.23. The example corresponds to an amorphous carbon film grown on Si with a thickness of ~200 nm. In order to obtain the hardness as a function of depth, three increasing indentations are performed at low (top panel) and high load (bottom panel) during each experiment. As mentioned above, each experiment is repeated ten times and the average value is obtained. The resulting hardness of this film is ~16 GPa. The value is taken for that found at a penetration depth of ~10% of the film thickness, i.e. 20 nm. The initial increase in the hardness is due to the effect of the soft layer of surface contaminants. Finally, for large indentation depth the hardness tends to the substrate value (12

GPa). The elastic modulus and the hardness follow the rule of thumb relation E/H~10. Therefore, in this kind of films, the elastic modulus is an additional indication of the hardness.

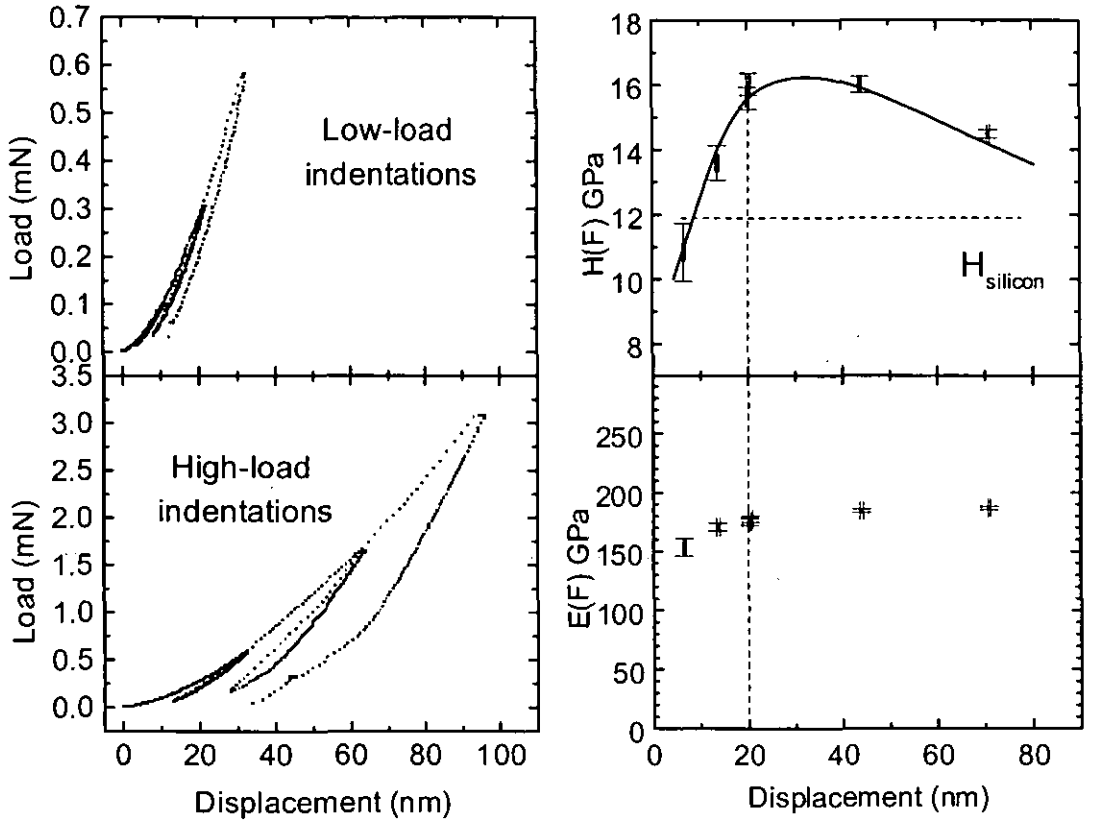

Figure 2.23. Load-displacement curves (left panels) at different penetration depth and the corresponding results of the analysis (right panels). The sample corresponds to a 200 nm thick amorphous carbon layer on silicon.

REFERENCES

1. D.L. Smith, *Thin Film Deposition*, McGraw-Hill (1995).

2. D.H. Blackburn, W. Haller, The Rev. of Sci. Inst. 36 (7) (1965) 901.

3. S. Aisenber, R.W. Chabot, J. Vac. Sci. Technol. 10 (1) (1973) 104.

4. G. Dearnaley, Nucl. Inst. and Methods in Phys. Research B 40/41 (1989) 571.

5. G. Dearnaley, Surf. Eng. 7 (2) (1991) 127.

6. J.S. Colligon, Mat. Sci. and Eng. A 139 (1991) 199.

7. D.M. Mattox, J. Vac. Sci. Technol. A 7(3) (1989) 1105.

8. T. Takagi, J. Vac. Sci. Technol. A 2 (2) (1984) 382.

9. L.I. Massiel, P.M. Schaible, J. Appl. Phys. 36 (1965) 237.

10. Z.W. Kowalski, J. Mater. Sci. Lett. 6 (1987) 69.

11. J.J. Cuomo, S.M. Rossnagel, H.R. Kauffman, *Handbook of ion beam processing technology*, Noyes Publications (1989).
12. C.D.Child, Phys. Review 32 (1911) 492.
13. J.W. Coburn, H.F. Winters, T.J. Chuang, J. Appl. Phys. 48 (1977) 3532.
14. *"Vacuum Vademecum"*, Leybold.
15. D. Van Vechten, G.K. Hubler, E.P. Donovan, Vacuum 36 (11/12) (1986) 841.
16. B.P. Strangham, S. Walker, *Spectroscopy 2*, Chapman and Hall, New York (1976).
17. R. Geik, C.H. Perry, Phys. Rev. 146 (1966) 543.
18. S.P.S. Arya, A. D'amico, Thin Solid Films 157 (1988) 267.
19. P.J. Gielisse, S.S. Mitra, J.N. Plendl, R.D. Griffis, L.C. Mansur, R. Marshall, E.A. Pascoe, Phys. Rev. 155 (1967) 1039.
20. U. Kuhlmann, H. Werheit, K.A. Schwetz, J. of Alloys and Compounds, 189 (1992) 249.
21. K. Shirai, S. Emura, S. Gonda, Y. Kumashiro, J. Appl. Phys., 78 (5) (1995) 3392.
22. M. Friedrich, Th. Welzel, R. Rochotzki, H. Kupfer, D.R.T Zahn, Diam. Rel. Mat. 6 (1997) 33.
23. T.G. Finstad and W.K. Chu. Academic Press, San Diego, CA (1988) 391.
24. E. Rutherford and H. Geiger. Phil. Mag. 22 (1911) 621.
25. Y. Feng, Z. Zhou, Y. Zhou, and G. Zhou. Nucl. Instrum. Methods B 86 (1994) 225.
26. J.A. Leavitt, L.C. McIntyre Jr., P. Stoss, J.G. Oder, M.D. Ashbaugh, B. Dezfouly-Arjomandy, Z.M. Yang and Z. Lin, Nucl. Instrum. Methods B 40/41 (1989) 776.
27. M. Mayer, SIMNRA User's Guide v.4.0, Max-Plank-Institute für Plasmaphysik, 1997/98
28. J.L'Ecuyer, C.Brassard, C.Cardinal, J.Chabbal, L.Deschenes, J.Labrie, B.terrault, J.G.Martel y R.St-Jacques 47 (1976) 881.
29. H.J. Withlow, G. Possnert, C.S. Petersson, Nucl. Instr. and Meth. B 27 (1987) 448.
30. P. Auger, J. Phys. Radium 6 (1925) 205.
31. *Handbook of X-ray Photoelectron Spectroscopy*, Perkin-Elmer Physical Electronics (1979).
32. J. Stöhr, *NEXAFS Spectroscopy*, Springer, Berlin (1990).
33. D.C. Koningsberger, R. Prins, *X-ray Absorption: Principles and Techniques of EXAFS, SEXAFS and XANES*, J. Wiley, New York (1988).
34. Ph. Redlich, J. Loeffler, P.M. Ajayan, J. Bill, F. Aldinger, M. Rühle, Chem. Phys. Lett. 260 (1996) 465.
35. D.M. Gruen, A.R. Krauss, C.D. Zuiker, R. Csencsits, L.J. Terminello, J.A. Carlisle, I. Jiménez, D.G.J. Sutherland, D.K. Shuh, W. Tong, F.J. Himpsel, Appl. Phys. Lett. 68 (1996) 1640.
36. J. Hay, *"Mechanical testing by indentation"*, Applied Nano Metrics, Inc.
37. W.C. Oliver, G.M.J. Pharr, J. Mater. Res. 7 (6) (1992) 1564.

Chapter 3:

Amorphous carbon films (a-C)

3. AMORPHOUS CARBON FILMS (a-C)

In this chapter we present the results obtained on the growth of amorphous carbon films with our IBAD system. The films are grown by evaporation of a graphite target and the concurrent ion bombardment with inert Ar^+ ions. We correlate the bonding structure and film properties with the deposition parameters and post-deposition treatments.

3.1. INTRODUCTION

Amorphous carbon films either hydrogenated (a-C:H) or hydrogen free (a-C) have been the object of intense research in the last decades because of their unique properties and applications, particularly as a solid lubricant. The structure and properties of this material are defined by the sp^3/sp^2 ratio and by the hydrogen content [1]. This is the basis of a classic classification of carbon films, which is summarised in the well-known triangle of compositions with sp^3-carbon, sp^2-carbon and hydrogen located at the vertices, as shown in Figure 3.1.

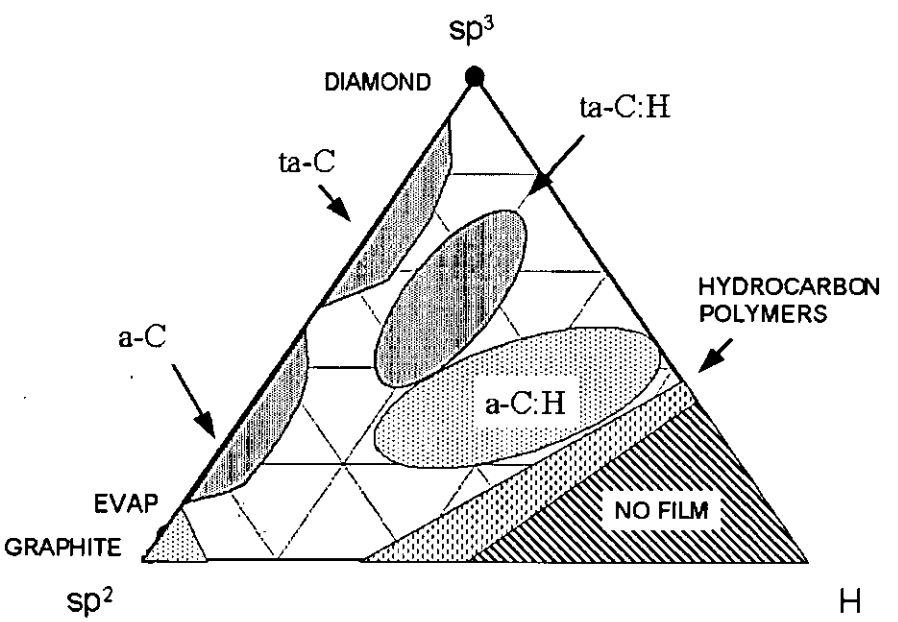

Figure 3.1. Classification of amorphous carbon films as a function of the sp^3, sp^2 and hydrogen percentage (from ref. 1).

Energetically, a sp^2-based arrangement is the most favourable structure for amorphous carbon. This structure is found in hydrogen-free thermally evaporated or sputtered carbon films (e-C), with a sp^2 content around 90-95% [2]. The energy of the carbon atoms that reach the substrate is ~0.1 eV for evaporation and ~10 eV for sputtering. A high promotion of sp^3 sites can be attained if hyperthermal carbon atoms are used during deposition (>10 eV). In all of the amorphous carbon structures, the

promotion of sp^3 sites is explained by a subplantation mechanism [3,4,5]. In this model, incident carbon atoms in the range of 10-1000 eV penetrate into subsurface sites and provide a quenched-in increase in density, which favours the formation of sp^3 bonds. The sp^3 content confers diamond-like (DLC) properties to this material such as high hardness, IR transparency and chemical inertness [6]. The number of sp^3 sites that can be attained depend on the energy and distribution of the species involved in each growth method. Figure 3.2 indicates the range of non-hydrogenated sp^3 sites achieved for different deposition methods and illustrates the relation between the sp^3 content and hardness [7].

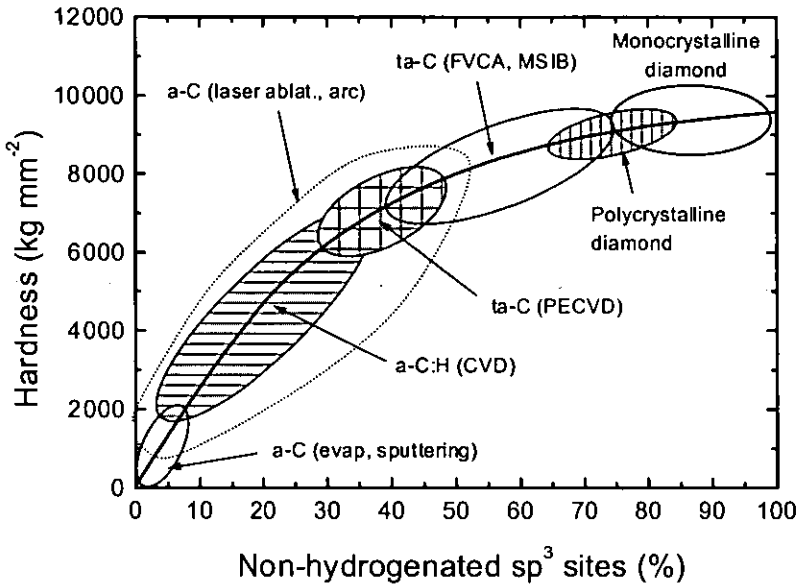

Figure 3.2. Non-hydrogenated sp^3 content achieved for different deposition methods and relation between the sp^3 content and hardness in for hard carbon (from Ref. 7).

The carbon atoms can be accelerated in the hyperthermal range either directly or indirectly. The first case occurs when the carbon atoms are ionised and accelerated by means of an external voltage. In the second case, the carbon atoms are accelerated by knock-on collisions with a concurrent ion assisting flux (ion beam assisted deposition or IBAD). In the case of IBAD, the resulting amorphous carbon films (a-C) present different mixtures of sp^3 and sp^2 carbon sites and the sp^3 content can be increased up to 50% [8]. In the case of direct acceleration, the sp^3 content can be raised up to 80% if a monochromatic beam of ~100 eV/atom is attained. In this case, the films are labelled as tetrahedral amorphous carbon (ta-C). The production of ta-C films is made with filtered cathodic vacuum arc (FCVA) [9,10] or mass selected ion beam (MSIB) [11] methods. However, the mechanical stability of the ta-C is poor due to a compressive stress of ~10 GPa [12].

The mechanical stability of the films can be improved by the addition of hydrogen to the structure (a-C:H). Normally, a-C:H films are grown by plasma CVD methods starting from a mixture of hydrocarbon precursor gasses [13]. In this case, the films present a high content of hydrogen (~60 at. %) and, as a consequence, a large content of sp^3 sites can be accommodated (>50%) [14]. However, the mechanical properties are considerably reduced due to the polymeric character of the films [15].

An intermediate situation between a-C:H and ta-C films are hydrogenated tetrahedral amorphous carbon films (ta-C:H). This films present a hydrogen content < 20 at. % reducing the stress (< 8GPa) but keeping to a high extent the mechanical properties of ta-C. These films are grown by plasma beam sources (PBS) [16] and high plasma density glow discharges [17].

Although the search of a-C with good mechanical properties was focused on the promotion of sp^3 sites, a new scenario appears with the discovery of fullerenes [18] and carbon nanotubes [19]. In the 90's it has been realised that a-C composed of 100% sp^2 carbon with curved basal planes resembling fullerene structures can exhibit extreme hardness and elasticity [20]. Therefore, there is a renewed interest in graphitic carbon films with good mechanical properties, like hardness up to 40 GPa and free from internal stresses. These properties are explained by the curvature and cross-linking of basal planes, due to the presence of pentagonal and heptagonal ring defects [21] or sp^3 line defects [22].

The IBAD process has been previously studied in the growth of amorphous carbon films [23,24,25,26]. Experimentally, the film properties have been found to vary systematically with the ion energy, ion to carbon arrival ratio (I/A) and ion mass. In this process, the incident carbon atoms present a wide energy spread as a result of random collisions. This fact precludes the formation of a highly tetrahedral material since a monochromatic beam is necessary. However, more effort has to be made in order to understand the complexity of the processes taking place during the atom arrival, i.e. atom impingement to the growing surface (incorporated either with sp^2 or sp^3 character), atom-ion collisions and/or atom re-emission from the surface due to sputtering effects.

We face the previous problem considering a set of samples grown with our IBAD system under different deposition conditions. One of the key parameters in the deposition process is the energy of the impinging carbon atoms after colliding with the Ar ions. However, this is not a well-defined value since there is a broad distribution of energies as a result of the random Ar-C collisions. In addition, the I/A ratio also plays an important role in the deposition and it depends on both ion flux and evaporation rate. For these reasons, we consider the energy per incoming carbon atom, $E/A=E_i \times I/A$, as the parameter to compare different samples. The I/A value is obtained from the current density values that were measured with the probe, as it is described in Chapter 2. The growth conditions for the films considered in this study are summarised in Table 3.1. The ion assistance was performed with a gas pressure of 2×10^{-4} mbar using an Ar flux of 4 sccm (standard cubic centimetre per minute).

Table 3.1. Growth parameters for the amorphous carbon films grown by IBAD.

Sample	Evaporation rate (Å/s)	Ion energy (eV)	I/A	E/A (eV/atom)
AC1	2	0	0	0
AC2	2	120	0.3	40
AC3	5	360	0.3	90
AC4	5	360	0.3	99
AC5	5	360	0.3	117
AC6	2	240	0.5	120
AC7	5	360	0.4	162
AC8	5	360	0.6	224
AC9	2	360	0.7	269
AC10	2	480	2.2	1047
AC11	2	600	3.4	2019
AC12	2	720	3.7	2691

3.2. FILM COMPOSITION

The techniques RBS, detecting C, N, O and Ar, and ERDA, detecting C, H and O, give complementary information on the film composition. The use of both ion beam techniques (RBS and ERDA) provides a better accuracy in the analysis, since the same sample composition is assumed in the simulation of both spectra.

Figure 3.3 shows the RBS (panel a) and ERDA (panel b) spectra for an amorphous carbon film grown with an evaporation rate of ~2 Å/s, ion energy of 120 eV and ion current density of 1.4 mA. Similar spectra were obtained for the rest of the films. The experimental curve is represented with dots and the simulated spectrum with a continuous line. The films are mainly composed of carbon (97-98 at. %) with a small amount of argon, oxygen and hydrogen. The enhancement of the C signal in the RBS spectrum is due to the non-Rutherford cross section value.

As a result of the compositional analysis we confirm the non-hydrogenated character of the films since the hydrogen content is below 2 at. % for all the samples analysed. In addition, the hydrogen content in the films comes mainly from surface hydrocarbon contamination. This assumption was corroborated by simulating a thin contamination layer (~10 Å) of hydrocarbons ($C_{50}H_{30}O_{20}$) in the surface of the film. The argon content that is incorporated to the film as a result of the ion bombardment is limited to 3 at. %. Finally, the oxygen content is below 2 at. % and it is attributed to surface contamination. This is also verified by the reduction of the oxygen signal in the AES and XANES upon ion irradiation and annealing process for temperatures over 250°C, respectively.

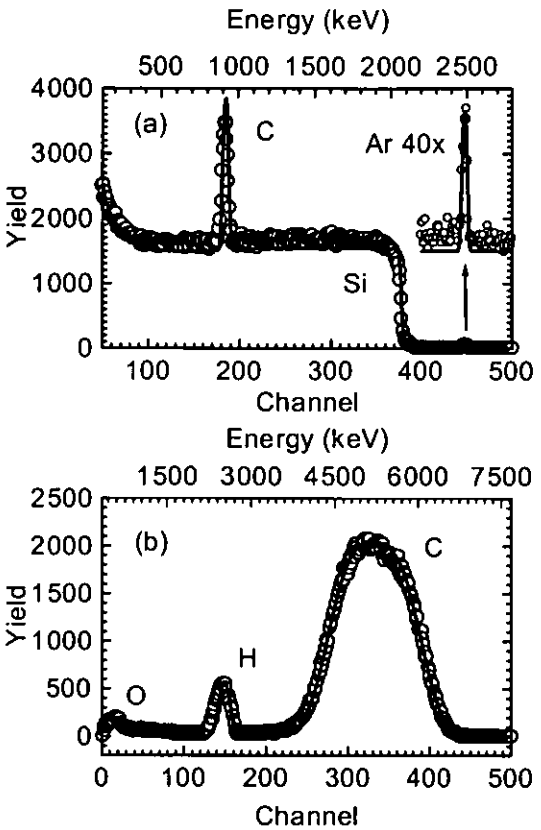

Figure 3.3. RBS (a) and ERDA (b) spectra of the film grown with an energy per carbon atom of 40 eV/atom.

3.3. DEPOSITION RATE AND FILM DENSITY.

The deposition rate is defined as the film thickness grown per unit time whereas the evaporation rate corresponds to the deposition rate for the samples grown without ion assistance. Typical evaporation rates achieved for the evaporation of graphite range between 1-3 Å/s. The deposition rates, normalised to the corresponding evaporation rate for each film, is illustrated in Figure 3.4 for the a-C films as a function of the ion energy per incoming carbon atoms.

The assistance process produces a reduction of the deposition rate as we increase the energy per carbon atom. Since the flux of carbon atoms reaching the substrate is kept constant during deposition, the reduction of the deposition rate can be explained by several factors. First, the reduction can be attributed to a densification process. In this case, the ion bombardment favours the formation of dense sp^3 configurations and anneals out the vacancies present in evaporated carbon films [27]. Second, part of the evaporated atoms can be re-emitted or sputtered and do not contribute to the film growth. The sputtering process should present a threshold value of the momentum transfer since it is necessary to overcome the displacement energy of the deposited atoms [28]. This process can be also accompanied of two effects that depend on the ion energy and flux. First, upon high ion energy bombardment the sp^3 sites are

transformed into less energetic sp^2 sites. The evolution of diamond and amorphous carbon films towards a graphitic structure upon ion irradiation is well reported in the literature [29,30,31]. Second, for low energies, the less dense sp^2 phase may be preferentially etched, thus enriching the film with denser sp^3 carbon atoms.

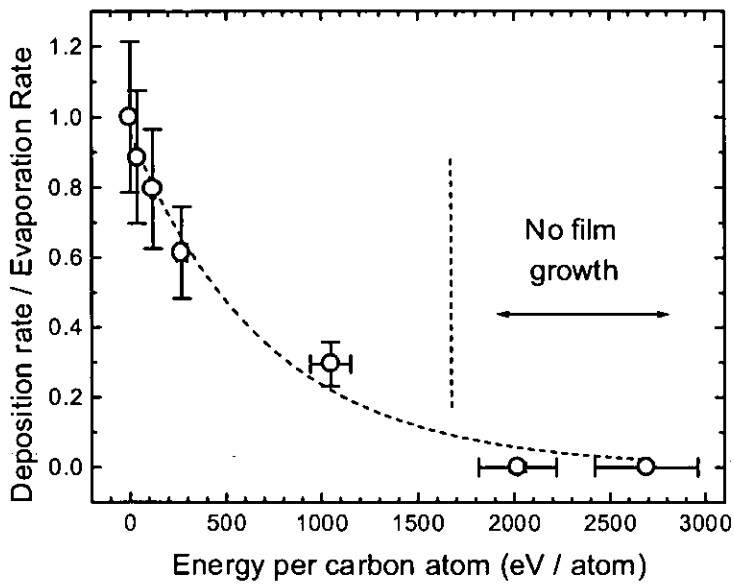

Figure 3.4. Deposition rate normalised to the evaporation rate, as a function of the ion energy per carbon atom during deposition.

Considering the density of sp^2 and sp^3 phases as ρ_{SP2}=2.25 g/cm^3 and ρ_{SP3}=3.5 g/cm^3, respectively, in the case of a transformation of half of the sp^2 carbon atoms into sp^3 sites (maximum achieved in IBAD methods [8]) the thickness would decrease a 65% of the initial value. Therefore, it is clear that above 500 eV/atom the sputtering process dominates the deposition. The sputtering yield increases with the ion energy and, therefore, the reduction of the deposition rate is higher for increasing energies. For ion energies per carbon atom above 1500 eV/atom sputtering exceeds deposition and no film growth is appreciable.

In order to discern if there is densification at any energy range, the film density was determined by dividing the areal density provided by the ion beam analysis (RBS and ERDA) over the thickness of the films as measured by profilometry. In our case, we have only taken into account the atomic density of carbon atoms to avoid that the higher mass of Ar atoms mask the calculated values. The uncertainty of the density values ranges between 5-10%, mainly affected by the accuracy of the thickness measurements. This analysis could not be performed in the thinnest films since the results are not

reliable due to large uncertainty in the thickness values. Figure 3.5 shows the resulting values as a function of the ion energy per incoming carbon atom.

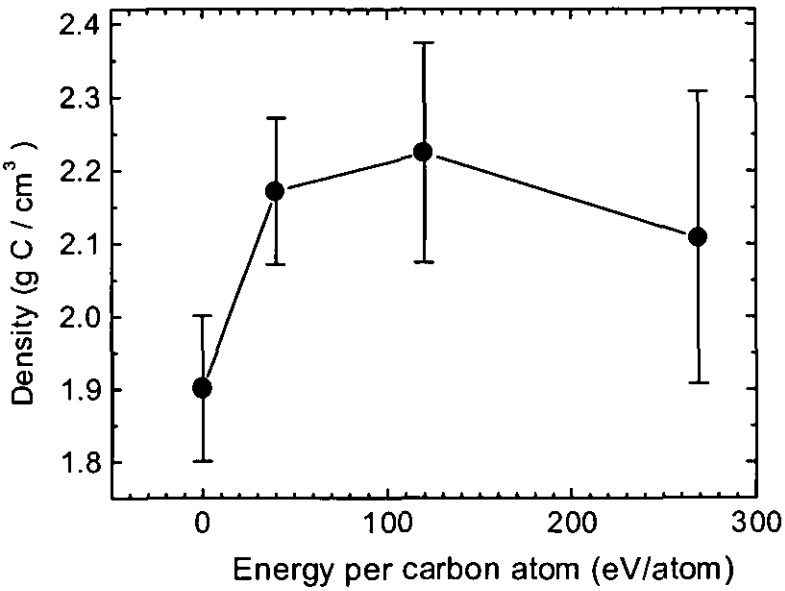

Figure 3.5. Density as a function of the energy per incoming carbon atom.

The density of the e-C film is ~1.9 g/cm^2. Since this film is grown without assistance, it is reasonable to expect that some of the properties of the evaporated target material would be maintained in the deposited film. As described in the introduction, similar films have been found to contain ~90-95% of sp^2 sites and, hence, the structure should be graphitic-like. However, the density is lower than the ~2.2 g/cm^{-3} value of graphite. This difference is attributed to the presence of micro-voids in the evaporated amorphous graphitic network [32]. As a result of the ion assistance the density is increased between 2.0-2.2 g/cm^{-3}, supporting a densification mechanism. However, it is not clear if the densification is due to the reduction of micro-voids, preferential sputtering or creation of sp^3 sites. Further study of the bonding structure is necessary in order to understand the film growth mechanism.

3.4. BONDING STRUCTURE

3.4.1. Auger electron spectroscopy (AES)

The derivative Auger (AES) spectra for representative IBAD films are shown in Figure 3.6. The experimental data were smoothed with a five-points Fast Fourier Transform (FFT) filter. Other smoothing techniques, like adjacent averaging, led to identical results. We have used the Ar LMM line at 215 eV for calibration.

The elements present in the film, argon, carbon and oxygen, can be identified by the appearance of the respective Auger transition in Fig. 3.6. The composition of the samples was determined using the relative peak to peak heights in the Auger spectra and the sensibility factors at a primary energy of 3 keV. The argon and oxygen contents are around 3-4%, in agreement with the ion scattering results shown in the section 3.2.

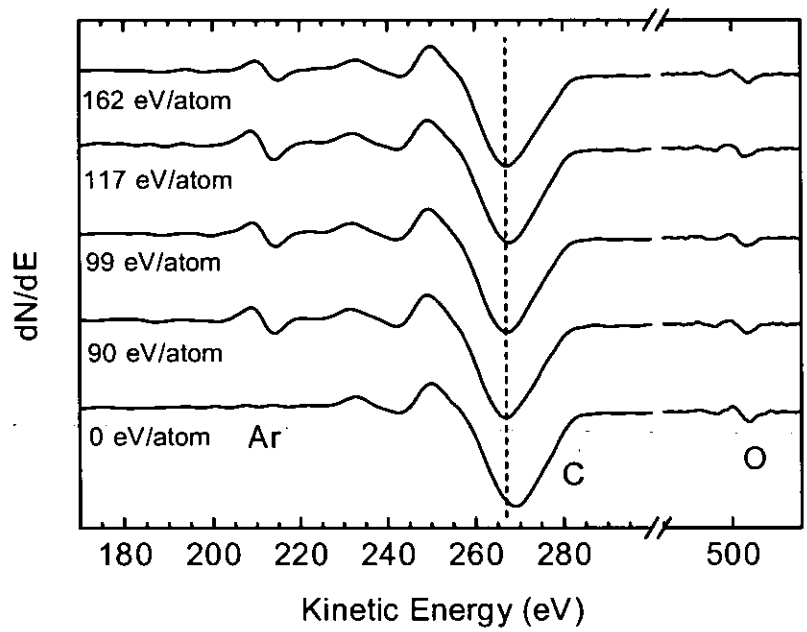

Figure 3.6. Survey Auger scans of a-C films grown by IBAD under different ion energy per carbon atom.

The shape analysis of the C KVV transition was performed with a detailed scan between 200 and 300 eV, as shown in Figure 3.7. We have included the spectra of polycrystalline graphite and CVD diamond for comparison. The spectrum of graphite has a main Auger minimum at 271 eV due to the $\pi^*\pi$ fold and a feature around 250 eV assigned to $\sigma^*\sigma$ fold in the heterocyclic ring structures [33]. On the other hand, CVD diamond presents a minimum at 267 eV associated with the $\sigma_p^*\sigma_p$ fold and two peaks at 247 and 255 eV, respectively. The features found in our films indicate a predominant sp^2 content in the samples.

The graphite-like structure of the films is also derived from the symmetry of the derivative lineshape. The formation of sp^2 bonding is characterised by an asymmetric shape due to the presence of a shoulder at 278 eV [34]. The origin of this shoulder seems related to damaged sp^2 hybrids [35]. On the contrary, diamond has a symmetric lineshape, as shown in Fig. 3.7. All of the films show the shoulder at 278 eV and, hence, have an asymmetry similar to graphite. Note that the shoulder at 278 eV is more pronounced in the evaporated film than in the polycrystalline graphite reference, as expected for a defect in the graphitic network.

The presence of sp^3 bonding can be studied considering the position of the main Auger transition. The spectrum of the evaporated film grown without assistance (0 eV/atom) has a minimum around 270 eV, indicating a sp^2 content close to graphite (100%). This minimum shifts towards lower energies with the assistance due to the increase of the diamond-like character. The sp^2 content can be directly quantified from the position of the minimum of the Auger spectrum from 267 eV (0%) to 271 eV (100%). However, the best procedure consists in fitting the experimental points with a linear combination of the graphite and diamond spectra [35]. For this calculation we have assumed that the Auger sensitivity for both phases is the same. This assumption is reasonable since the intensity of the Auger transition depends in the probability of creating a core hole, which should not depend on the chemical bonding [35]. The results indicate that the evaporated film has a sp^2 content around 90%, in agreement with previous reports. The assisted films have a similar sp^2 content around 60-75%. The small change observed in the sp^2 content is due to the narrow range of assisting energies (below 200 eV/atom). This study is completed and corroborated by a more detailed analysis performed with XANES.

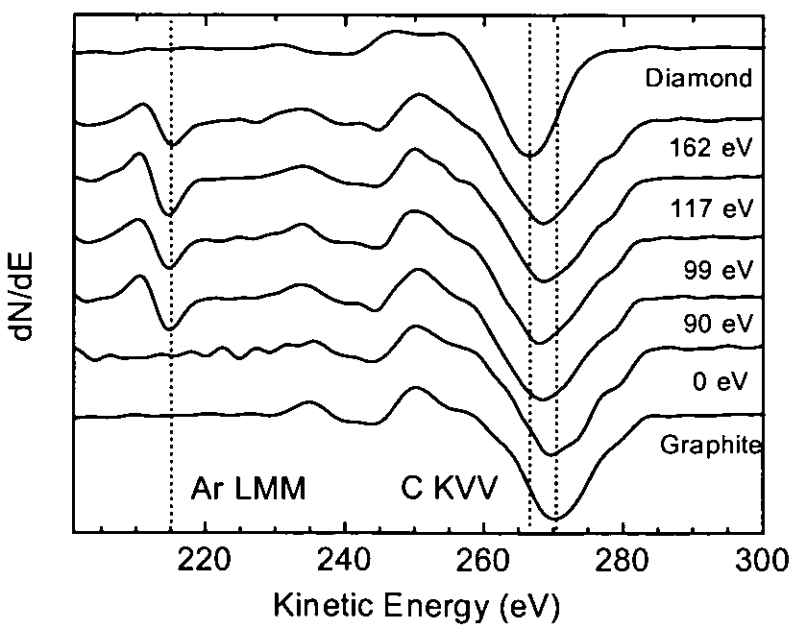

Figure 3.7. Detailed AES spectra for the samples shown in Fig. 3.6

3.4.2. X-Ray Absorption Near Edge Spectroscopy (XANES).

X-Ray Absorption Near Edge Spectroscopy (XANES) has been used to quantify the sp^3 content and obtain information on the bonding structure. The measurements were repeated in several points of each sample to confirm the homogeneity of the coating. In all the cases, identical spectral shape was obtained.

Figure 3.8 displays the photo-absorption spectra at the C(1s) edge for a set of a-C films grown with different values of E/A. The spectra are normalised to the same height for comparison purposes. In the figure, the reference spectra from highly oriented pyrolitic graphite (HOPG), crystalline diamond and disordered graphite as a result of irradiation with 1 keV Ar^+ ions are also included. The latter case is representative of an amorphous carbon film with 100% sp^2. The graphite spectrum shows an absorption threshold of the transition 1s → π* states at 284 eV and a second threshold of transitions 1s → σ* states at 291 eV. The resonance peak at 285.4 eV is a fingerprint of sp^2 coordinated carbon [36]. Diamond lacks of π* states and, hence, shows a single absorption edge at 289 eV.

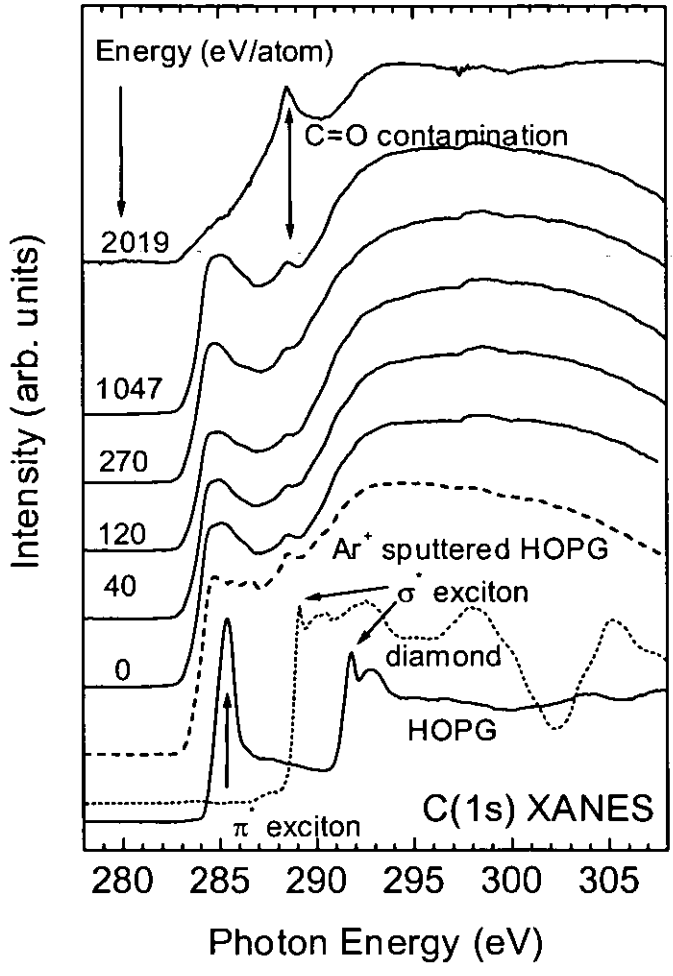

Figure 3.8. XANES spectra as a function of the energy per incident carbon atom.

The overall shape of the spectra for all the amorphous carbon films is similar, except for the sample grown with the highest assisting energy. As shown in section 3.2, under these conditions no film is grown due to dominant sputtering processes. In this case, the XANES signal is dominated by the C=O surface contamination on the silicon substrate [37]. The spectra for the rest of the films show a π^* peak

characteristic of sp^2 bonded carbon, although much broader than the graphite reference. The broad π^* feature in the a-C films has structure, indicating the presence of several bonding environments related to defects in the graphitic coordination and bonding between sp^2 and sp^3 hybridised carbon atoms. The σ^* region starts at 289 eV, representing states from sp^3 hybrids, and merges with the σ^* states from sp^2 hybrids that appear beyond 291 eV. The spectra do not show separated σ^* absorption edges related to segregated sp^2 and sp^3 phases and indicates that mixing of sp^2 and sp^3 carbon occurs at the atomic level. These are the features commonly found in amorphous diamond-like carbon [38,39].

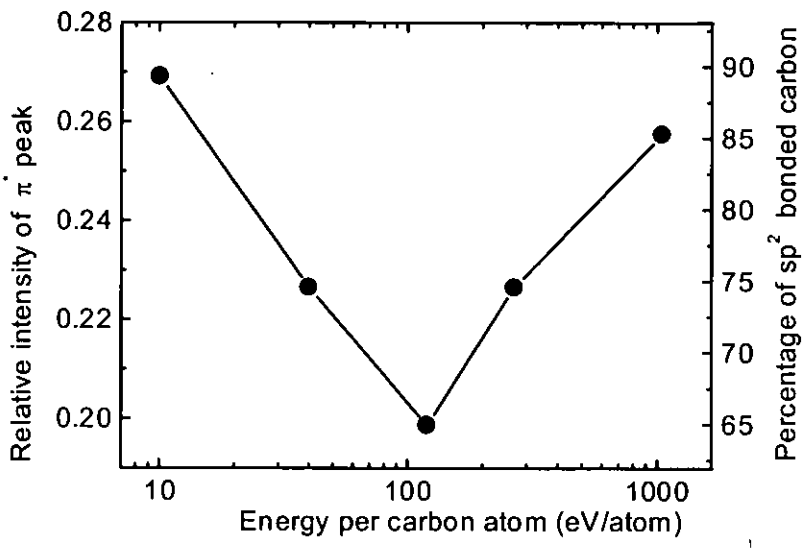

Figure 3.9. Relative intensity of π^* respect to σ^* states (left axis) and the corresponding sp^2 content (left panel) derived from the XANES spectra.

The quantification of the sp^2/sp^3 content in the films is derived from the relative intensity ratio of π^*/σ^* states, a procedure similar to that employed in EELS [40]. This method considers the decrease of the π^* intensity as due to the increase of the sp^3 content, and is nowadays accepted as the most reliable way of quantifying the sp^3 content in a-C films. The use of XANES has the advantage over EELS of a better resolution. For computing purposes, the area between 282 and 287 eV was assigned to π^* states and the area between 294 and 301 eV to σ^* states. The intensity ratios were compared with the spectrum from the Ar^+ sputtered HOPG reference, whose sp^2 content is ~100%. The reference spectrum for HOPG can not be used for this purpose because the π^* peak has an excitonic origin and its intensity depends on the microstructure which affects electron localisation [36]. Actually, the relative π^* intensity from the Ar^+ sputtered HOPG is only 80% of the intensity from HOPG. The film grown without assistance contains a sp^2 content of ~90%, in agreement with AES. The π^* intensity ratio and the corresponding sp^2 content for

the assisted films are displayed in Figure 3.9. The analysis reveals an optimal range around ~100 eV/atom for the promotion of sp^3 atoms.

Finally, an angle dependent XANES study is shown in Figure 3.10. This study has been performed on several samples to check if preferential orientation of sp^2 phases with respect to the substrate surface occurs in the films, as has been observed in other ion assisted growth processes [41]. According to the photo-absorption dipole selection rules, the intensity from π^* states follows a cosine-squared dependence with the angle between the light and the π bonds [42]. The angle that is considered in Fig. 3.10 is the angle between the incident beam and the substrate normal. The XANES spectra obtained are similar and identical intensity of the π^* states are found for all the orientations (inset figure). Therefore, the films are completely isotropic, without any preferential orientation.

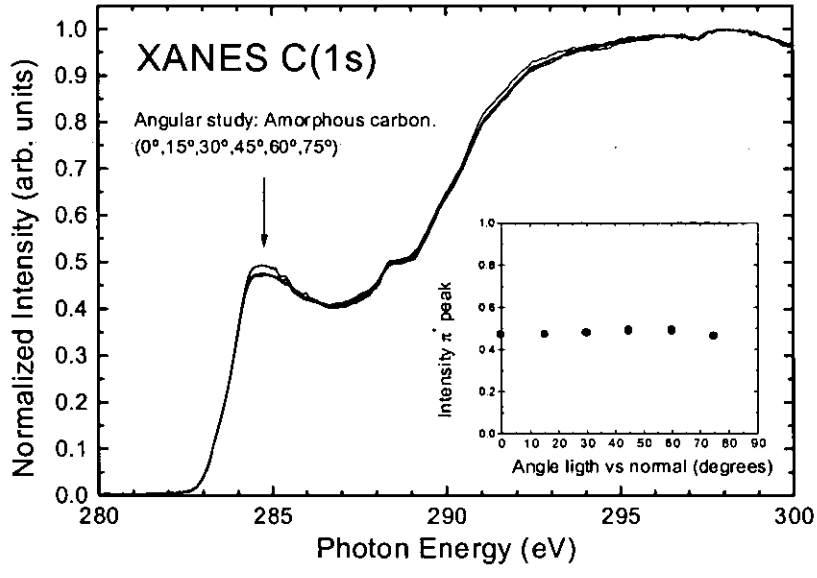

Figure 3.10. XANES angle dependence study on an amorphous carbon film.

3.5. MICROSTRUCTURE.

The microstructure of the a-C films has been studied with Raman spectroscopy, since it is a technique sensitive to changes in the domain size when it approaches the nanometric range. The typical Raman spectrum of an amorphous carbon film is shown in panel (a) of Figure 3.11. There are three broad bands at 690, 1500 and 3000 cm^{-1}, respectively. The first band is due to C-C vibrations out of the basal planes and only occur when there is structural disorder in the graphitic network [43,44]. The other two bands correspond with the first and second order of disordered sp^2 carbon, respectively. The first order band is normally decomposed into two peaks, as illustrated in panel (b) of Figure 3.11 for our amorphous carbon samples grown under different ion assisting energy per incoming carbon atom. The first peak,

labelled "G" (graphite), is located around 1580 cm^{-1} and arises from in-plane vibrations of the graphite-like rings. This band is related to the sharp and intense Raman peak at 1580 cm^{-1} in crystalline graphite [45]. This peak broadens and shifts to lower values with decreasing crystallite size. The second band, labelled as D (disorder), is located around 1360 cm^{-1} and only appears when small crystallites are formed [45]. It corresponds to phonons with non-zero wavevector in a graphitic network, which are selection rule prohibited in a perfect crystal but becomes visible in nanodomains due to uncertainty in the wavevector.

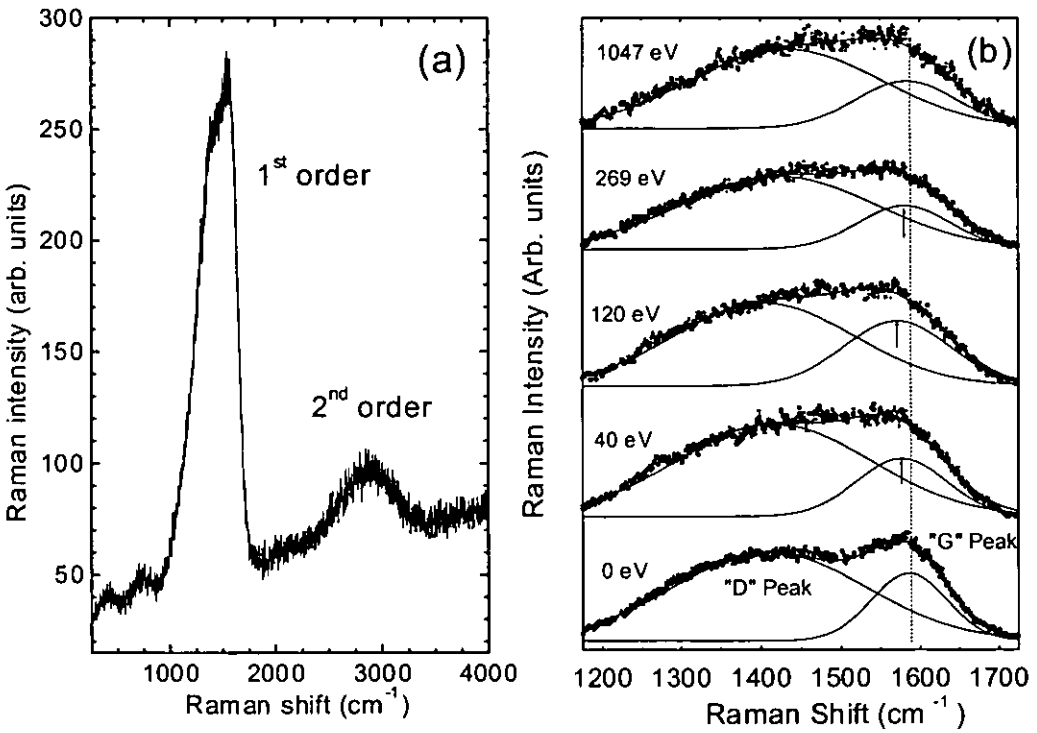

Figure 3.11. Raman spectra of an amorphous carbon film (a) and first order band of graphitic carbon films grown under different ion assisting energy per carbon atom (b).

Despite the indirect information obtained with Raman, this technique has been widely used to characterise amorphous carbon films. Raman cannot guarantee the presence of sp^3 bonding unless the 1330 cm^{-1} peak of crystalline diamond [46] is observed, but provides interesting information on the microstructure of graphitic domains based on the following. First, the downshifting of the G peak is due to the graphitic bond angle disorder [47]. Second, the width of the G peak increases with decreasing graphitic domain size [48,49], ranging its full width at half-maximum (FWHM) from 14 cm^{-1} in crystalline graphite to ~100-200 cm^{-1} in amorphous films. Finally, the intensity ratio I(D)/I(G) of the D to G peaks increases inversely proportional to the grain diameter in the 300 to 2.5 nm range [45] and

decreases directly proportional for smaller domain sizes [50]. To determine the parameters of the G and D peaks one needs to perform a curve fitting analysis. Different criteria and curve fitting methods of the Raman spectra from amorphous carbon appear in the literature, though none of them is totally accepted. The most simple and common procedure considers two gaussian distributions related to the G and D components, centred at ~1580 and ~1350 cm^{-1} [51,52] and it is the one used here.

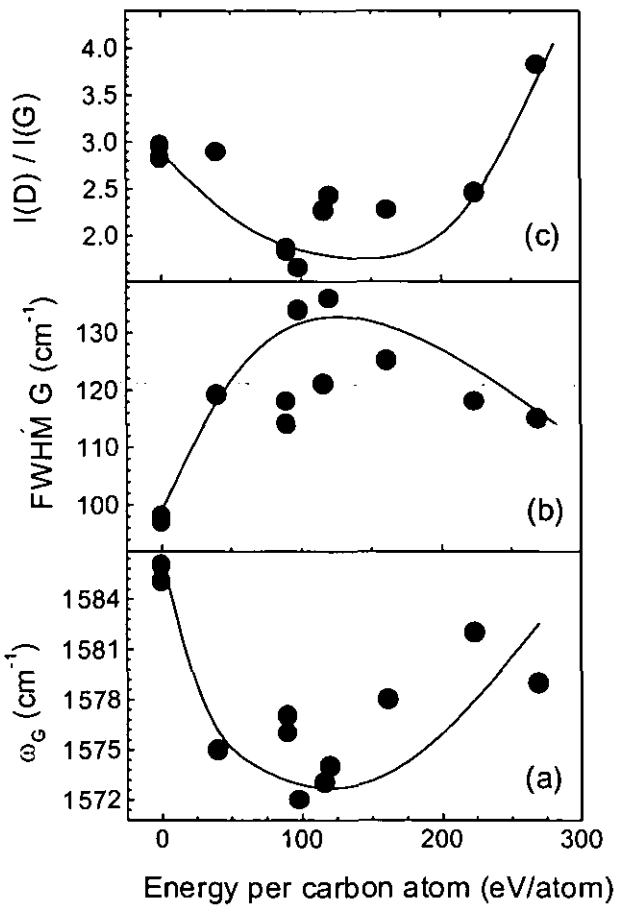

Figure 3.12. Raman fitting parameters of the first order Raman spectra of graphitic carbon for a-C films grown under different ion energy per carbon atom: (a) Position of the G peak, (b) Full width at half maximum (FWHM) of the G peak and (c) relative intensity of the D and G peaks.

The fitting parameters of the Raman spectra are shown in Figure 3.12. The position of the G peak (Fig. 3.12a) shows a minimum around 100 eV/atom, which should correspond to a maximum bond-angle disorder. The similar behaviour of the sp^3 content found in Fig. 3.8 indicates a correlation between both parameters. The values of the FWHM (Fig. 3.12b) are consistent with the lack of long range order in the graphitic phases of our films, with a maximum disorder for the highest sp^3 content. The values of

I(D)/I(G) (Fig. 3.12c) also indicate a minimum size of the graphitic grains for the maximum sp^3 content. From this results we can point out that the formation of sp^3 content and disorder in the sp^2 phases are close related. With this premise and the curves displayed in Fig. 3.12, we find that the optimal parameter range for promoting sp^3 bonds would be 50-200 eV per carbon atom.

3.6. THERMAL STABILITY

The final application of a coating depends on its stability, either thermal or mechanical. The thermal stability is an important factor in cutting tools or other devices that reach high temperatures during operation. In our films we have studied the thermal stability with XANES. The samples were heated in vacuum in the measurement chamber for temperatures up to 500°C by direct flow of current through the Si substrates.

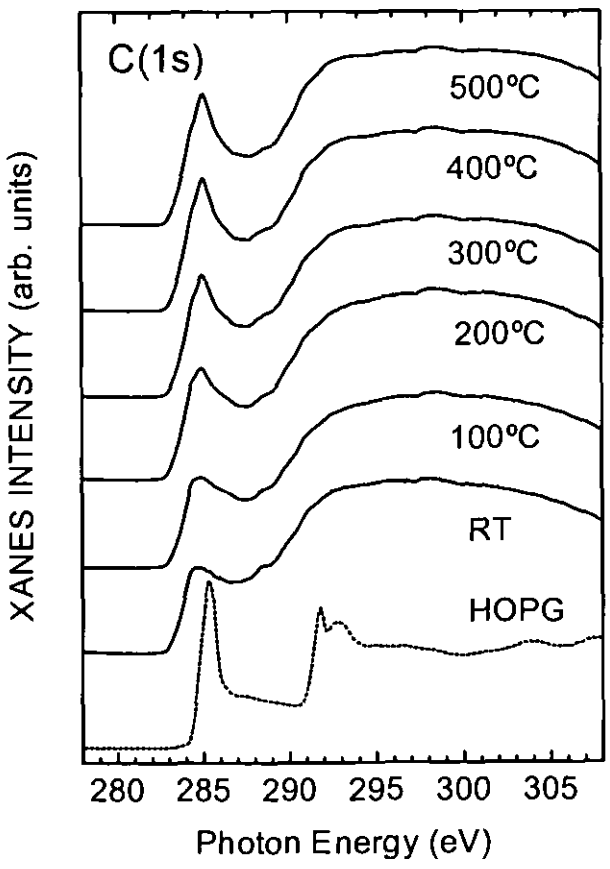

Figure 3.13. XANES annealing process of an amorphous carbon film grown with an evaporation rate of 2 Å/s, 360 eV and 1.4 mA/cm^2.

The results of the annealing process are similar for all the samples. An example is shown in Figure 3.13 for a selected sample grown with an evaporation rate of 2 Å/s, 360 eV and 1.4 mA/cm^2. We

can point out that the samples are thermally unstable since a graphitization process is evident in the structure above 200°C. The graphitization is revealed by the increase of the graphite peak around 285 eV. The increase of this peak is related to a higher size of the graphitic domains as a result of the ordering induced by the annealing process. Similar temperature behaviours have been reported in the literature [53,54].

3.7. MECHANICAL PROPERTIES

Figure 3.14 displays the hardness as a function of the ion assisting energy per incoming carbon atom. The results for the samples grown with energies above 300 eV/atom are not reliable since those films are too thin (<50 nm) and the hardness measurements are affected by the substrate. The hardness increases with the ion assistance energy from 8 GPa up to ~20 GPa.

The maximum hardness is found in the optimal range for promotion of sp^3 sites discussed previously but slightly shifted. The maximum sp^3 content was found around 100 eV/atom whereas the maximum hardness is around 200 eV/atom. This is not contradictory since the hardness is affected by other factors such as the microstructure, apart from the atomic bonding. This trend is discussed below. The elastic modulus follows well the relation H/E~0.1 found in diamond and indicates a good elastic behaviour.

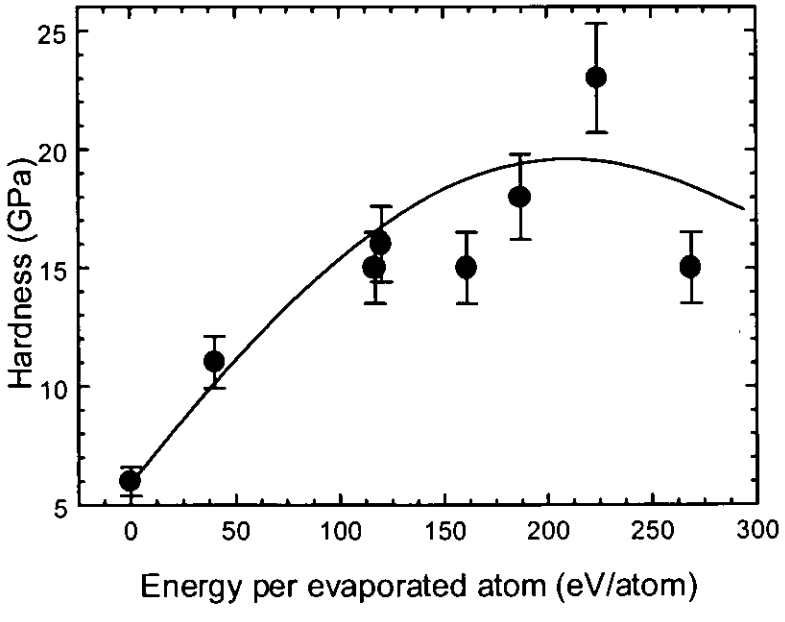

Figure 3.14. Hardness for a-C films grown with different assisting parameters.

3.8. GROWTH MECHANISM.

3.8.1. The IBAD growth method.

The synthesis of diamond and other sp^3-based materials requires of high pressure and high temperature (HPHT) conditions. These conditions may occur in thin film deposition in local regions leading to the promotion of sp^3 sites. In the case of amorphous carbon films, a subplantation mechanism has been proposed to explain the formation of sp^3 sites [4]. In order to achieve subplantation sites, the incident carbon atoms must penetrate the surface with energies in the range of 10-1000 eV. In the case of evaporation or sputtering of graphite, the species are emitted with energies between 0.1 and 10 eV. Therefore, the assistance process with simultaneous ion bombardment with energetic particles (~100-1000 eV) during deposition in IBAD methods is aimed at the transference of energy to the carbon atoms in the ion-atom collisions.

In the simplest subplantation case, all the carbon atoms reach the surface with the same energy. In this way, carbon films with a sp^3 content up to 80-90% have been grown within a range of incident energies between 50-200 eV [55]. In the case of IBAD, the carbon atoms are accelerated through momentum transfer in Ar^+-C collisions. In the collision, the energy transfer depends on the ion energy, ion to carbon atom ratio, assisting ion mass (M), atom mass (m) and scattering angle (ϕ). The statistical nature of these collisions imply that only a small fraction of the carbon atoms reaching the substrate penetrate the subsurface layers within the optimal energy range necessary for sp^3 promotion [56]. This fact limits the sp^3 content that can be achieved and explains the moderate sp^3 content (<40%) found in our films.

In the Ar^+/C collision, the maximum energy transfer is derived from the cinematic factor γ (see equation 2.4), which is 0.36 for our experimental set-up. In our case, the maximum of sp^3 content is achieved for incident ion energies per condensing atom between 50-200 eV, which correspond to incident carbon atoms with energy of 20-70 eV. Similar results have been reported by other IBAD systems [57,58]. Normally, optimal ion energies of ~100 eV are reported for the promotion of sp^3 sites and the high proportion of tetrahedral bonding is maintained for energies up to 1000 eV, provided the substrate is accurately kept at room temperature [59]. In the case of IBAD, the energy shift could be attributed to contribution of additional ion bombardment effects like preferential sputtering.

In the IBAD process, we also have to consider additional ion-induced effects on the growing film apart from those derived from ion-atom collisions. In particular, Ar^+ bombardment may produce large damage in the growing film due to sputtering and irradiation effects [60]. Both effects should be dominant for high ion energy per incoming atom since it implies a high ion energy and/or high ion doses. This fact explains the reduction of the sp^3 content above 200 eV/atom.

3.8.2. Microstructure and bonding structure.

In the optimal energy range of ion assistance, the previous results indicate the promotion of sp^3 hybrids in the amorphous carbon network. This change is followed by a decrease in the graphitic domain size as revealed by Raman. Both results are consistent with the formation of a network of graphitic planes interconnected through sp^3 sites. In this case, a smaller graphitic domain size corresponds to a larger fraction of sp^3 connecting sites. The interconnectivity should be close related with the film density. The above argument is supported by the linear dependence of the density with the sp^3 content, as shown in Figure 3.15.

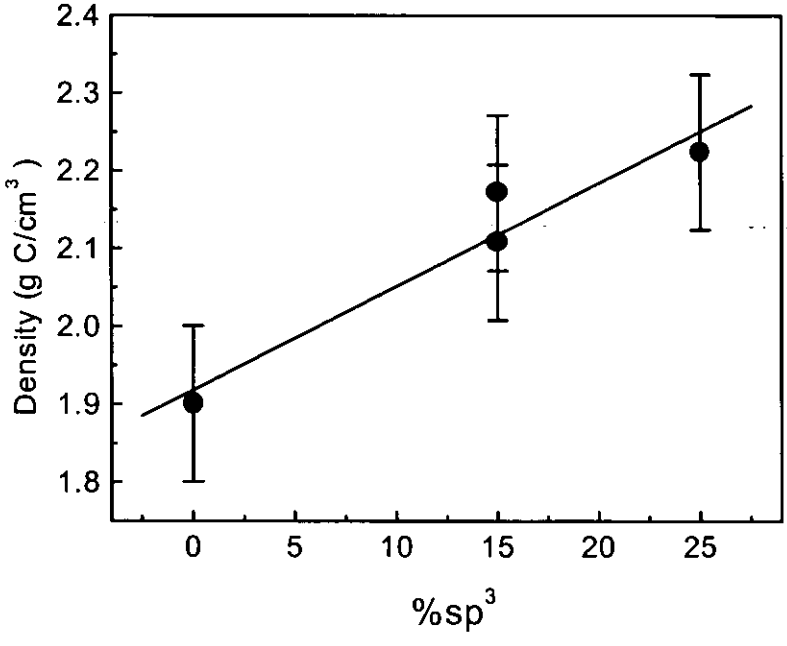

Figure 3.15. Relation between density and sp^3 content in our amorphous carbon films.

Regarding the types of bonding present in the films, we anticipated a mixing of sp^2 and sp^3 sites at the atomic level. This means that there are no segregated sp^3 or sp^2 phases. The bonding between sp^2 and sp^3 sites is of σ type. The π bonding within the graphitic domains reflects on the XANES π^* density of states, which is shown in detail in the lower panel (a) of Figure 3.16. The HOPG and Ar^+ sputtered references are also displayed. Note how the π^* states from defective graphitic environments in sputtered HOPG extend ~1 eV below the π^* resonance in HOPG. The a-C spectra were normalised to the minimum intensity at 287 eV, in the valley between the π^* and the σ^* states. Small differences are found in the spectral lineshape of a-C that are highlighted in the top panel (b) of Fig. 10 by subtracting from each spectrum the signal from the evaporated film without assistance.

For bombardment with ions of energy below 120 eV/atom, i.e. the region where formation of new sp^3 sites takes place, there is a decrease of the density of π^* states in the 284.5-287 eV region, and a slight increase of defect states at ~284 eV, labelled as A states. For ion energies beyond the optimal 120 eV/atom value, the amount of defect states A increases significantly, and new defect states B at ~285 eV appear. This is explained by the damage created by the increasing ion bombardment that transforms sp^3 sites into sp^2 sites, with an enlargement of the graphitic domains. Finally, at ion energy of 1047 eV/atom the initial lineshape is almost recovered, presumably due to the annealing induced by the ion stopping.

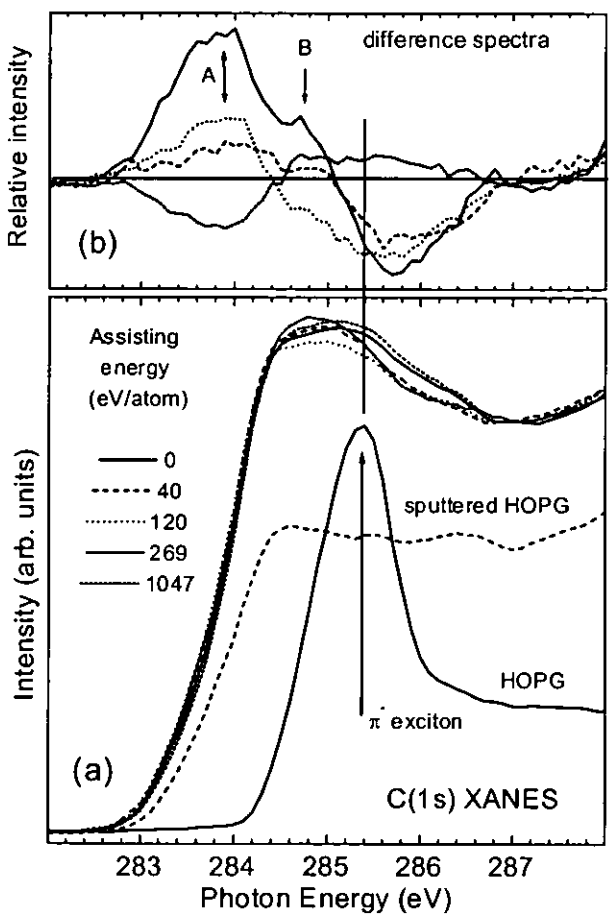

Figure 3.16. (a) Detailed view of the π^* region of the XANES C(1s) spectra and (b) difference spectra obtained by subtracting from each spectrum the signal from the evaporated film without assistance.

The proposed bonding scheme permits to explain the observed mechanical properties of the films, with a significant increase of the hardness from 8 to ~20 GPa for a change of ~30% in the sp^3 content. The cross-linking of graphitic planes through tetragonal sp^3 sites would confer the carbon network a three-dimensional structure, with a moderate hardness. Note that sp^3 content is not the only

factor affecting the mechanical properties of the carbon film, since hardness values similar to ours have been reported for much higher sp^3 contents [61,62] and very hard all-sp^2 structures can be synthesised [21]. The discrepancy between the optimal assisting energy for the promotion of sp^3 sites and hardness supports the presence of this superstructure. In the case of fullerene-like films the high hardness is the result of the folding and cross-linking of basal planes. These fullerene-like structures are especially important in the case of graphitic carbon nitride films [20,63], which would be discussed in the next chapter.

3.9. CONCLUSIONS

The IBAD method based on carbon evaporation with concurrent ion bombardment allows the synthesis of hydrogen-free carbon films with a moderate sp^3 content of ~30%. The process is controlled by densification and sputtering of the growing film. The densification process occurs for ion energies per incoming evaporated carbon atom below 500 eV/atom. For energies above this value, the sputtering process dominates and the deposition rate is considerably reduced. For ion energies above 1500 eV the sputtering rate equals deposition and no film is obtained.

The subplantation model can be applied to the IBAD growth process although some peculiarities must be considered. In this context, additional effects induced by the concurrent ion bombardment apart from the energy transfer in the Ar^+-C collisions have to be included in the discussion. First, the optimal range for ion assistance is found in the range between 50-200 eV/atom, which corresponds to incident carbon atoms with a maximum energy within 20-70 eV. The shift towards lower energies respect to a pure subplantation model (~100 eV) is explained by additional contribution of preferential sputtering of sp^2 phases. Second, the sharp reduction of the sp^3 content for energies above 200 eV/atom should be related to ion induced damage for large ion energies that result in the transformation of sp^3 into sp^2 sites. Finally, the moderate sp^3 content achieved in our films is explained by the random nature of the Ar^+-C collisions. This fact implies that the energy transferred presents a broad distribution and, therefore, only a fraction of the carbon atoms penetrate the subsurface layer within the optimal energy range necessary for sp^3 promotion.

The sp^3 content affects macroscopic properties such as density and hardness. However, the hardness increases significantly (by a factor of ~3), suggesting that the moderate sp^3 content is not the only parameter affecting the mechanical performances. In this way, folding of graphitic planes and cross-linking through sp^3 sites seem to be of major importance.

REFERENCES

1. J. Robertson, Current Op. in Solid State and Mat. Sci. 1 (1996) 557.
2. H. Pan, M. Pruski, B.C. Gerstein, F. Li, J.S. Lannin, Phys. Rev. B 44 (13) (1991) 6741.
3. J. Robertson, Diam. Rel. Mat. 3 (1994) 361.
4. Y. Lifshitz, S.R. Kasi, J.W. Rabalais, Phys. Rev. B 41 (15), 10468 (1990).
5. P.J. Fallon, V.S. Veerasamy, C.A. Davis, J. Robertson, G.A.J. Amaratunga, W.I. Milne, J. Koskinen, Phys. Rev. B 48 (7) (1993) 4777.
6. J. Robertson, Adv. Phys. 35 (1986) 317.
7. S. Neuville, A. Matthews, MRS Bulletin 9 (1997) 22.
8. J.J. Cuomo, J.P. Doyle, J. Bruley, J.C. Liu, Appl. Phys. Lett. 58 (5) (1991) 466.
9. P.H. Gaskell, A. Saeed, P. Chieux, D.R. M. McKenzie, Phys. Rev. Lett. 67 (10) (1991) 1286.
10. P.J. Fallon, V.S. Veerasamy, C.A. Davis, J. Robertson, G.A.J. Amaratunga, W.I. Wilne, J. Koskinen, Phys. Rev. B 48 (7) (1993) 4777.
11. E. Grossman, G.D. Lempert, J. Kulik, D. Marton, J.W. Rabalais, Y. Lifshitz, Appl. Phys. Lett. 68 (9) (1996) 1214.
12. M. Basu, J. Dutta, S. Chaudhuri, A.K. Pal, M. Nakayama, Vacuum 47 (3) (1996) 233.
13. G.J. Vandentop, M. Kawasaki, R.M. Nix, I.G. Brown, M. Salmeron, G.A. Somorjai, Phys. Rev. 41 (5) (1990) 3200.
14. J.C. Angus, C.C. Hayman. Science 241 (1988) 913.
15. J.C. Angus, F. Jansen, J. Vac. Sci. Technol. A 6 (3) (1988) 1778.
16. M Weiler, S. Sattel, T. Giessen, K. Jung, H. Ehrhardt, Phys. Rev. B 53 (1996) 1594.
17. J. Schwan, S. Ulrich, K. Jung, H. Ehrhardt, R. Samlenski, R. Brenn, Diam. Rel. Mat. 4 (1995) 304.
18. H.W. Kroto, J.R. Heath, S.C. O'Brien, R.F. Curl, R.E. Smalley, Nature 318 (1985) 162.
19. S. Iijima, Nature 354 (1991) 56.
20. H. Söjström, S. Stafström, M. Boman, J.E. Sundgre, Phys. Rev. Lett. 75 (7) (1995) 1336.
21. I. Alexandrou, H.J. Scheibe, C.J. Kiely, A.J. Papworth, G.A.J. Amaratunga, B. Schultrich, Phys. Rev. B 60 (1999) 10903.
22. H. Hiura, T.W. Ebbesen, J. Fujita, K. Tanigaki, T. Takada, Nature 367 (1994) 148.
23. B. André, F. Rossi and H. Dunlop, Diam. Rel. Mat. 1 (1992) 307.
24. R. Kleber, M. Weiler, A. Krüger, S. Sattel, G. Kunz, K. Jung, H. Ehrhardt, Diam. Rel. Mat. 2 (1993) 246.
25. J. Ullmann, U. Falke, W. Scharff, A. Schröer, G.K. Wolf, Thin Solid Films 232 (1993) 154.
26. W. Gissler, P. Hammer, J. Haupt, Diam. Rel. Mat. 3 (1994) 770.
27. F. Rossi, B. Andrè, A. van Veen, P.E. Mijnarends, H Schut, M.P. Delplancke, W. Gissler, J. Haupt, G. Lucazeau, L. Abello, J. Appl. Phys. 75 (6) (1994) 3121.

28. W. T. Zheng, E. Broitman, N. Hellgren, K.Z. Xing, I. Ivanov, H. Sjöström, L. Hultman, J. E. Sundgren, Thin Solid Films 308-9 (1997) 243.
29. I. Gouzman, R. Brener, C. Cytermann, A. Hoffman, Surf. Interf. Anal. 22 (1994) 524.
30. P. Reinke, G. Franz, P. Oelhafen, Phys. Rev. B 54 (10) (1996) 7067.
31. A. Fuchs, J. Scherer, K. Jung, H.Ehrhardt, Thin Solid Films 232 (1993) 51.
32. J. Schwan, S. Ulrich, T. Theel, H. Roth, H. Ehrhardt, P. Becker, S.R.P. Silva, J. Appl. Phys. 82 (12) (1997) 6024.
33. K.J. Boyd, D. Marton, S.S. Todorov, A.H. Al-Bayati, J. Kulik, R.A. Zuhr, J. W. Rabalais, J. Vac. Sci. Technol. A 13 (4) 2110.
34. J.A. Martín-Gago, J. Fraxedas, S. Ferrer, F. Comin, Surf. Sci. Lett. 260 (1992) L17.
35. H.J. Steffen, C.D. Roux, D. Marton, J.W. Rabalais, Phys. Rev. B 44 (8) (1991) 3981.
36. J. Díaz, S. Anders, X. Zhou, E.J. Moler, S.A. Kellar, Z. Hussain, J. Electron Spectrosc. Relat. Phenom. 103 (1999) 545.
37. I. Jiménez, D. G. J. Sutherland, J. A. Carlisle, A. van Buuren, L. J. Terminello, F. J. Himpsel., Phys. Rev. B 57 (1998) 13167.
38. L. Fayette, B. Marcus, M. Mermoux, G. Tourillon, K. Laffon, P. Parent, F. Le Normand, Phys. Rev. B 57 (1998) 14123.
39. J. Fink, T. Müller_Heizerling, J. Plüger, A. Bubenzer, P. Koidl, G. Crecelius, Solid State Commun. 47 (1983) 687.
40. J. Kulik, G. D. Lempert, E. Grossman, D. Marton, J. W. Rabalais, Y. Lifshitz, Phys. Rev. B 52 (1995) 15812.
41. I. Jiménez, M. M. García, J. M. Albella, L. J. Terminello, Appl. Phys. Lett. 73 (20) (1998) 2911.
42. J. Stöhr, *NEXAFS spectroscopy*, Springer, Berlin (1992).
43. F. Parmigiani, E. Kay, H. Seki, J. Appl. Phys. 64 (1988) 3031.
44. M.Y. Chen, D. Li, X. Lin, V.P. Dravid, Y. Chung, M. Wong, W.D. Sproul, J. Vac. Sci. Technol. A 11 (3) (1993) 521.
45. F. Tuinstra, J.L. Koenig, J. Chem. Phys. 53 (3) (1970) 1126.
46. P. Bou, L. Vandenbulcke, J. Electrochem. Soc. 138 (10) 1991.
47. D. Beeman, J. Silverman, R. Lynds, M.R. Anderson, Phys. Rev. B 30 (1984) 870.
48. R.O.Dillon, J.A.Woollam, Phys. Rev. B 29 (6) (1984) 3482.
49. H.J. Scheibe, D. Drescher, P. Alers, Fres. J. of Anal. Chem. 353 (1995) 695.
50. D.C. McCulloch, S. Prawer, A. Hoffman, Phys. Rev. B 50 (9) (1994) 5905.
51. M.A. Tamor, W.C. Vassell, J. Appl. Phys. 76 (6) (1994) 3823.
52. M. Yoshikawa, G. Katagari, H. Ishida, A. Ishitani, T. Akamatsu, J. Appl. Phys. 64 (11) (1988) 6464.

53. S. Sattel, M. Weiler, J. Gerber, T. Giessen, K. Jung, H. Ehrhardt, H. Roth, M. Scheib, J. Robertson, Diam. Rel. Mat. 4 (1995) 333.

54. R. Gago, O. Sánchez-Garrido, A. Climent-Font, J.M. Albella, E. Román, J. Räisänen, E. Rauhala, Thin Solid Films 338 (1999) 88.

55. Y. Lifshitz, S.R. Kasi, J.W. Rabalais, Phys. Rev. Lett. 62 (1989) 1290.

56. R. Gago, I. Jiménez, J.M. Albella, A. Climent-Font, D. Cáceres, I. Vergara, J.C. Banks, B.L. Doyle, L.J. Terminello, J. Appl. Physics 87 (2000) 8174.

57. J. Schwan, S. Ulrich, H. Roth, H. Ehrhardt, S.R.P. Silva, J. Robertson, R. Samlenski, R. Brenn, J. Appl. Phys. 79 (3) (1996) 1416.

58. B.André, F. Rossi, A. van Veen, P.E. Mijnareds, H. Schut, M.P. Delplancke, Thin Solid Films 241 (1994) 171.

59. E. Grossman, G. D. Lempert, J. Kulik, D. Marton, J. W. Rabalais, Y. Lifshitz, Appl. Phys. Lett. 68 (1996) 1214.

60. R. Gago, O. Böhme, J.M. Albella, E. Román, Diam. Rel. Mat. 8 (1999) 1944.

61. S. Logothetidis, C. Charitidis, Thin Solid Films 353 (1999) 208.

62. N. Savvides, T.J. Bell, Thin Solid Films 228 (1993) 289.

63. N. Hellgren, M.P. Johansson, E. Broitman, L. Hultman, J. Sundgren, Phys. Rev. B 59 (1999) 5162.

Chapter 4:

Amorphous carbon nitride films ($a\text{-}CN_x$)

4. AMORPHOUS CARBON NITRIDE FILMS (a-CN_x)

4.1. INTRODUCTION

Carbon nitride films have been the aim of intense research since the theoretical work of Cohen and Liu predicting a β-C_3N_4 phase harder than diamond [1]. Ever since, many thin film growth methods have attempted the synthesis of this phase [2]. Most of the reports deal with amorphous carbon nitride (a-CN_x) films with a graphitic-like structure and a nitrogen content below 50 at. % [3,4,5]. Despite this fact, graphitic a-CN_x films present good mechanical properties, including high elasticity and hardness values of ~20 GPa for low nitrogen contents [6] and up to ~60 GPa for higher nitrogen concentrations [7]. These experimental results have stimulated theoretical work on graphitic carbon nitrides, both on hypothetical crystalline phases [8,9,10] and on amorphous structures [11,12,13,14].

The first attempts in the synthesis of carbon nitride looked mostly at the nitrogen content in order to achieve the [N]/[C] value of 1.33 present in the C_3N_4 phase. However, the reported data have shown that the amount of N incorporated is not a sufficient characterisation parameter of the film, since similar N contents have led to very different film properties as it is described below. Therefore, the bonding structure is the main parameter controlling the physical properties. The different bonding structures are obtained as a result of the deposition conditions developed in each growth method.

Most of the results on the synthesis of carbon nitride films are consistent with the existence of four different bonding structures. First, a β-C_3N_4 phase with theoretical extreme hardness that corresponds to σ bonds between sp^3 hybridised carbon and sp^2 nitrogen. Only a few reports are consistent with the synthesis of β-C_3N_4 nanocrystals embedded in an amorphous matrix, making difficult a clear characterisation of the actual material [15]. A second possible structure consists in a network of sp^3 carbon atoms, capable of accommodating a certain amount of substitutional nitrogen. The tetrahedral carbon network is stable for a nitrogen doping < 10 at. % [16], transforming into a graphitic structure beyond that value with a substantial hardness decrease [17]. The third possibility is a polymeric paracyanogen-like structure containing a large proportion of C≡N bonds [18,19]. In this case, the hardness decreases with the nitrogen content. Finally, the fourth structure is based on a graphitic network with substitutional nitrogen in the hexagonal rings, with a hardness that increases with the nitrogen content as it is found experimentally [13,20].

In this chapter we report the results on the synthesis of a-CN_x films grown with our IBAD system. The deposition procedure consists in the evaporation of graphite and concurrent ion assistance at different energy and flux from N_2/Ar gas mixtures. The use of nitrogen ions is obviously aimed at the achievement of CN compounds. As derived from chapter 2, the addition of Ar to the assisting gas increases the momentum transfer in the ion assistance process. In this way, we will attempt the formation of sp^3 hybrids typical of hard phases, may be promoted. In the synthesis of tetrahedral carbon and cubic boron nitride

films, it is well established that one needs the assistance of heavy noble ions to increase the momentum transfer in the collisions in order to promote the formation of sp^3 hybrids [21,22]. However, this point remains unclear in the growth of carbon nitride films.

The resulting carbon nitrie films were found to be hard (~20 GPa) and graphitic. Therefore, they belong to the fourth category described above. In this discussion, we relate the deposition parameters with film composition and bonding structure in order to understand the properties of graphitic carbon nitride structures. The I/A ratio and E/A values for films grown at room temperature and under ion assistance with 100% N_2 are summarised in Table 4.1. The ion assistance was performed with a gas pressure of 2×10^{-4} mbar using a N_2 flux of 4 sccm.

Table 4.1. Growth parameters for the amorphous carbon films grown by IBAD for 100% N_2 .

Sample	Evaporation rate (Å/s)	Ion energy (eV)	I/A	E/A (eV/atom)
CN1	4	0	0	0
CN2	3	120	0.04	5
CN3	3	180	0.08	15
CN4	3	240	0.12	30
CN5	4	360	0.09	34
CN6	4	360	0.12	45
CN7	3	300	0.17	50
CN8	4	360	0.16	56
CN9	4	360	0.19	67
CN10	4	360	0.25	90
CN11	3	420	0.62	262
CN12	3	480	0.83	400

4.2. FILM COMPOSITION AND DEPOSITION RATE

We have checked the lateral and transversal homogeneity of our films by determining the composition at different points of each film and by using techniques with different depth sensitivity, respectively. In this context, the film composition was measured with X-Ray Photoemission (XPS), X-Ray Absorption (XAS or XANES) and Time-of-Flight Elastic Recoil Detection (TOF-ERDA). The results from the different techniques are consistent within 15-20%, depending on the sample. The N

content presented throughout this discussion corresponds to the XANES analysis except in the cases indicated.

In XPS measurements, electrons from the whole film area (~1 cm^2) were collected. The nitrogen fraction (X=[N]/[C]) was computed from the relative intensity of the N(1s) and C(1s) core level spectra, corrected for the atomic sensitivity factor [23]. XPS is a conventional technique for composition analysis with an analysis depth of ~2 nm.

XANES analyses the area of the synchrotron spot size, in our case ~1 mm^2. The measurement was repeated in several points of each sample leading to identical results and indicating good lateral homogeneity in the deposit. XANES provides a more detailed information about the bonding structure than XPS, with an analysis depth of ~10 nm. In this case, the computation of the N content is performed from the relative height of the N(1s) respect to the C(1s) absorption edges, corrected with a proportionality factor determined from comparison with reference samples of crystalline h-BN and B_4C. The proportionality factor has been found to depend on the cleanliness of the grid used for signal normalisation. Therefore, *in situ* calibration with reference samples is preferred to the use of tabulated absorption cross sections.

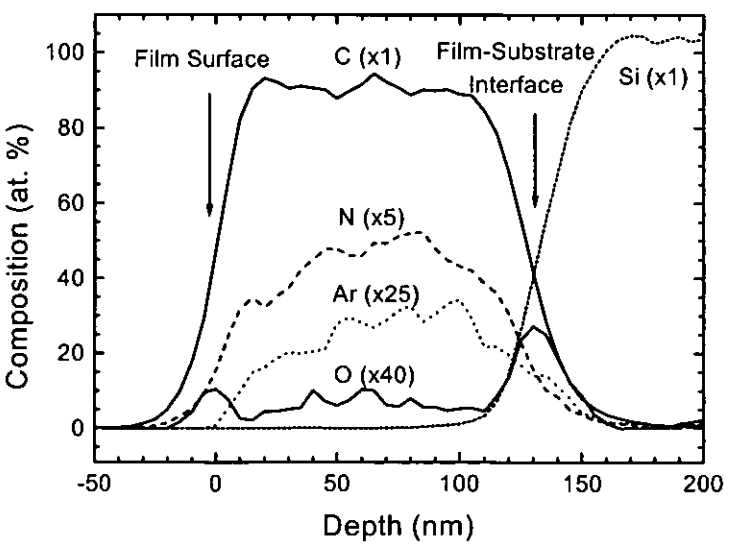

Figure 4.1. TOF-ERDA composition depth profile of a carbon nitride film grown by IBAD (91% N_2 and 9% Ar in the gas mixture, 360 eV and 1 mA/cm^2).

In the case of TOF-ERDA, the analysis area is ~10 mm^2 and the whole composition depth profiles is obtained in a single experiment. Figure 4.1 shows the composition depth profile of a sample grown with 91% N_2 and 9% Ar ion assistance, 360 eV and 1 mA/cm^2. The shape of the profile indicates that the nitrogen content is distributed over the whole film thickness, within a concentration variation of ~20%. This can be considered as a good transversal homogeneity in the film composition. The hydrogen

content is below 1 at. % for all the films measured. The oxygen signal is detected at the film-substrate interface with a content of ~0.5 at. % and at the film surface with a content ~0.25%. The oxygen in the bulk of the film is below 0.25 at. %.

4.2.1. Ion assistance with 100% N_2.

The deposition rate (panel a) and film composition (panel b) are shown in Figure 4.2 for ion assistance with nitrogen ions. These values are represented as a function of the ion energy per evaporated carbon atom. This energy is the result of the ion energy times the ion to carbon ratio (see section 2.1.2c). In this way, we take into account both ion energy and flux, i.e. ion assisting parameters, normalised to the evaporation rate.

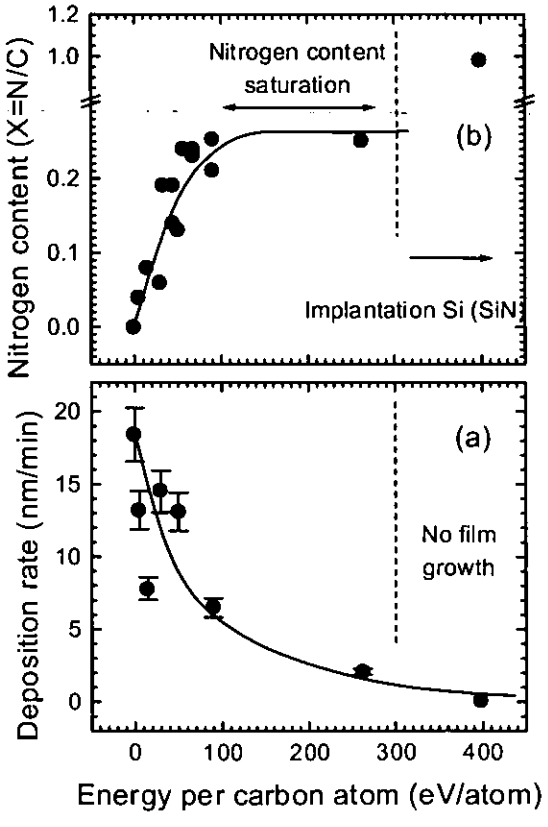

Figure 4.2. Deposition rate (a) and nitrogen content measured with XANES (b) as a function of the ion energy per incoming carbon atom (E= I/A E_i).

The deposition rate decreases as the energy increases until, above 300 eV/atom, no film growth is appreciable. The reduction of the deposition rate is a consequence of the physical re-sputtering and formation of C-N volatile compounds induced by the nitrogen ions [14,24]. The reduction in the

deposition rate is accompanied by an initial increase in the nitrogen fraction and a saturation above 100 eV/atom of X~0.25. For energies above 300 eV/atom, the nitrogen fraction is ~1. However, since in this regime the sputtering yield exceeds the deposition rate, nitrogen is directly implanted in the Si substrate and, therefore, a larger amount of nitrogen can be incorporated. This fact was corroborated by the XANES spectrum, which was similar to that found in SiN_x films.

4.2.2. Ion assistance with N_2/Ar gas mixtures.

Regarding the effect of Ar addition to the assisting gas, Figure 4.3 displays the composition for a set of samples grown with different Ar/N_2 mixtures. The Ar content incorporated in the film is very low as one could expect for an inter gas. Identical values were found in the synthesis of the amorphous carbon films described in Chapter 3. In addition to the incorporation of Ar, the nitrogen intake decreases with the Ar content in the gas mixture.

The decrease of the nitrogen content as a function of the Ar content is not linear as one would expect for a linear decrease in the number of incident nitrogen ions. We must consider several factors affecting the nitrogen decrease: (1) the reduction of the total number of incident nitrogen ions, (2) the higher ionisation cross-section for Ar than for N_2 and (3) the breakage of polar C-N bonds upon Ar^+ bombardment and preferential sputtering of carbon nitride areas. A small decrease of the deposition rate with increasing Ar contents takes place supporting the consideration of the last argument.

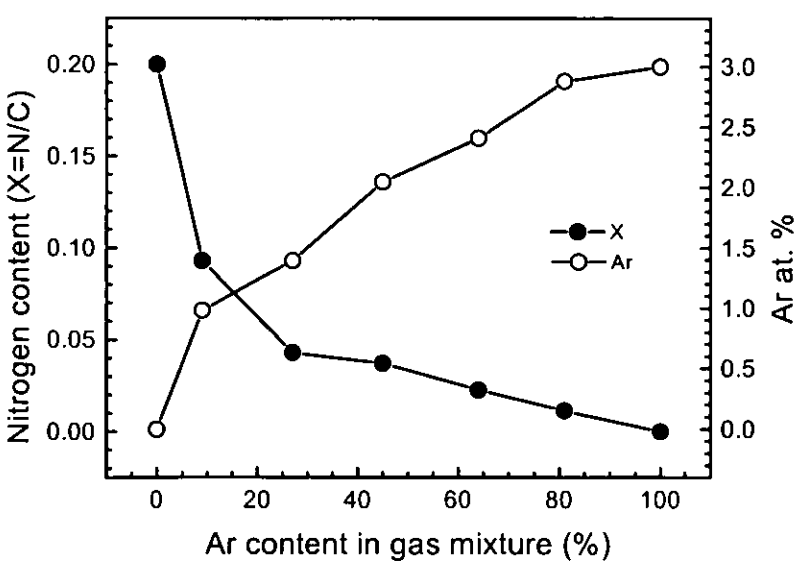

Figure 4.3. Nitrogen fraction (X=[N]/[C]) and Ar content measured with TOF-ERDA for a set of samples grown with different N_2/Ar gas mixtures (360 eV, 1 mA/cm^2).

4.3. BONDING STRUCTURE

4.3.1. X-Ray Photoemission Spectroscopy (XPS)

XPS is the most common characterisation tool of the bonding structure of a-CN_x films. However, the XPS peaks are not well resolved and the number of bonding states is unclear since both the charge transfer in polar C-N bonds and the hybridisation affect the binding energy. The high number of states in the C(1s) core level spectra makes difficult a clear interpretation and, normally, most of the reports focus their study in the N(1s) core level.

The first reports in XPS, aiming toward the production of β-C_3N_4, claimed for a two-phase system composed of C(sp^3)-N and C(sp^2)-N [25,26]. However, this simple assignment was soon abandoned and a more complex bonding structure has to be considered [3]. Previous XPS data on graphitic carbon nitride reveal the presence of two clear features in the N(1s) core level spectra around 398 eV and 401 eV [27,28,29]. An additional intermediate component has to be considered for a good fit when ion bombardment is involved in the deposition [27]. Some reports have assigned the latter feature to a defect and the other lines to nitrogen atoms with two and three carbon neighbours [27]. The discovery of fullerene-like structures and buckling in carbon nitride films has suggested a new interpretation of the XPS features in graphitic films [7]. In this context, the two N(1s) XPS peaks are attributed to nitrogen with four first neighbours in a pentagonal structure responsible of buckling and nitrogen with three first neighbours in a hexagonal graphite-like structure [29].

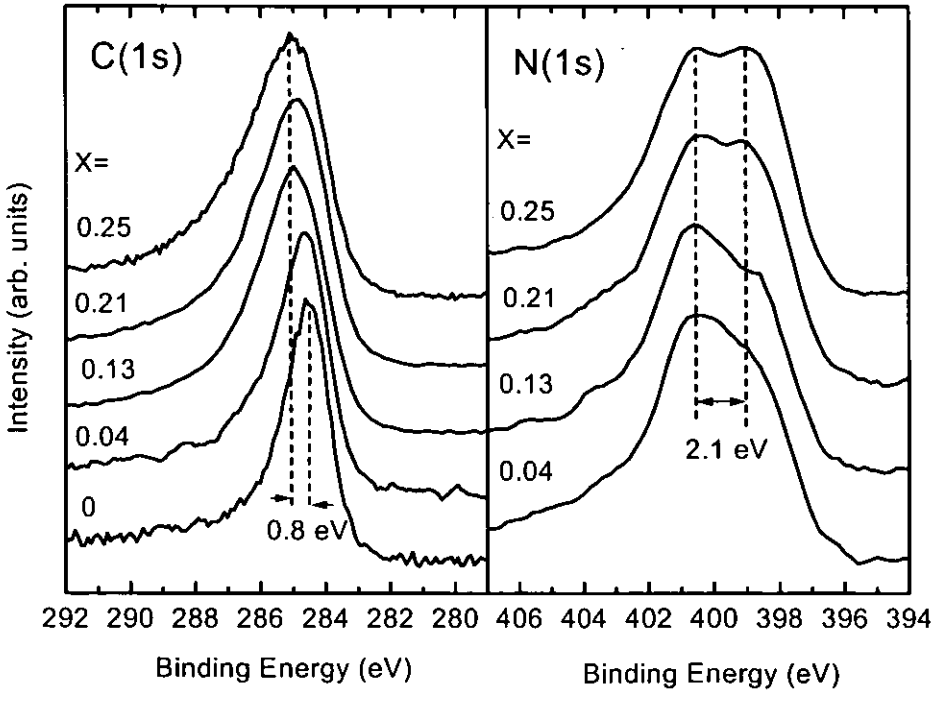

Figure 4.4. C(1s) (left panel) and N(1s) (right panel) core level photoemission spectra for a set of samples with different nitrogen fraction.

Although the information by XPS is ambiguous we have performed XPS in order to compare our results with existing data in the literature. Figure 4.4 shows the C(1s) and N(1s) photoemission spectra for a series of samples with increasing nitrogen content. The C(1s) spectrum (left panel) appears as a single peak that broadens and moves towards higher binding energies with increasing nitrogen content. This trend results from charge transfer from the carbon atoms to the more electronegative nitrogen atoms. The centroid of the curve shifts ~0.8 eV over the composition range considered, without any resolvable component. The N(1s) spectrum (right panel) is apparently composed of two peaks separated ~2 eV. The intensity of the low binding energy peak increases with increasing nitrogen contents in agreement with previous reports.

Our results are similar to previous XPS reports of amorphous carbon nitride films [13], similar to the XPS data from samples claimed to have a certain proportion of the β-C_3N_4 [25] and similar to very elastic samples claimed to contain nitrogen with fourfold coordination compatible with the graphitic matrix [29]. Therefore, further information cannot be derived from the XPS data regarding either different coordination or different hybridization, since both factors affect the energy shifts.

4.3.2. X-Ray Absorption Near Edge Spectroscopy (XANES)

Further information of the bonding structure can be extracted with XANES spectroscopy. XANES analysis is becoming more attracting as revealed by recent works on graphitic a-CN_x with a [N]/[C] ratio below 0.5 [27,30,31], a few articles dealing with a-CN_x films with larger nitrogen content [5,32,33] and recent reports on single phase carbon nitride with presumable sp^3 carbon hybrids [34].

The characteristic C(1s) XANES spectra from a set of carbon nitride films with different nitrogen contents are shown in the left panel of Figure 4.5. The shape of the C(1s) edge for all the carbon nitride films resembles the spectrum from an amorphous carbon film (a-C) (lowest curve). The presence of C-N bonds of π^* character is revealed by the shift of the absorption threshold to higher energies due to charge transfer to the more electronegative N atoms and by the appearance of several peaks in the 285-290 eV region. Similar features, although with different relative intensities, have been reported in previous XANES studies [5,32]. The different states that appear in this region have been tentatively assigned to carbon atoms with different number of nitrogen neighbours [33].

The N(1s) XANES spectra from the a-CN_x films are shown in the right panel of Fig. 4.5. The N(1s) spectra were normalised to the maximum height for comparison purposes. The presence of several peaks in the 396-402 eV range indicates a dominant π^* bonding. Similar spectral shape has been observed by other groups [27,35,36] and seems typical of carbon nitride films with an [N]/[C] ratio < 0.4. For higher nitrogen contents, the N(1s) XANES contains a single broad π^* peak [5,32] that can be understood from the merging of the peaks observed here for low nitrogen concentration [33].

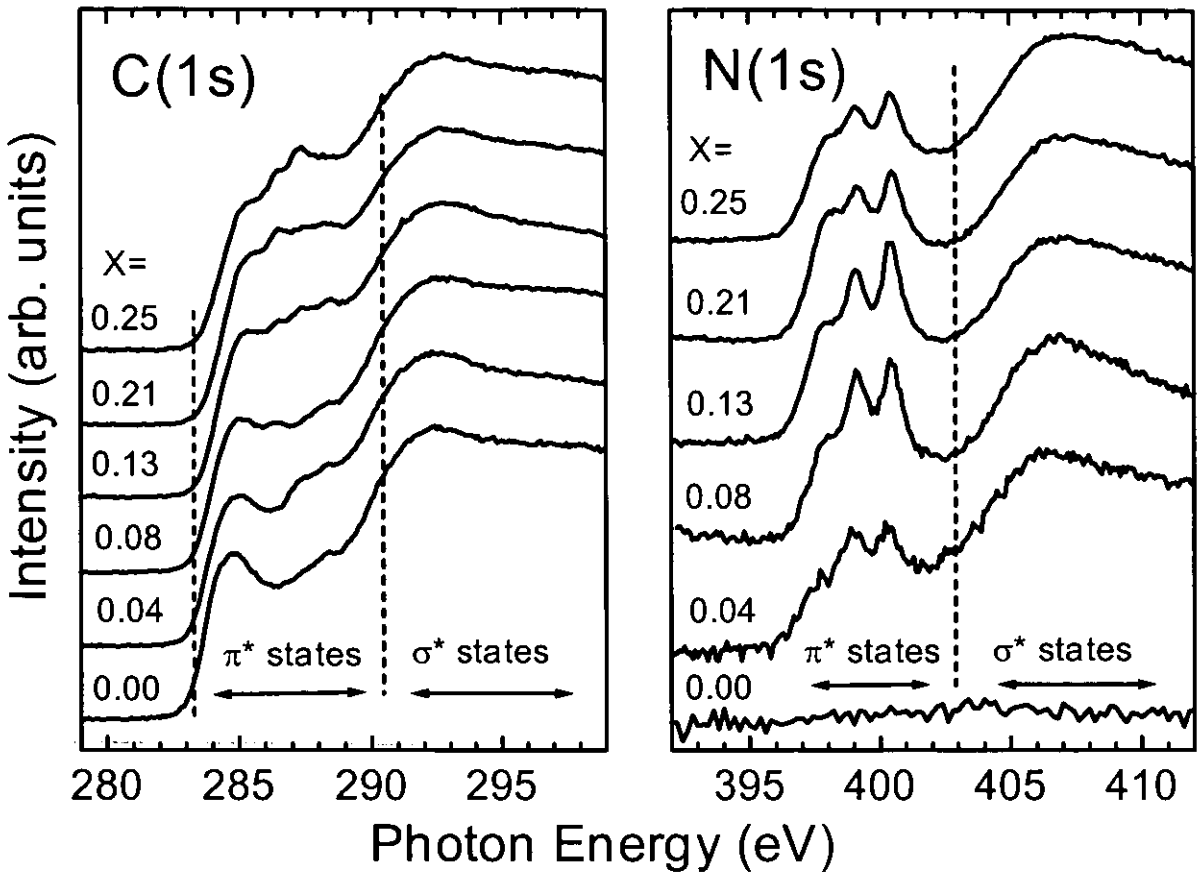

Figure 4.5. C(1s) (left panel) and N(1s) (right panel) XANES spectra for different nitrogen contents.

4.3.3. Identification of different bonding environments in graphitic a-CN_x

Discerning the total number of bonding environments is a difficult task. Among the multiples analysis techniques available, only XANES [33] and Nuclear Magnetic Resonance in the magic angle spinning mode (MAS-NMR) [37], have been capable of resolving different bonding environments for carbon and nitrogen atoms. In this context, NMR suffers the drawback of requiring a minimum amount of material (typically 1 mm^3) that is only achieved by collecting a large number of samples grown in thin film form. On the contrary, XANES can be directly performed in each individual sample. We have contrasted the XANES data existing in the literature in order to establish the number and possible assignments of the different bonding environments of graphitic a-CN_x. It is noteworthy that all the reports of graphitic a-CN_x films found similar spectral shapes independently of the growth method, conferring more generality to the results.

a) Ion assistance with 100% N_2.

In Figure 4.6 we have gathered the C(1s) and N(1s) spectra for several samples grown in our IBAD system with ion assistance with 100% N_2 and relevant data found in the literature. We have also included reference spectra from graphite, diamond, h-BN and c-BN, as prototype materials with sp^2 and

sp^3 hybridizations. Samples #A-E are spectra of a-CN_x films grown by us using IBAD methods. Curve #F corresponds to a CN_x/ZrN multilayer taken from Ref. 34 (the corresponding N(1s) was not reported). Curves #G-H correspond to a film grown by arcjet deposition and have been taken from Ref. 33. In this case, curve #G was measured at RT and curve #H after annealing in vacuum to 700°C.

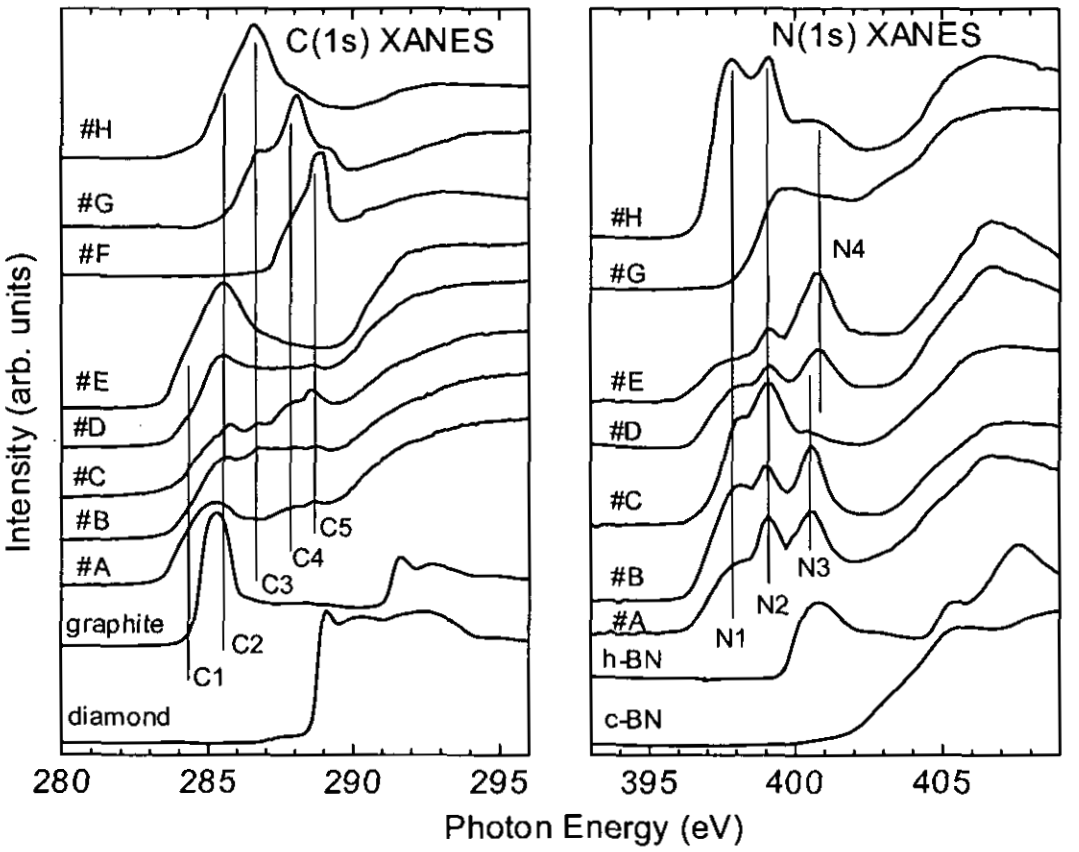

Figure 4.6. XANES C(1s) (left panel) and N(1s) (right panel) absorption edges for selected carbon nitride films.

Five different peaks are distinguished at the C(1s) edge, labelled as C1-C5, with a separation of ~1.1 eV between them. We have considered the graphite π^* resonance peak at 285.4 eV as the energy reference for calibration. In the amorphous network, the C=C bonding environments should be similar to that found in graphite and, therefore, these states are assigned to the peak C2 at 285.6 eV. In this case, the amorphization induces a slight shift of the state energy respect to the polycrystalline sample. Peak C1 at 284 eV appears upon amorphization of graphite and should be related to C=C bonding with defects [38]. Finally, peaks C3-C5 are presumably assigned to different C-N environments.

Four different peaks are distinguished at the N(1s) edge, labelled as N1-N4, whose position is referenced to the π^* resonance from h-BN at 400.9 eV [39]. Peaks N3 and N4 have a distinct origin as will be discussed below. Peak N3 appears at 400.5 eV, and has a FWHM of ~1.2 eV, roughly equal to

that of N1 and N2. However, peak N_4 appears at 400.8 eV and presents a broader feature, with a FWHM of ~1.5 eV.

Samples #A-B represent the effect of different nitrogen contents on the bonding structure. Sample #A is a film grown by IBAD at room temperature (RT) with a low nitrogen content of [N]/[C] ~0.05. Sample #B is another RT-IBAD film with [N]/[C] ~0.25. The larger nitrogen content reflects on the appearance of new states in the 286-289 eV region of the C(1s) spectra compared to sample #A. This support the assignment of peaks C3-C5 to C-N environments. This trend is also followed by a higher intensity of peak N1 on the N(1s) spectrum.

Samples #C-E illustrate the effect of temperature on the bonding structure. Sample #C has a nitrogen content equal to sample #B, i.e. [N]/[C] ~0.25, but was grown at 250°C. The substrate temperature affects the bonding structure, and reflects on the C(1s) spectrum as dominant C4 and C5 features. In addition, there is a substantial decrease of N3 on the N(1s) spectrum. According to this result, N3 seems related to a weakly bonded configuration. Sample #D is an IBAD film grown at 600°C during deposition. The fourth peak N4 appears in the spectrum of this film. The high deposition temperature also induces a graphitization of the structure as revealed by the dominant graphitic peak C2 of the C(1s). Curve #E corresponds to sample #B after annealing to 1000°C. The C(1s) is clearly graphitic, and the N(1s) has a dominant peak N4.

Sample #F, taken from Ref. 34, corresponds to $CN_{1.33}$ in a multilayer with ZrN, where the multilayer is claimed to stabilise the sp^3 bonding structure of carbon in the carbon nitride network. The spectrum is dominated by an intense feature at ~289 eV. The energy position of this peak makes possible two interpretations that are totally different. First, it can be attributed to a σ^* resonance typical of a sp^3 bonding structure since it appears at an energy near the diamond σ^* resonance. Second, it can correspond to a superimposed feature of the C4 and C5 π^* peaks. Additional information is required to clarify this question. At any rate, curve #F has a lineshape very different from that observed in graphitic a-CN_x films #A-E with [N]/[C] ratios below 0.5, hence supporting the hypotheses of a sp^3 bonding structure.

Curves #G-H, taken from Ref. 33, correspond to amorphous CN_x films with a [N]/[C] ratio greater than 1. Curve #G corresponds to the as-grown sample and shows a C(1s) spectrum dominated by peak C4. The corresponding N(1s) spectrum presents a double edge with a first threshold at ~398 eV assigned to π^* states lacking any of the sharp resonance features N1-N4, and a second threshold at ~403 eV for σ^* states. Curves #H represent the same sample after annealing in vacuum to 700°C. Upon annealing, the initially featureless N(1s) π^* states split into peaks N1 and N2, with N1 being the dominant peak. Also, peak N4 appears as is always observed for any carbon nitride annealed over 600°C. The dominance of peak N1 in the N(1s) spectrum has a correspondence in a dominance of peak C3 in the C(1s) edge.

The apparent relationship between the features in the N(1s) and C(1s) edges can be summarised as follows. N1 seems related to C3 as is clear from curve #H. The relationship between N2 with peaks C4 and C5 is apparent from curve #C. N3 seems a weak bonding state without a clear correspondence on the C(1s) spectra. N4 only appears after annealing at high T or growth at high T, and is dominant when the graphitic peak C2 is intense. C1 seems also typical of defective or incomplete C=C coordination. Apparently, peaks C1 and C2 are related to amorphous carbon rather than to carbon nitride, and peaks N3 and N4 are not directly related to any of the C(1s) peaks of CN_x suggesting an origin as nitrogen embedded in a carbonaceous matrix rather than to actual C-N bonds. Therefore, the remaining peaks, i.e. C3, C4, C5, N1 and N2, seem to be the genuine carbon nitride peaks.

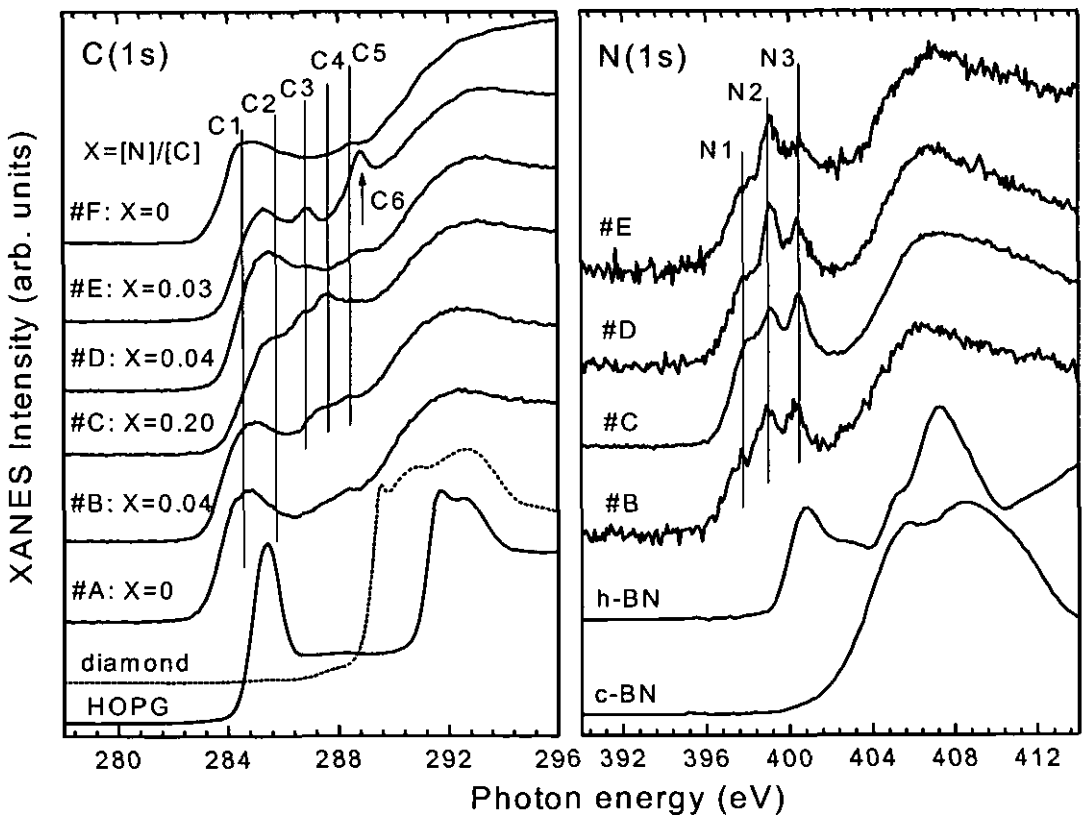

Figure 4.7. C(1s) (left panel) and N(1s) (right panel) XANES spectra for selected samples grown with different N_2/Ar gas mixtures.

b) Ion assistance with N_2/Ar gas mixtures.

Additional information can be extracted from the XANES data of films grown with Ar/N_2 mixtures. As it was previously discussed, the addition of Ar to the assisting gas was aiming at the promotion of sp^3 hybrids by increasing the momentum transfer in the ion assistance process. Figure 4.7 displays a comparison between samples grown with 100% N_2 ion assistance, 100% Ar ion assistance and samples grown with Ar/N_2 gas mixtures. Sample #A corresponds to an evaporated carbon film, hence,

without ion assistance. Samples #B and #C are carbon nitride films grown with 100% N_2 ion assistance and [N]/[C]=0.04 and 0.2, respectively. Samples #D and #E were grown with Ar/N_2 ratio of 0.37 and 0.82, respectively. Finally, sample #F correspond to a film grown with 100% Ar ion assistance and represents an amorphous carbon film with ~30% sp^3 sites.

The C(1s) and N(1s) peaks described above are indicated in Fig. 4.7. As we can see, peaks C3, C4 and C5 do not appear unless nitrogen ions are used in the deposition. This supports the assignment of these peaks to C-N environments. An additional carbon peak, C6, attributed to surface C=O contamination appears in sample #E. Although the structure remains graphitic, the formation of sp^3 hybrids is derived from the reduction of the relative intensity of the π^* states, as will be discussed in section 4.3.5. Finally, the C3 peak corresponds to the most stable configuration for carbon under heavy ion bombardment.

Regarding the N(1s) edge, the intensity of peak N3 is reduced when Ar ions are used. This reduction is higher as we increase the Ar content in the gas mixture. This result corroborates the weakness of the bonding state associated with this peak. On the contrary, peaks N1 and N2 are stable configurations under ion bombardment with heavy ions.

4.3.4. Dependence of XANES features on X=[N]/[C].

At this stage, two main questions can be posed. The first one is the actual bonding environment corresponding to the carbon nitride peaks discussed above. At present, we do not have enough evidence to give a conclusive answer, and this question remains open. The second one is if obtaining a certain bonding structure, i.e. a specific XANES lineshape, depends only on the nitrogen content in the films or if it also depends on the film growth conditions.

The large number of ill-resolved states at the C(1s) edge makes difficult a quantitative study, so that is why we focus here on the N(1s) peaks. Therefore, in order to obtain further information of the bonding environments we have related the nitrogen peaks N1, N2 and N3 with the nitrogen content. The deconvolution of the N(1s) spectra was performed by a curve fit analysis similar to that contained in Ref. 33, and is illustrated in Figure 4.8a. Three gaussian peaks representing the resonance N1, N2 and N3 are considered, together with two gaussian-broadened step functions to describe the transitions to the continuum of π^* and σ^* states.

The intensities of peaks N1, N2 and N3 are obtained from the curve fit analysis. The relative intensity of each peak referred to the total intensity (N1+N2+N3) is shown in Figure 4.8b as a function of the nitrogen content for samples grown by IBAD at RT. The intensity of peak N3 seems independent of the nitrogen content, with a constant value of ~33%. This is in agreement with the previous discussion indicating that N3 is not directly related with any of the C(1s) peaks. On the contrary, peaks N1 and N2 change significantly and systematically as a function of the nitrogen content, with an increase of N1 at the

expense of N2. These peaks can be related with different bonding configurations or functionality of nitrogen in the carbon network. In this context, the possibility of a superstructure in graphitic carbon nitride films [7] adds new environments related to the topology of this superstructure. Further work regarding this latter hypothesis is presented in the next section.

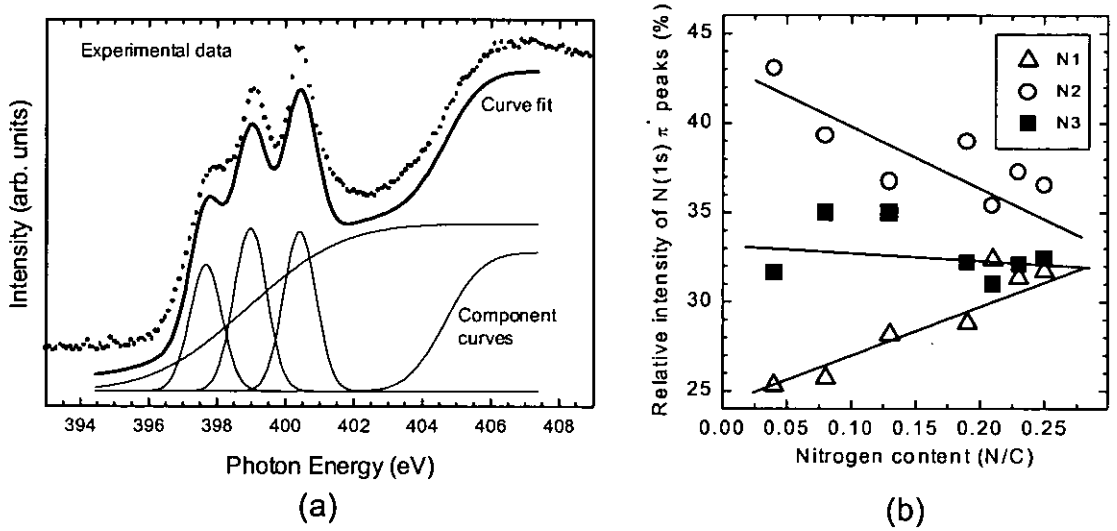

Figure 4.8. (a) Curve fit analysis of the N(1s) XANES spectra. (b) Relative intensity of N(1s) π^* peaks as a function of the nitrogen content for samples grown at RT.

4.3.5. Superstructure of graphitic planes.

An important finding with regards to graphitic structures is the presence of a superstructure that improves significantly the hardness and elasticity of the material [7]. The orientation, corrugation, folding and cross-linking of basal planes give shape to this superstructure, which determines the actual physical properties of the graphitic solid. This result seems valid for other laminar materials, similarly to what is found with fullerene-like structures [40].

Previous work on graphitic carbon nitride has reported a decrease of the electric charge in π bonds with increasing nitrogen contents [13,20] that was explained by the curvature induced in the basal planes due to the presence of nitrogen. Some authors consider that the presence of nitrogen is enough to explain the bending of basal planes formed only by six-member rings, and that the cross-linking of different planes can go through threefold coordinated sp^2 hybridised carbon atoms [14]. Other authors consider that it is necessary to include five-member rings in the basal planes to explain their curvature, and that cross-linking takes place through fourfold coordinated sp^3 hybridised atoms, either carbon [7,20] or nitrogen [41]. Discerning the mechanism ruling the bending and cross-linking of basal planes seems of major interest to understand the properties of graphitic carbon nitride.

Obtaining information on the superstructure is a difficult task since, on the one hand, it lacks long range order and, on the other hand, the bonding structure remains essentially graphitic. Hitherto, only

high-resolution transmission electron microscopy (HRTEM) has been capable of detecting the superstructure of graphitic planes [7]. An alternative method to study the graphitic superstructure is to consider the contribution to π bonding of electrons from C and N atoms separately [42]. This can be computed from the XANES spectra considering the intensity of the whole π^* state region relative to the total absorption intensity in the C(1s) and N(1s) spectra, respectively. The limits of integration to compute the π^* intensity are not crucial, as long as one includes the whole π^* region and that the σ^* region does not to overlap with the π^* states. Changing the limits of integration within these constraints yields always a similar result within a proportionality factor. To keep the scale factors as similar as possible for C and N, the same energy interval of integration is considered for both π^* and σ^* states. The proportion of π^* states in the C(1s) spectra was computed from the ratio of the area between 282-289 eV representing π^* states, to the area between 292-299 eV representing σ^* states. The N(1s) π^* intensity was computed from the ratio of the area between 396-402 eV and between 405-411 eV for π^* and σ^* states, respectively.

a) Ion assistance with 100% N_2.

The relative total intensity of π^* states for films grown with 100% N_2 assistance is displayed in Figure 4.9 as a function of the nitrogen content. The relative C(1s) π^* intensity remains constant within 5% for the whole composition range. This intensity is the same than for the evaporated carbon (X=0), which is composed of ~95% sp^2 carbon as discussed in Chapter 3. For the N(1s) spectra, however, a variation of ~50% takes place.

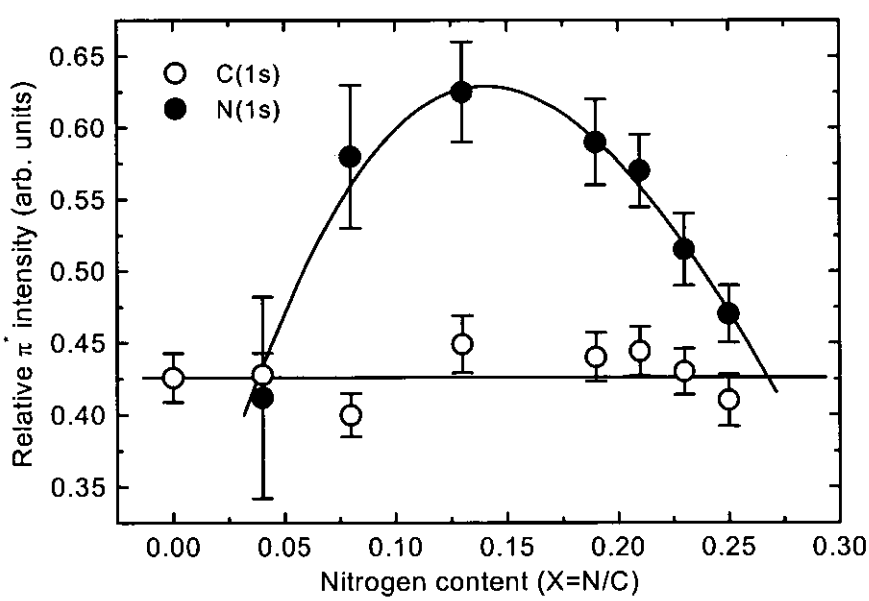

Figure 4.9. Relative intensity of π^* respect to σ^* states for the C(1s) (open dots) and N(1s) (solid dots) XANES spectra.

Before discussing the change in the π intensity, it is important to note that the striking point of the XANES results is the contribution of nitrogen atoms with sp^2 hybridisation to π bonding. Regarding to its electronic structure ($2s^2 2p^3$) nitrogen can only can account for three bonds. Therefore, if nitrogen with sp^2 hybridisation forms three σ bonds within a graphitic structure the remaining two electrons in the lone p_z orbital should not contribute to π bonding. However, conjugation of the filled N-p_z orbital with the half-filled p_z orbitals of the neighbouring carbon atoms, can explain a charge transfer from the nitrogen orbitals to the carbon p_z orbitals, leaving the N one partially unfilled and, hence, allowing the formation of π bonding.

Generally, the π intensity from EELS or XANES spectra is simply related to the number of atoms with sp^2 hybridization. However, a change in the bonding angle would result also in a variation of the electric charge contributing to π bonding. The maximum charge density in π bonds for the nitrogen atoms will occur when the three σ bonds lie in a basal plane and it will decrease when the σ bonds are not coplanar [14]. A schematic drawing of this situation is illustrated in Figure 4.10. The fact is well known from model molecules like pyrrole, where the three coplanar sp^2 hybrid orbitals of nitrogen form three σ bonds and the remaining two p electrons in the lone orbital are delocalised with a partial flow of charge (~0.2 e) away from the nitrogen [43]. In this way, nitrogen participates in π bonding and exhibits π^* unoccupied states that can be observed by XANES spectroscopy [44]. When the ring is not planar, the lone pair is not accurately of π type and conjugation with the ring is inhibited [45].

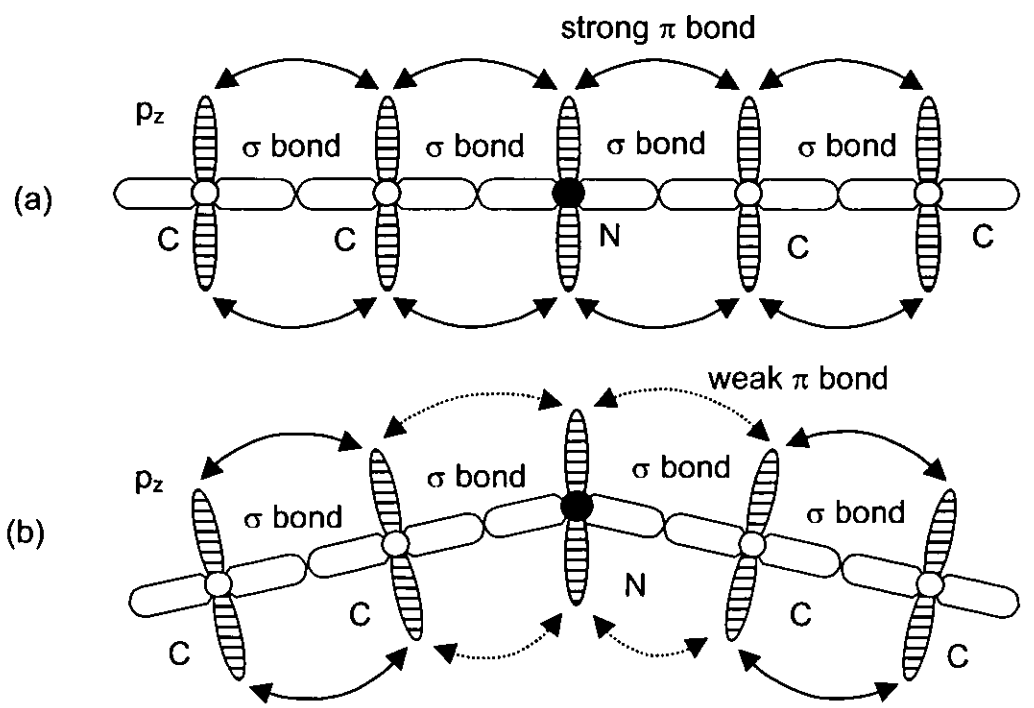

Figure 4.10. Schematic view of different degrees of conjugation between the nitrogen and carbon p_z orbitals. The maximum charge transfer is obtained for the planar configuration (case a).

The N(1s) π^* intensity in Fig. 4.9 increases with the nitrogen content until reaching a maximum around X~0.15 and decreases for larger nitrogen contents. The increase of the N(1s) π^* intensity with the nitrogen content for X<0.15 can be explained by a transition from non-planar to planar nitrogen bonding geometry. The maximum contribution to π bonding for the nitrogen atoms occurs for X=0.15, which correspond to the composition of one nitrogen atom per hexagonal ring (X=1/6). The subsequent decrease observed for X>0.15 can be explained by two different factors. First, the accommodation of nitrogen atoms above one atom per hexagonal ring may increase the corrugation of the basal planes and distort the planar configuration. Second, the nitrogen atoms may be in non-planar bonding configurations acting as cross-linking sites of the basal planes. Since the formation of sp^3 carbon sites does not take place, only nitrogen atoms can be considered as possible cross-linking sites.

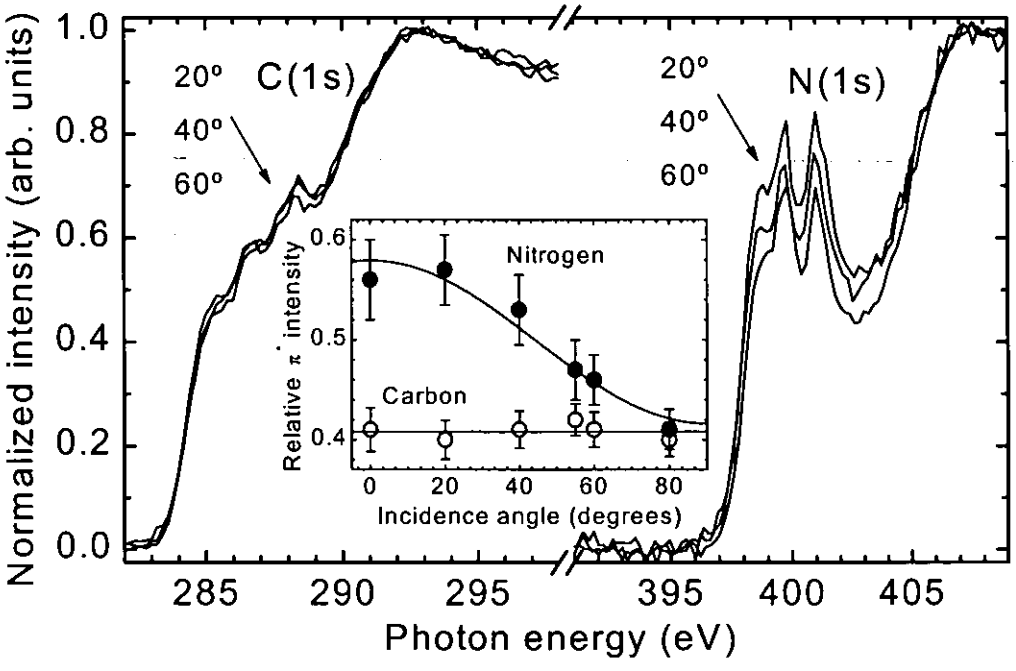

Figure 4.11. XANES spectra for different angles of incidence of the light. Inset: dependence of the relative π^* intensity with the incidence angle.

Further evidence of the presence of a superstructure in the graphitic carbon nitride films can be obtained from an angle dependent study. As discussed previously, the superstructure can also be related with certain orientation of the basal planes. In this context, we have performed the angular study with XANES since the absorption intensity depend on the angle between the electromagnetic field of the radiation and possible preferential direction of the bonds present in the material. In particular, the intensity of π^*-states follows a cosine-square dependence with the angle between the light and the π bonds [46]. This fact can be used to detect the texture of graphitic films, even when long range order is lacking [47]. The measurements were performed on the sample with a largest nitrogen content, X=0.25, and the

results are shown in Figure 4.11. The spectra are normalised to the maximum intensity and were measured with different angles of incidence of the synchrotron light. The inset displays the dependence of the relative π^* intensity with the incidence angle, curve fitted to a $cos^2\theta$ law. The anisotropy of the signal can be quantified as the difference between the maximum and minimum intensity. In this way, the N(1s) signal shows an anisotropy of ~0.2, which is absent in the C(1s) signal. The anisotropy, of the N(1s) π^* signal corresponds to a preferential orientation of the nitrogen p orbitals parallel to the surface since the maximum of intensity is found for normal incidence, i.e. the electromagnetic field of the radiation parallel to the substrate surface. This result implies that the basal planes are perpendicular to the surface, as has been observed in other ion beam grown films [47].

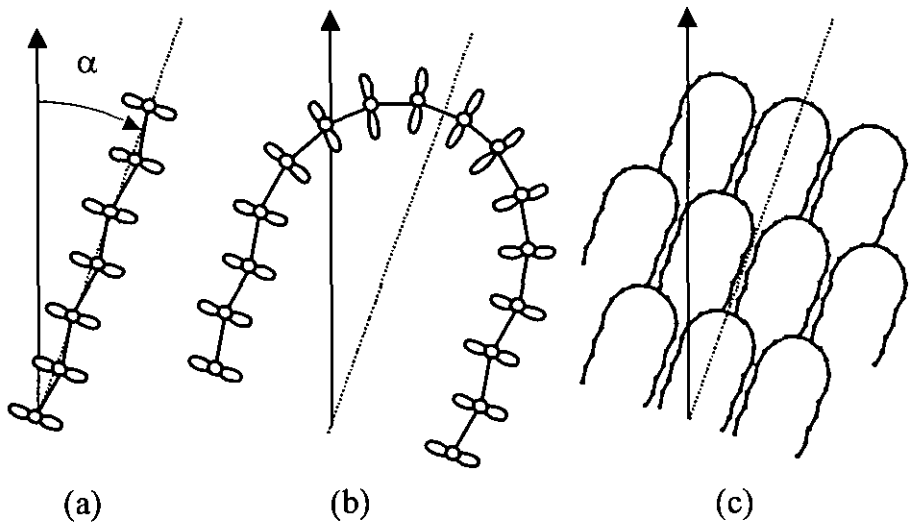

Figure 4.12. Simple geometrical models representing the side view of the basal planes. The white dots represent the nitrogen atoms with their respective p orbital with 8-shape. The models consider corrugation (a), folding (b) and cross-linking (c) of the graphitic basal planes.

In the case of flat basal planes, C and N atoms would present the same orientation of π bonding and, therefore, the distinct angular behaviour observed for the C and N signal could not be explained. To verify if corrugation, folding and cross-linking of basal planes can account for the observed behaviour, we perform an analysis of the π^* states anisotropy for simple geometries. The models are displayed in Figure 4.12. The drawings represent side views of the basal planes, forming a misorientation angle α with the sample normal. The white dots represent the nitrogen atoms and the 8-shapes sketch the orientation of their p orbitals. The segments represent a section of carbon flat basal planes. The bending angle caused by the insertion of a nitrogen atom in the plane will depend on the nitrogen hybridization, ranging from 0° for pure sp^2 to 19.5° for pure sp^3. For simplicity we consider an intermediate 10° angle, without losing generality. Model (a) is the simplest case that can be considered, i.e. a corrugated chain. Since we try to

correlate the results with folding and cross-linking we proposed models (b) and (c), respectively, to account for these effects.

The angular dependence of the absorption intensity for each model is computed considering the average value separately for the nitrogen atoms and the carbon linear chains. We assume that the intensity dependence is proportional to $\cos^2\theta$, with θ being the angle between the p orbital and the incidence light. The top panels of Figure 4.13 represent the predicted angular dependence of the π^* intensity at the C and N edges for each model, assuming a perfect orientation with α=0°. The displayed values of the anisotropy correspond to the maximum intensity change. The bottom panels of Fig. 4.13 represent the dependence of the C and N π^* anisotropy with the disorder of the structure. This is modelled with a gaussian distribution of α angles centred in α=0, with a certain full width at half maximum (FWHM). Model (a) represents a corrugated plane, accounting for a 6% larger anisotropy of the nitrogen signal compared to the carbon signal. Model (b) considers a curved plane, that yields a ~17% larger anisotropy of the N signal compared to the C signal. Model (c) considers a periodic structure of curved basal planes, linked through nitrogen atoms that do not contribute to π bonding. In this case the N anisotropy is ~45% larger than for C. However, for perfectly oriented structures the carbon anisotropy remains large. Assuming a certain disorder of the structure, as shown in the bottom panels of Fig. 4.13, the signal anisotropy is reduced. In this way, the C anisotropy can get too small to be detected, while the N anisotropy is still appreciable. This situation is found in model (c) for a FWHM of α ~100°.

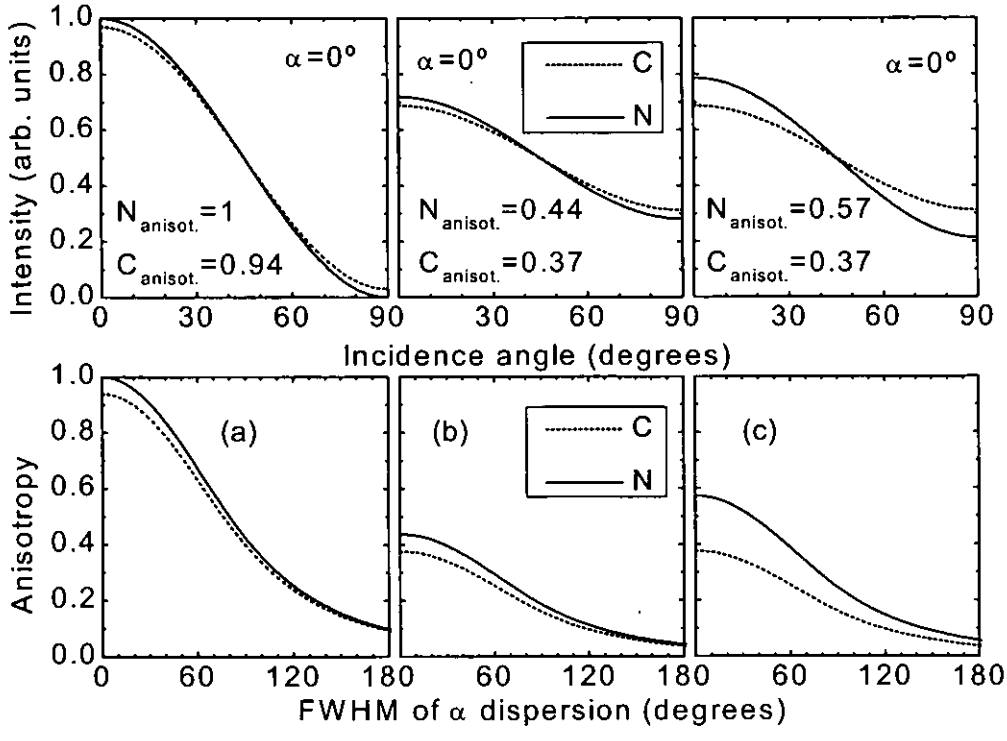

Figure 4.13. Calculated anisotropy of the XANES signal at the C and N edges for the models proposed in Fig. 4.12.

b) Ion assistance with N_2/Ar gas mixtures:

To examine the changes introduced in the bonding structure by Ar bombardment a similar analysis, considering the relative intensity of π^* states, was performed in the samples grown with different N_2/Ar gas mixtures in the ion assistance process. The results are shown in Figure 4.14 as a function of the resulting nitrogen content (bottom axis) of the films and the corresponding Ar content in the gas mixture (top axis). The dashed lines correspond to the development of the density of π^* states for samples grown with nitrogen assistance, which is extracted from Fig. 4.9. The solid dots represent the N(1s) density of π^* states and the open dots the C(1s) data from the samples grown with N_2/Ar assistance. The solid lines represent the trends in the intensity development.

The samples grown with Ar in the gas mixture show a constant density of π^* states from nitrogen, indicating that changes in the corrugation of basal planes are not taking place. A plausible explanation stems from the breakage of graphitic planes into small fragments or the presence of a large vacancy concentration in the graphitic planes due to the Ar^+ bombardment. In this case, the stress introduced by N insertion in hexagonal rings is released without changes of corrugation in the basal planes. This argument is also supported by the Raman microstructural information presented in the next section. Finally, the samples obtained with more that 50% Ar in the gas mixture show the formation of carbon sp^3 sites as evidenced by the decrease of the C(1s) π^* intensity.

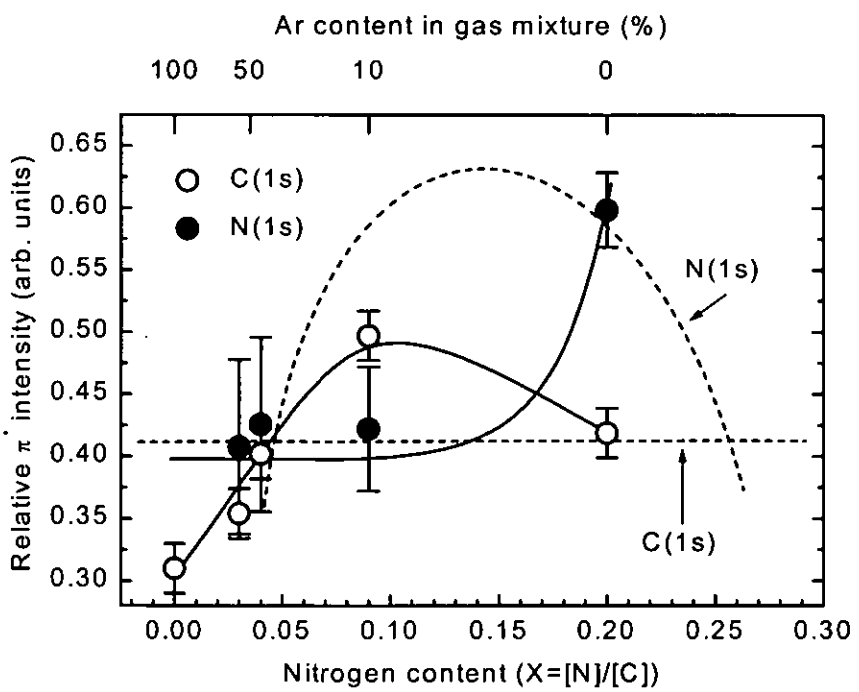

Figure 4.14. XANES relative intensity of π^* respect to σ^* states for the C(1s) (open dots) and N(1s) (solid dots) edges for different N_2/Ar mixtures as a function of the nitrogen content. The dashed lines correspond to the behaviour for 100% N_2 assistance.

4.4. MICROSTRUCTURE

The cross-linking of graphitic planes must reflect in the microstructure of the films. Raman is a suitable technique since it is sensitive to the grain size in nanometric and amorphous graphitic films [48,49]. The visible Raman spectra for the set of samples considered in Fig. 4.7 are shown in Figure 4.15 in order to account for the effect of nitrogen uptake and Ar/N_2 ion assistance.

The graphitic nature of the a-CN_x films reflects in the similar spectra found between the a-CN_x films (curves #B-E) and the evaporated carbon film (curve #A). The band around 690 cm^{-1} is due to C-C vibrations out of the basal planes, that only occur when there is structural disorder in the graphitic network [50,51]. The bands between 1000-2000 cm^{-1} and 2500-3500 cm^{-1} correspond to the first and second order Raman spectrum of disordered sp^2 carbon, respectively. The presence of a small nitrile (C≡N) feature around 2200 cm^{-1} is only found for nitrogen fractions over 0.1. A prominent nitrile band (not in our case) is typical of polymeric paracyanogen-like films [18].

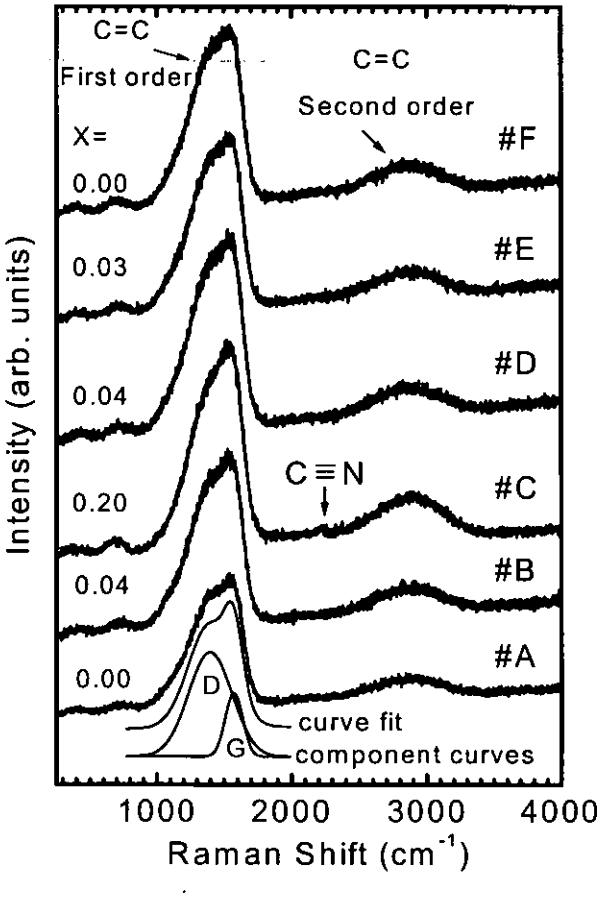

Figure 4.15. Visible Raman spectra for different nitrogen contents.

In order to obtain information about the microstructure of the films, the first order band of the carbon stretching mode between 1000-2000 cm^{-1} has been fitted with a linear background and two

gaussian distribution, labelled "G" (graphite) and "D" (disorder). The fitting procedure is illustrated in curve #A of Fig. 4.15. This analysis is similar to what it was done in the previous chapter to study the amorphous carbon films [52]. The position, width and relative intensity of these peaks are found to vary systematically with deposition conditions and film properties [53,54]. The results of the fitting analysis are shown in Figure 4.16. The black dots correspond to samples grown under 100% N_2 ion assistance and the white dots to Ar+N_2 gas mixtures.

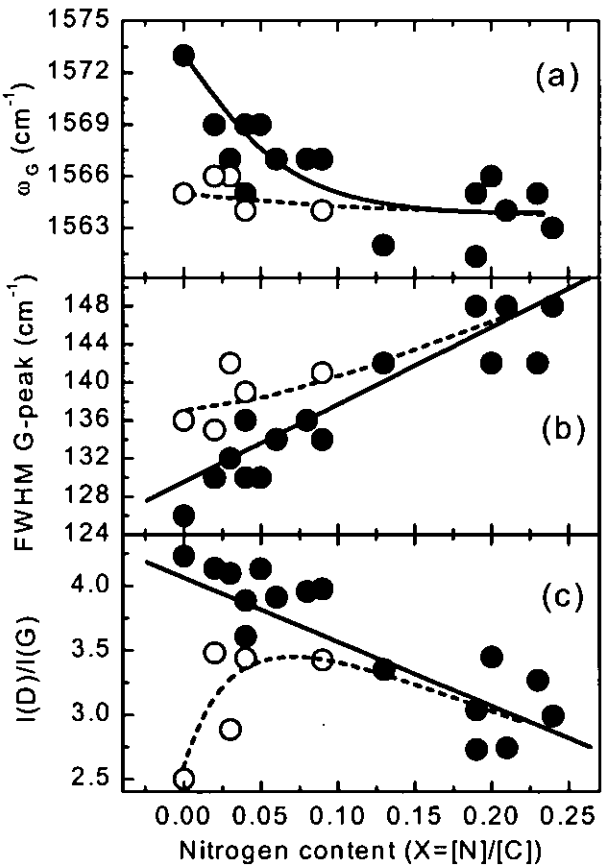

Figure 4.16. Fitting parameters of the Raman spectra as a function of the nitrogen fraction for ion assistance with 100% N_2 (solid dots) and different N_2/Ar gas mixtures (open dots): (a) Position of the G peak, (b) full width at half maximum (FWHM) of the G peak and (c) relative intensity of the D and G peaks.

First, we describe the effect of nitrogen incorporation for samples grown with 100% N_2 ion assistance. For the evaporated film without ion assistance, the position of the G peak is around 1575 cm^{-1} and close to the crystalline graphite value (1580 cm^{-1}). With increasing nitrogen content, the G band position shifts towards lower frequencies indicating a distortion of the graphitic network [55]. Figure 4.16 also shows the width of the Raman "G" peak in panel (b) and the relative intensity of the D and G peaks, I(D)/I(G), in panel (c). The incorporation of nitrogen induces the widening of the G peak and the decrease of the I(D)/I(G) ratio, indicating an amorphization of the graphitic network. These results

corroborate the distortion of the graphitic network and imply a decrease of the graphitic domain size with increasing nitrogen contents. This behaviour is consistent with the cross-linking of graphitic planes through nitrogen atoms.

Regarding samples grown with $Ar+N_2$ gas mixtures, the data in Fig. 4.16 indicate that the degree of amorphization is larger than what correspond to their nitrogen content. This effect is due to the additional Ar^+ bombardment, which in principle, can contribute to both promotion of C sp^3 hybrids and breakage of the graphitic network by creation of defects. Comparison with the mechanical properties of the samples indicates that the effect of Ar^+ bombardment is to induce defects by breakage of the basal planes.

4.5. THERMAL STUDIES OF a-CN_x FILMS

4.5.1 Influence of the substrate temperature during deposition.

The XANES C(1s) and N(1s) spectra of graphitic a-CN_x films grown by IBAD at different substrate temperatures during deposition are shown in Figure 4.17. The shape of the C(1s) spectra remains unperturbed for temperatures below 250°C, indicating that the bonding structure of a-CN_x remains stable. However, peak N3 at the N(1s) edge decreases significantly in this temperature range, corroborating that N3 corresponds to an unstable bonding configuration, not related with C-N bonds.

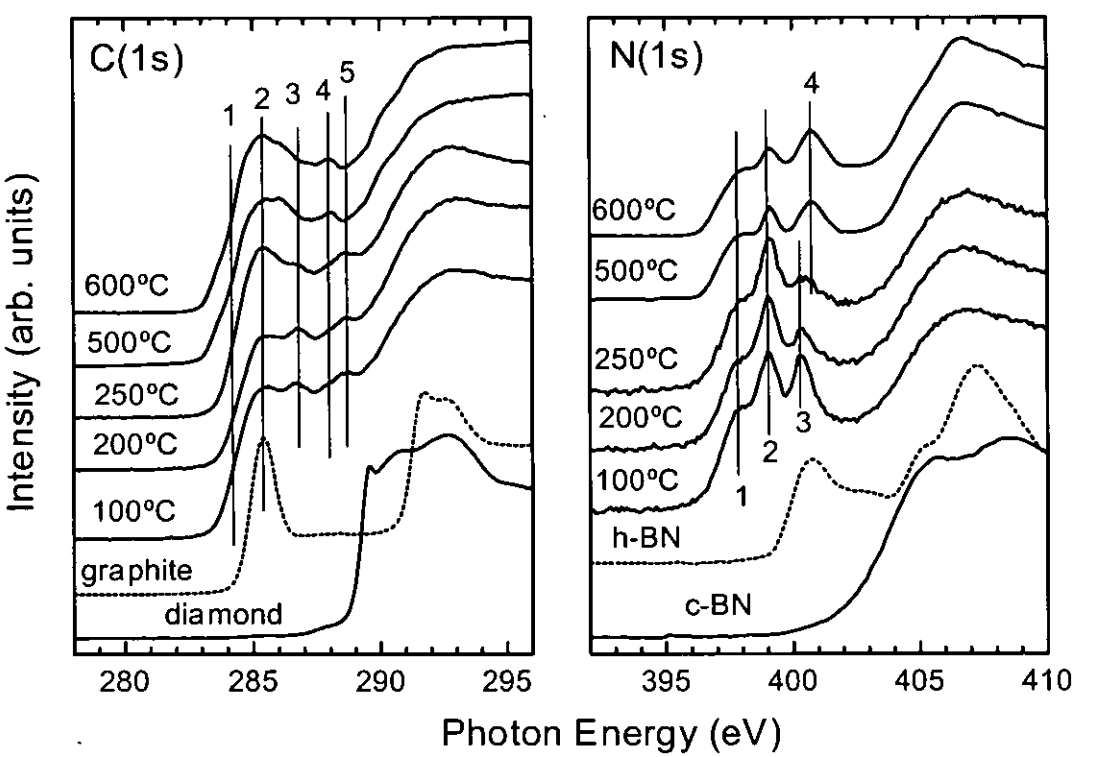

Figure 4.17. XANES C(1s) and N(1s) spectra of graphitic a-CN_x films grown by IBAD at different substrate temperatures.

For deposition temperatures above 250°C, the C(1s) spectra shows an increase of the C2 peak, associated to the graphite exciton, indicating a graphitization process. This graphitization is a common process found in amorphous carbon-based materials [56]. In the meanwhile, the N(1s) spectra show an increase of the new feature N4, which is broader than N3 and appears at ~0.3 eV higher energy. Therefore, increasing the substrate temperatures favours the elimination of weak C-N environment but produces a graphitization process.

4.5.2. Influence of post-deposition annealing.

To examine the variations of the bonding structure of graphitic a-CN_x films upon annealing, the films were heated in-situ in the ultra-high-vacuum (UHV) analysis chamber by flowing current through the silicon substrate. The corresponding XANES spectra at different annealing temperatures are displayed in Figure 4.18.

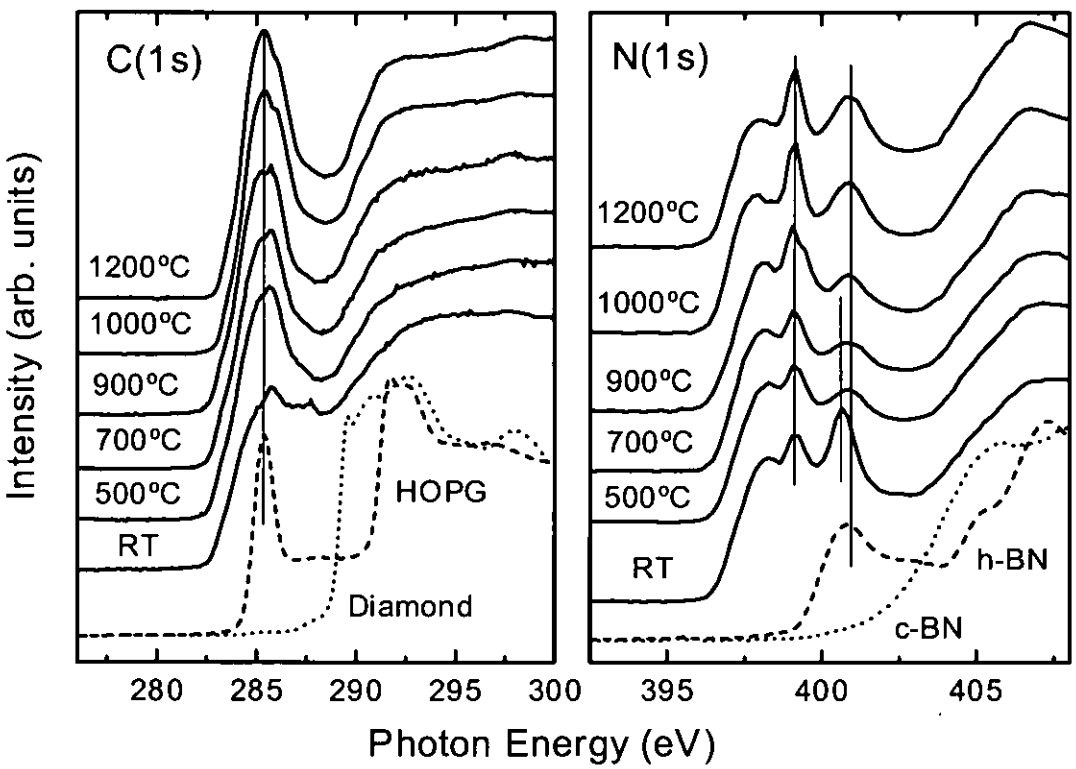

Figure 4.18. XANES C(1s) (left panel) and N(1s) (right panel) of an a-CN_x film for different annealing temperatures. The sample was grown with 100% N_2, 400 eV and 1 mA/cm^2.

The trends observed as the result of the annealing process are the same for all the a-CN_x samples studied. The changes observed in the XANES spectra are similar to those shown in Fig. 4.17. However, some peculiarities are worth discussing. First, the non-disappearance of peak N2 after annealing to 1000°C indicates that this state does not correspond to a defect as claimed in Ref. 27. Second, the

maximum decrease of the N3 peak occurs at 700°C with annealing. This decrease is followed by the increase of peak N4 at higher temperatures than those reported for deposition temperatures. Finally, the C(1s) graphitization is larger than that observed in Fig. 4.17.

It is also interesting a direct comparison of our annealed samples with the previous annealing XANES study of Ref. 33 on samples with larger nitrogen content. The conclusion of this comparison is that the bonding structure after annealing at temperatures around 1000°C is the same in both cases. Therefore, the final bonding configuration is an intrinsic feature of carbon nitride films and it is independent of the starting bonding structure or deposition method.

Finally, in Figure 4.19 we plot the nitrogen content as a function of the annealing temperature for samples with different starting nitrogen contents. The nitrogen content is referred to the maximum [N]/[C] ratio found in each sample. The ratio of the nitrogen content can be considered as an indication of the thermal stability of these films. The range of thermal stability is important in order to discern the applicability of these coatings in high temperature cutting tools.

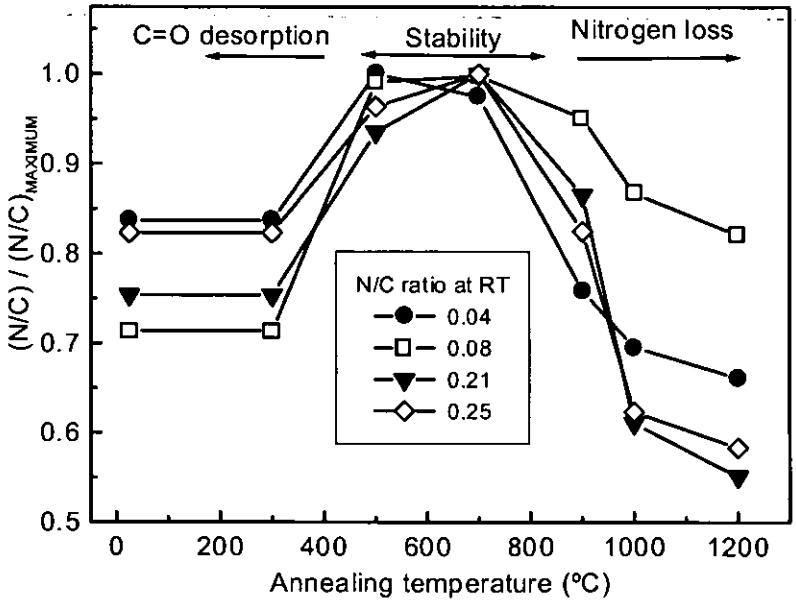

Figure 4.19. Variation of the nitrogen content with the annealing temperature, referred to the maximum [N]/[C] ratio in each film, for various nitrogen contents.

For annealing temperatures below 300°C, the apparent [N]/[C] ratio increases due to desorption of C=O surface contamination, as was verified by monitoring the oxygen signal. The nitrogen content remains stable for temperatures below 700°C. Above this temperature, a sharp decrease is found followed by a substantial graphitization process, in agreement with previous annealing studies [33]. It is noteworthy that these a-CN_x films present higher thermal stability (up to 700°C) than the amorphous carbon films studied in Chapter 2 (up to 200°C).

4.6. MECHANICAL PROPERTIES

In the previous sections we have shown different results suggesting the formation of a superstructure of graphitic planes. If this is the case, there must be a significant enhancement of the mechanical properties as a consequence of this superstructure [7]. Nanoindentation experiments were used to determine the elastic modulus, hardness and elastic recovery of the films. The values are derived from the penetration depth versus load curves.

4.6.1. Ion assistance with 100% N_2.

The elastic modulus and hardness values follow well the rule E/H~10 and, therefore, we have only considered the hardness values in the discussion. The hardness of the CN_x films as a function of the nitrogen fraction is illustrated in panel (a) of Figure 4.20. It is clear that the nitrogen incorporation in the graphitic network produces a film hardening, mostly for [N]/[C] above a threshold value of ~0.15. The hardness increase with the nitrogen content confirms the non-polymeric nature of our films. The elastic recovery data shown in panel (b) also show a change of tendency for [N]/[C] ~0.15, suggesting a structural transformation for this nitrogen content.

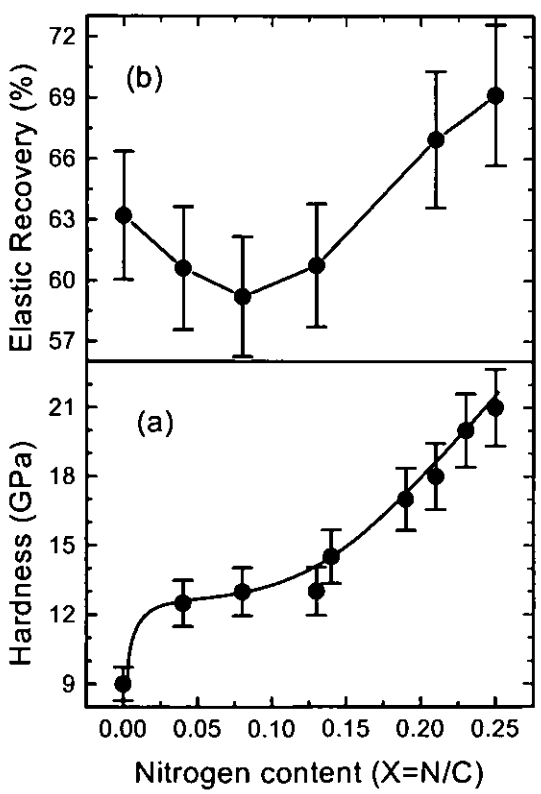

Figure 4.20. Hardness (a) and elastic recovery (b) of carbon nitride films as a function of the nitrogen fraction.

The trends found in the mechanical properties are consistent with the structural change based on the corrugation and interconnection of basal planes, as was discussed for the development of the XANES density of π^* states shown in Fig. 4.9. Since the density of π^* states at the C(1s) edge remains constant for all the nitrogen contents, hardening by formation of sp^3 carbon hybrids is excluded. Therefore, although the bonding structure remains graphitic, the superstructure of graphite basal planes is composition dependent. For X<0.15, the corrugation decreases with increasing nitrogen contents. For X>0.15 the corrugation increases with the nitrogen content, and is accompanied by cross-linking through nitrogen atoms. Therefore, the hardness and elasticity increase beyond 0.15 can be explained by the cross-linking mechanism. The minimum elastic recovery at 0.15 corresponds to basal planes with a minimum corrugation, a situation found for one substitutional nitrogen atom per hexagonal ring.

4.6.2. Ion assistance with N_2/Ar gas mixtures.

The addition of Ar^+ to the assisting ions was aimed at an increase in the momentum transfer during deposition. The momentum transfer is necessary to promote the formation of sp^3 sites but also can induce large damage in the growing films. In this context, the study of the mechanical properties can add additional information to the spectroscopic results.

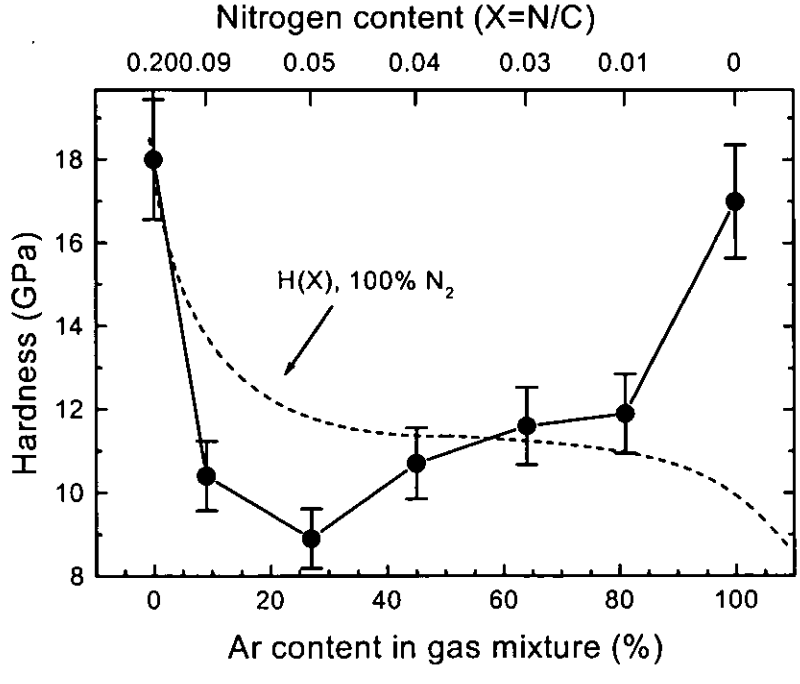

Figure 4.21. Hardness of a set of samples grown with different argon contents in the N_2/Ar gas mixture (360 eV, 7.5 mA).

Figure 4.21 shows the hardness values obtained as a function of the nitrogen content in the gas mixture. The nitrogen content of the films is shown in the top axis. The dashed line displays the hardness

that corresponds to films with the same X value grown with 100% N_2 in the gas mixture, as derived from Fig. 4.20. The samples grown with less than 50% Ar in the gas mixture are softer than would correspond to samples grown without Ar. This indicates that the Ar^+ bombardment is not promoting sp^3 sites, but it is disrupting the graphitic network by defect creation. However, for Ar contents in the gas mixture above 50% the samples are harder than would correspond to their nitrogen content. In the latter case, the hardness increase is directly related to the formation of carbon sp^3 sites, as evidenced by the decrease of the C(1s) π^* intensity in Fig. 4.7.

It is noteworthy that similar hardness values are obtained for CN_x films with a nitrogen content of ~20 at. % and for an amorphous carbon film with a similar sp^3 content. In both cases the proposed hardening mechanism is the same, i.e. cross-linking of graphitic planes but through different linking sites: nitrogen atoms for CN_x films and sp^3 carbon atoms for amorphous carbon films. The hardening mechanisms of cross linking through N-atoms and C-sp^3 hybrids are competitive since the samples grown with intermediate N_2/Ar values in the gas mixture are softer.

4.7. CONCLUSIONS.

The carbon nitride films grown by carbon evaporation with N_2/Ar ion assistance have a graphitic structure, with C-N π bonds and a low content of C≡N bonds. The films are homogeneous laterally and in depth, with a negligible amount of oxygen and hydrogen.

The nitrogen content is limited to [N]/[C]~0.3. This limitation seems related to the volatility of CN_x nitride moieties with larger nitrogen contents, formed during the film growth. The formation of C-N volatile compounds during deposition also implies a reduction of the deposition rate as nitrogen is incorporated. The addition of Ar to the assisting gas increases the ion bombardment effects due to the higher effective mass of the ions and, as a consequence, there is a reduction on the nitrogen content as compared with films grown under 100% N_2 assistance.

The structure of graphitic a-CN_x seems to be composed of numerous bonding states for carbon and nitrogen atoms. In this work we have resolved five different states for carbon and four for nitrogen, as derived from the XANES lineshape analysis. The relation between the carbon and nitrogen states remains an open question although some assignments could be established. In addition, the structure of these graphitic carbon nitride films is thermally stable up to 700°C

There is a relationship between the contribution of electrons from C and N atoms to the π bonds and the mechanical properties of the films. This is consistent with the arrangement of the basal planes, the softer films consisting in the pileup of weakly interacting graphitic planes, and the harder films consisting in a superstructure of interconnected and corrugated basal planes. The formation of this superstructure depends on the growth parameters, mainly on the mixture of bombarding ions and their energy. In

particular, films with a similar nitrogen content grown with different N_2/Ar gas mixtures exhibit different mechanical properties and charge distributions in the π bonds.

The hardening mechanism for graphitic films containing more than 70% carbon atoms with sp^2 hybridization and hardness around 20 GPa seems to be cross-linking of graphitic planes. For carbon nitride films grown with dominant nitrogen assistance the linking sites are nitrogen atoms. For films with a very low nitrogen content grown with dominant Ar ion assistance, the linking sites are carbon sp^3 hybrids. Promotion of both linking sites is competitive and is not obtained simultaneously.

REFERENCES

1. A.Y. Liu, A.Y., M.L. Cohen, Science 245 (1989) 841.
2. S. Muhl, J.M. Méndez, Diam. Rel. Mat. 8 (10) (1999) 1809.
3. C. Ronning, H. Feldermann, R. Merk, H. Hofsäss, P. Reinke, J.U. Thiele, Phys. Rev. B 58 (4) (1998) 2207.
4. A.R. Merchant, D.G. McCulloch, D.R. McKenzie, Y. Yin, L. Hall, E.G.J. Gerstner, Appl. Phys. 79 (9) (1996) 6914.
5. B.C. Holloway, D.K. Shuh, M.A. Kelly, W. Tong, J.A. Carlisle, I. Jiménez, D.G.J. Sutherland, L.J. Terminello, P. Pianetta, S. Hagstrom, Thin Solid Films 290/291 (1996) 94.
6. M. Kohzaki, A. Matsumuro, T. Hayashi, M. Muramatsu, K. Yamaguchi, Thin Solid Films 308-309 (1997) 239.
7. H. Sjöstrom, S. Stafsröm, M. Boman, J.E. Sundgren, Phys. Rev. Lett. 75 (7) (1995) 1336.
8. M. Côté, J.C. Grossman, M.L. Cohen, S.G. Louie, Phys. Rev. B 58 (1998) 664.
9. G. Jungnickel, P.K. Sitch, T. Frauenheim, B.R. Eggen, M.I. Heggie, C.D. Latham, C.S.G. Cousins, Phys. Rev. B 57 (1998) R661.
10. J. E. Lowther, Phys. Rev. B 59 (1999) 11683.
11. F. Weich, J. Widany, Th. Frauenheim, Phys. Rev. Lett. 78 (1997) 3326.
12. J. E. Lowther, Phys. Rev. B 57 (1998) 5724.
13. S. Souto, M. Pickholz, M.C. dos Santos, F. Álvarez, Phys. Rev. B 57 (1998) 2536.
14. M. C. dos Santos and F. Álvarez, Phys. Rev. B 58 (1998) 13918.
15. K. Yamamoto, Y. Koga, K. Yase, S. Fijiara, M. Kubota, Jap. J. Appl. Phys. Part 2, 36 (1997) L230.
16. J. Hu, P. Yang, C.M. Lieber, Phys. Rev. B 57 (1998) R3185.
17. E. Liu, X. Shi, H.S. Tan, L.K. Cheah, L.K., Z. Sun, B.K. Tay, J.R. Shi, Surf. and Coat. Tech. 121 (1999) 601.
18. Y.M. Ng, C.W. Ong, X.A. Zhao, C.L. Choy, J. Vac. Sci. Technol. A 17(2) (1999) 584.

19. A.K.M.S. Chowdhury, M. Monclus, D.C. Cameron, J. Gilvarry, M.J. Murphy, N.P. Barradas, M.S.J. Hashmi, Thin Solid Films 308-309 (1997) 130.

20. N. Hellgren, M.P. Johansson, E. Broitman, L. Hultman, J.E. Sundgren, Phys. Rev. B 59 (1999) 5162.

21. D.J. Kester, R.J. Messier, Appl. Phys 72(2) (1992) 504.

22. F. Rossi, B. Andrè, A. van Veen, P.E. Mijnaredns, H. Schut, M.P. Delplancke, W. Gissler, J. Haupt, G. Lucazeau, L.J. Abello, Appl. Phys. 75(6) (1994) 3121.

23. *Handbook of x-ray Photoelectron Spectroscopy*; Perkin Elmer-Physical Electronics, 1979.

24. P. Hammer, W. Gissler, Diam. Rel. Mat. 5 (1996) 1152.

25. D. Marton, K.J. Boyd, A.H. Al-Bayati, S.S. Todorov, J.W. Rabalais, Phys. Rev. Lett. 73 (1) (1994) 118.

26. Å. Johansson, S. J. Stafström, Chem. Phys. B 111 (1999) 3203.

27. J.M. Ripalda, E. Román, N. Díaz, L. Galán, I. Montero, G. Gomelli, Phys. Rev. B 60(6) (1999) R3705.

28. H. Sjöstrom, L. Hultman, J.E. Sundgren, S.V. Hainsworth, T.F. Page, G.S.A.M. Theunissen, J. Vac. Sc. Technol. A 14 (1) (1996) 56.

29. B.C. Holloway, O. Kraft, D.K. Shuh, M.A. Kelly, W.D. Nix, P. Pianetta, S. Hagström, Appl. Phys. Lett. 74 (22) 3290.

30. C. Quirós, PhD. Thesis, Universidad Autónoma de Madrid (2000).

31. S. Bhattacharyya, M. Hietschold, F. Richter, Diam. Rel. Mat. 9 (2000) 544.

32. S. López, H.M. Dunlop, M. Benmalek, G. Tourillon, M.S. Wong, W.D. Sproul, Surf. Interface Anal. 25 (1997) 827.

33. I. Jiménez, W.M. Tong, D.K. Shuh, B.C. Holloway, M.A. Kelly, P. Pianetta, L.J. Terminello, F.J. Himpsel, Appl. Phys. Lett. 74 (1999) 2620.

34. M.L. Wu, M.U. Guruz, V.P. Dravid, Y.W. Chung, S. Anders, F.L. Freire Jr, G. Marlotto, Appl. Phys. Lett. 76 (2000) 2692.

35. C. Quirós, R. Nuñez, P. Prieto, I. Vergara, D. Cáceres, L. Soriano, G.G. Fuentes, E. Elizalde, J.M. Sanz, Surf. & Coat. Technol. 125 (1-3) (2000) 284.

36. M. Lübbe, S. Park, P.R. Bressler, W. Braun, D.R.T. Zahn, BESSY Jahresberich (1998) p. 378.

37. D. Li, Y.W. Chung, S. Yang, M.S. Wong, F. Adibi, W.D. Sproul, J. Vac. Sci. Technol. A 12 (1994) 1470.

38. R. Gago, I. Jiménez, J.M. Albella, A. Climent-Font, D. Cáceres, I. Vergara, J.C. Banks, B.L. Doyle, L.J. Terminello, J. Appl. Phys. 87 (2000) 8174.

39. I. Jiménez, A.F. Jankowski, L.J. Terminello, J.A. Carlisle, D.G.J. Sutherland, G.L. Doll, W.M. Tong, D.K. Shuh, F.J. Himpsel, Phys. Rev. B 55 (1997) 12025.

40. I. Alexandrou, H.J. Scheibe, C.J. Kiely, A.J. Papworth, G.A.J. Amaratunga, B. Schultrich Phys. Rev. B 60 (15) (1999) 10903.

41. B.C. Holloway, O. Kraft, D.K. Shuh, M.A. Kelly, W.D. Nix, P. Pianetta, S. Hagstrom, Appl. Phys. Lett. 74 (22) (1999) 3290.

42. I. Jiménez, R. Gago, J.M. Albella, D. Cáceres, I. Vergara, Phys. Rev. B 62 (7) (2000) 4261.

43. R.L. Miller, P. G. Lykos, and H. N. Schmeising, J. Am. Chem. Soc. 84 (1962) 4623.

44. Q. Zhu, S.L. Money, A.E. Russell, K.M. Thomas, Langmuir 13 (7) (1997) 2149.

45. R. McWeeny, *Coulson's Valence* (Oxford University Press, Oxford, 1979).

46. J. Stöhr, *NEXAFS Spectroscopy*, (Springer, Berlin, 1992).

47. I. Jiménez, M.M. García, J.M. Albella, L.J. Terminello, Appl. Phys. Lett. 73 (20) (1998) 2911.

48. F. Tuinstra, J.J. Koenig, Chem. Phys. 53(3) (1970) 1126.

49. D.C. McCulloch, S. Prawer, A. Hoffman, Phys. Rev. B 50 (9) (1994) 5905.

50. F. Parmigiani, E. Kay, H.J. Seki, Appl. Phys. 64 (1988) 3031.

51. M.Y. Chen, D. Li, X. Lin, V.P. Dravid, Y. Chung, M. Wong, W.D.J. Sproul, J. Vac. Sci. Technol. A 11(3) (1993) 521.

52. R.O. Dillon, J.A. Woollam, V. Katkanant, Phys. Rev. B 29(6) (1984) 3482.

53. M.A. Tamor, W.C. Vassell, J. Appl. Phys. 76(6) (1994) 3823.

54. S. Prawer, K.W. Nugent, Y. Lifshitz, G.D. Lempert, E. Grossman, J. Kulik, I. Avigal, R. Kalish, Diam. Rel. Mat. 5 (1996) 433.

55. D. Beeman, J. Silverman, R. Lynds, M.R. Anderson, Phys. Rev. B 30 (1984) 870.

56. R.Gago, O. Sánchez, A. Climent-Font, J.M. Albella, E. Román, J. Raisanen, E. Rauhala, Thin Solid Films, 338 (1999) 88.

Chapter 5:

Ternary boron-carbon-nitrogen compounds

5. TERNARY BORON-CARBON-NITROGEN FILMS

5.1. INTRODUCTION.

As was discussed in the introduction, among the proposed alternatives in the search of new materials for hard coating applications, ternary Boron-Carbon-Nitrogen (BCN) films are one of the most promising candidates. The ternary cubic structures (c-BCN) are expected to combine the properties of diamond and c-BN, with hardness between 40-90 GPa and high thermal stability. In addition, these films may be free from internal stress since it has been found that the stress is reduced by the addition of small amounts of boron [1] or nitrogen [2] in amorphous carbon, and carbon in c-BN [3]. Hard materials, thermally stable and with low stress, would be optimal for high-speed cutting and polishing of ferrous alloys where high temperatures are commonly involved. The synthesis of ternary BCN compounds seems possible based on the similar structure between graphite and hexagonal boron nitride (h-BN) and between diamond and c-BN.

The possibility of synthesising ternary BCN compounds has been the object of numerous theoretical works [4,5,6,7]. Experimentally, BCN films have been produced with a large variety of compositions and methods, although the bonding structure of the resulting compounds is poorly known [8,9]. BCN films have been prepared by high pressure and high temperature synthesis (HPHT) [5,10,11,12] shock synthesis [13,14], mechanical milling [15], chemical vapour deposition (CVD) methods [16,17,18,19,20,21,22,23], physical vapour deposition (PVD) [8,24,25,26,27,28,29,30] and ion implantation [31]. Generally, only soft and hexagonal phases are obtained. Cubic structures have been produced in a few cases but phase segregation precludes the formation of a true solid ternary solution [8,10,12].

Regarding the characterisation of BCN films, XPS, Infrared or Raman, reveal the presence of BC, BN and CN bonding but this is not enough to justify the formation of a ternary phase. In addition, they can hardly proof the formation of sp^2 and sp^3 phases. More information can be extracted from the K-1s shell near-edge fine structure since it is very sensitive to local order arrangements and can be used to identify phases in complex systems [32]. Therefore, XANES and EELS are suitable techniques for the study of these compounds. In addition, they are especially sensitive for light elements like boron, carbon and nitrogen [33]. In order to understand the experimental results, the spectra for existing and predicted phases in the BCN system have been simulated theoretically [34]. Experimentally, the structure of BCN has been studied with EELS [13,35,36,37,38], although a definitive proof of the synthesis of a ternary compound is still lacking. In certain cases, phase segregation has been observed in both hexagonal [13] and cubic structures [35]. EELS presents more accessibility than XANES but has a resolution of ~1 eV, compared with the resolution of ~0.1 eV of XANES. This fact is important to resolve sharp features and

in systems with a large number of different bonding possibilities, like in BCN structures. Despite this fact, no report of XANES results in BCN films have been published so far.

In this chapter we report the synthesis of ternary BCN films by IBAD. The films were grown by evaporation of B_4C lumps and concurrent ion assistance with N_2+Ar+CH_4. We take special attention to the bonding environment by XANES.

5.2. FILM COMPOSITION AND DEPOSITION RATE.

The composition of the films was measured with XANES and TOF-ERDA. The XANES analysis was performed systematically in all the samples and the results were compared with TOF-ERDA values measured in selected samples. XANES is sensitive to the near-surface region in the total electron yield mode with an analysis depth of ~10 nm while TOF-ERDA provides a concentration depth profile over the whole film thickness. The results from both techniques are consistent in the near surface region.

The computation from the XANES spectra was performed considering the relative intensity of each absorption edge, as illustrated in Figure 5.1 for several examples. As in the case of a-CN_x, the relative intensities were corrected with a proportionality factor determined from comparison with reference crystalline h-BN and B_4C samples.

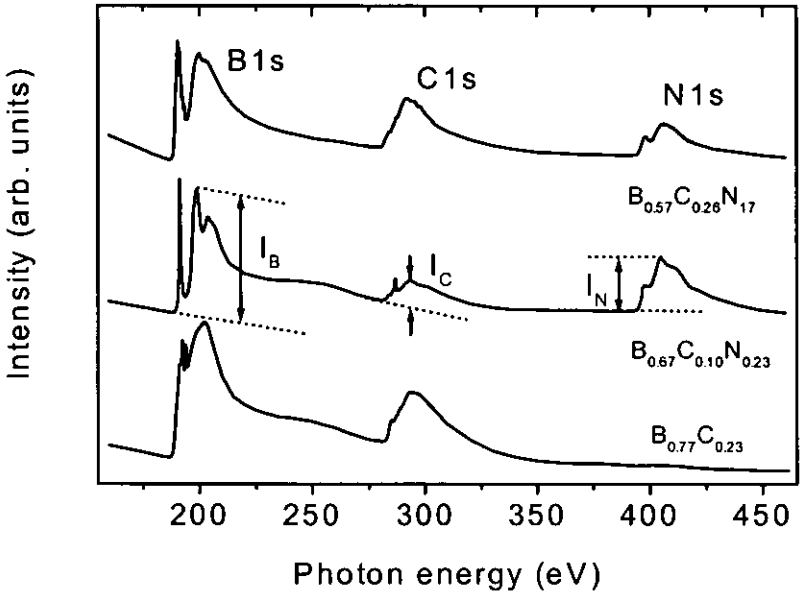

Figure 5.1. XANES survey scan to illustrate the compositional analysis. The atomic percentage is calculated from the relative intensity of the corresponding absorption edges.

5.2.1. Ion assistance with 100% N_2.

Figure 5.2 shows the TOF-ERDA concentration depth profile of a BCN sample grown with ion assistance with 100% N_2. The film thickness is ~150 nm and the growth conditions are indicated in the

caption of the figure. The shape of the profile indicates that the film composition is constant within a variation of 20%. The hydrogen content in the film is negligible. The film are also free from contamination since the oxygen content in the bulk of the film falls below 0.25 at. %.

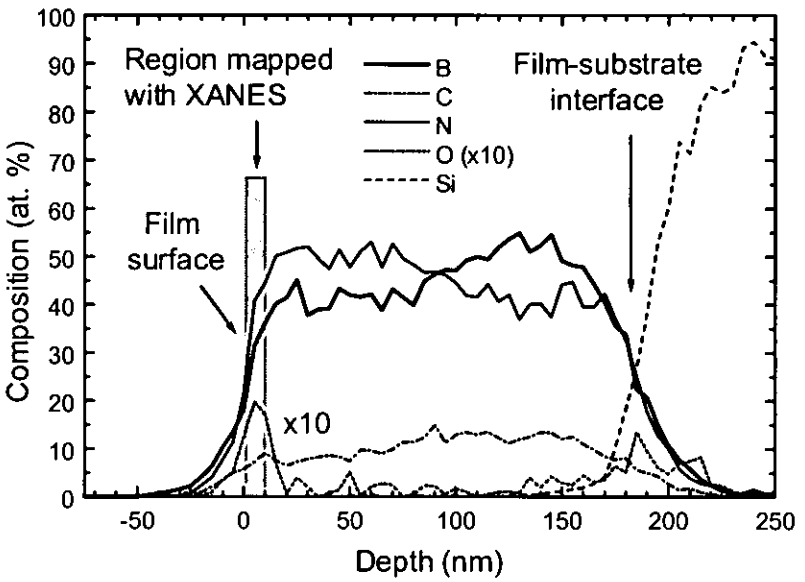

Figure 5.2. TOF-ERDA concentration depth profile of a BCN sample grown under ion assistance with 100% N_2. The deposition parameters were ion energy of 900 eV, ion current density of 1 mA/cm^2, substrate temperature of 150°C.

Panel (a) of Figure 5.3 shows the composition as a function of the ion energy per condensing carbon atom for ion assistance with 100% N_2. As in the previous chapters, we consider this parameter instead of the individual values of ion energy and flux in order to compare set of samples grown with different evaporation rates and due to non-independence of the ion energy and flux. In the case of B_4C evaporation we have to consider a density of 2.45 g/cm^3 and a composition of 80 at. % B and 20 at. % C to calculate the atom flux in the evaporated film.

The relevant trend found in the composition is that nitrogen increases with the ion energy in detriment of a reduction of the boron and carbon contents. Since the starting point is B_4C, the carbon content is intrinsically limited to ~20 at. %. The film composition saturates for ion energies per atom of ~200 eV/atom at $B_{60}C_{10}N_{30}$.

For ion energies per atom above 1000 eV/atom the deposition rate is very low (top panel of Fig. 5.3) and the thickness of the coating is below the detection limit of profilometry. For the films grown in this range, XANES detects some boron and carbon since an ultra thin BCN film may be formed. The XANES spectra of the N(1s) edge for these films shows that most of the nitrogen signal comes from SiN_x. Therefore, in this energy range, we are directly implanting the ions on the substrate.

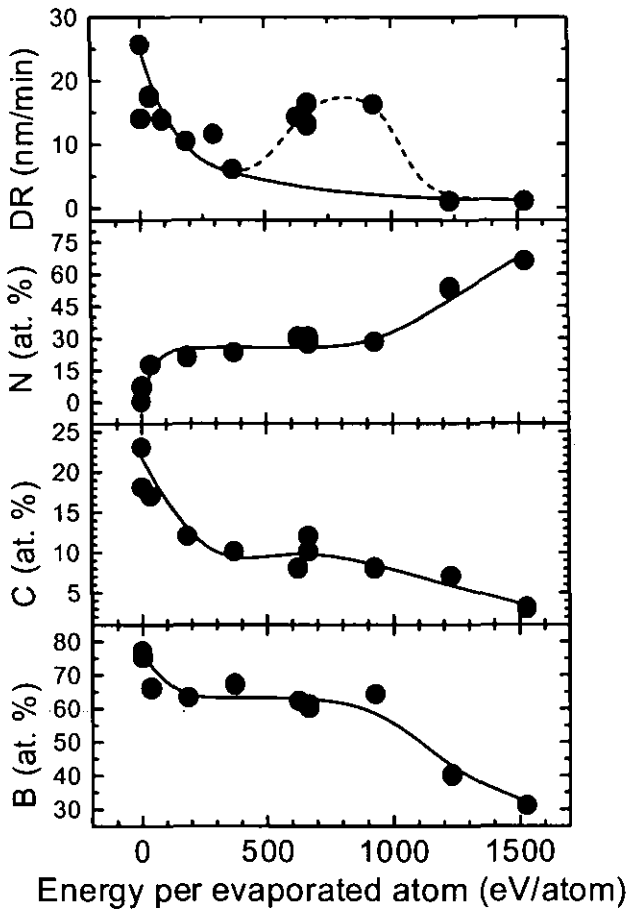

Figure 5.3. Deposition rate (top panel) and composition of BCN samples grown under ion assistance with 100% N_2 as a function of the ion energy per evaporated atom.

The ion bombardment induces two competitive processes in the deposition rate. On the one hand, an sputtering process (solid line) decreases the deposition rate, the sputtering yield increasing with the ion energy per atom. As anticipated above, for ion energies above 1000 eV/atom the sputtering overcomes deposition and no film is obtained. On the other hand, for ion energies per evaporated atom between 500 and 1000 eV/atom the nitrogen bombardment induces a reactive growth with incorporation of nitrogen to the film structure (dashed line) resulting in an increase of the deposition rate. As will be shown below, in this composition range a hexagonal structure is formed, which should be energetically very favourable.

The sputtering process is attributed to the formation of volatile C-N compounds during deposition, leading to a chemical sputtering of the deposited material [39,40]. This fact is illustrated in Figure 5.4 since the deposition rate is directly related with the nitrogen intake. Therefore, the reduction of the carbon content displayed in Fig. 5.3 can not be only attributed to the dilution of nitrogen in the BCN solution, but also to the loss of C atoms as a consequence of the sputtering.

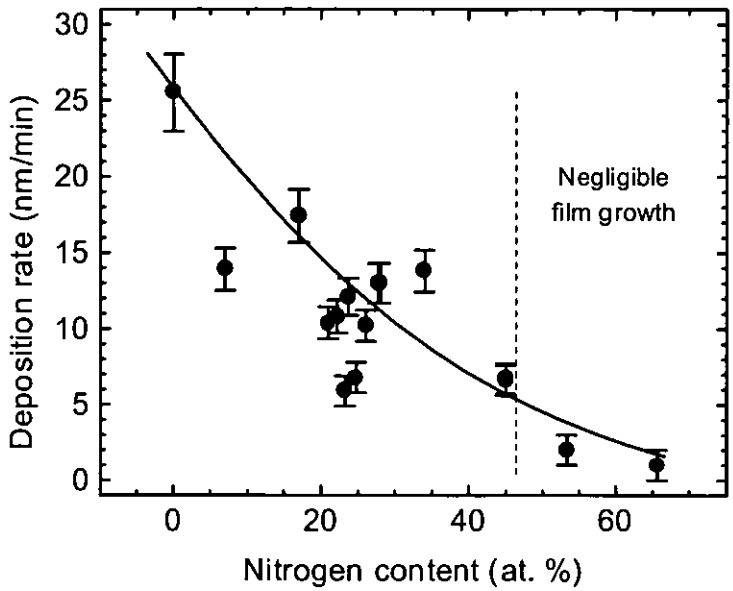

Figure 5.4. Deposition rate as a function of the nitrogen content for ion assistance with 100% N_2.

5.2.2. Ion assistance with N_2/Ar gas mixtures

The composition for the case of N_2+Ar ion assistance as a function of the Ar content in the gas mixture is displayed in Figure 5.5. The film were grown with an ion energy of 600 eV, ion current of 10 mA and substrate temperature of 450°C.

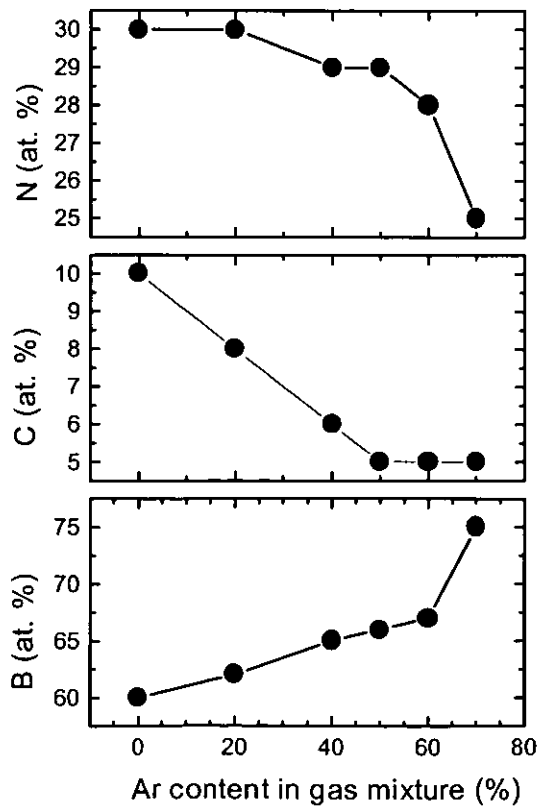

Figure 5.5. Composition of BCN samples grown with different N_2 + Ar gas mixtures.

The addition of Ar to the gas mixture implies a reduction of the number of nitrogen ions in the gas beam and, therefore, the nitrogen content in the film decreases with the Ar content in the gas mixuter. This reduction is considerable for Ar contents above 60% and it is also followed with a boron enrichment of the film. Regarding carbon, the concentration decreases from 10 to 5 at. % quickly as Ar is added to the gas mixture. The reduction of carbon could be the result of a higher momentum transfer during deposition due to the use of heavy ions. In fact, a decrease in the deposition rate as the Ar content increases is also observed. However, as we shall see later, the higher momentum transer is necessary to achieve cubic phases.

The TOF-ERDA analysis on BCN samples grown with N_2/Ar mixture reveals that the films are also free from hydrogen and oxygen. The use of Ar ions results in an incorporation of Ar atoms to the film between 3-6 at. %. Figure 5.6 shows the TOF-ERDA composition depth profile for a BCN film, ~75 nm thick, with a high cubic content. The growth conditions for this sample were a gas mixture of N_2/Ar=1, ion energy of 600 eV, ion current density of 1.06 mA/cm^2 and substrate temperature of 450°C during deposition.

The most remarkable feature comparing with BCN films grown with ion assistance with 100% N_2 is a heterogeneous composition in depth, with a surface region of ~25 nm thick and composition near $B_{45}C_5N_{50}$ and a deeper region of ~50 nm with composition near $B_{50}C_{20}N_{30}$. The in-depth heterogeneous composition is always found in the samples with a certain percentage of cubic content. This heterogeneity seems related to the change of bonding structure found in previous reports of c-BN:C [41] and c-BN [42] films. In those works, a hexagonal or turbostratic buffer layer of ~50 nm appears before the nucleation of the cubic phase. This is further analysed in the next sections.

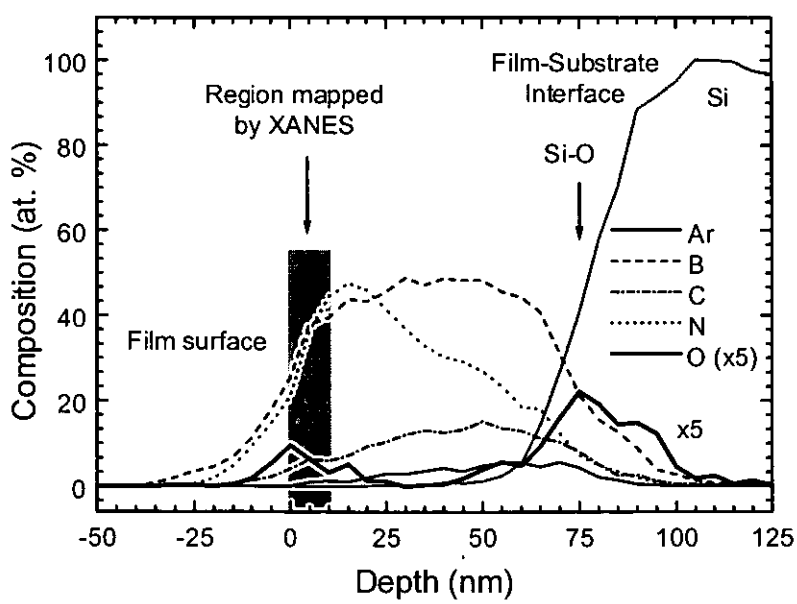

Figure 5.6. Compositional depth profile for a sample with 95% cubic content.

5.2.3. Ion assistance with N_2/CH_4 gas mixtures.

As we have previously discussed, the use of B_4C as the only source for carbon and boron atoms limits the carbon content to 20 at. %. In addition, the ion bombardment induces a further reduction of the carbon content as nitrogen is incorporated. The addition of CH_4 to the assisting gas is aimed at a major control over the carbon content. Figure 5.7 shows the composition for samples grown with the same ion energy and flux and different N_2+CH_4 gas mixtures. The boron, carbon and nitrogen fractions are derived from the XANES measurements while the hydrogen content is derived from TOF-ERDA analysis. It is evident that the addition of methane to the assisting gas results in an increase of the carbon content in the film. In this way, carbon fractions up to 0.8 can be achieved. The drawback of the use of CH_4 is the incorporation of hydrogen, which can be up to 20 at. % for the highest CH_4 contents (~40%).

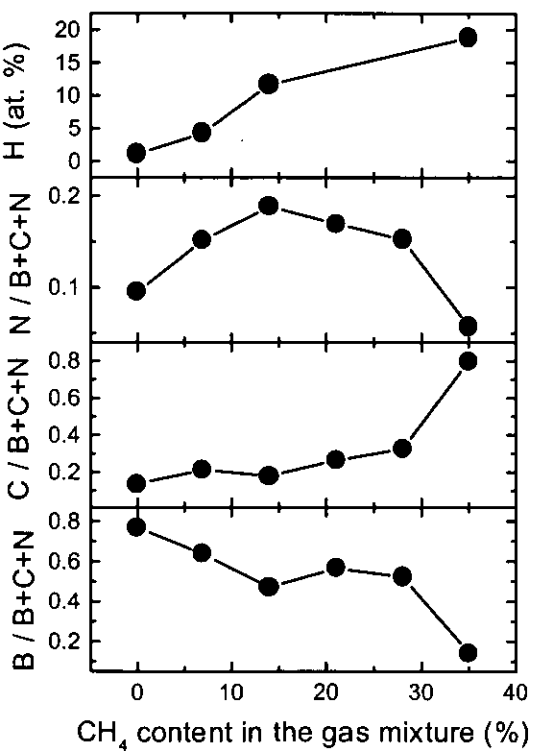

Figure 5.7. Composition of BCN films grown with different N_2/CH_4 gas mixtures. The fraction of boron, carbon and nitrogen is derived from XANES and the hydrogen content from TOF-ERDA.

5.2.4. Ion assistance with N_2+Ar+CH_4 gas mixtures.

The study of carbon incorporation to the cubic structures achieved with N_2+Ar ion assistance is of prime relevance. Since c-BCN films are expected to combine the properties of diamond and c-BN, high carbon contents with sp^3 hybridisations are supposed to maximise the hardness. As in the case of N_2+CH_4 ion assistance, we expect that the carbon content can be increased by the addition of CH_4 to the assisting gas mixture while keeping the cubic structure in the film.

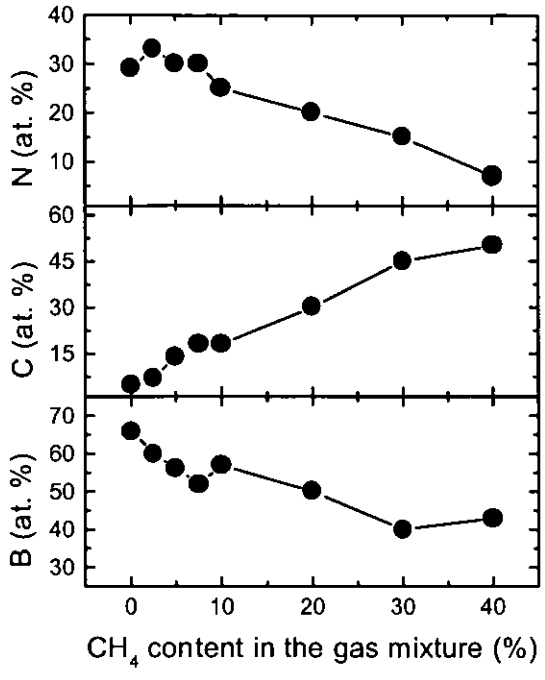

Figure 5.8. Composition of BCN films grown with different $N_2/Ar/CH_4$ gas mixtures as derived from the XANES spectra.

Figure 5.8 displays the composition as a function of the methane content in the N_2+Ar+CH_4 gas mixture. In this case, as for ion assistance with N_2+CH_4, the use of methane also increases the carbon content. However, the maximum carbon content is limited to 50 at. %, below the 80 at. % found in section 5.2.3. The reduction of the carbon content could be attributed to the use of heavy Ar ions as previously discussed for N_2/Ar ion assistance.

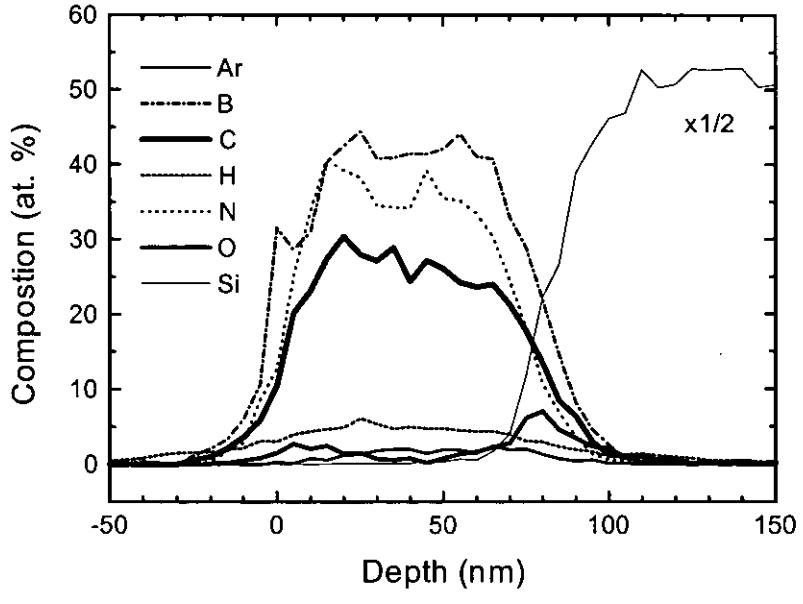

Figure 5.9. Compositional depth profile for a sample grown with N_2+Ar+CH_4.

The TOF-ERDA profile for a BCN film grown with a N_2+Ar+CH_4 gas mixture is shown in Figure 5.8. The composition is homogeneous in depth within a 10%. Since the heterogeneous composition was attributed to the formation of cubic structures, this result suggests that the cubic network may be loss with the addition of CH_4. This is further analysed in the following section.

5.3. IDENTIFICATION OF TERNARY PHASES

The results of the compositional analysis are summarised in the ternary diagram of Figure 5.10. This diagram shows that we can obtain different BCN stoichiometries depending on the kind of bombarding ions, ion energy and flux. The film composition seems confined in two regions. For low carbon contents the composition is close to a BN-like environment while, for high carbon contents, the films evolve towards a BC-like compound. This suggests a competition between the incorporation of carbon and nitrogen atoms, which precludes the formation of BCN stoichiometries in the central region of the ternary diagram. This result is consistent with the problems found in carbon nitride to obtain N/C ratios over 0.5, as we discussed in Chapter 4.

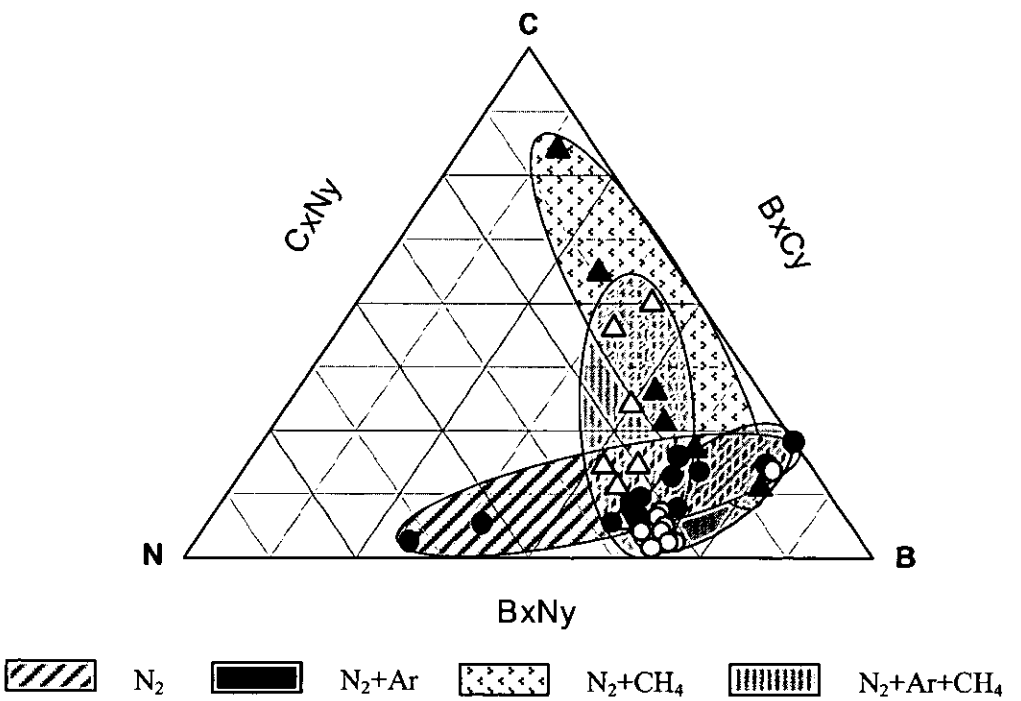

Figure 5.10. Ternary diagram with the BCN composition achieved for different ion assisting gas mixtures.

The confinement of the composition to BN and BC-like structures could to be attributed to the formation of binary films accommodating a small concentration of impurities. However, the composition

values represent the average value over the mapped area in the measurement process. Therefore, different ternary, single and/or binary phases could be present in the film leading to the same composition value. In order to discern if a ternary compound is formed, a deeper analysis with techniques sensitive to the bonding structure is required.

5.3.1. Ion assistance with 100% N_2: Identification of hexagonal ternary phases

In order to show the presence of ternary BCN hexagonal phases we have selected five samples with different structure, which have been labelled as #A, #B, #C, #D and #E. The deposition parameters, composition and thickness are shown in Table 5.1.

Table 5.1. Deposition parameters, composition and thickness of the selected BCN samples grown under ion assistance with 100% N_2.

Sample	Ion energy (eV)	Ion current density (mA/cm^2)	T (°C)	B (at. %)	C (at. %)	N (at. %)	Thickness (nm)
#A	0	0	125	77	23	0	255
#B	120	1.1	125	75	18	7	139
#C	240	1.1	125	66	17	17	174
#D	860	1.1	125	62	8	30	142
#E	900	1.4	125	61	12	27	130

a) Infrared spectroscopy (IRS)

IRS is a common characterisation tool of boron nitride because gives different spectral signals for c-BN and h-BN. The spectrum of h-BN is composed of two bands at 800 and 1400 cm^{-1}, which arise from in-plane stretching B-N and bending B-N-B vibrations, respectively [43,44]. The c-BN band appears around 1050 cm^{-1}, clearly separated from the h-BN features [45]. However, in BCN films the identification of the different phases is more complicated due to the high number of possible combinations that appear in the same region. Another disadvantage of IRS comes from the higher cross-section for BN bonds that could mask the presence of B-C and C-N bonds.

Figure 5.11 shows the IRS spectra for the selected BCN samples. The peak positions of BC, BN, CN and CC phases are marked as a reference on the top of the figure. The sharp band at 600 cm^{-1} appears in all the samples and comes from Si-Si vibrations of the substrate. The 2900 cm^{-1} C-H and 3300 cm^{-1} N-H stretching modes have not been observed, in agreement with the absence of hydrogen observed with TOF-ERDA.

The film grown without N_2 assistance, sample #A, presents a weak band at 1100 cm^{-1}. The incorporation of nitrogen to the film structure induces two main changes. The spectra of samples #B and #C reveal that, for nitrogen contents below 20 at. %, there appears a new band around 1200 cm^{-1}. Finally,

for nitrogen contents above 20 at. %, as in the case of samples #D and #E, the spectrum is dominated by the h-BN features.

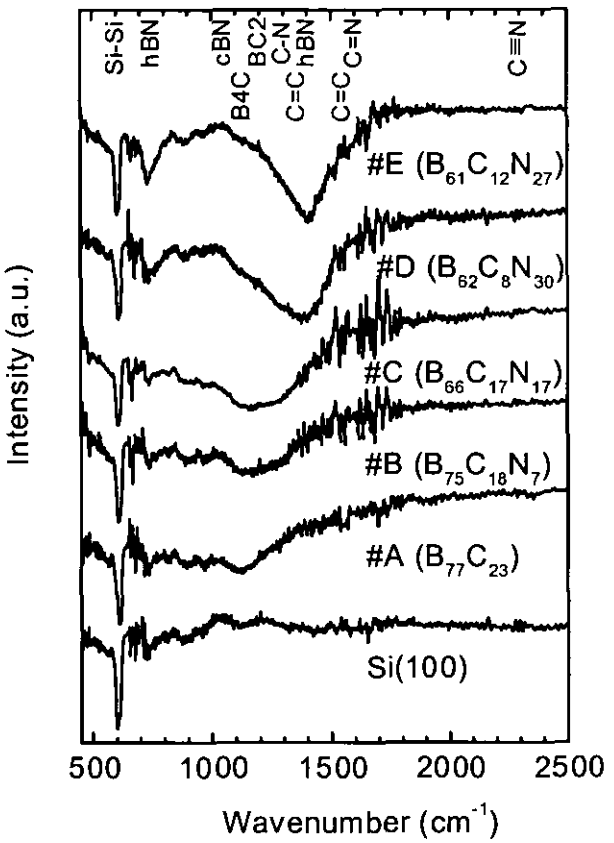

Figure 5.11. IRS spectra for the selected BCN films grown under ion assistance with 100% N_2.

The band around 1100 cm^{-1} is attributed to B_4C [46] and indicates that the evaporated film keeps the structure of the evaporation target. The structure of B_4C is a rhombohedral lattice with a unit cell composed of a $B_{11}C$ icosahedron and a C-B-C linear chain [47]. The changes observed in the IRS spectra indicate that the film structure evolves from the B_4C bonding structure to a hexagonal arrangement as nitrogen is incorporated to the film structure. The band at 1200 cm^{-1} can be assigned to a B_xC structure without icosahedral units [48]. Therefore, the presence of this band in our films can be explained by the distortion of the icosahedral units, leading to the formation of an amorphous B_xC. This distortion should arise from the evolution of the film structure to accommodate the hexagonal arrangement induced by the nitrogen intake.

From the IRS results we can conclude that BC and BN-like phases are present in the films. The bands related to CN phases [49] present a very low cross section by IRS and are hardly detected. For nitrogen contents below 20 at. % the structure is dominated by BC phases. As the nitrogen content is increased above 20 at. %, the structure evolves towards a hexagonal arrangement, which corresponds to

the most stable configuration for such nitrogen contents. Note that the IRS spectra of sample #D corresponds to an intermediate situation between BC and BN dominant environments, that could be indicative of the formation of a ternary compound.

b) Visible micro-Raman spectroscopy.

As introduced in the experimental chapter, Raman and IRS give complementary information due to the different selection rules that determine the active modes for each technique. In particular, Raman is very sensitive to graphitic-carbon arrangements, which are hardly detected by IRS. A detailed discussion of the Raman spectra for graphitic-carbon structures has been given in Chapter 2.

Figure 5.12 shows the Raman spectra for the selected BCN samples grown under ion assistance with 100% N_2. These films are transparent in the visible and IR range, which permits the observation of the first and second order of Si-Si vibrations coming from the substrate at 520 and 960 cm^{-1}, respectively. The spectrum of sample #A shows no appreciable bands except the substrate signals. The spectrum of this sample should be compared with B_4C reference spectra. The vibrational modes of B_4C are complex and still not well understood [47]. The experimental Raman spectra of crystalline B_4C shows several weak peaks in the 250-1000 cm^{-1} region related to intra-icosahedral and inter-icosahedral modes [50,51]. The spectrum of sample #A shows no appreciable bands although some weak structure, resembling that of B_4C, is observed between 250-1000 cm^{-1}. The amorphous character of this film probably precludes the appearance of well-resolved peaks as in B_4C.

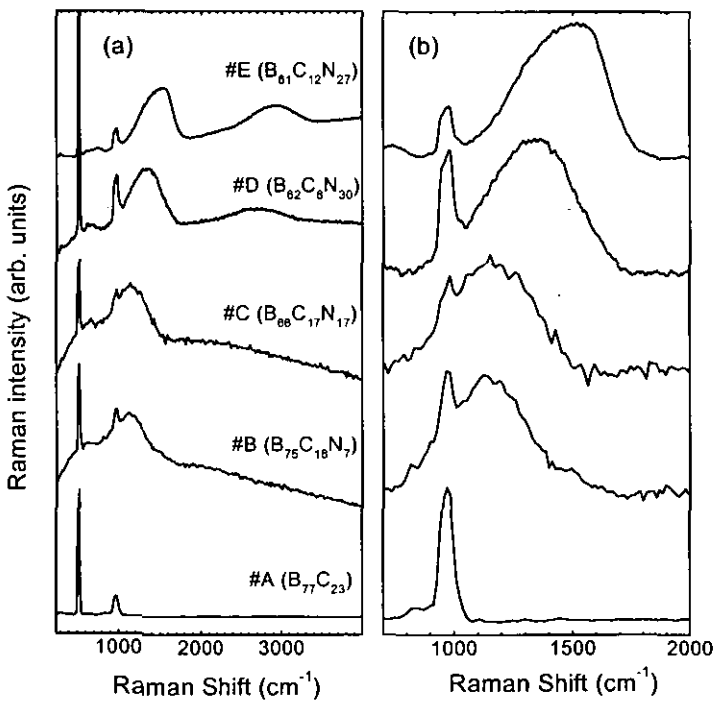

Figure 5.12. Full (a) and detailed (b) Raman spectra for the BCN selected samples.

In samples #B and #C, as nitrogen is incorporated into the B_4C structure, a band around 1200 cm^{-1} dominates the spectrum. This band coincides with the one observed by IRS, and corroborates the distortion of the icosahedral units. In the spectrum of sample #E the typical broad band of amorphous graphitic carbon between 1200-1800 cm^{-1} appears [52]. The second order of this band around 3000 cm^{-1} is also evident. The presence of these features implies segregation of graphitic carbon. Raman is very sensitive to this carbon phase and, hence, the intensity of this band is high when compared to the second order band of silicon. In addition, although IRS showed that this sample corresponded basically to h-BN, there is no Raman band related to this bonding due to the low Raman cross-section for h-BN

As in IRS, sample #D shows an intermediate situation between those described above. In this case, a band around 1400 cm^{-1} appears in the Raman spectrum. This band can not be attributed to h-BN as we have seen that the Raman cross-section for h-BN is very low. On the contrary, this Raman band resembles the graphite signal, but shifted to lower frequencies. Therefore, these bands should be related to carbon vibrations in a hexagonal network. The shift in the Raman frequencies could be attributed to a vibration change due to the substitution of carbon nearest neighbours in a hexagonal network for boron and/or nitrogen in the ternary BCN structure.

c) X-Ray Absorption Near Edge Spectroscopy (XANES)

Although IRS and Raman provide important information on the bonding structure, they are not capable of giving a conclusive proof of the formation of a ternary phase. A more detailed information can be obtained with X-Ray Absorption Near Edge Spectroscopy (XANES) since different spectra for boron, carbon and nitrogen are obtained containing information on the local structure around each type of atom. Therefore, we can discern if mixing at an atomic level is produced.

Figure 5.13 displays the B(1s), C(1s) and N(1s) XANES edges for the same BCN films considered above. The films were measured as received and after annealing in vacuum at 500°C. We have observed that the annealing process removes the surface contamination without affecting the film structure. The spectra were normalised to the same height for comparison purposes. The spectra of highly oriented pyrolitic graphite (HOPG), diamond, boron carbide (B_4C), h-BN and c-BN are shown as reference spectra.

The B(1s) edge shows sharp peaks in the π^* region, between 188 and 196 eV, and a broad structure in the σ^* region, between 196-205 eV. The sample grown without nitrogen assistance (sample #A) shows the typical spectral shape of an amorphous boron carbide film [53]. The π^* resonance of h-BN at 192 eV [54,55] is evident for nitrogen contents around 20 at. % and becomes the dominant feature for higher nitrogen contents.

The shape of the N(1s) confirms the formation of a h-BN-like compound. As the nitrogen content increases the N(1s) spectra resembles that of h-BN and the π^* resonance peak at 401 eV [55] becomes

more evident. The N(1s) features are broad and impede extracting further information although subtle lineshape changes are observed.

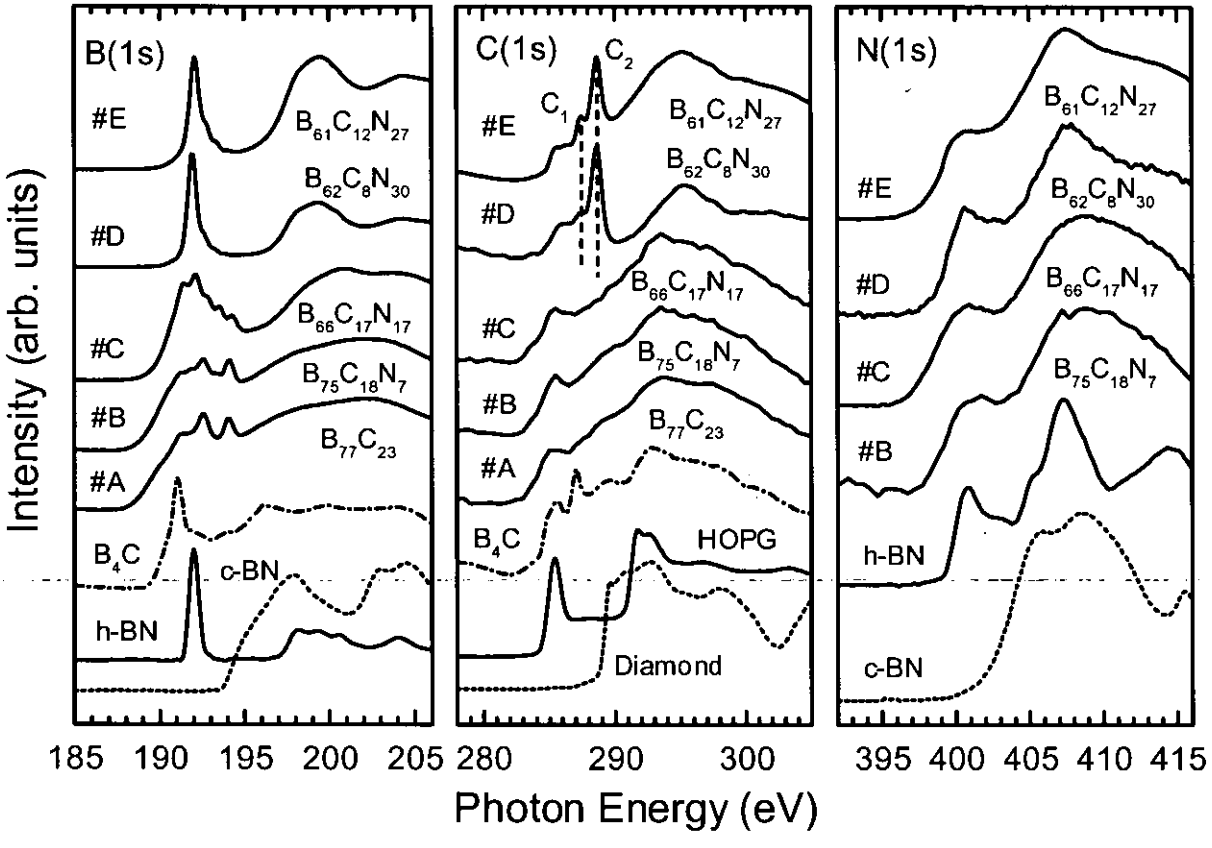

Figure 5.13. XANES spectra for the selected BCN samples grown under ion assistance with 100% N_2. The presence of the π^* peaks C_1 and C_2 in the C(1s) edge reveals the formation of a hexagonal ternary compound.

From the C(1s) features we can discern if carbon is incorporated into the h-BN-like network, therefore, if a true ternary compound is formed. The C(1s) spectrum of boron carbide shows four edges at 283, 287, 288, 291 eV, which are sharper in crystalline B_4C than in amorphous B_xC [53,56]. This structure is further smoothed as nitrogen is incorporated to the film in samples #B and #C. This result is in agreement with the distortion of the B_{12} icosahedral units observed by Raman and IRS. With further nitrogen intake, a series of sharp carbon peaks resembling π^* resonances appear in the 285-290 eV region, superimposed to the boron carbide signal. The main peaks at 287.3 and 288.5 eV are labelled as C_1 and C_2 in the figure. These peaks become the dominant features when the B(1s) and N(1s) edges indicate the formation of a h-BN-like material. We carefully checked that none of these peaks correspond to carbon surface contamination by monitoring also the oxygen signal. Therefore, the C(1s) features reveal the presence of carbon into the hexagonal BCN network. The presence of different peaks seems related to the different possible nearest neighbour environments of carbon in the network. These carbon states have different stability since some are more intense than others.

From the above results we can see that sample #D shows the most intense ternary signal, in agreement with IRS and Raman results. The presence of graphitic carbon, observed by Raman in sample #E, suggests that there is a limit of solubility of carbon in the ternary phase. In this context, for carbon contents above 10 at. % carbon is segregated in graphitic regions, while for contents below 10 at. % it is mostly incorporated in the ternary phase.

5.3.2. Ion assistance with N_2+Ar gas mixture: Identification of cubic ternary phases

A recent approach to the production of c-BCN films is based on the use of ion assistance bombardment during deposition, in analogy to what is done in the growth of tetrahedral amorphous carbon (ta-C) and c-BN [8]. The use of heavy inert ions seems crucial in order to confer the momentum transfer necessary for the promotion of sp^3 sites. Films grown by sputtering or evaporation of a B_4C target under N_2+Ar ion assistance have been considered either as c-BN [57,58], c-BN with carbon impurities (c-BN:C) [41] or as a ternary BCN compound [59]. Therefore, the role of carbon in this type of films has not been carefully studied. When the growth of c-BN is searched, the carbon content is an undesired impurity to be reduced. However, when the growth of ternary BCN compounds is the goal, it is desirable to control the carbon content.

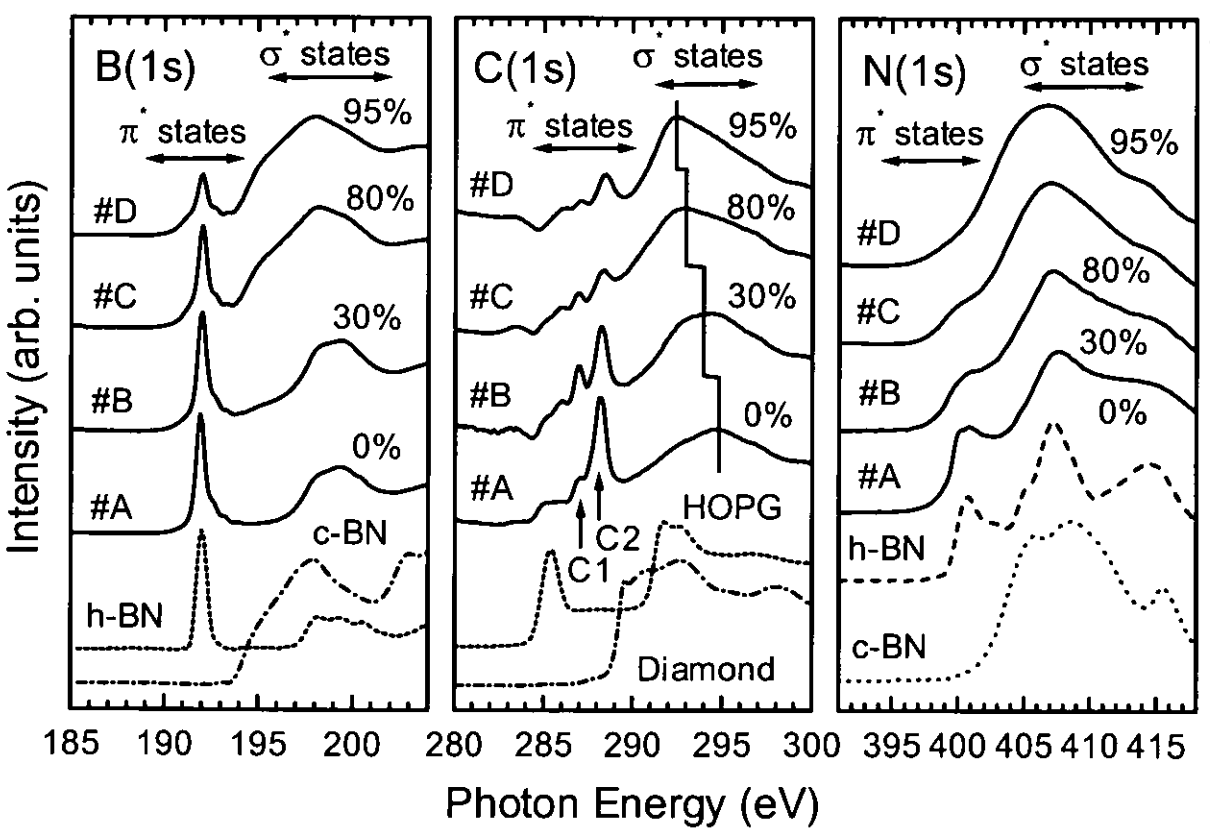

Figure. 5.14. XANES B(1s), C(1s) and N(1s) edges for BCN films with different cubic percentages and reference spectra from h-BN, c-BN, HOPG and diamond. The corresponding cubic percentages are indicated in the figure.

Figure 5.14 displays the B(1s), N(1s) and C(1s) XANES absorption spectra for BCN films grown under different deposition conditions, with composition near $B_{50}C_{10}N_{40}$ and different percentages of cubic phase. From samples #A to #D, the decrease of the π^* peak at 192 eV and the appearance of new σ^* states starting at ~194 eV in the B(1s) spectra indicate the transition from a hexagonal to a cubic structure. The N(1s) spectra confirm the production of cubic structures by the decrease of the π^* peak at ~401 eV.

The percentage of cubic phase in each film has been quantified by curve fitting the B(1s) spectra to a linear combination of the hexagonal and cubic reference spectra. This fitting procedure is illustrated in Figure 5.15 for two films with a cubic content of 95 and 23 %, respectively. The open dots represent the experimental data and the solid lines correspond to the fitted spectra.

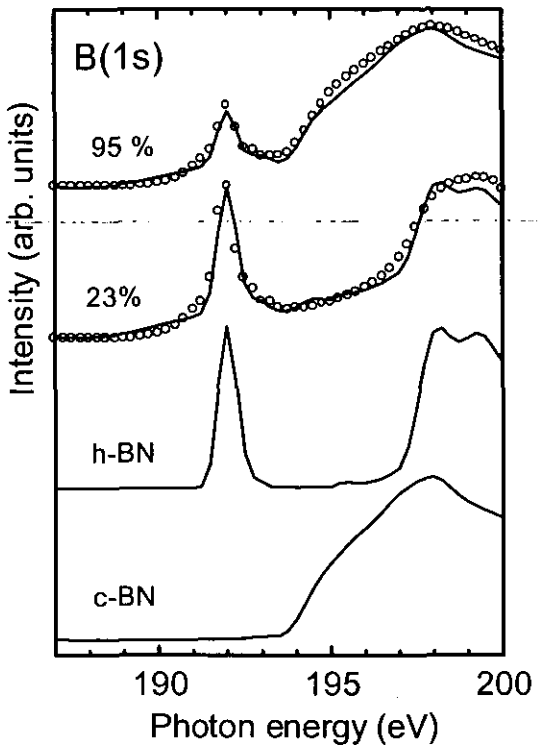

Figure 5.15. An illustrative example of the cubic content computation for two films with a 95% and a 23% cubic content, respectively. The experimental data (solid dots) is fitted to a linear combination (dashed line) of the h-BN and c-BN spectra.

Discerning if carbon is forming part of the cubic structure is not so straightforward. First of all, it is essential a correct normalisation of the C(1s) XANES signal to exclude the contribution from carbon contamination in the beamline optics, since the carbon content in the films is low. This was done by a double normalisation procedure. At a first step, the film signal is divided by the gold grid photocurrent to compensate photon flux variations. In the second step, the resulting spectrum is divided over the signal measured from a Si substrate, cleaned in ultra high vacuum by flashing to 1200°C, and also normalised

previously to the grid photocurrent. Since the Si signal must be completely flat at the C(1s) absorption region, the signal from contamination in the beamline optics is eliminated using this method.

After carefully proceeding in this way, several features are distinguished in the C(1s) region. The peak at 285.4 eV corresponds to graphitic domains and the additional sharp peaks in the 286-289 eV regions to the h-BCN structures described in the previous section. As a result of the increment of the cubic phase, the h-BCN features in the C(1s) edge decrease in the same way as the B(1s) and N(1s) π^* peaks. In addition, the shape of the σ edge changes from a rounded and broad structure in sample #A (h-BCN) to a much sharper edge for sample #D. This is also followed by a downshifting of the σ^* states maximum from 295 to 292 eV, as illustrated in Fig. 5.12. These results support that carbon is also arranged with tetrahedral bonding in the cubic BCN network. However, the shape of the C(1s) σ^* states in sample #D (maximum cubic content) differs from the diamond reference, whereas the B(1s) and C(1s) edges are almost identical to the c-BN references. This could be attributed to a stress induced distortion of the c-BCN network at the C sites. This distortion would inhibit the incorporation of substitutional carbon above ~5 at. %.

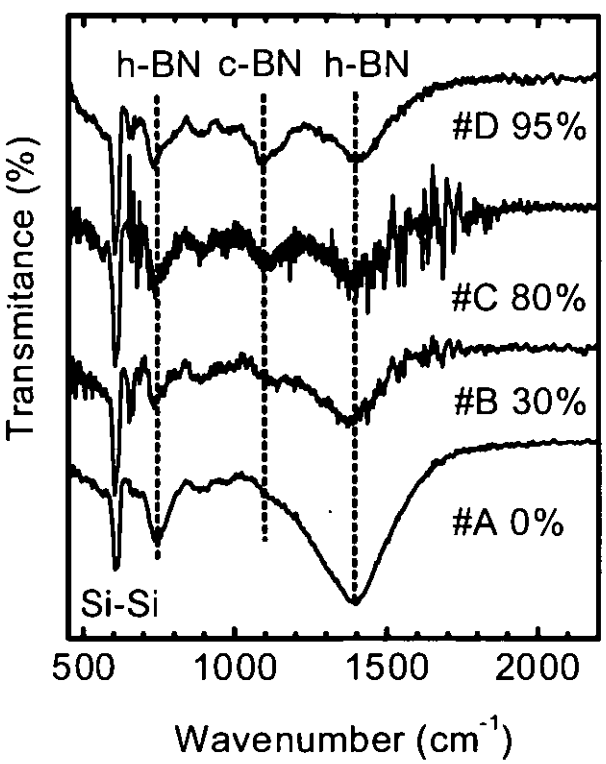

Figure 5.16. IRS spectra for BCN films with different cubic contents. The cubic percentages shown in the figure are derived from the XANES spectra.

We have also analysed our films with IRS, since this technique probes the whole film thickness and gives complementary information to XANES on the bonding structure. Figure 5.16 displays the IRS

spectra for the same samples shown in Fig. 5.14. Sample #A shows clear h-BN features around 750 and 1400 cm^{-1}, as corresponds to h-BCN. Samples #B, #C and #D show an increasing intensity of the c-BN signal at ~1100 cm^{-1}, in agreement with the increasing sp^3 ratios observed by XANES. However, the maximum proportion of the c-BN signal in the IRS spectra is always below 50%, much lower than the ~95% found by XANES. This is explained by the in-depth heterogeneity of the bonding structure, consistent with the compositional profile, previously described.

5.3.3. Ion assistance with N_2/CH_4 gas mixtures: Effect of the carbon content on h-BCN.

In section 5.2 we have shown up that the addition of CH_4 to the assisting gas permit the additional intake of carbon to the BCN films. However, we have to discern if carbon is efficiently incorporated to the ternary structure or segregated and, in the former case, how the network evolves to accommodate the higher carbon content.

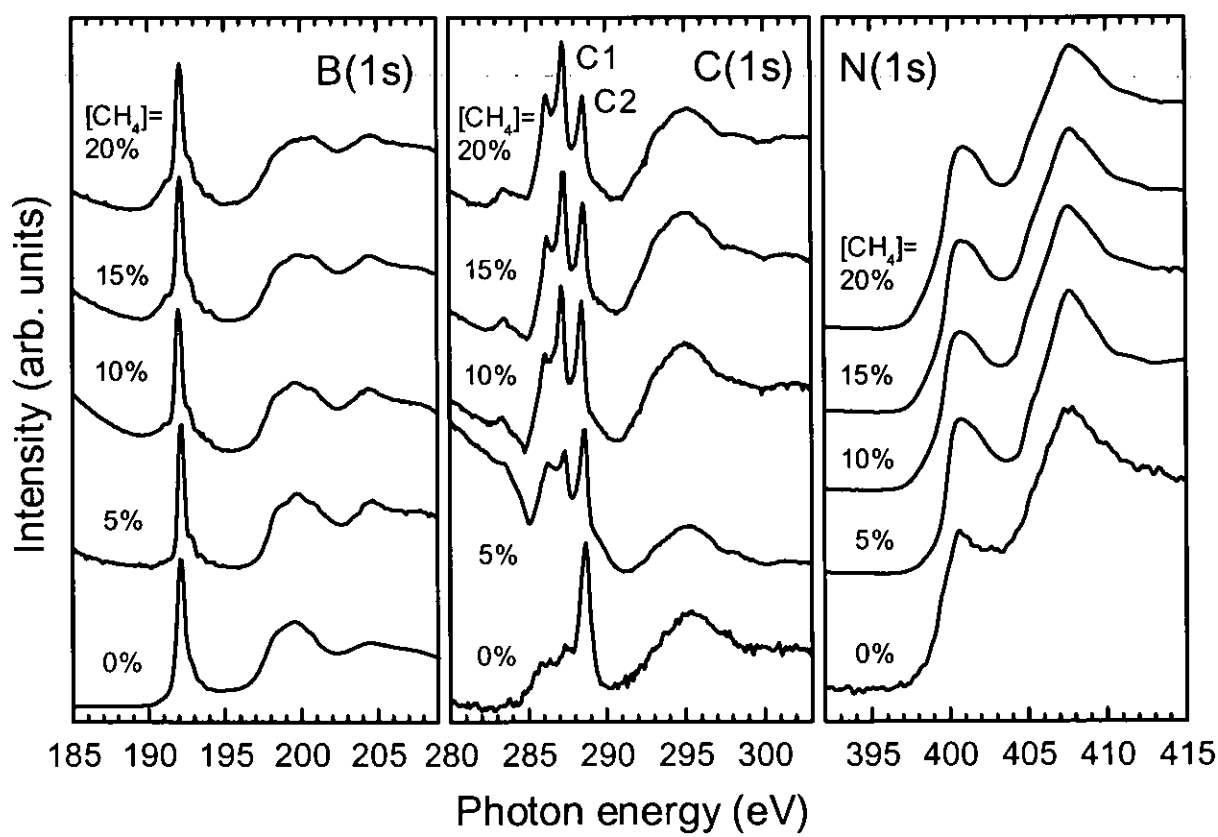

Figure 5.17. XANES spectra for BCN films grown with different CH_4+N_2 gas mixtures. The CH_4 content in the gas mixture is displayed in the figure for each film.

Figure 5.17 shows the XANES B(1s), C(1s) and N(1s) edges for different methane concentrations in the assisting gas. The samples were grown at room temperature and ion assistance parameters of 600 eV and 1.1 mA/cm^2. The structure of the film grown with $[CH_4]$=0 corresponds to h-BCN, similar to

those described in section 5.3.1. The incorporation of carbon as the CH_4 content is increased (see section 3.5.3) induces changes in the film structure, mostly appreciated in the C(1s) edge. The addition of carbon by methane bombardment induces an increase of the state C1. There is also a parallel increase of the BC_x signal as revealed by the increase of the states below the π^* resonance at 192 eV.

5.3.4. Ion assistance with N_2/Ar/CH_4 gas mixtures: Effect of the carbon content on c-BCN.

We have seen that the carbon content in c-BCN is limited to ~5 at. %. At this point, the question posed is if this carbon content is a limitation of the deposition method or it is intrinsic to the tetrahedral structure. For this reason, a mixture of N_2+Ar+CH_4 was employed. In order to preserve the cubic structure as much as possible, the addition of CH_4 was performed at low concentrations (<10%). Since we search to combine the properties of diamond and c-BN, it is desirable to obtain a c-BCN compound with a large carbon content. This possibility is analysed in this section.

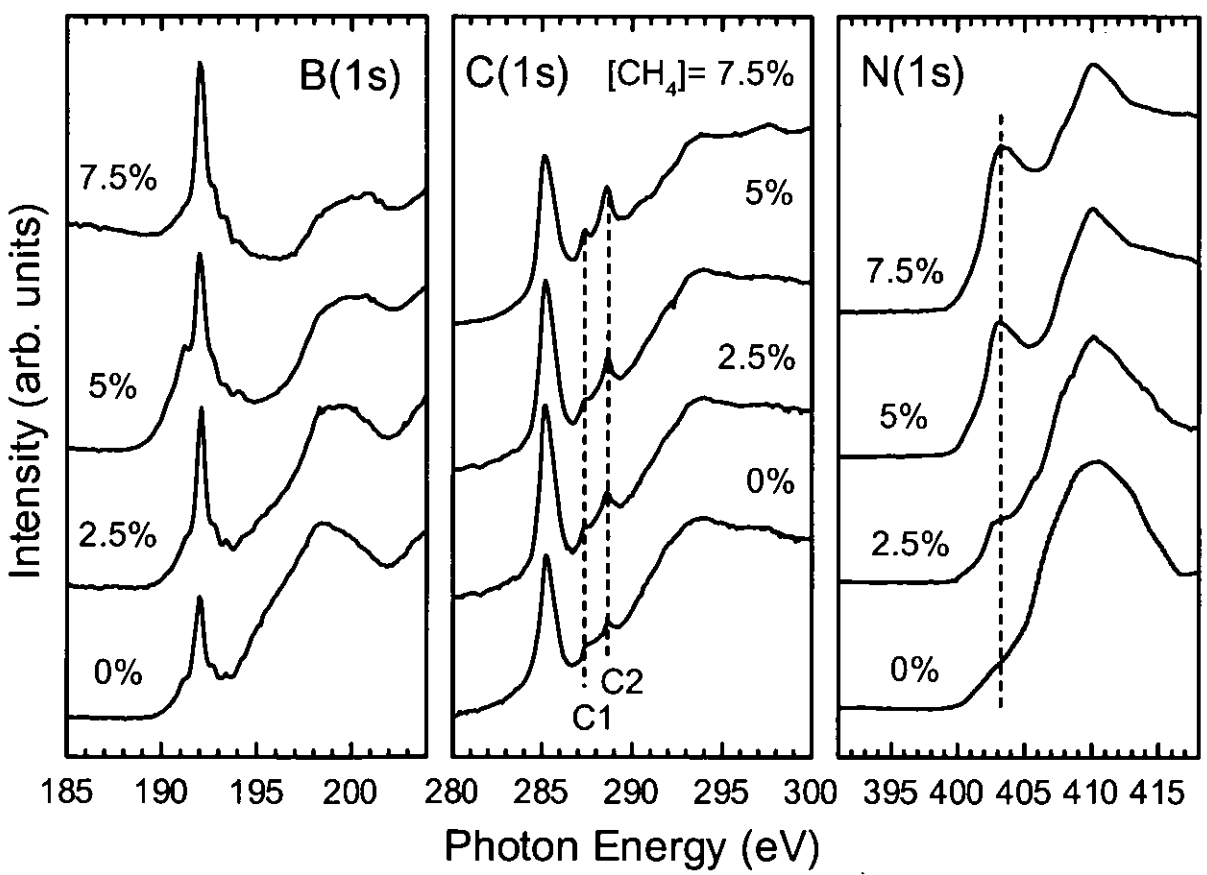

Figure 5.18. XANES spectra for BCN films grown under ion assistance with different N_2+Ar+CH_4 gas mixtures. The CH_4 content is indicated in the figure.

Figure 5.18 displays the B(1s), C(1s) and N(1s) XANES edges for different CH_4 contents in the N_2+Ar+CH_4 mixture. The ion assisting conditions were chosen at the values found under N_2+Ar ion

assistance for maximum promotion of the cubic content (T=450°C, N_2/Ar=1, E_i=600 eV, J_i=1 mA/cm^2). Therefore, the sample grown with [CH_4]=0 represents a sample with ~95% of cubic content. As we add CH_4 to the gas mixture the cubic content decreases and the h-BCN signals become more intense. Therefore, the addition of carbon does not keep the cubic structure as would be desirable.

Apart from the reduction of the cubic content other trends are observed as we increase the CH_4 content in the gas mixture. The graphite peak increases indicating that part of the additional carbon atoms segregate into graphitic regions. In addition, the carbon hexagonal features, C_1 and C_2, are also more intense showing that carbon is also efficiently incorporated to the hexagonal structure. In this case, peak C_2 is the most favourable arrangement in contrast with ion assistance with N_2+CH_4 gas mixtures.

Finally, we have also swept other deposition parameters (ion energy, ion flux and substrate temperature) but we have found that the addition of CH_4 always precludes the formation of cubic structure. Better results would be expected for independent control of the CH_4 and N_2/Ar ion beams. However, this implies the use of an additional ion gun, which was not available during the course of this work.

5.4. PREFERENTIAL ORIENTATION OF TERNARY PHASES

We have shown that different hexagonal and cubic phases are obtained in our BCN sample. From the XANES measurements we can also detect if these phases present any preferential orientation since the intensity from π^* states follows a cosine-squared dependence with the angle between the light and the π bonds [60].

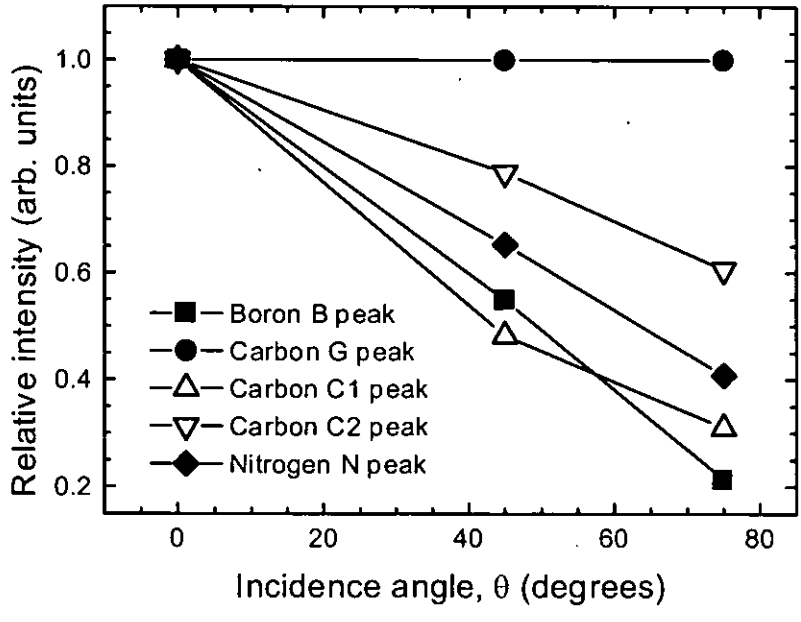

Figure 5.19. Intensity of the different B(1s), C(1s) and N(1s) peaks as a function of the incidence angle of the synchrotron light respect to the substrate normal.

Figure 5.19 shows, as a function of the incidence angle of the synchrotron light, the relative intensity of the π^* peaks from B(1s) at 192 eV (labeled as B), N(1s) at 401 eV (labeled as N) and the C(1s) peaks from graphite at 285.4 eV (labeled as G), C_1 at 287.3 eV and C_2 at 288.5 eV. The graphitic signal shows no preferential orientation. However, the intensity from the rest of the peaks decreases with the incidence angle. This corresponds to a preferential orientation of the hexagonal planes perpendicular to the film surface. It is important to note that the anisotropy found in C_1 and C_2 confirms the π character of these states. Since the hexagonal structures are mechanically anisotropic, the compressive stress induced in the films by the ion bombardment during deposition is easily relaxed when the basal planes orient perpendicular to the substrate.

The presence of an oriented hexagonal buffer layer seems necessary to promote the growth of cubic phases, as in the case of c-BN [61] and diamond [62]. In the case of c-BCN, a similar behaviour is observed by XANES. Figure 5.20 shows the dependence of the B(1s) signal with the angle between the sample normal and the incident beam for the sample with ~95% cubic content. The observed tendency indicates that in c-BCN, the hexagonal layers are also orientated perpendicular to the substrate surface.

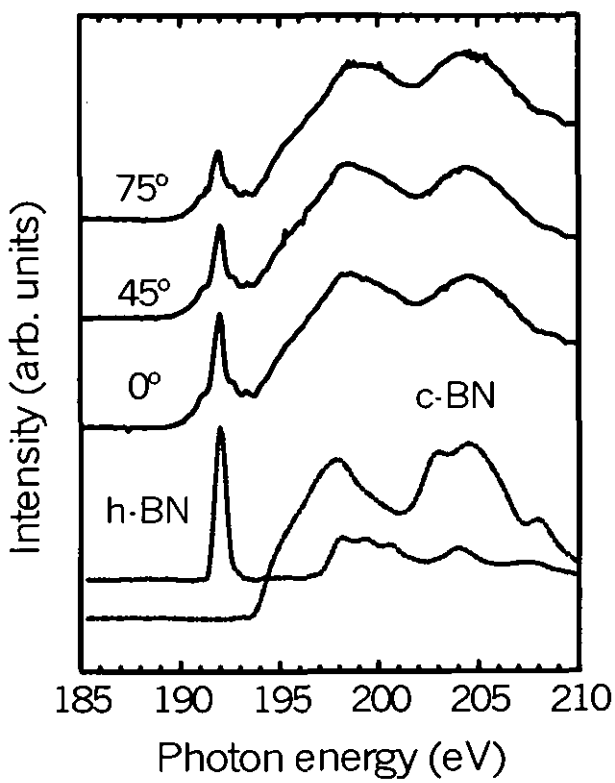

Figure 5.20. Angle dependent study of the XANES B(1s) edge for a c-BCN film with 95% of cubic phase.

5.5. CONTROL OF HEXAGONAL/CUBIC PHASES: Growth mechanisms.

The similar structure between c-BN and c-BCN suggests that the same growth mechanisms and conditions may be prevalent. The formation of c-BN is ruled by a momentum transfer mechanism [63,64]. The ion assisting variables such as energy, flux and species are incorporated into the momentum transfer value. The formation of c-BN has been related with high levels of induced compressive stress [65]. The high stress leads to high-pressure regions that drive a transformation from sp^2 to sp^3 hybrids. The stress in a large number of materials has been found to scale with the momentum of the impinging ions [66]. Therefore, the momentum transfer and stress induced transformation mechanisms should be equivalent. The origin of the stress has been proposed to depend on the concentration of defects, mainly interstitials and vacancies, which are generated upon ion irradiation [64]. Figure 5.21 shows the cubic content found as a function of deposition parameters for films grown under N_2/Ar ion bombardment.

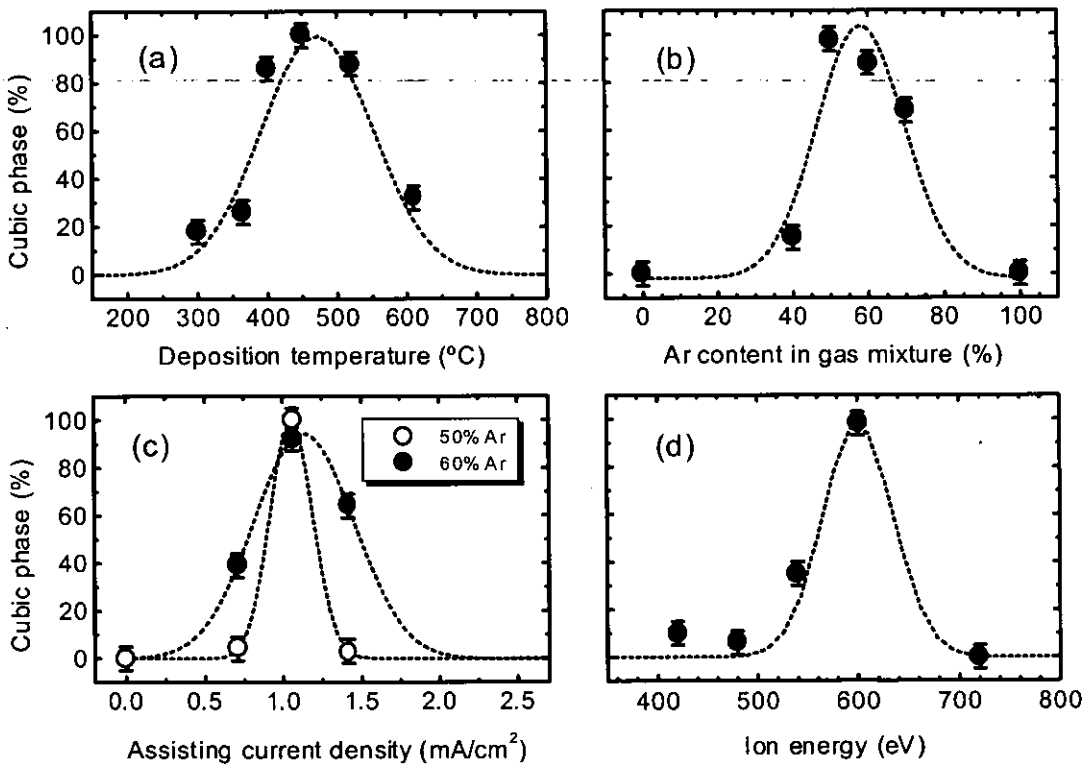

Figure 5.21. Cubic percentage as a function of deposition parameters.

The cubic content as a function of the substrate temperature is displayed in panel (a) of Fig. 5.21. Temperatures between 300 and 600°C are required to achieve a certain amount of cubic phase. Similar temperature windows have been reported in the literature for c-BN [67]. It is clear that temperature is an important factor in the formation of c-BCN films although the mechanisms that drive to the promotion of the cubic for a certain window of temperatures are still not clear. Several explanations have been

proposed: (i) The dependence of the cubic content with the concentration of defects implies a balance between formation and recombination rates [64]. Therefore, the dependence with the deposition temperature of the cubic content suggests an influence over these rates. At high temperatures, the higher mobility could lead to the annealing or relaxation of defects and, hence, the growth of the hexagonal structure should be more favourable. (ii) Another possible explanation of the reduction of the cubic content at increasing temperatures is that the free energy of the deposit is lower at high temperatures since the crystallinity is improved. Therefore, more damage should be required at those temperatures to convert a given volume to c-BN. (iii) The reduction of the cubic content could also be the result of the hexagonal interfacial layer becoming thicker [67]. (iv) Finally, another effect that has been considered is the need to maintain a certain stoichiometry since at low temperatures the films are nitrogen-deficient [67].

The promotion of c-BN growth is found in a narrow window in the momentum space. The promotion of cubic phase requires a momentum transfer above a certain threshold in order to introduce sufficient stress for the c-BN to be the stable phase under those conditions [65]. The dependence of the cubic phase growth with the momentum transfer is derived by the increase of the cubic percentage as Ar is added to the gas mixture, as shown in panel (b) of Figure 5.21. The increase in the Ar content in the gas mixture implies a higher apparent mass of the ions, while keeping the ion energy constant. Therefore, momentum and not energy is the key parameter affecting the deposition. The decrease of the cubic phase for Ar contents above 60% is attributed to the film deterioration by ion irradiation damage.

Panels (c) and (d) of Figure 5.21 show, for a gas mixture of $Ar/N_2=1$, the dependence with the ion flux and energy, respectively. To achieve the momentum necessary for growth of cubic phase, ion energies and fluxes above a certain value are required. For a higher content of Ar in the gas mixture a lower current is needed to achieve the same cubic content and the region of maximum promotion of cubic content broadens.

The sharp dependence found with ion energy and flux is a consequence of the ion assistance process since simultaneous ion bombardment implies a competition between film growth and induced damage. It has been reported that irradiation with N_2 and Ar ions causes a transformation from c-BN into h-BN [68]. Therefore, ion induced damage becomes dominant at high energies and fluxes and produces the sharp decrease in the cubic content.

5.6. THERMAL STABILITY OF TERNARY PHASES

5.6.1. Influence of the deposition temperature

From the results shown in section 5.5, it is clear that the deposition temperature plays an important role in the growth of c-BCN. However, this question remains unknown for the case of h-BCN, i.e. ion assistance with 100% N_2. Figure 5.22 shows the B(1s), C(1s) and N(1s) edges for a set of samples

grown under ion assistance with 100% N_2 at different substrate temperatures during deposition. All the samples were grown with ion energy and flux of 1000 eV and 1.4 mA/cm^2, respectively.

The corresponding composition is around $B_{60}C_{15}N_{30}$ for the whole temperature range. The B(1s) and N(1s) edges indicate a dominant hexagonal arrangement for all the cases. As the temperature is increased, there appears some structure in the B(1s) edge below the 192 eV π^* resonance peak. We attribute this trend to the formation of B-C bonds with a B_xC-like structure.

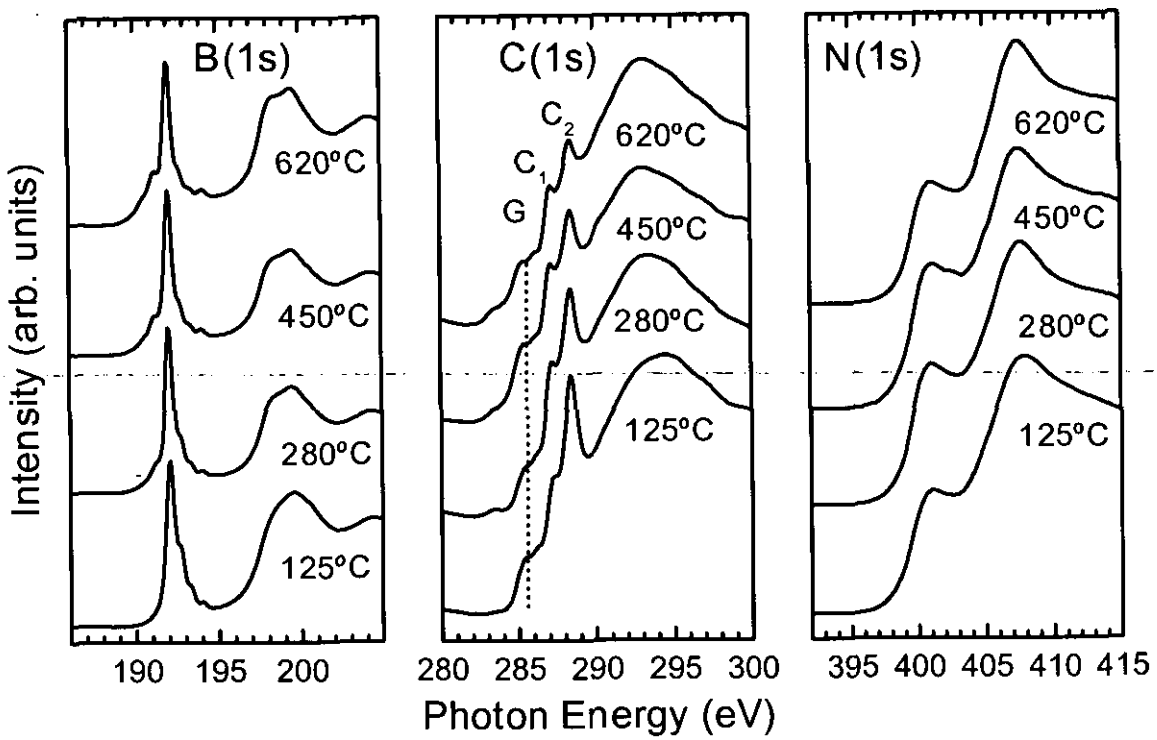

Figure 5.22. XANES spectra of BCN films grown with 100% ion assistance under different substrate temperatures.

The main carbon peaks related to the h-BCN structure, C_1 and C_2, are marked in the figure. The intensity of peak C_2 decreases as the temperature is increased. Apart from these peaks, the C(1s) reveals a fine structure with more features, clearly observed in the sample grown at 625°C, which suggests different carbon environments in the hexagonal BCN and B_xC networks. The states that appear below 285.4 eV seems related to B_xC formation, in correlation with the observed changes in the B(1s) edge.

The above considerations indicate that two competitive processes rule the carbon incorporation under ion assistance with N_2. At low substrate temperatures, the incorporation of carbon to the h-BCN structure is more favourable. However, as the temperature is increased, the incorporation of carbon can also occur in B_xC arrangements, which reduces the carbon content in h-BCN sites as revealed by the decrease of the C_1 intensity.

5.6.2. Influence of the annealing temperature.

a) Hexagonal ternary phases:

In order to study the stability of the h-BCN phases a film with h-BCN structure and composition $B_{44}C_9N_{47}$, was annealed in vacuum up to temperatures of 1000°C. The sample was grown with a substrate temperature of 125°C, ion energy of 960 eV and ion flux of 1.06 mA/cm^2. The corresponding XANES spectra for three annealing temperatures, together with reference samples, are shown in Figure 5.23.

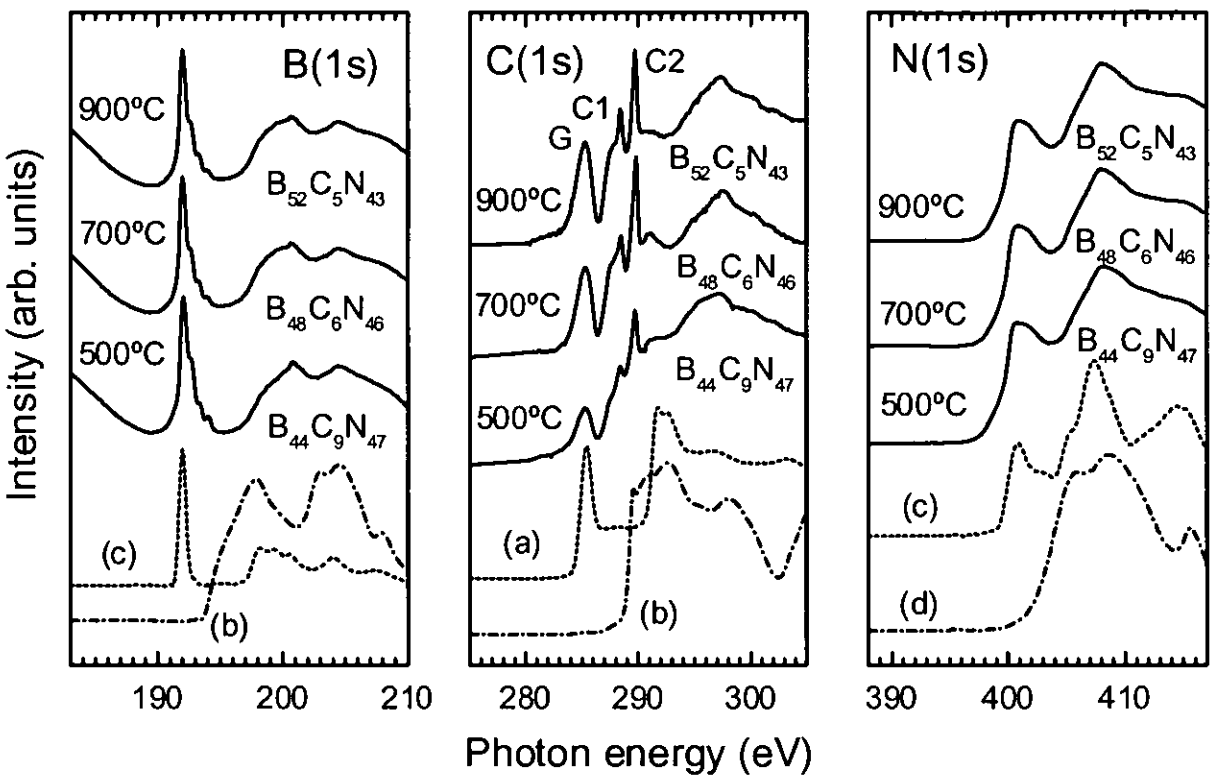

Figure 5.23. Annealing study of the h-BCN phase at different temperatures and reference spectra: (a) graphite, (b) diamond, (c) h-BN and (d) c-BN.

As the annealing temperature is increased, there is a progressive reduction of the C and N content probably due to the formation of volatile C-N compounds. The shape of the B(1s) and N(1s) edges does not change significantly for the temperature range, indicating that the h-BN-like structure is very stable. However, the π^* peaks in the B(1s) edge above 192 eV, related to defects in the h-BN-like network [55], decrease as a result of ordering induced by the annealing process.

For temperatures above 500°C, the intensity of the graphitic peak at 285.4 eV and also of the C_1 and C_2 peaks, typical of h-BCN, increases. The intense increase of both features, the π peaks of graphite and h-BCN, can not be attributed to carbon segregation between both phases since both signals can not

increase at the same time. Therefore, the increase in the π^* features should be the result of an ordering process induced by the annealing of the previously segregated regions. Also, we can conclude that the h-BCN structure is stable in vacuum up to temperatures of 1000°C.

b) Cubic ternary phases.

Annealing processes analogous to those for the hexagonal phases were performed in films with high cubic content. Figure 5.24 displays the XANES B(1s), C(1s) and N(1s) edges for a BCN film with a cubic content of ~70%. The composition of the film is $B_{49}C_{10}N_{41}$ and the deposition conditions were a gas mixture of Ar/N_2=1, substrate temperature of 400°C, ion energy of 600 eV and ion flux of 1.1 mA/cm^2.

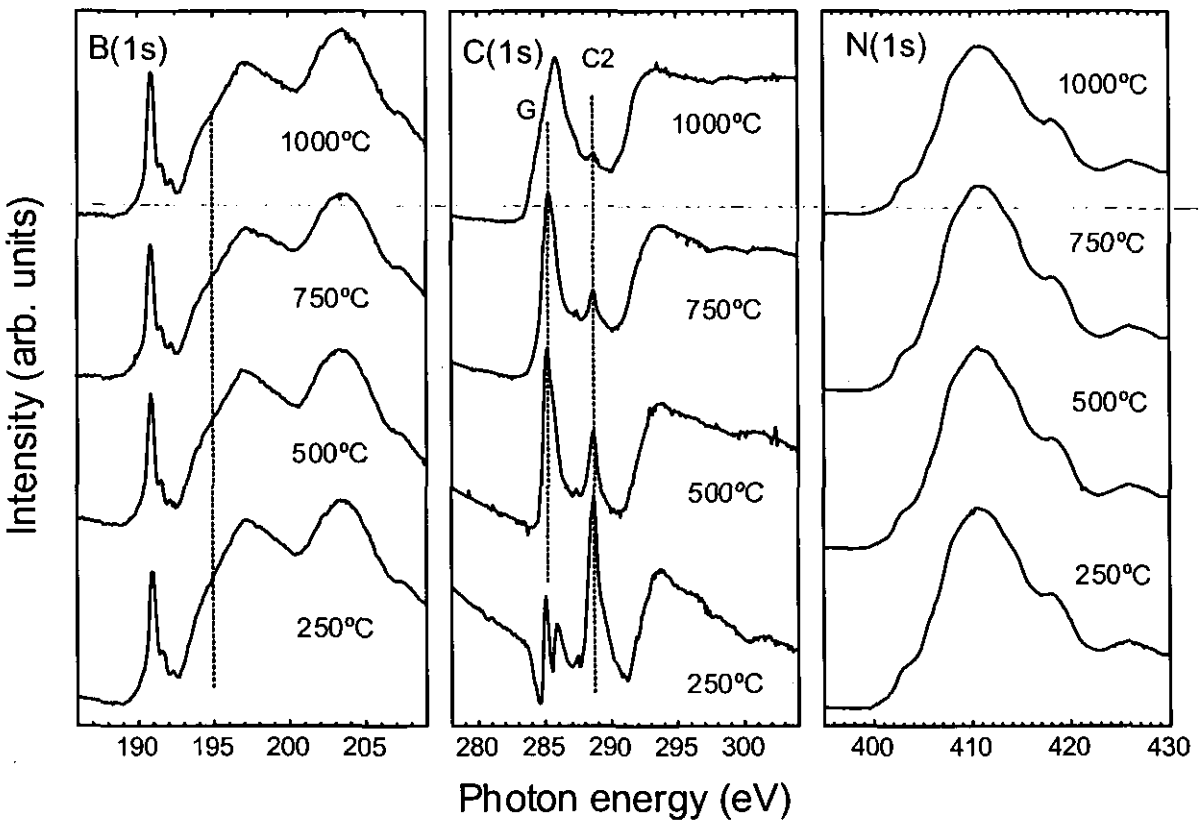

Figure 5.24. XANES annealing study of the bonding structure of a BCN film with a high cubic content. The high cubic content is kept for temperatures up to 1000°C indicating very good thermal stability of this phase. However, some carbon segregation is also induced.

The shape of the B(1s) and C(1s) edges indicate that the high cubic content is kept for temperatures up to 1000°C. Therefore, the bonding structure is very stable as in the case of c-BN. Although the cubic content is maintained, there is a slight increase of the B(1s) resonance π^* peaks at 192 eV. This trend can not be attributed to the formation of h-BCN since the carbon signal corresponding to the h-BCN structure at ~288.5 eV decreases with the annealing temperature. Therefore, it should be

related with some ordering of the h-BCN regions. Finally, carbon segregation is induced as the temperature is increased, as derived in the C(1s) edge from the growth of the graphite peak at 285.4 eV.

5.7. MECHANICAL PROPERTIES

The hardness of B_4C is around 30-40 GPa and, hence, it is the third hardest material known. We have found that the films grown under evaporation of B_4C present also a hardness value around 30 GPa. This result indicates that the bonding structure of B_4C is maintained in the evaporation process. This is in agreement with the presence of icosahedrons detected with Raman and IRS in the evaporated film.

In the case of 100% N_2 assistance we have seen that the nitrogen intake induces the formation of a hexagonal BCN network. Figure 5.25 shows the hardness of the resulting films as a function of the nitrogen content. We can see that the hexagonal structure is softer than the B_4C. Despite this result, the hardness values obtained around 22-25 GPa are hard as compared with other hexagonal structures like graphite and h-BN, with hardness around ~1 GPa. In hexagonal structures, the hardness depends on the orientation of the basal planes due to the anisotropy of the bonding. The high hardness in our case is related to the orientation of the basal planes perpendicular to the film substrate.

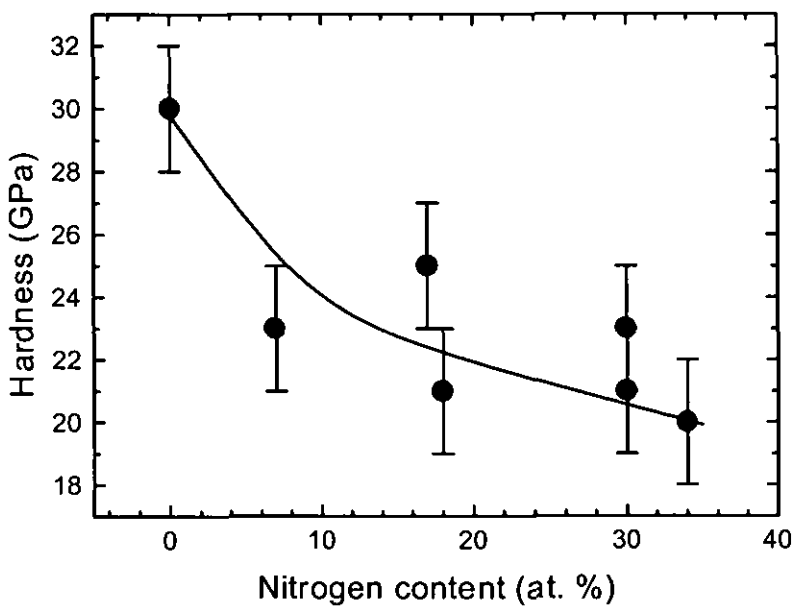

Figure 5.25. Hardness of BCN samples grown under ion assistance with 100% N_2 as a function of nitrogen content. The nitrogen intake induces the formation of hexagonal structures and decreases the hardness of the films.

The hardness for the BCN films as a function of the cubic content is displayed in Figure 5.26. There is a slight increase in the hardness with the cubic content. However, the values obtained are not as high as expected for cubic phases, i.e. in the range of 30-40 GPa. The data obtained can be explained if

we take into account the thickness of the c-BCN layer. As we have shown in the previous chapter, the c-BCN structure grows on top of a buffer h-BCN layer. The c-BCN layer was found to be ~25 nm thick and, therefore, the measure hardness is not reliable since the value is greatly influenced by the hardness of the thicker h-BCN layer (~50 nm). This assumption is supported by the similar hardness values found for ~100% c-BCN (~22 GPa) and 100% h-BCN films (~20 GPa). We have tried to grow thicker films in order to avoid this drawback, but it was difficult to control the evaporation process over the long deposition times required (~ 60 min) to achieve thickness of ~0.5 μm.

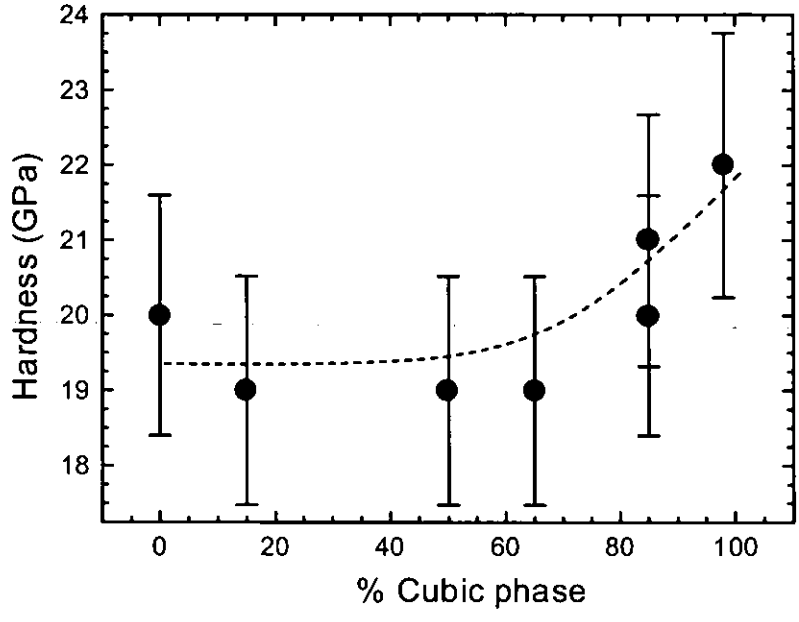

Figure 5.26. Hardness of c-BCN/h-BCN films as a function of the cubic content.

5.8. CONCLUSIONS.

Different BCN compositions and bonding structures have been obtained depending on the IBAD deposition parameters. In the process, the incorporation of nitrogen is competitive with the deposition rate since nitrogen also induces the formation of C-N volatile compounds.

As nitrogen is incorporated to the film structure (< 20 at. %) the icosahedral units of the B_4C structure are distorted to accommodate a hexagonal BN-like structure. The hexagonal structure is dominant for nitrogen contents over 20 at. %. In the hexagonal network carbon is placed in substitutional sites and appears in the XANES spectrum as π^* resonances shifted in energy compared to graphite. As a result, a ternary h-BCN compound is obtained. The h-BCN phase shows a carbon solubility limit of ~10 at. %. Above this value, carbon is segregated in graphitic regions.

The basal planes of the h-BCN structure are oriented perpendicular to the substrate. This preferential orientation is observed in the π features of the XANES B(1s), N(1s) and C(1s) edges. In addition, this anisotropy proves the π character of the carbon bonding in the BCN network.

The assistance with a mixture of N_2 + Ar ions during the evaporation of B_4C lead to the formation of a mixture of hexagonal and cubic ternary structures, depending on growth parameters. The cubic/hexagonal percentage is temperature driven and, for a given temperature, depends on the momentum transfer during deposition. This deposition mechanism implies a narrow window of the deposition parameters (temperature, $Ar+N_2$ gas mixture, ion energy and ion current density) for promotion of tetrahedral bonding. The XANES analysis indicates that carbon is incorporated with tetrahedral bonding in the c-BCN matrix. However, the carbon content is limited to ~5 at. % in the c-BCN phase. This phase grows on top of a 50 nm h-BCN layer with a preferential orientation of the basal planes perpendicular to the surface. The hexagonal structure accommodates between 10-15 at. % of C atoms. Therefore, the C solubility limit in c-BCN seems ~5% while in h-BCN is in the range 10-15%.

The addition of methane to the gas mixture increases the carbon content beyond the values obtained for N_2 and N_2/Ar ion assistance. In the case of h-BCN, the incorporation of carbon in the hexagonal network is effective although changes in the stability of the carbon states are observed. In the case of c-BCN, the additional intake of carbon atoms through CH_4 bombardment induces a transformation from c-BCN to h-BCN and segregation of graphitic regions.

The h-BCN structure is promoted for substrate temperatures below 300°C during deposition. For temperature above 300°C, carbon incorporation in the BCN film competes between the formation of B_xC and h-BCN phases. Once the h-BCN and c-BCN structures are formed, they are stable up to 1000°C.

REFERENCES

1. M. Chhowalla, Y. Yin, G.A.J. Amaratunga, D.R. McKenzie, T. Frauenheim, Appl. Phys. Lett. 69 (16) (1996) 2344.
2. D.F. Franceschini, F.L. Freire Jr., C.A. Achete, G. Mariotto, Diam. Rel. Mat 5 (1996) 471.
3. C.W. Ong, X.A. Zhao, K.F. Chan, Y.M. Ng, P.W. Chan, C.L. Choy, R.W.M. Kwok, Thin Solid Films 307 (1-2) (1997) 152.
4. A.Y. Liu, R.M. Wentzcovitch, M.L. Cohen, Phys. Rev. B 39 (3) (1989) 1760.
5. E. Knittle, R.B. Kaner, R. Jeanloz, M.L. Cohen, Phys. Rev. B 51 (18) (1995) 12149.
6. W.R.L. Lambrecht, B. Segall, Phys. Rev. B 47 (15) (1993) 9289.
7. Y. Tateyama, T. Ogitsu, K. Kusakabe, S. Tsuneyuki, Phys. Rev. B 55 (16) (1997) R10161.
8. S. Ulrich, H. Ehrhardt, T. Theel, J. Schwan, S. Westermeyr, M. Scheib, P. Becker, H. Oechsner, G. Dollinger, A. Bergmaier, Diam. Rel. Mat. 7 (1998) 839.

9. M. Kawaguchi, Adv. Mat.9 (8) (1997) 615.
10. A.R. Badzian, Mat. Res. Bull. 16 (1981) 1385.
11. T. Sasaki, M. Akaishi, S. Yamaoka, Y. Fujiki, T. Oikawa, Chem. Mater. 5 (1993) 695.
12. S. Nakano, M. Akaishi, T. Sasaki, S. Yamaoka, Chem. Mater. 6 (1994) 2246.
13. K. Yamada, J. Am. Ceram. Soc. 81 (7) (1998) 1941.
14. T. Komatsu, Y. Kakudate, S. Fujiware, J. Chem. Soc. Faraday Trans. 92 (24) (1996) 5067.
15. B. Yao, L. Liu, W.H.J. Su, Appl. Phys. 86 (5) (1999) 2464.
16. M.O. Watanabe, S. Itoh, K. Mizushima, T. Sasaki, Appl. Phys. Lett. 68 (21) (1996) 2962.
17. M. Kawaguchi, T. Kawashima, T. Nakajima, Chem. Mater. 8 (1996) 1197.
18. R.B. Kaner, J. Kouvetakis, C.E. Warble, M.L. Sattler, N. Bartlett, Mat. Res. Bull. 22 (1987) 399.
19. J. Yu, E.G. Wang, G. Xu, J. Mater. Res. 14 (3) (1999) 1137.
20. T.M.J. Besmann, Am. Ceram. Soc. 73 (8) (1990) 2498.
21. E.H.A. Dekempeneer, J. Meneve, S. Kuypers, J. Smeets, Thin Solid Films 281-283 (1996) 331.
22. K. Montasser, S. Hattori, S. Morita, Thin Solid Films 117 (1984) 311.
23. A. Weber, U. Bringmann, R. Nikulski, C.P. Klages, Diam. Rel. Mat. 2 (1993) 201.
24. A. Perrone, A.P. Caricato, A. Luches, M. Dinescu, C. Ghica, V. Sandu, A. Andrei, Appl. Surf. Sci. 133 (1998) 239
25. M. Dinescu, A. Perrone, A.P. Caricato, L. Mirenghi, C. Gerardi, C. Ghica, L. Frunza, Appl. Surf. Sci. 127-129 (1998) 692.
26. C. Popov, B. Ivanov, K. Masselli, V. Shanov, Laser Physics 8 (1) (1998) 280.
27. X.A. Zhao, C.W. Ong, Y.M. Ng, K.F. Chan, Y.C. Tsang, C.L. Choy, P.W. Chan, R.W.M. Kwok, J. Mat. Sci. Lett. 16 (1997) 1910.
28. Y. Kusano, J.E. Evetts, I.M. Hutchings, Thin Solid Films 343-344 (1999) 250.
29. Z. Ren, Y. Du, Z. Ying, F. Li, J. Lin, Y. Ren, X. Zong, Mat. Chem. and Phys. 50 (1997) 98.
30. A. Lousa, J. Esteve, S. Muhl, E. Martínez, Diam. Rel. Mat. 9 (3-6) (2000) 502.
31. I. Montero, L. Galán, J. Mat. Res.12 (6) (1997) 1563.
32. R. Brydson, R.; Sauer, H.; Engel, W. Transmission Electron Energy Loss Spectrometry in Material Science, The Minerals, Metals & Materials Society: Warrendale, PA, 1992.
33. Ph. Redlich, J. Loeffler, P.M. Ajayan, J. Bill, F. Aldinger, M. Rühle, Chem. Phys. Lett. 260 (1996) 465.
34. M. Wibbelt, H. Kohl, Ph. Kohler-Redlich, Phys. Rev. B 59 (18) (1999) 11739.
35. K. Suenaga, C. Colleix, N. Demoncy, A. Loiseau, H. Pascard, F. Willaime, Science 278 (1997) 653.
36. R. Brydson, A.V.K. Westwood, X. Jiang, S.J. Rowen, S. Collins, S. Lu, B. Rand, K. Wade, R. Coult, Carbon 36 (7-8) (1998) 1139.

37. J. Kouvetakis, T. Sasaki, C. Shen, R. Hagiwara, M. Lerner, K.M. Krishnan, N. Bartlett, Synthetic Metals 34 (1989) 1.

38. J. Bill, M. Frieβ, R. Riedel, Eur. J. Solid State Inorg. Chem. 29 (1992) 195.

39. R. Gago, I. Jiménez, J.M. Albella, Thin Solid Films (2000, in press)

40. P. Hammer, W. Gissler, Diam. Rel. Mat. 5 (1996) 1152.

41. M.P. Johansson, L. Hultman, S. Daaud, K. Bewilogua, H. Lüthje, A. Schütze, S. Kouptsidis, G.S.A.M. Theunissen, Thin Solid Films 287 (1996) 193.

42. D.J. Kester, K.S. Ailey, R.F. Davis, K.L. More, J. Mat. Res. 8 (6) (1993) 1213.

43. R. Geik, C.H. Perry, Phys. Rev. 146 (1966) 543.

44. S.P.S. Arya, A. D'amico, Thin Solid Films 157 (1988) 267.

45. P.J. Gielisse, S.S. Mitra, J.N. Plendl, R.D. Griffis, L.C. Mansur, R. Marshall, E.A. Pascoe, Phys. Rev. 155 (1967) 1039.

46. U. Kuhlmann, H. Werheit, K.A. Schwetz, J. of Alloys and Compounds 189 (1992) 249.

47. R. Lazzari, N. Vast, J.M. Besson, S. Baroni, A. Dal Corso, Phys. Rev. Lett. 83 (16) (1999) 3230.

48. K. Shirai, S. Emura, S. Gonda, Y. Kumashiro, J. Appl. Phys. 78 (5) (1995) 3392.

49. M. Friedrich, Th. Welzel, R. Rochotzki, H. Kupfer, D.R.T. Zahn, Diam. Rel. Mat. 6 (1997) 33.

50. D.R. Tallant, T.L. Aselage, A.N. Campbell, D. Emin, Phys. Rev. B 40 (1989) 5649.

51. T.L. Aselage, D.R. Tallant, D. Emin, Phys. Rev. B 56 (6) (1997) 3122.

52. R.O. Dillon, J.A. Woollam, V. Katkanat, Phys. Rev. B 29 (6) (1984) 3482.

53. I. Jiménez, D.G.J. Sutherland, T. Van Buuren, J.A. Carlisle, L.J. Terminello, F.J. Himpsel, Phys. Rev. B, 57 (20) (1998) 13167.

54. A.S. Vinogradov, S.V. Nekipelov, A.A. Pavlychev, Sov. Phys. Solid State 33 (3) (1991) 508.

55. I. Jiménez, A.F. Jankowski, L.J. Terminello, D.G.J. Sutherland, J.A. Carlisle, G.L. Doll, W.M. Tong, D.K. Shuh, F.J. Himpsel, Phys. Rev. B 55 (18) (1997) 12025.

56. I. Jiménez, L.J. Terminello, F.J. Himpsel, M. Grush, T.A. Callcott, J. Elect. Spect. and Rel. Phenom. 101-103 (1999) 611.

57. S. Kouptsidis, H. Lüthje, K. Bewilogua, A. Schütze, P. Zhang, Diam. Rel. Mat. 7 (1998) 26.

58. P.B. Mirkarimi, D.L. Medlin, K.F. McCarty, D.C. Dibble, W.M. Clift, J.A. Knapp, J.C. Barbour, J. Appl. Phys. 82 (4) (1997) 1617.

59. Z. Ren, Y. Du, Z. Ying, F. Li, J. Lin, Y. Ren, X. Zong, Mat. Chem. and Phys. 50 (1997) 98.

60. R.A. Rosenberg, P.J. Love, V. Rehn, Phys. Rev. B 33 (1986) 4034.

61. D.J. Kester, K.S. Ailey, R.F. Davis, Diam. Rel. Mat. 3 (1994) 332.

62. I. Jiménez, M.M. García, J.M. Albella, L.J. Terminello, Appl. Phys. Lett. 73 (20) (1998) 2911.

63. D.J. Kester, R. Messier, J. Appl. Phys. 72 (2) (1992) 504.

64. P.B. Mirkarimi, K.F. McCarty, D.L. Medlin, W.G. Wolfer, T.A. Friedmann, E.J. Klaus, J. Mat. Res. 9 (1994) 2925

65. D.R. McKenzie, W.D. McFall, W.G. Sainty, C.A. Davis, R.E. Collins, Diam. Rel. Mat. 2 (1993) 970.

66. H. Windischmann, J. Appl. Phys. 62(5) (1987) 1800.

67. T.A. Friedmann, P.B. Mirkarimi, D.L. Medlin, K.F. McCarty, E.J. Klaus, D.R. Boehme, H.A. Johnsen, M.J. Mills, D.K. Ottesen, J. Appl. Phys. 76 (5) (1994) 3088.

68. R. Trehan, Y. Lifshitz, J.W. Rabalais, J. Vac. Sci. Technol. A 8 (6) (1990) 4026.

Chapter 6:

Applications and future directions of this work

6. APPLICATIONS AND FUTURE DIRECTIONS OF THIS WORK

6.1. HARD COATING APPLICATIONS

We have shown in the previous chapters the possibility of growing films in the BCN system with different film structure and composition by adequate selection of the processing parameters. However, we are mostly interested in the final properties of the coating in order to discern if they are appropriate or not for a certain tribological application. In this section we show a comparative study between all the deposited films based on the results from several mechanical tests.

Figure 6.1 shows the elastic modulus values as a function of the hardness for all the films studied in this work. Both parameters were determined by nanoindentation. The hardest compounds correspond to evaporated boron carbide films, B_xC, with hardness around 30-35 GPa (open squares). The hardness of BCN compounds that contain a large contribution of B_xC to the bonding structure but accommodate a certain amount of nitrogen (< 20 at. %) is also high, with values around 25-30 GPa (crosses). The BCN films with h-BCN structure, which corresponds to large nitrogen contents (~30 at. %), present a hardness around 20-25 GPa. Regarding carbonaceous compounds, evaporated carbon is the softer material found in this work, which presents a hardness of 8 GPa. The hardness of the film can be increased by means of the ion assistance during the evaporation process either by promotion of sp^3 carbon sites (a-C) or nitrogen insertion in the network (a-CN_x). In both cases, the hardness reaches maximum values around 20 GPa.

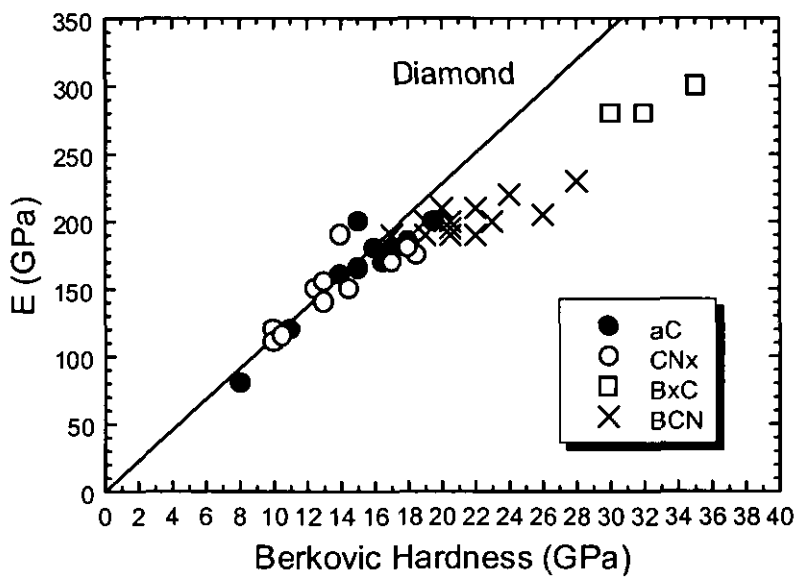

Figure 6.1. Elastic modulus values as a function of hardness for all the different types of films studied in the previous chapters.

As it is well known, the elasticity of a material is closed related to the hardness, since both parameters are directly related to the bonding configuration. Diamond is the hardest material known

(H~100 GPa) and presents a high elastic behaviour (E~1140 GPa). Therefore, the relation between the elastic modulus and hardness for diamond, i.e. E/H~10, can be taken as an ideal reference of the mechanical properties of a material. The solid line in Fig. 6.1 represents this behaviour. Although the B_xC films are the hardest structures grown in this work, they are fragile and present a lower elastic behaviour with respect to diamond. This is also the case of the ternary BCN films. This result can be explained by the presence of segregated regions or heterostructures in the growth process. Finally, amorphous carbon (a-C) and carbon nitride (a-CN_x) films follow the E/H~10 relation indicating a good elastic response.

Hardness and elasticity are not the only mechanical properties of interest. The performance of the coatings can be more affected by the adhesion to the substrate or the coefficient of friction (COF). Figure 6.2 shows the average COF value for selected films within each family of coatings. The COF values were measured by linear reciprocation, applying a force of 0.5 N with a corundum ball over 10000 cycles. The measurements were performed with 50% of relative humidity and 22°C of ambient temperature.

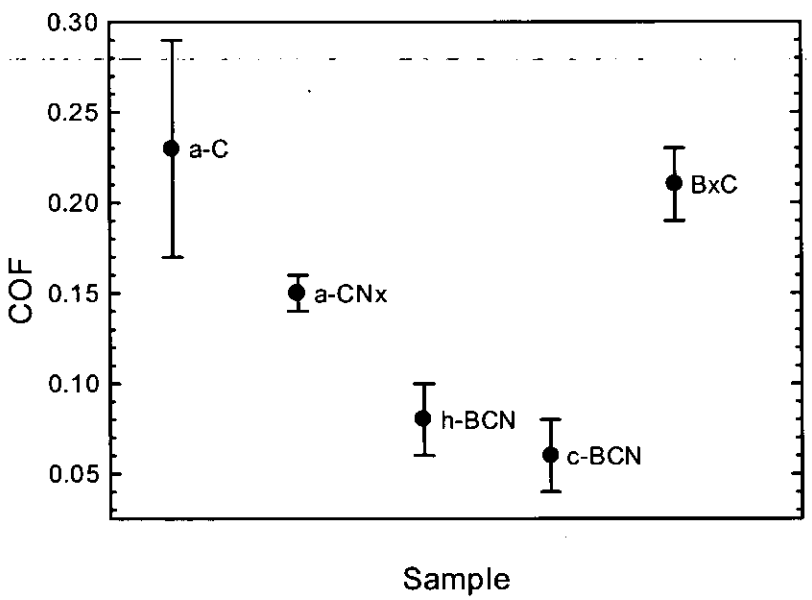

Figure 6.2. Coefficient of friction (COF) for selected films within each family of films studied in this work.

The B_xC coatings exhibit a moderate COF despite of being very hard. On the contrary, ternary films are softer than B_xC compounds but have an extremely good friction coefficient and a good adhesion. The COF for the ternary BCN films suggest potential applications since values below 0.1 are considered appropriate for low friction coatings. Finally, the a-C and a-CN_x films do not present as good friction characteristics as the other films. Amorphous carbon films have been extensively used as lubricant coatings due to the low COF value normally achieved (<0.1). In our case, we found a high COF

probably due to the non-hydrogenated character of our films. In the case of hydrogenated films, the saturation of dangling bonds by hydrogen at the film surface is one of the reasons explaining the significant reduction of the COF value [1]. This mechanism has been proposed to explain the COF of polished diamond surfaces [2]. In addition, a-CN_x present better COF than a-C, which reinforces the actual tendency of replacing the a-C coatings for a-CN_x in the hard disk industry [3].

Finally, the thermal stability of the different compounds has to be considered for practical applications. It is especially important in high temperature cutting tools and devices subjected to high friction. In these systems, the coating should be stable in order to stand the high temperature developed during operation. In this context, the highest thermal stability is found in h-BCN and c-BCN compounds since their structure is based on h-BN and c-BN, respectively. The a-C films present a poor thermal behaviour since the structure turns graphitic over 200°C. Therefore, their application in cutting tools is limited. In addition, a-CN_x has a better applicability since they are thermally stable up to 700°C.

In summary, films with different composition and structure within the B-C-N triangle of compositions present distinct mechanical properties. In this way, given a certain application and requirements, the optimal coating attending its characteristics can be chosen. Regarding other considerations, carbonaceous films like a-C and a-CN_x present lower performances than ternary films but their synthesis requires a lower cost since graphite targets are cheaper than B_4C ones.

6.2 FIELD EMISSION DISPLAYS

6.2.1. Introduction.

Carbonaceous materials have been proposed as optimal field emitters due to the possibility of combining a low surface potential barrier with surface stability and inertness [4]. In particular, it is well known that diamond surfaces can exhibit a negative electron affinity [5], that corresponds to low work function values [6]. Another material with reported negative electron affinity is cubic boron nitride (c-BN) [7], a compound isoelectronic to diamond. Also, hexagonal BCN ternary compounds have been reported as good emitters [8].

The field emission can be estimated by monitoring the total electron emission during the course of the XANES studies. The variations in the total photo-emitted current reflect changes in the average work function of the surface, which is the main parameter affecting the field emission from a given material. Therefore, we can obtain relevant information connected to the field emission characteristics while performing a spectroscopic study of the material. An important point is that the photoelectric emission is independent of the surface morphology, hence providing information intrinsic to the material and not affected by the presence of nanotips at the surface, as occurs in field emission measurements.

In this section, we present a comparative study of the variations of the photoelectric yield as a function of the composition and bonding structure of the films deposited in the BCN system. In this way we search information on the best type of coating for field emission applications.

6.2.2. Experimental set-up: Measurement of the electron emission.

In this section we explain how x-ray absorption spectroscopy in the total electron yield mode (XAS-TEY) can be used to obtain information about the variations of the photoelectric yield and, hence, on the average work function of a material.

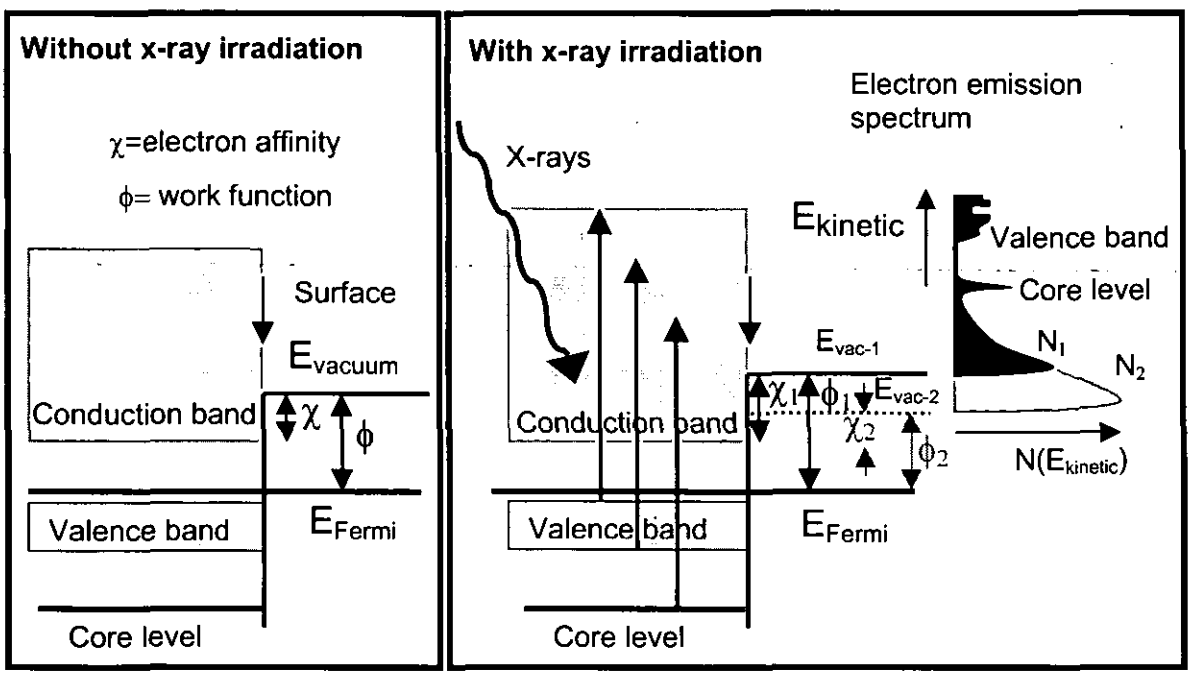

Figure 6.3. Schematics of the electronic structure of a p-type semiconductor in equilibrium (left panel) and under x-ray excitation (right panel), explaining the origin of the electron emission spectrum and how is affected by work function changes.

The left panel of Figure 6.3 sketches the electronic structure of a solid in equilibrium. For generality purposes a p-type semiconductor is considered. The electron affinity and work function are represented in the figure as the energy from the vacuum level to the bottom of the conduction band and to the Fermi level, respectively. In the right panel of Fig. 6.3, it is sketched the situation under monochromatic x-ray irradiation. Excited electrons from occupied states gain the energy of the incoming photons and are promoted to unoccupied states. The electrons that do not suffer inelastic collisions are emitted and appear in the electron emission spectrum as valence band or core level peaks. The electrons suffering energy loses populate the bottom of the conduction band. Only those with an energy higher than the vacuum level are emitted, yielding a tail of secondary electrons with an abrupt threshold related to the

work function, as is displayed in black colour in the figure. If the work function of the surface is reduced, more electrons can escape from the material and the tail of secondary electrons will extend to the new value of the work function, as is represented in grey colour. Therefore, the total electron emission current, i.e. the integral of the electron emission spectrum, is directly related to the work function of the material and can be used to obtain information on the emission behaviour from a set of related samples. The total electron emission current is the quantity monitored in XAS-TEY experiments.

To compare the photoelectric yield from different samples, we integrate the XAS-TEY spectra within fixed integration limits. Since we are considering here relative changes of the photoelectric yield, we take as unity the value for an evaporated amorphous carbon film. When the samples contain more than one type of atom, the integrated absorption intensity for the *1s* core level of a certain atom is normalised to the concentration of that atomic species.

6.2.3. Electron emission of BCN films

a) Amorphous carbon films.

The total electron emission for the amorphous carbon films as a function of the sp^3 content is shown in Figure 6.4 (solid dots). The emission increases with the sp^3 content of the film. The maximum sp^3 content achieved in the our IBAD a-C films is ~25%. For this sp^3 content the emission is doubled respect to an evaporated carbon film (~0% of sp^3 sites).

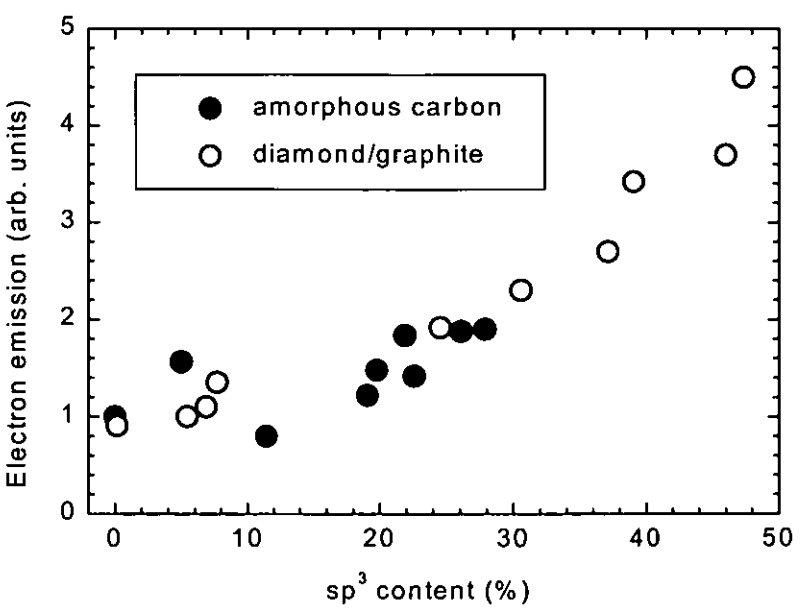

Figure 6.4. Integrated intensity of the XAS-TEY spectra from the amorphous carbon samples (solid dots) and the diamond/graphite composite surface (open dots), both as a function of the percentage of carbon atoms with sp^3 hybridization.

The high emission efficiency related to sp^3 sites has been previously introduced [4]. Therefore, the increase of the emission with the sp^3 content suggests that sp^3 sites in the amorphous carbon network can behave as local emitters, similar to what is found for segregated-diamond nuclei [9]. The open dots in Fig. 6.4 correspond to that reported in ref. 9 for diamond/graphite composite surfaces with different diamond coverage percentage. The enhancement of the emission for the 25% sp^3 content agrees with that found for a 25% diamond coverage. The enhanced emission from sp^3 sites, in connection with local variations of the surface work function, is a hot research topic in the area of electron spectro-microscopy [10,11].

b) Amorphous carbon nitride.

The integrated intensity from the C(1s) spectra for the a-CN_x films is shown in Figure 6.5. The signal has been normalised to the carbon content in the film to correct the dilution of carbon atoms in the binary compound. Similar results are obtained by plotting the integrated N(1s) intensity normalised to the nitrogen content.

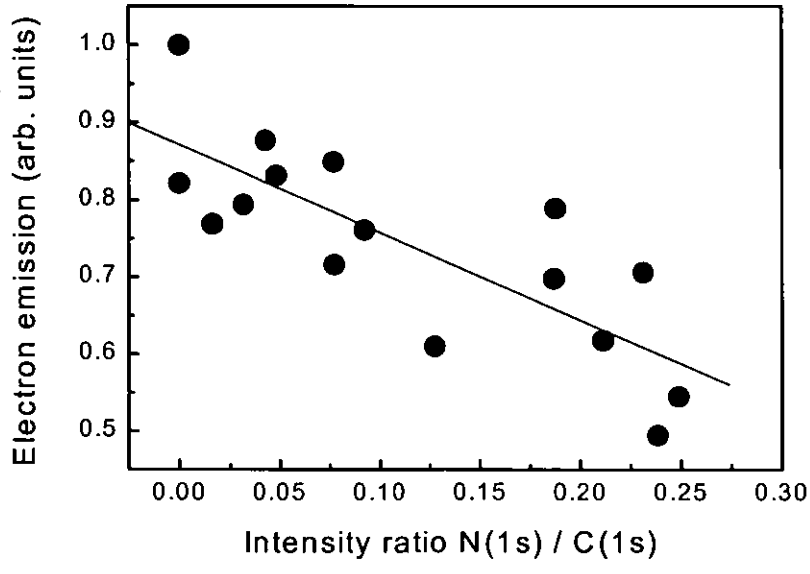

Figure 6.5. Integrated intensity of the C(1s) spectra for the a-CN_x samples, normalized to the carbon content in the film, as a function of the nitrogen content.

The photoelectric yield decreases with the nitrogen content in graphitic carbon nitride. Therefore, amorphous graphitic carbon nitride is not of interest as a field emission coating. Our results contrast with previous reports of enhancement of field emission with nitrogen contents of a few percent [12,13]. However, the film structure reported in these works differs from that presented in this work since corresponds to a tetrahedral carbon network with substitutional nitrogen. The field emission behaviour of C_3N_4 remains unknown.

c) Hexagonal/B_xC-like ternary BCN compounds.

Figure 6.6 shows the dependence of the composition of the BCN as a function of the photoelectric yield. These films present a different structure regarding the film composition. In this way, as nitrogen is inserted in the B_xC structure, there is a transition towards a hexagonal arrangement, h-BCN, as indicated in the upper x-axis.

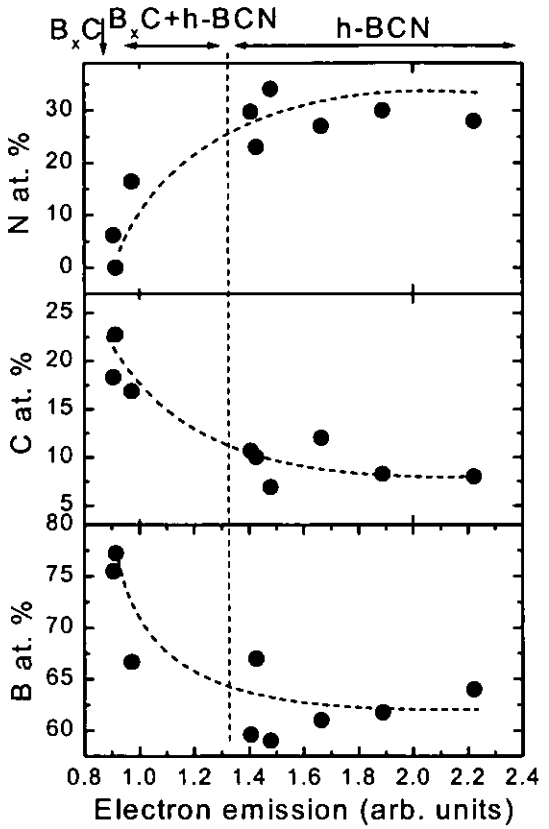

Figure 6.6. Dependence of the electron emission yield with the composition of ternary h-BCN samples grown with N_2^+ bombardment.

A first result is that the hexagonal structure obtained by the insertion of ~30% nitrogen is a better electron emitter than the B_xC like structure. However, different coatings with a similar composition of about $B_{0.6}C_{0.1}N_{0.3}$ exhibit different photoelectric yields. The explanation seems related to microstructure and grain domain size in the films, according to the following evidence.

Figure 6.7 shows the photoelectric yield data from the same set of BCN films considered above, displayed as a function of the relative intensity of the B(1s) π^* peak. This peak represents h-BN-like environments, and its relative intensity was computed from the ratio between the height of the π^* peak and the σ^* edge in each spectrum. The relationship between the photoelectric yield and the π^* intensity is

clear. Note that the samples with a relative π^* intensity below unity correspond to mixtures of B_xC and h-BN like environments, while those with a relative intensity above unity correspond to hexagonal BCN environments.

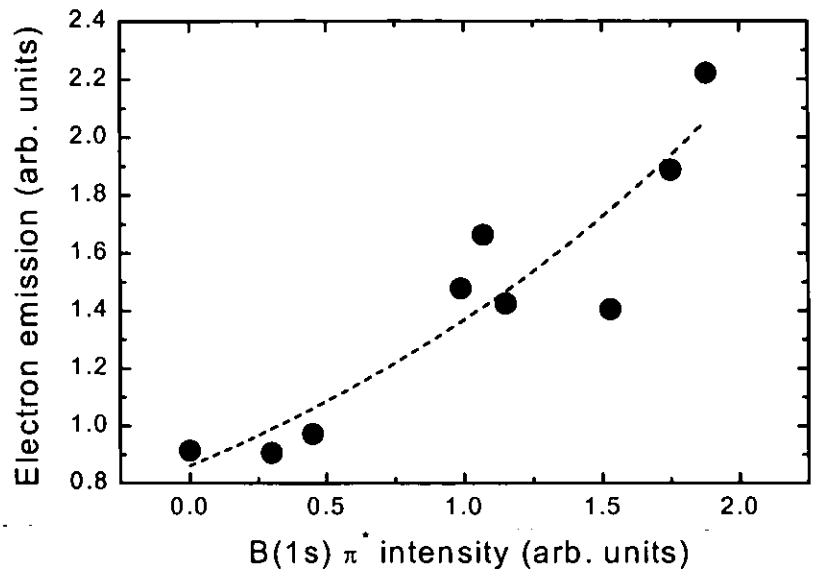

Figure 6.7. Electron emission as a function of the relative B(1s) π^* peak intensity for ternary h-BCN samples.

To understand the different height of the π^* peak in samples with a similar composition, we must recall its excitonic nature, with an exciton binding energy of ~1.5 eV [14] and a certain spatial extent of the perturbation produced by the *1s* hole. Calculations for the π^* excitonic resonance of graphite, which is an isoelectronic compound of h-BN, indicate that the resonance peak is only observed for cluster radius above five bond lengths [15]. Accordingly, the intensity of the π^* peak seems related to the hexagonal domain size or the size of the fragments of basal planes. For crystalline h-BN, the height of the π^* exciton is 3-5 times larger than the height of the σ^* edge, while for amorphous or nanocrystalline h-BN the relative π^* intensity decreases. According to the results of Fig. 6.7, the average work function of the h-BCN coating decreases for increasing the h-BCN domain size.

d) Hexagonal/cubic BCN ternary compounds.

Figure 6.8 displays the integrated intensity for a set of samples with a similar composition, approximately $B_{0.55}C_{0.1}N_{0.35}$, but different sp^3 contents. The photoelectric yield clearly increases with the sp^3 content, as was found for carbon materials, though the emission enhancement is not as large as in the case of diamond. However, the possibility of obtaining a better emission enhancement for a different film composition cannot be ruled out.

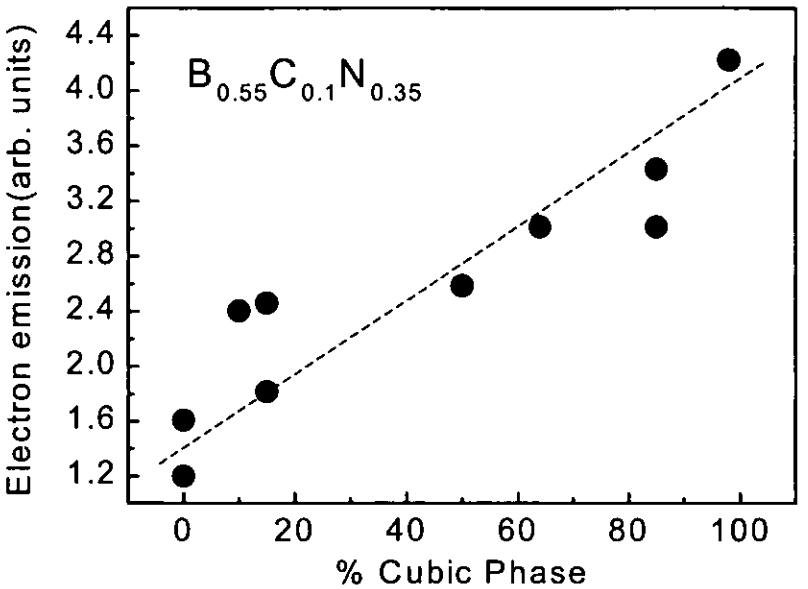

Figure 6.8. Electron emission from ternary BCN samples with similar composition and different sp^3 contents.

6.3. MULTILAYERS

6.3.1. Introduction.

Up to now, we have discussed the synthesis of materials in thin film form searching hardness values above 40 GPa (superhard materials). In these materials, the hardness is intrinsically related with their bonding structure. However, as also discussed, the hardness is mainly determined by the microstructure, which can efficiently hinder the multiplication and movement of dislocations and the growth of micro-cracks [16]. Therefore, the design of nano-structured materials with appropriate microstructure to achieve hardness above 40 GPa opens the path to a new field in the search of superhard materials [17]. In this case, the hardness is extrinsically conferred to the material.

Koehler originally suggested the possibility of achieving high hardness values in the superhardness range (H > 40GPa) in heterostructures or superlattices [18]. These new structures are composed of a periodic arrangement of thin layers of two different materials (multilayer). The remarkable property of these nanostructured materials is the fact that the hardness significantly exceeds that given by the rule of mixture for two compounds, A and B,

$$H(A_xB_y) = \frac{xH(A) + yH(B)}{x + y} \tag{6.1}$$

where x and y denotes the relative concentration of each compound.

The concept of heterostructures was originally designed for multilayers of different metals, M(1) and M(2) [18]. The success in the design requires elastic constants $E_{M(2)}<E_{M(1)}$ as different as possible, similar thermal expansion and strong bonds. This configuration permits that, under applied stress, the dislocations are formed in the softer layer, M(1), and move toward the interface where are hindered as a result of the repulsion force induced by elastic strain in M(2). This process is only effective for sharp or abrupt interfaces. Finally, the thickness of the layers should be small in order to preclude the formation of dislocation sources within the layers.

Koehler's prediction was further developed and experimentally confirmed in Al/Cu and Al/Ag heterostructures [19,20]. This work was then followed by the production of multilayers from materials with hardness ≥ 20 GPa such as transition metal nitrides (TiN, VN, NbN, WN, HfN, etc). In this way, hardness above 50 GPa have been obtained [21,22].

6.3.2. Multilayers of BCN materials.

The above discussion suggests that the use of alternative layers of two materials can increase the hardness value by a factor of 2-4 respect to the value of the hardest material [17]. We have seen that with our IBAD system we can synthesise different BCN structures varying the deposition conditions. Therefore, if we could change the ion assisting parameters sequentially during normal operation in a fast way, we would obtain multilayers of different materials with an abrupt interface. This idea opens up new perspectives for future aims to carry on with this work.

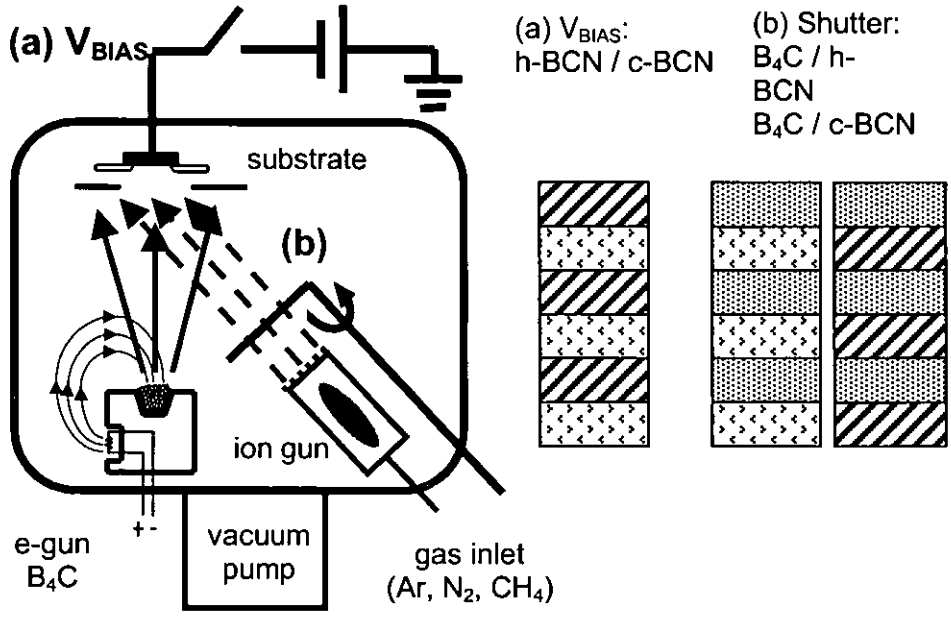

Figure 6.9. Possible modifications of the actual deposition chamber in order to produce multilayers of BCN compounds.

Based on the above premises, we have designed several changes in the deposition chamber that would permit the production of multilayers. We consider three possible candidates, B_xC/h-BCN, c-BCN/B_xC and c-BCN/h-BCN. In all the cases, the last phase represent the softer layer. The suggested changes are illustrated in Figure 6.9.

The structure displayed as (a) can be obtained by the addition of an external polarisation of the substrate during the deposition. We have seen that the ion energy plays a crucial role in the production of hexagonal and cubic BCN phases. Therefore, switching between two energy values where hexagonal and cubic phases are obtained allows a fast and easy way of growing the multilayers.

The change labelled (b) takes into account the production of ternary phases as a result of the ion assistance. Without ion assistance, B_xC films are obtained with hardness around 30 GPa. Therefore, using a shutter for the ion gun permit the addition or exclusion of the assistance process. This leads to the formation of heterostructures with B_xC and ternary BCN materials. In the case of h-BCN, the hardness is around 22 GPa and, hence, this should be the softer phase in the multilayer. On the contrary, for c-BCN where hardness around 40-60 GPa is expected, the B_xC should be the softer phase.

6.4. CONCLUSIONS

The IBAD technique permits the selection among a wide range of compositions within the BCN triangle and bonding structures. This feasibility stems from the flexible election of the evaporated material and assisting ions. The mechanical properties of the BCN compounds cover a wide range and, therefore, the choice of a proper material can be performed aiming at a specific application. In this sense, remarkable properties as hardness values up to 35 GPa, friction coefficients below 0.06 and thermal stability up to 1000°C have been obtained.

In section 6.2 we have discussed the information that can be obtained from monitoring the total electron emission upon x-ray irradiation regarding potential applications as field emission coatings. The variations in the total emission yield are related to changes in the average work function of the material, and provide interesting information on how sample preparation parameters affect the electron emission characteristics. The method has been applied to several materials within the BCN triangle of compositions as they are expected to be optimal field emitters. Our results indicate that the main parameter affecting the photoelectric yield is the proportion of atoms with sp^3 hybridization, either for carbonaceous and BN-like materials.

Finally, our IBAD system also offers the possibility of exploring new alternatives like multilayers structures for the search of superhard materials. In this way, several modifications of the actual set-up of our deposition system would permit the production of multilayers. Among all the possible configurations, it would be feasible to grow B_xC/h-BCN, c-BCN/B_xC and c-BCN/h-BCN multilayers.

REFERENCES

1. S.V. Pepper, J. Vac. Sci. Technol. 20 (3) (1982) 643.
2. M.N. Gardos, B.L. Soriano, J. Mat. Res. 5 (11) (1990) 2599.
3. A. Khurshudow, K. Kato, S. Daisuke, J. Vac. Sci. Technol. A 14 (5) (1996) 2935.
4. A. Hart, B. S. Satyanarayana, W. I. Milne, and J. Robertson, Appl. Phys. Lett. 74 (1999) 1594, and references therein.
5. F. J. Himpsel, J. A. Knapp, J. A. Van Vechten, and D. A. Eastman, Phys. Rev. B 20 (1979) 624.
6. Z. Zhang, M. Wensell, and J. Bernholc, Phys. Rev B 51 (1995) 5291.
7. M. J. Powers, M. C. Benjamin, L. M. Porter, R. J. Nemanich, R. F. Davis, J. J. Cuomo, G. L. Doll, and S. J. Harris, Appl. Phys. Lett. 67 (1995) 3912.
8. J. Yu and E. G. Wang, Appl. Phys. Lett. 74 (1999) 2948.
9. I. Jiménez, R. Gago, M.M. García, J.M. Albella, J. Vac. Sci. Technol. (submitted for publication).
10. S. Anders, J. Díaz, J. W. Ager III; R. Y. Lo, and D. B. Bogy, Appl. Phys. Lett. 71 (1997) 551.
11. J. Díaz, S. Anders, A. Cossy-Favre, M. Samant and J. Stöhr, J. Vac. Sci. Technol. A 17 (1999) 2737.
12. G.A.J. Amaratunga, S.R.P. Silva, Appl. Phys. Lett. 68 (1996) 2529.
13. J.H. Moon, S.J. Chung, E.J. Han, J. Jang, J.H. Jung, B.K. Ju, M.H. Oh, J. Vac. Sci. Technol. B 17 (1999) 241.
14. J. A. Carlisle, E. L. Shirley, L. J. Terminello, J. J. Jia, T. Callcott, D. L. Ederer, R. C. C. Perera, and F. J. Himpsel, Phys. Rev. B 59 (1999) 7433.
15. R. Ahuja, P. A. Brühwiler, J. M. Wills, B. Johansson, N. Martensson, and O. Eriksson, Phys. Rev. B. 54 (1996) 14396.
16. C. Kittel, *Introduction to Solid* State Physics, Wiley, New York (1971).
17. S. Veprek, J. Vac. Sci. Technol. A 17 (5) (1999) 2401.
18. J.S. Koehler, Phys. Rev. B 2 (1970) 547.
19. S.L. Lehoczky, J. Appl. Phys. 49 (1978) 5479.
20. S.L. Lehoczky, Phys. Rev. Lett. 41 (1978) 1814.
21. U. Helmersson, S. Todorova, S.A. Barnett, J.E. Sundgreen, L.C. Markert, J.E. Greene, J. Appl. Phys. 62 (1987) 481.
22. M. Shinn, L. Hultman, S.A. Barnett, J. Mater. Res. 7 (1992) 901.

Chapter 7:

Conclusions

7. CONCLUSIONS

7.1. Ion assistance during graphite evaporation.

- The IBAD method based on graphite evaporation with concurrent N_2/Ar ion bombardment allows the synthesis of films that are homogeneous laterally and in depth. The films have a negligible amount of oxygen (< 1 at. %) and hydrogen (< 0.5 at. %).
- The assistance with Ar^+ results in the growth of amorphous carbon films (a-C) with a moderate sp^3 content of ~30%. The deposition process is controlled by densification for ion energies per incoming evaporated carbon atom below 500 eV/atom and a dominant sputtering of the growing film for ion energies above 1500 eV/atom.
- The promotion of sp^3 sites in the growth of a-C is explained by the formation of a local region with high density due to the penetration of carbon atoms into subsurface sites (subplantation). This mechanism depends on the incoming particle energy, which is controlled through momentum transfer in the Ar^+-C collisions. The moderate sp^3 content achieved in our films is explained by the random nature of the Ar^+-C collisions, which implies a broad energy distribution and, therefore, only a fraction of the carbon atoms penetrate the subsurface layer within the optimal energy range.
- The use of N_2 reactive ions permits the growth of carbon nitride films (a-CN_x) with a nitrogen content limited to [N]/[C]~0.3. The films present a graphitic structure, with C-N π bonds and a low content of C≡N bonds.
- The structure of graphitic a-CN_x seems to be composed of numerous bonding states for carbon and nitrogen atoms. In this work we have resolved five different states for carbon and four for nitrogen, as derived from the XANES lineshape analysis. The relation between the carbon and nitrogen states remains an open question although some assignments could be established. In addition, the structure of these graphitic carbon nitride films is thermally stable up to 700°C
- The hardening mechanism for graphitic films containing more than 70% carbon atoms with sp^2 hybridization and hardness around 20 GPa seems to be cross-linking of graphitic planes. For carbon nitride films grown with dominant nitrogen assistance the linking sites are nitrogen atoms. For films with a very low nitrogen content grown with dominant Ar ion assistance, the linking sites are carbon sp^3 hybrids. Promotion of both linking sites is competitive and is not obtained simultaneously.

7.2. Ion assistance during boron carbide (B_4C) evaporation.

- Different BCN compositions and bonding structures have been obtained during boron carbide (B_4C) evaporation under concurrent ion assistance from a gas mixture of N_2/Ar/CH_4. XANES analysis

reveals the presence of ternary compounds with either cubic (c-BCN), hexagonal (h-BCN) and B_xC-like structures.

- The formation of cubic phases is governed by the substrate temperature and momentum transfer through ion/atom collisions during deposition. The promotion of the cubic phases is attained in a narrow window of the momentum space, which depends on the ion energy, ion flux and gas mixture. This window of momentum is only reached when Ar ions are used in the assistance process.
- The carbon content in h-BCN is limited to ~10-15 at. % whereas the carbon limit in the c-BCN structure is ~5 at. %.
- The cubic structure (c-BCN) grows on top of an h-BCN buffer layer where the basal planes are orientated perpendicular to the substrate surface.
- The addition of methane (CH_4) to the gas mixture increases the carbon content beyond the values obtained for N_2 and N_2/Ar ion assistance. In the case of h-BCN, the incorporation of carbon in the hexagonal network is effective although changes in the stability of the carbon states are observed. In the case of c-BCN, the additional intake of carbon atoms through CH_4 bombardment induces a transformation from c-BCN to h-BCN and segregation of graphitic regions.
- The h-BCN and c-BCN structures are stable up to 1000°C.

7.3. Applications and future directions of this work.

- The IBAD technique permits the selection among a wide range of compositions within the BCN triangle and bonding structures. The mechanical properties of the BCN compounds cover a wide range and, therefore, the choice of a proper material can be performed aiming at a specific application. In this sense, remarkable properties as hardness values up to 35 GPa, friction coefficients below 0.06 and thermal stability up to 1000°C have been obtained.
- The total electron emission upon x-ray irradiation can be used to characterise the potential applications of our coatings as field emitters. The variations in the total emission yield are related to changes in the average work function of the material, and provide interesting information on how sample preparation parameters affect the electron emission characteristics. Our results indicate that the main parameter affecting the photoelectric yield is the proportion of atoms with sp^3 hybridization, either for carbonaceous and BN-like materials.
- Finally, our IBAD system also offers the possibility of exploring new alternatives like multilayers structures for the search of superhard materials. In this way, several modifications of the actual set-up of our deposition system would permit the production of multilayers. Among all the possible configurations, it would be feasible to grow B_xC/h-BCN, c-BCN/B_xC and c-BCN/h-BCN multilayers.

Appendix:

Resumen y conclusiones

A. RESUMEN.

En esta tesis se recoge el estudio realizado desde 1996 en el departamento de Física e Ingeniería de Superficies del Instituto de Ciencia de Materiales de Madrid (C.S.I.C.). La supervisión del trabajo ha sido realizada por los doctores J.M. Albella e I. Jiménez pertenecientes al ICMM. Por otro lado, la tutoría desde la Universidad Autónoma de Madrid (UAM) ha estado a cargo del doctor A. Climent-Font del Departamento de Física Aplicada de la Facultad de Ciencias.

Durante la última década, nuestro grupo de investigación viene desarrollando el estudio de diversos materiales en forma de lámina delgada. Dentro de los campos abarcados, un trabajo muy extenso ha sido realizado en el estudio de materiales duros. Este tipo de materiales poseen una elevada dureza y se aplican, en forma de recubrimiento o lámina delgada, sobre un sustrato con el objeto de proteger la superficie de las agresiones externas. De esta forma, la fricción, el rayado, desgaste, etc, pueden verse considerablemente reducidos. Este aspecto es de especial importancia en herramientas de corte u otros dispositivos que estén sometidos a una fricción elevada durante su operación.

Los primeros pasos en el campo de recubrimiento duros se realizaron en la producción de capas de diamante y nitruro de boro mediante crecimiento químico a partir de la activación por plasma de una mezcla gaseosa (PACVD). Como es bien sabido, estos dos materiales presentan las durezas más altas. Dentro de los trabajos realizados, cabe destacar el estudio de las etapas de nucleación y crecimiento de muestras de diamante mediante plasma de microondas de un plasma de metano e hidrógeno y el estudio de capas de BN mediante plasma de radiofrecuencia de una mezcla de diborano y nitrógeno.

El problema tecnológico que presenta el crecimiento tanto del diamante como del nitruro de boro cúbico (altas temperaturas, etc.) ha planteado el crecimiento de capas alternativas a estos materiales, con unas condiciones menos severas de crecimiento y propiedades competitivas. Dentro de la posibilidad de obtener materiales con propiedades comparables a las del diamante, los candidatos que más se discuten en la literatura son la fase del nitruro de carbono β-C_3N_4 y los compuestos ternarios BCN con estructura cúbica. La fase β-C_3N_4 ha motivado numerosos estudios pues se le atribuyen unas propiedades incluso superiores al diamante. Los compuestos amorfos también son muy interesantes desde el punto de vista aplicado pues requieren de unas condiciones de crecimiento muy asequibles (temperatura ambiente) y poseen buenas propiedades mecánicas.

La ampliación de las líneas de investigación de nuestro grupo se planteó siguiendo los argumentos anteriores. De esta forma, se realizó el estudio del crecimiento de carbono amorfo hidrogenado o diamond-like carbon (DLC). Este material consiste en una mezcla amorfa de átomos de carbono con enlaces híbridos del tipo grafito (sp^2) y diamante (sp^3), y una cantidad apreciable de hidrógeno (40-60%). En este caso, el carácter diamante, grafítico o polimérico de las películas viene dado por la interconectividad de la red, que depende de la relación sp^2/sp^3 y del contenido de hidrógeno. Este material supone una gran ventaja pues se crece a temperatura ambiente. Sin embargo, la dureza obtenida

es bastante inferior (~15-20 GPa) a la del diamante y se incorpora una gran cantidad de hidrógeno a la película. El hidrógeno juega un papel muy importante pues estabiliza la estructura (reduce las tensiones) aunque baja la interconectividad de la red y, con ello, las propiedades mecánicas. Los resultados más relevantes conseguidos sobre este material se reflejan en la tesina *"Preparación y Caracterización de láminas delgadas de DLC crecidas mediante PACVD a 35 kHz"* presentada por el candidato a doctorando en Abril de 1998.

En el desarrollo de nuevos materiales se debe considerar en gran medida la aplicabilidad industrial de la técnica de crecimiento. Por ello, se precisa el desarrollo de técnicas con un bajo coste económico y se sean factibles para la producción a larga escala. Las técnicas asistidas por plasma suponen un problema en este sentido debido a la dificultad de crear plasma en espacios grandes y a la adición de un gran contenido de hidrógeno a la estructura debido al uso de hidrocarburos como gases precursores. Por estos motivos, se ha abierto un nuevo campo de estudio considerando el crecimiento de películas a partir de técnicas físicas (PVD). De esta forma, se han puesto en marcha sistemas basados en las técnicas de sputtering y de evaporación.

Este trabajo recoge los resultados obtenidos en el estudio de capas de Boro-Carbon-Nitrógeno crecidas mediante evaporación asistida con haces de iones. Este método pertenece al grupo genérico de técnicas denominadas de asistencia con haces de iones (IBAD). La ventaja de utilizar la técnica de evaporación radica en la versatilidad a la hora de crecer diferentes materiales, la alta velocidad de crecimiento de las capas y la posibilidad de depositar sobre grandes superficies. El proceso de asistencia con un bombardeo iónico durante la evaporación permite controlar la energía de llegada de los átomos, pudiendo alcanzar energías por encima del rango térmico (~KT). La asistencia se suele realizar con iones pesados e inertes, como por ejemplo Ar^+, para que la transferencia de momento y energía sea máxima. Sin embargo, el proceso también puede ser realizado con iones reactivos como el nitrógeno o con una mezcla de iones reactivos e inertes. El uso de iones reactivos es importante cuando la estequiometría de las capas juega un papel fundamental en las propiedades del material.

El trabajo realizado engloba una parte de puesta a punto del dispositivo experimental, realización de muestras, posterior caracterización de las muestras crecidas mediante técnicas analíticas y, finalmente, una labor de síntesis de los resultados.

Dentro de las técnicas de caracterización cabe mencionar el uso de métodos exóticos o novedosos como medidas de tiempo de vuelo en procesos de retroceso elástico de iones (TOF-ERDA) para el análisis del perfil de composición y la absorción de rayos-x cerca del borde (XANES) para el estudio de la estructura de enlace. Estas técnicas presentan una accesibilidad limitada pues requieren de grandes instalaciones para su realización. Para el análisis de TOF-ERDA se ha colaborado con la Universidad de Helsinki mientras que las medidas de XANES se han llevado a cabo en el LURE y SSRL. Las propiedades mecánicas de las capas (dureza y módulo elástico) han sido determinadas mediante

nanoindentación. Finalmente, el análisis de las capas está complementado con técnicas más convencionales como IR, Raman, fotoemisión de rayos-x (XPS) y espectroscopia Auger (AES).

Gran parte de los resultados se basan en el análisis mediante XANES. La principal ventaja de esta técnica es que permite estudiar por separado los entornos químicos de los elementos presentes en la muestra y es capaz de diferenciar entre las configuraciones cúbicas (tipo diamante) y hexagonales (tipo grafito). Complementariamente, esta técnica permite realizar un estudio de la composición de la muestra con una profundidad de análisis de ~10 nm.

Dentro del contenido de este trabajo podemos diferenciar tres bloques principales atendiendo al crecimiento de diferentes tipos de materiales:

1. Estudio de películas de **carbono amorfo** (a-C) o DLC mediante la evaporación de grafito asistida con bombardeo de Ar^+. Este trabajo complementa el estudio anterior realizado sobre capas de DLC y permite el estudio de películas sin hidrógeno incorporado en la estructura.
2. Estudio de capas de **nitruro de carbono** (a-CN_x) mediante la evaporación de grafito y la asistencia con una mezcla de iones N_2/Ar. Debido a las condiciones empleadas en la técnica de crecimiento las muestras presentan un carácter amorfo y, por lo tanto, no hemos enfocado nuestro trabajo hacia la síntesis de la fase β-C_3N_4. Por el contrario, hemos abordado el estudio de los diferentes tipos de enlace C-N y su relación con las propiedades mecánicas.
3. Estudio de capas ternarias **Boro-Carbono-Nitrógeno** ($B_xC_yN_z$) mediante la evaporación de carburo de boro (B_4C) y asistencia con iones N_2/Ar/CH_4. El interés principal de estos materiales consiste en la posibilidad de mezclar las fases isoelectrónicas de nitruro de boro y carbono (grafito con h-BN y diamante con c-BN) para dar lugar a un compuesto sólido ternario. De esta forma, nuestro trabajo se ha centrado en la identificación de fases sólidas ternarias BCN y la caracterización de sus propiedades mecánicas.

Los resultados más relevantes que se han obtenido se recogen en el apartado de las conclusiones. Este trabajo se completa con la discusión de las posibles aplicaciones de los recubrimientos obtenidos y las posibles perspectivas de futuro (capítulo 6). Las propiedades de los diferentes materiales se ha comparado con el fin de establecer la mejor opción para diversas aplicaciones. En particular, se considera el uso de las capas crecidas atendiendo a su aplicación como recubrimiento duro y como materiales en dispositivos de emisión de campo (FED). Finalmente, se presenta la posible continuación de este trabajo con la producción de multicapas con los diferentes materiales crecidos.

B. CONCLUSIONES.

B.1. Asistencia con iones durante la evaporación de grafito.

- La técnica IBAD basada en la evaporación de grafito con bombardeo simultáneo con una mezcla de iones N_2/Ar permite la síntesis de capas homogéneas lateralmente y en profundidad. Las capas no contienen hidrógeno (< 0.5 at. %) y la contaminación de oxígeno es despreciable (< 1 at. %).
- La asistencia con iones Ar^+ conlleva al crecimiento de capas de carbono amorfo (a-C) con un contenido moderado (~30%) de átomos de carbono en la configuración sp^3. El proceso de deposición está controlado por la densificación de la película para energías por átomo por debajo de 500 eV/átomo y por la re-emisión (sputtering) dominante de la capa crecida para energías por encima de 1500 eV/átomo.
- La promoción de carbonos tipo sp^3 durante el crecimiento de a-C se explica mediante la creación de una región de alta densidad al penetrar los átomos incidentes por debajo de la capa superficial (modelo de subplantación). Este mecanismo depende de la energía de las partículas incidentes, la cual se controla mediante la transferencia de momento en las colisiones ión/átomo. El moderado contenido de carbono sp^3 alcanzado en nuestras muestras es debido a la naturaleza aleatoria de las colisiones Ar^+-C. En este sentido, tenemos una distribución de energías muy ancha y, por lo tanto, solamente una fracción de los átomos incidentes penetra en el rango óptimo de energía.
- El uso de iones reactivos de N_2 permite el crecimiento de películas amorfas de nitruro de carbono (a-CN_x). El contenido de nitrógeno que puede ser incorporado está limitado a [N]/[C]~0.3. La estructura de las películas es grafítica, con enlaces C-N tipo π y un bajo contenido de enlaces tipo nitrilo (C≡N).
- La estructura grafítica de a-CN_x parece estar compuesta de numerosos entornos de enlace para el nitrógeno y el carbono. En este trabajo hemos resuelto cinco diferentes estados para el carbono y cuatro para el nitrógeno a partir del análisis del espectro XANES. La estructura de las capas de a-CN_x es estable térmicamente hasta 700°C
- El mecanismo que confiere alta dureza (~20 GPa) a capas grafíticas con un contenido de átomos de carbono de tipo sp^2 por encima del 70% parece atribuirse a la interconectividad de los planos grafíticos. En el caso de películas de nitruro de carbono con un contenido alto de nitrógeno, el enlace entre los diferentes planos es realizado por átomos de nitrógeno. Sin embargo, para películas con un bajo contenido de nitrógeno en las películas y asistencia con un alto contenido de iones Ar^+ en la mezcla gaseosa, el enlace entre los planos grafíticos se atribuye a carbono tipo sp^3. La promoción de ambos tipos enlaces puente entre los planos grafíticos no puede obtenerse simultáneamente.

B.2. Asistencia con iones durante la evaporación de carburo de boro (B_4C).

- El proceso de IBAD a partir de la evaporacion de carburo de boro (B_4C) y la asistencia con una mezcla de iones $N_2/Ar/CH_4$ permite obtener diferentes composiciones dentro del triángulo BCN. El análisis por XANES muestra la presencia de compuestos ternarios con estructura cúbica (c-BCN), hexagonal (h-BCN) y de tipo B_xC.
- El crecimiento de fases cúbicas está controlado por la temperatura del sustrato y la transferencia de momento en las colisiones ión/átomo durante la deposición. La promoción de fase cúbica se obtiene en una ventana estrecha en el espacio de momento, que depende la energía de los iones, el flujo de iones y la mezcla de gases. Esta ventana solamente se alcanza cuando la asistencia se realiza con un alto contenido de iones Ar^+.
- El contenido de carbono en la fase h-BCN está limitado al ~10-15 % atómico mientras que en la fase cúbica es ~5 % atómico.
- La estructura cúbica (c-BCN) crece encima de una capa intermedia de h-BCN orientada con los planos basales perpendiculares a la superficie del sustrato.
- El uso de metano (CH_4) en la mezcla de gases para la asistencia permite incrementar el contenido de carbono más allá de los valores obtenidos con la asistencia de N_2 o N_2/Ar. En el caso de h-BCN, la incorporación de carbono en la red hexagonal es efectiva aunque se modifica la estabilidad de los diferentes entornos de carbono. En el caso de c-BCN, la incorporación adicional de carbono a través de la asistencia con CH_4 induce una transformación del c-BCN a h-BCN y el carbono se segrega en regiones grafíticas.
- Las estructuras h-BCN y c-BCN son estables térmicamente hasta 1000°C.

B.3. Aplicaciones y perspectivas de futuro.

- La técnica IBAD permite seleccionar entre un amplio rango de composiciones dentro del triángulo BCN y entre diferentes estructuras. De esta forma, las propiedades mecánicas de los compuestos BCN son muy variadas y, por lo tanto, se puede elegir el material más adecuado para una aplicación específica. Entre los resultados más destacados, se han obtenido durezas hasta 35 GPa, coeficientes de fricción por debajo de 0.06 y estabilidades térmicas por encima de 1000°C.
- La emisión de electrones bajo la irradiación con rayos x puede usarse para caracterizar la potencial aplicación de los recubrimientos de BCN como emisores de campo. Las variaciones de la emisión de electrones en el campo total pueden relacionarse con cambios en la función de trabajo del material. Los resultados obtenidos indican que el principal parámetro que afecta la emisión es la fracción de átomos con la hibridación tipo sp^3, tanto en materiales basados en el carbono como en nitruro de boro.

- Finalmente, nuestro sistema IBAD ofrece la posibilidad de explorar nuevas alternativas en la búsqueda de materiales superduros como son las multicapas. De esta forma, se han descrito varias modificaciones del dispositivo experimental con el objeto de obtener estas estructuras. Entre los posibles configuraciones, sería factible crecer multicapas B_xC/h-BCN, c-BCN/B_xC y c-BCN/h-BCN.

Reunido el tribunal que suscribe en el día de la fecha, acordó calificar la presente Tesis doctoral con SOBRESALIENTE CUM LAUDEM

MADRID 14/11/03

C. Palacín

Asunto

P. Clitalde